Ricardo Alexandre de Azevedo

EFEITOS ANTITUMORAIS DO MASTOPARANO E DO PEPTÍDEO INKKI EM MODELO DE MELANOMA EXPERIMENTAL “*in vitro*” E “*in vivo*”

Tese apresentada ao Programa de Pós-graduação em Toxinologia do Instituto Butantan para obtenção do Título de Doutor em Toxinologia.

São Paulo
2014

Ricardo Alexandre de Azevedo

EFEITOS ANTITUMORAIS DO MASTOPARANO E DO PEPTÍDEO INKKI EM MODELO DE MELANOMA EXPERIMENTAL “*in vitro*” E “*in vivo*”

Tese apresentada ao Programa de Pós-graduação em Toxinologia do Instituto Butantan para obtenção do Título de Doutor em Toxinologia

Orientador: Prof. Dr. Ivo Lebrun

São Paulo
2014

AUTORIZAÇÃO

Eu, Ricardo Alexandre de Azevedo, aluno regular do Programa de Pós-Graduação em Toxinologia, do Instituto Butantan, em nível de Doutorado, sob orientação do Prof. Dr. Ivo Lebrun, declaro estar de acordo com a divulgação da minha Tese em arquivo tipo pdf no site da Secretaria da Saúde do Estado de São Paulo apenas 6 meses após a defesa.

São Paulo, 23 de Julho de 2014

Assinatura do Aluno: ______________________________________

De acordo: ____

Orientador – Prof. Dr. Ivo Lebrun

POS-GRADUAÇÃO EM TOXINOLOGIA
INSTITUTO BUTANTAN

RESULTADO DA DEFESA DE TESE

DOUTORADO

NOME DO ALUNO(A):...

DATA DO EXAME:.............../................ /.................

BANCA EXAMINADORA: Profs. Drs.

NOME	Assinatura	Aprovado(a)	Reprovado(a)
____________________________ (Presidente)	__________________________	( )	( )
____________________________	__________________________	( )	( )
____________________________	__________________________	( )	( )
____________________________	__________________________	( )	( )
____________________________	__________________________	( )	( )

DECISÃO FINAL: APROVADO(A) (   ) REPROVADO(A) (   )

***Comentários da Banca (opcional)*:**

Dedico esse trabalho a Deus e minha família; minha querida e amada esposa Sheila Gil de Azevedo, Pais e irmãos que sempre estiveram presente, incentivando, apoiando e por muitas vezes, me conduzindo em seus braços.

AGRADECIMENTOS

Agradeço a Deus, fonte inesgotável de sabedoria, que possibilitou o desenvolvimento do trabalho.

Á minha querida e amada esposa Sheila Gil de Azevedo por ser mais do que minha companheira, ser meu farol, que diante de todas as dificuldades encontrada durante meu árduo caminho, sempre me conduziu ao porto seguro do meu lar.

Aos meus pais e irmãos pelo incentivo, amor incondicional e por proporcionar as condições de tornar-me a pessoa que sou. Se hoje consigo dar mais um passo em busca dos meus objetivos, devo tudo a vocês.

Ao Prof. Dr. Ivo Lebrun, meu orientador, por acreditar em meu trabalho, pela convivência amiga, pelos ensinamentos, discussões científicas, pela amizade e principalmente, pela imensa contribuição em minha formação acadêmica.

Ao Prof. Dr. Luiz R. Travassos, por ter me recebido em seu laboratório onde foi possível desenvolver todo o presente trabalho. Prof. Travassos, obrigado pelos ensinamentos, não só acadêmicos, mas, pelos diversos conhecimentos compartilhados. Tive o privilégio de conviver e aprender com um grande mestre e pesquisador.

Ao Dr. Alisson Leonardo Matuso, pela imensa contribuição no desenvolvimento racional do trabalho, bem como nas discussões acadêmicas. Dr. Alisson, obrigado pela valiosa contribuição.

Aos amigos da Unidade de Oncologia Experimental da UNIFESP, Carlos Rogério Figueiredo, Marina H. Massaoka, Natália Girola, Camila Fernandes e Rodrigo, pela forma acolhedora que todos me receberam e a enorme amizade desenvolvida no transcorrer de todo trabalho. Meu amigo Carlos, não conseguiria obter grande parte desses resultados sem sua colaboração e amizade, muito obrigado.

Ao amigo e irmão Dr. Adilson Kleber Ferreira, pela amizade, contribuição acadêmica e diversos trabalhos desenvolvidos em conjunto. Meu irmão, através da sua amizade conversamos, discutimos e até divergimos em alguns pontos, mas, tudo isso fez com que eu pudesse dar um passo a mais no meu desenvolvimento acadêmico e pessoal.

À Dra. Norma Yamanouye, do Laboratório de Farmacologia do Instituto Butantan, por gentilmente ceder à linhagem de queratinócitos humanos.

Ao Prof. Dr. Alexandre Marzagão Barbuto, pelas inúmeras discussões e valiosa colaboração nos resultados obtidos em células dendríticas.

Á Dra. Sylvia Carneiro, por sua valiosa colaboração nos experimentos de microscopia eletrônica.

Á Dra. Kerly Fernandes Pasqualoto, pela amizade e contribuição nos dados de modelagem molecular.

Ao Dr. Márcio Zaim, pela amizade e inúmeros ensinamentos correlacionados a síntese que contribuíram para o aperfeiçoamento acadêmico.

Agradeço imensamente aos meus amigos Marcos Antonio de Oliveira Costa e sua esposa Márcia Vieira de Carvalho Costa, pela amizade, companheirismo e apoio nos últimos 15 anos. Vocês expressam fielmente o conceito da amizade verdadeira.

Agradeço ao Dr. Rafael Marques Porto, pela amizade, discussão científica e principalmente pela imensa contribuição para o aperfeiçoamento dos conhecimentos da língua inglesa.

A todos os funcionários do Laboratório de Bioquímica e Biofísica do Instituto Butantan, pelo amparo e apoio para a execução dos ensaios.

Aos novos amigos do Laboratório de Imunologia de Tumores do Instituto de Ciências Biomédicas da USP, pela receptividade e pronto atendimento no delineamento dos ensaios com células dendríticas humanas.

Agradeço a todos os docentes da Pós-graduação em Toxinologia do Instituto Butantan, pela imensa contribuição acadêmica.

Aos membros da Secretaria da Pós-Graduação em Toxinologia do Instituto Butantan, em nome da Kimie e Rosana, pela enorme colaboração administrativa.

Agradeço a todos que de forma direta ou indireta, contribuíram para o desenvolvimento do trabalho.

"Aprendi que as oportunidades nunca são perdidas; alguém vai aproveitar as que você perdeu."

William Shakespeare

RESUMO

Azevedo, Ricardo Alexandre. Efeitos antitumorais do mastoparano e do peptídeo INKKI em modelos de melanomas experimentais *“in vitro”* e “*in vivo****”.*** 2014. 210f. Tese (Toxinlogia) Instituto Butantan, São Paulo, 2014.

O mastoparano (INLKALAALAKKIL) é um tetradecapeptídeo α-hélice e anfipático obtido do veneno da *Vespula lewissi*. O casoparano é um peptídeo catiônico (INKKI) isolado a partir da hidrólise da β-caseina bovina e apresenta motivo homólogo ao matoparano. O objetivo deste trabalho foi avaliar o efeito antitumoral *“in vitro”* e *“in vivo”* do mastoparano e do INKKI em modelo de melanoma experimental. A viabilidade foi avaliada em linhagens tumorais e não tumorigênicas através do método MTT. Adicionalmente, os efeitos do INKKI foram avaliados sobre a cinética de crescimento, adesão, migração e invasão celular em culturas de B16F10. O estudo das fases do ciclo celular foi analisado por citometria de fluxo. A via de sinalização foi padronizada por Western blotting. Os modelos metastáticos e dorsais *in vivo* foram padronizados em animais C57BL/6 e em modelo NOD/SCID/γ_c^{null}. Simultaneamente, a morte celular por apoptose induzida pelo mastoparano foi determinada pelo ensaio de Anexina V-FITC/PI. A perda do potencial de membrana mitocondrial ($\Delta\Psi$m) foi avaliada por citometria em células marcadas com sonda TMRE. A geração da espécie reativa de oxigênio (ROS) foi padronizada usando a sonda DHE. A fragmentação do DNA foi avaliada por eletroforese em gel de agarose e a condensação da cormatina foi analisada pela marcação nuclear com DAPI. O estudo *in vivo* foi padronizado sobre o modelo de melanoma dorsal. Os resultados mostraram que o mastoparano apresentou atividade citotóxica e o INKKI apresentou atividade antiproliferativa. Em adição, os dados mostraram que o INKKI foi capaz de inibir o crescimento celular, a adesão, a migração e invasão. Em complemento, a análise das proteínas mostraram redução nos níveis de GSK3β, N-caderina, fosfo Src Tyr 416 e fosfo FAK Tyr 925 e 397. A análise do ciclo celular mostrou que peptídeo INKKI foi capaz de aumentar a porcentagem da população na fase G1 e diminuição da proporção da fase S. Esses dados foram confirmados por Western blotting onde o tratamento mostrou redução nos níveis das ciclinas D1, D3, NFκ-β e Erk1/2. Adicionalmente, os resultados dos ensaios *in vivo* mostraram que o INKKI reduziu a formação de metástases, inibiu o crescimento do melanoma cutâneo, aumentou a taxa de sobrevida, porém, não apresentou efeito em camundongos imunocomprometidos. Os resultados com o mastoparano mostraram que o peptídeo foi capaz de induzir aumento da população de células positivas para Anexina V. Além disso, induziu diminuição do potencial de membrana mitocondrial, aumentou a geração de ROS, induziu fragmentação do DNA e condensação da cromatina. Também, o mastoprano aumentou a expressão das caspases clivadas 3, 9 e 12, PARP, Bim, Bak, citocromo c, bem como redução da expressão de fosfo BAD

(S112), VDAC, PHB1 e Bcl-XL. Mais importante, o mastoparano reduziu o crescimento do melanoma cutâneo e aumentou a sobrevida. Em conclusão, o mastorparano e INKKI apresentam diferentes mecanismos de ação. O mastoparano induz morte celular através da via mitocondrial intrínseca e o peptídeo INKKI induz parada no ciclo celular. Nós também demonstramos que o INKKI teve um efeito antimetastático e inibiu o volume tumoral *in vivo*. O mastoparano apresentou efeito terapêutico *in vivo.*

Palavras chave: Mastoparano, peptídeo INKKI, efeito antitumoral *in vivo*, parada do ciclo celular; apoptose.

ABSTRACT

Azevedo, Ricardo Alexandre. Antitumor effects of mastoparan and INKKI peptide on "*in vitro*" and "*in vivo*" experimental model melanoma*.* 2014. 210p. PhD Thesis (Toxinlogy). Instituto Butantan, São Paulo, 2014.

Mastoparan (INLKALAALAKKIL) is a α-helical and amphipathic tetradecapeptide obtained from wasp venom *Vespula lewissi*. Casoparan is a cationic peptide (INKKI) originated from the hydrolysis of bovine β-casein, exhibit a motif homology with mastoparan. The aim of this study was to evaluate the effect *in vitro* and *in vivo* of mastoparan and INKKI on an experimental melanoma model. Cytotoxicity was evaluated on tumor or non-tumor lines by MTT assay. INKKI effects on growth kinetics, adhesion, migration and invasion assay on B16F10 cells were evaluated. Study of the cell cycle phases was analyzed by flow cytometry. Cell signaling was carried out by Western blotting. Metastatic and dorsal model *in vivo* tumor was standardized using C57BL/6 male mice and NOD/SCID/γ_c^{null} mice. Simultaneously, tumor cell death by apoptosis induced by mastoparan was determined using the Annexin V-FITC/PI assay. The loss of mitochondrial membrane potential ($\Delta\Psi$m) was evaluated by cytometry on staining cells with TMRE probe. Generation of reactive oxygen species (ROS) was performed using DHE probe. DNA fragmentation was evaluated by electrophoresis in an agarose gel and chromatin condensation was assessed by DAPI staining. *In vivo* study was performed on dorsal melanoma model. The results showed that mastoparan presented cytotoxic activity and INKKI exhibited antiproliferative effects. In addition, date showed that INKKI was able to inhibit growth kinetics, cell adhesion, invasion and migration. Complement, protein analyzes showed decrease of GSK3β, phosphor Src Tyr 416, phosphor FAK Tyr 925 and 397 levels. Cell cycle analysis showed that the INKKI was able arrest in the G0/G1phases and decreased the proportion of the S phase. These data were confirmed by Western blotting, showing that INKKI reduces of Cyclin D1 and D3, NFΚ-β and MAPK/Erk1/2 expression. Additionally, the treatment with INKKI induced reducing metastasis, inhibit of melanoma cutaneous growth, increase of survive rate and did not showed antitumor activity on immunocompromised mice. The results with mastoparan showed that peptide was able to induce increase positive cells populations for annexin V. Furthermore, induced decrease of ΔΨm, increased generation (ROS), induced DNA fragmentation and chromatin condensation. Also, mastoparan increases the expression of cleaved caspases-3, -9 and -12, PARP, Bim, Bak, Cytochrome c as well as decrease of expression of phospho Bad (S112), VDAC, PHB1 and Bcl-2. Most importantly, mastoparan reduced the growth of subcutaneous melanoma and increases of survive. In conclusion, mastoparan and INKK presents different mechanism action. Mastoparan induces apoptosis in melanoma cells through of intrinsic mitochondrial pathway and INKKI induces arrest cell cycle. We also demonstrated that INKKI has antimetastatic effects and inhibited growth of the volume tumor on melanoma cutaneous. Mastoparan presented therapeutic effects *in vivo*.

Keywords: Mastoparan; INKKI peptide; *in vivo* antitumor effects; cell cycle arrest; apoptosis

SUMÁRIO

1. INTRODUÇÃO

1.1 Mastoparanos

Mastoparanos são peptídeos que apresentam de 10 a 14 resíduos de aminoácidos e classificados como degranuladores de mastócitos (ARGIOLAS; PISANO, 1983; HIRAI et al., 1979; NAKAJIMA et al., 1986; KATSU et al., 1990; MENDES et al., 2004). São obtidos a partir do veneno de insetos da família *Vespidae* (NAKAJIMA, 1986) e compartilham importantes características bioquímicas como catiônicos, resíduos hidrofóbicos, possuem região C-terminal amidado e normalmente estão em conformação helicoidal anfipática quando interagem com biomembranas (KATSU et al., 1989). Esses peptídeos apresentam um grande espectro de atividade biológica como, por exemplo, antimicrobianos, ação hemolítica (ARGIOLAS; PISANO, 1983; Nakajima et al. 1986), aumento da ação quimiotática para macrofagos humanos e leucócitos polimorfonucleares (NAKAJIMA et al., 1986), ligação à calmodulina (NAKAJIMA et al., 1986), regulação da proteína G (HIGASHIJIMA et al., 1990), estimulação das fosfolipases A2 e C (ARGIOLAS; PISANO, 1983; KATSU et al., 1990) e permeabilização de bicamadas planares a cátions (KATSU et al., 1990; NAKAJIMA et al., 1986;).

A classe dos mastoparanos foi assim denominada devido ao seu primeiro alvo reconhecido, os mastócitos (HIRAI et al., 1979). Juntamente com os basófilos, são células pertencentes ao sistema imunológico e responsável por desencadear reações alérgicas (IVANOVA et al., 2001). Além apresentarem efeitos contra infecções por algumas bactérias e parasitas, também estão envolvidos em desordens cardiovasculares, neurológicas e gastrointestinais. Quando estimulados os mastócitos induzem a liberação de compostos como a histamina dos basófilos, serotonina das plaquetas, catecolaminas e ácidos adenílicos de células adrenais, citocinas e produtos recém-produzidos como prostaglandina D2, leucotrieno C4 e hidroxi-ácidos graxos. (ENGELS et al., 1997; NAKAJIMA et al., 1986).

Os venenos de vespas sociais são ricos em peptídeos biologicamente ativos, responsáveis por dores prolongadas, edemas, eritemas, reações alérgicas e sistêmicas (LORENZI, 2002). Estes venenos são constituídos por vários tipos de aminas biogênicas, peptídeos e proteínas (NAKAJIMA et al., 1986). Constitutivamente, os componentes peptídicos mais abundantes desses venenos são os peptídeos pertencentes à classe dos mastoparanos. Esses peptídeos são ricos em aminoácidos hidrofóbicos, como leucina, isoleucina e alanina, e também apresentam algumas lisinas em suas sequências primárias, encontradas geralmente nas posições quatro, onze e doze da molécula. Normalmente possuem o resíduo C-terminal amidado, com sequências primárias compostas de resíduos de aminoácidos básicos e hidrofóbicos (NAKAJIMA et al., 1986).

Os mastoparanos de diversas espécies da família *Vespidae* apresentam diferentes graus de homologia em sua estrutura primária. Porém, é possível observar que algumas sequências (motivos) são conservadas entre as espécies e por se localizarem em posições estratégicas em sua conformação espacial, aparentemente são importantes para o desencadeamento dos diversos efeitos biológicos. A Tabela 1 demonstra uma lista dos principais mastoparanos isolados de venenos de vespas, com as respectivas sequências primárias. É importante observar em destaque que o motivo lisina, lisina e isoleucina (KKI) são conservados em pelo menos em 04 (quatro) das 10 espécies apresentadas. Nas outras 06 (seis) espécie é possível notar que o motivo KK (lisina, lisina) está amplamente conservado (NAKAJIMA et al., 1986; HO et al., 1994; HIRAI et al., 1979b; ARGIOLAS; PISANO, 1984; MENDES et al., 2004b; de SOUZA et al., 2004; KONNO et al., 2000).

Tabela 1: Sequência primária dos mastoparanos de diversas espécies de vespas

Espécie	**Peptídeo**	**Sequência Primária**
Vespula lewisii	Mastoparano1	I N L K A L A A L A K K I L
Vespa tropica	Mastoparano-T1	I N L K A I A A F A K K I L
Vespa orientalis	Mastoparano-II1	I N L K A L L A V A K K I L
Vespa crabro	Mastoparano-C1	I N W K A L L AV A K K I L
Vespa analis	Mastoparano A1	I K W K A I L D A V K K V L
Vespa basalis	Mastoparano B2	L K L K S I E S W A K K V L
Vespa mandarina	Mastoparano-M1	I N L K A I A A L A K K L L
Vespa orientalis	HR-I^{4}	I N L K A L A A L V K K V L
Vespa xanthoptera	Mastoparano-X3	I N W K G I A A M A K K L L
Protonectarina sylveirae	Protonectarina-MP 1	I N W K A L L D A A K K V L

Trabalhos publicados anteriormente relataram que em solução aquosa os mastoparanos apresentam uma conformação aleatória ou estrutura secundária não mensurável. Contudo, em solução com trifluoretanol (TFE) exibem hélice- α anfipática (CHUANG et al., 1996). Essa conformação espacial expõe os resíduos hidrofóbicos para um lado da hélice, e na outra face os positivamente carregados como o grupo amina e resíduos de lisina (Figura 1) (KATSU et al., 1990; JONES; HOWL, 2006). Esta configuração é fundamental para ação tóxica destes peptídeos, já que a interação da parte carregada dos fosfolipídeos da bicamada ocorre com a parte catiônica desses peptídeos (KONNO et al., 2000).

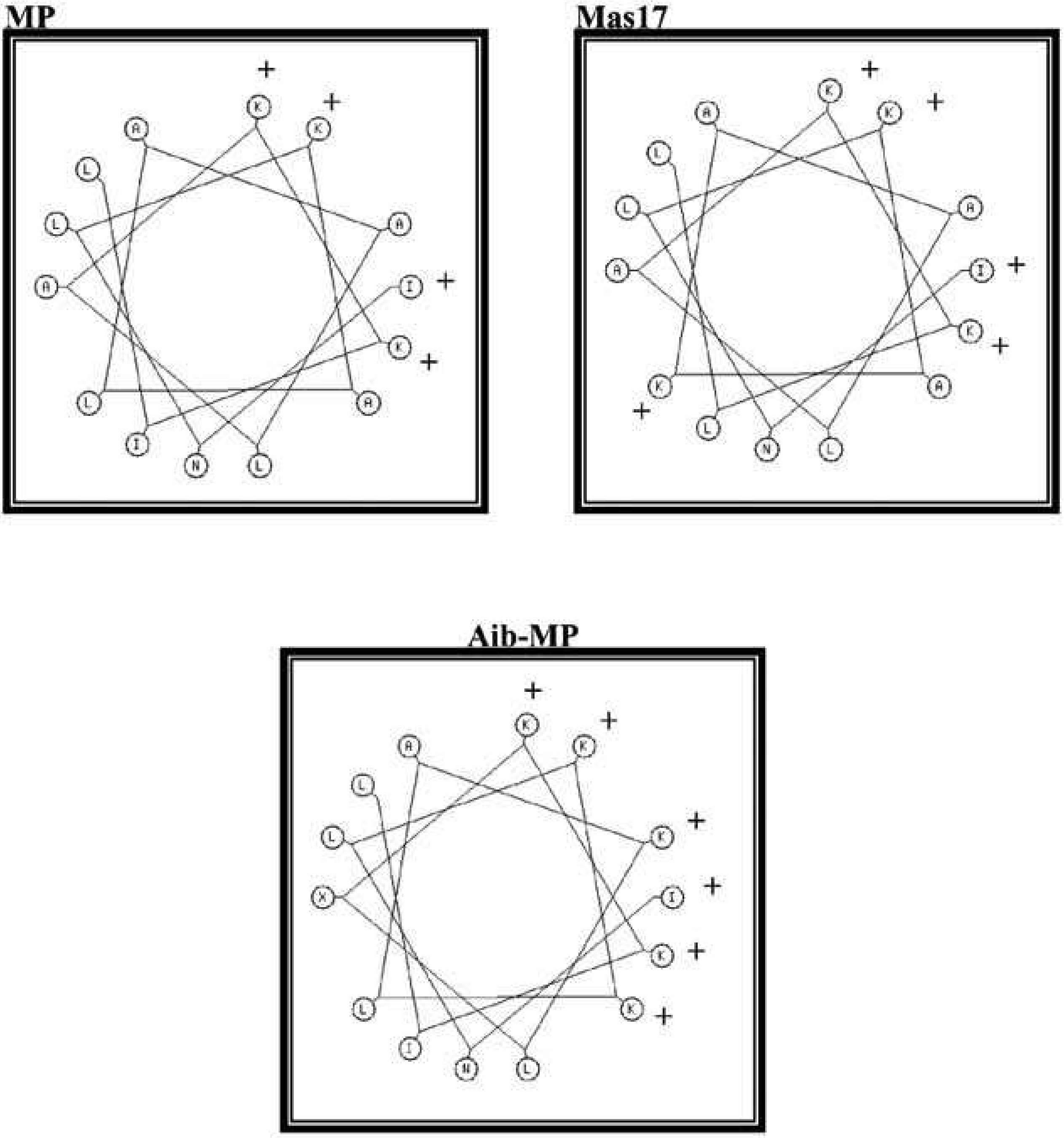

Figura 1. Predição conformacional da estrutura em α-hélice do mastoparan *Vespula lewisii* (MP) dos peptídeos sintéticos análogos Aib-MP e Mas17. Esses modelos suportam a hipótese da formação em α-hélice apresentando a exposição das faces hidrofóbicas, hidrofílicas e a distribuição das cargas positivas (JONES; HOWL, 2006).

As diversas atividades biológicas desempenhadas pelo mastoparan podem estar diretamente relacionadas com as interações dos peptídeos com membranas biológicas assumindo uma conformação em hélice-α anfipática (MATSUZAKI et al., 1996; SCHWARZ; BLOCHMANN,1993), a qual pode causar perturbações nas membranas, conduzindo para um aumento na permeabilidade, e consequentemente, induzir morte celular devido a formação de poros (DANILENKO et al., 1993; MELLOR; SANSOM, 1990).

Os mastoparanos facilitam as ações da fosfolipases purificadas, que causam mudanças na composição dos fosfoliídeos na membrana plasmática, no qual está associada com a degranulação de mastócitos. Essas Fosfolipases, que preferencialmente hidrolisam fosfatidilcolina (PC), provocam a degranulação em células RBL-2H3, uma linhagem de mastócitos de mucosa (IVANOVA et al., 2001).

Outro importante efeito biológico da classe dos mastoparanos está correlacionado com a regulação das funções da família da proteína G. Esses peptídeos atuam de maneira semelhante à dos receptores ligando-se a sítios negativamente carregados da proteína G. Apresentam ainda forte afinidade por fosfolipídeos, assumindo uma conformação ordenada ao se ligarem a eles nas membranas das células-alvo. Assim, a classe dos mastoparanos podem assumir uma orientação adequada em relação às moléculas da família da proteína G e com isso aumentando a sua concentração efetiva na superfície da membrana, próximo às moléculas dos receptores. Os efeitos de ativação pelos mastoparanos são seletivos dentre as proteínas G (WAKAMATSU, 1992).

Os mastoparanos também são considerados ativadores das fosfolipases A2 e C, induzindo um aumento na produção de ácido araquidônico. Peptídeos homólogos isolados do veneno de *Vespa crabro* e *Vespa orientalis* também são capazes de estimular a fosfolipase A2 (PLA2) e causam liberação de histamina de mastócitos peritoniais (ARGIOLAS; PISANO, 1984; NAKAJIMA et al., 1986).

Nas mitocôndrias, os mastoparanos podem desempenhar importantes atividades que conduz a apoptose. A estrutura α-hélice é requerida para que o mastoparanos penetre na membrana mitocondrial através de um mecanismo o qual é dependente do potencial de membrana, alterando a permeabilidade de transição (PT) mitocondrial, induzindo a célula a entrar em apoptose (ARMSTRONG, 2006). Desta forma os mastorapanos podem apresentar-se como uma possível estratégia terapêutica contra com câncer.

O mastoparano (INLKALAALAKKIL) foi isolado e descrito pela primeira vez por Hirai et al., (1979). É um tetradecapeptídeo catiônico, obtido do veneno da *Vespula lewisii,* possui conformação especial em α-hélice e diversos efeitos biológicos (Figura 2). Esse peptídeo é amplamente reconhecido como receptor independe e regulador alostérico da proteína G. Além de modular a atividade da proteína G, esse peptídeo pode se ligar a alvo intracelular como Ca^{2+}-ATPase e promover a liberação de Ca^{2+} a partir do retículo endoplasmático. Também pode se ligar a pequenas proteínas monoméricas GTP como Rho e Rac, fosfolipase D e a membrana mitocondrial. Sendo assim, os efeitos biológicos do mastoparano isolado da *Vespula lewisii*, pode downrregular como consequência da ativação da proteína G ou desencadear outros fenômenos totalmente independentes (JONES; HOWL, 2006).

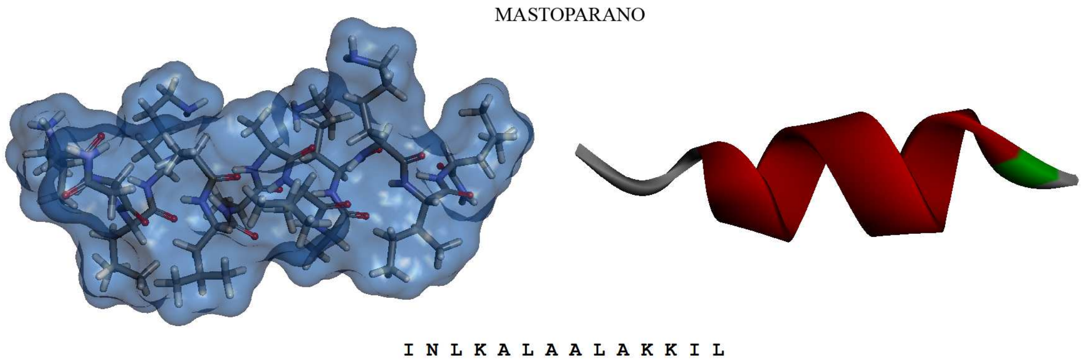

Figura 2. Estrutura tridimensional e conformação espacial do mastoparano. Estrutura demonstrando a α-hélice do mastoparano obtida a partir do software livre Marvin no endereço eletrônico http://chemaxon.com.

1.2 Peptídeo derivado do leite com motivo homólogo ao mastoparano

As proteínas do leite têm sido conhecidas pelo seu potente valor como alimentos funcionais e bebidas que confirmam os benefícios e cuidados com a saúde (FIAT et al., 1993). Essas proteínas são sintetizadas na glândula mamária na forma de precursores de alto peso molecular, sofrem modificações pós-transcricionais no complexo de Golgi, posteriormente são processadas por proteases e secretadas (FIAT et al., 1993).

No leite humano a caseína representa somente de 30-36% do total de proteínas e subdivide-se em, β-caseina, κ-caseína e α_{s1}-caseína. A cadeia α_{s1} da caseína humana é homóloga em sua porção N-terminal quando comparada com as cadeias α_{s1} de outras espécies, como a bovina, de ovelha, de rato, de coelho, e de cabra. A β-caseina humana possui 47% de homologia com a β-caseina bovina (MEISEL, 1997).

A cadeia β da caseína é a mais abundante quantitativamente, e dependendo da forma de obtenção, ela pode ser desmembrada na cadeia γ, que corresponde ao fragmento 29-209 da cadeia β (LAHOV; REGELSON, 1996).

A β-caseina bovina é uma proteína de estruturas abertas, com 5 resíduos de fosfoserina localizados na porção N-terminal, peso molecular de 23 a 980 Da e predominância de estruturas primárias (randomizadas), o que se deve em parte, aos altos teores de prolina distribuídas em toda cadeia polipeptídica. A β-caseina bovina apresenta tanto formação de estruturas em α-hélice quanto em folha β-pregueadas e são proteínas relativamente hidrofóbicas. Os resíduos hidrofóbicos, polares e carregados não se apresentam uniformemente distribuídos, sendo encontrado principalmente na porção C-terminal (resíduos 136-209) (KUMOSINSKI et al., 1993). Regiões fosforiladas podem desempenhar importante papel na ativação das células do sistema imunolgógico. Zhang e Otani (2003) em um estudo *in vivo* utilizando linhagens murinas relataram que os anticorpos reconhecem as regiões fosforiladas da β-caseina bovina (Ser(P)- Ser(P)- Ser(P)) como epítopos intactos ou parte deles.

Dentro dessa cadeia da β-caseina bovina encontram-se diversas sequencias de aminoácidos que podem gerar peptídeos bioativos. Esses peptídeos encontram-se na forma inativa dentro das cadeias polipeptídicas das proteínas originais, chamados de precursores peptídicos. Evidências indicam que os fragmentos peptídicos gerados após a hidrólise dessas macromoléculas, são capazes de atravessar o intestino delgado, atingir os tecidos periféricos, via circulação sistêmica, podendo apresentar ações específicas no trato gastrointestinal ou em sítios mais distantes, alterar o metabolismo celular ou ainda, atuar como vasorreguladores, fatores de crescimento, liberadores de hormônios ou neurotransmissores (ROBERTS; ZALOGA, 1994).

Nos últimos anos diversos autores veem descrevendo várias atividades biológicas atribuídas aos peptídeos gerados pela caseína. As atividades opiáceas como a tolerância, dependência, sedação, indução ao sono, depressão respiratória, bradicardia e hipotensão foram as primeiras a serem descritas. Todas essas atividades foram observadas com as β-casomorfinas e morficetina, além do que, altas concentrações desses peptídeos são encontradas em leite previamente digerido no sangue de recém-nascidos, sendo capazes de diminuir o choro dos bebês e aumentar seu tempo de sono (FIAT; JOLLÈS, 1989).

Entre os peptídeos biologicamente ativos liberados a partir de fragmentos da caseína, um dos mais estudados e caracterizados são os fosfopeptídeos. Esses fosfopeptídeos podem formar complexos com o íon de cálcio e inibir a formação de precipitado entre o cálcio e fosfato (OTANI et al., 2001). O aumento da absorção de cálcio foi demonstrado em ratos cuja dieta rica em caseína leva a formação e acumulo de fosfopeptídes (OTANI et al., 2001). As culturas de células esplênicas de camundongos incubadas com os fosfopeptídeos demonstram capacidade de estimular a proliferação de linfócitos T e B e aumentar os níveis de imunoglobulinas IgA, IgM e IgG (OTANI et al., 2001).

Em outro trabalho, Kawahara et al. (2004) mostraram que a sequência de aminoácidos da β-caseina (1-28) exerce expressivo efeito mitogênico em linfócitos T de linhagens celulares HUT-78, Clone Jurkat E6-1 e MOLT-4, em linfócitos B das linhagens de células BALL, KHM-1B e U266B1 e em monócitos das linhagens de células U939 e HL-60. Nesse trabalho também ficou evidenciado o aumento dos níveis de IgA pela expressão intracelular de IL-6 em culturas de U266B1 e KHM-1B.

A partir da β-caseina bovina foi isolado o peptídeo YPVEP correspondendo a sequência de aminoácidos (114-118), o qual exerce uma atividade quimiotáxica em macrófagos e monócitos, aumentando os níveis de peroxidases responsáveis pela modulação da resposta imune inata, e por induzir a migração e ativação de macrófagos residentes (KITAZAWA et al., 2007).

Outros autores como Maruyama e Suzuki (1982) e Henriques et al. (1987) descreveram peptídeos com atividades anti-hipertensiva agindo como inibidores da Enzima Conversora de Angiotensina (ECA). Esses inibidores podem também aumentar a atividade da bradicinina em várias preparações biológicas. Além dessas atividades, outros trabalhos mostraram que os peptídeos obtidos pela hidrólise apresentam propriedades antimicrobianas e antitumorais (LOPES-EXPÓSITO; RÉCIO, 2008).

Estudos anteriores realizados no Laboratório de Bioquímica e Biofísica do Instituto Butantan isolou, caracterizou e sintetizou o peptídeo INKKI. Esse peptídeo inicialmente foi denomiado de casoparan, por apresentar motivo de lisinha, lisina e isoleucina (KKI) homólogo ao motivo do mastoparano. Ele corresponde ao fragmento 41-46 da cadeia β da caseína, localiza-se inserido dentro de uma estrutura β-pregeadas, próximo de uma região fosforilada com uma sequência de serina fosfato e compartilha importante característica catiônica (Figura 3). Possui atividade potenciadora da bradicinina, aumento em até 80% a fagocitose dos macrófagos residentes peritoniais de camundongos e aumento na liberação de H_2O_2 por macrófagos (LEBRUN et al., 2004; LEBRUN et al., 1995).

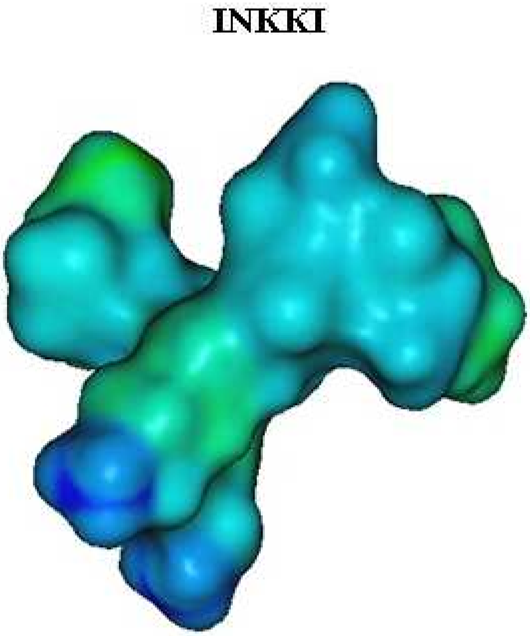

Figura 3.Estrutura do peptídeo INKKI gerada computacionalmente representando o cálculo da distribuição das cargas (hidrofilicicidade/lipofilicidade) usando o método de ClogP/ClogD do software livre Marvim http://www.chemaxon.com. O ClogP (coeficiente de partição *n*-octacnol/águats) expressa lipofilicidade e ClogD considera a ionização da molécula. A superfície verde representa a região pouco hidrofílica e a cor azul regiões mais hidrofílica (AZEVEDO et al., 2012)

1.3 Melanoma

Fatores ambientais como a urbanização, industrialização e exposição a agentes mutagênicos contribuem de forma decisiva para o aumento na incidência de câncer. No Brasil, em 2014, estima-se que surgirão 576 mil novos casos (INCA 2014). Dentre todos os tipos de câncer descritos pela literatura, o câncer de pele continua apresentando alta incidência para ambos os sexos. Apesar de sua letalidade ser considerada baixa, em alguns casos, principalmente onde o diagnóstico é realizado de forma tardio, pode levar a ulcerações e deformidades físicas graves. O melanoma foi descrito pela primeira vez por *Hipócrates* no século V sendo o termo melanoma proposto por CARSWELL em 1938, que relatou as características malignas do tumor (ROBERTS et al., 2002; ALONSO et al., 2004).

Apesar de apresentar uma baixa incidência dentre os tipos de câncer de pele, 3,03 casos por 100 mil, o melanoma apresenta elevada letalidade, com sobrevida abaixo dos 10% (INCA, 2014; STANLEY et al. 2011). O prognóstico desse tipo de câncer pode ser considerado bom, se detectado nos estágios iniciais. Nos últimos anos houveram significativas melhoras na sobrevida dos pacientes com melanoma, principalmente devido à detecção precoce (INSTITUTO NACIONAL DO CÂNCER, 2014).

O melanoma é um tipo de neoplasia que surge pela proliferação sem controle dos melanoblastos, células precursoras dos melanócitos, que são responsáveis pela produção do pigmento da pele. Embora represente apenas 4% dos tipos de câncer de pele, o melanoma é considerado o mais grave devido à sua alta capacidade metastática. Podem ocorrer em qualquer ponto da derme ou no leito ungueal, mesmo em locais não diretamente expostos ao sol, como os olhos, membranas mucosas (boca e genitais), ou dos órgãos internos (ELLERHORST et al., 2004). No processo de transformação e progressão das células tumorais ocorrem interações recíprocas onde há perda de contato com os queratinócitos, que são parceiros dominantes da epiderme capaz de controlar o crescimento, morfologia e fenótipo antigênico dos melanócitos. Esses fenômenos ocorrem através do estabelecimento de contato direto entre as células, feito pelo receptor de adesão E-caderina, que é uma molécula expressa por células endoteliais, e que se encontra mais freqüentemente alterada em tumores (LI GANG et al., 2004). Na epiderme, queratinócitos e melanócitos formam junções aderentes mediadas por proteínas de adesão e junções comunicantes por intermédio das conexinas. A perda de interações da glicoproteína E-caderina está associada à translocação de β-catenina para o núcleo, com consequente transcrição de genes associados à duplicação celular. Frequentemente, melanócitos não tumorais são encontrados na junção dermo-epidérmica, onde passam a interagir com fibroblastos estromais (LI GAN e HERLYN, 2000; HSU et al., 2000).

Os melanócitos são células originárias da crista neural, que migram durante o desenvolvimento embrionário para a epiderme e cuja principal função é a síntese e transferência dos grânulos de melanina para os queratinócitos circunvizinhos (SOUZA, 2004; ALBERTO et al., 2004). O tipo de grânulo de melanina sintetizado pelo melanócito pode ser composto por eumelanina (pigmento marrom ou preto), feomelanina (pigmento amarelo ou vermelho) ou uma mistura de ambos, que irá determinar a coloração da pele (SLOMINSKI, 2004). A progressão do melanoma pode ser dividida em algumas etapas, segundo modelo proposto por Clark et al. (1984). A primeira etapa corresponde á geração de uma lesão hiperplásica, lesão névica ou nevo maduro caracterizado pela proliferação aumentada de melanócitos. Esta lesão é comumente considerada um marcador de exposição a agentes com potencial carcinogênico como, por exemplo, luz ultravioleta. Alguns indivíduos apresentam lesões névicas com atipias arquiteturais importantes, sendo denominados de nevos displásicos (CLARK, et al., 1984; CLARK, 1991). O melanoma de crescimento radial (invasivo *in situ*) caracteriza-se por apresentar células neoplásicas com capacidade de proliferação limitada à epiderme; embora células tumorais possam ser encontradas na derme nestas lesões, mas não há evidencias de que estas células proliferem ativamente neste compartimento. No melanoma fase de crescimento vertical, o seu crescimento é acelerado através da espessura da pele, formando nódulos visíveis e palpáveis e manifestando-se como uma lesão profundamente invasiva, capaz de sofrer metástases precoces. Eles invadem a cavidade da membrana radialmente para a epiderme onde em seguida, se infiltrando verticalmente na derme e o tecido subcutâneo, finalmente entram na microvascularização invadindo os gânglios linfáticos (GRAY-SCHOPFER et al., 2007).

O modelo de estudo de melanoma cutâneo além de ser um excelente modelo para a triagem e estudos pré-clínicos de compostos candidatos a agentes antitumorais, também é considerado um modelo de fácil acompanhamento e avaliação do tratamento. A literatura tem descrito como um modelo clínico para estudo de metástases tumorais (STANLEY et al. 2011).

Desde o surgimento do emprego da quimioterapia para o câncer na década de 40 pós-guerra foram identificados muitos caminhos pelos quais as células cancerosas “escapam” dos agentes químicos. Embora a terapia atual para o câncer dependa principalmente do emprego de cirurgia, radioterapia, quimioterapia e imunoterapia a evolução na compreensão da biologia da transformação maligna e das diferenças no controle da proliferação e morte das células normais e tumorais, proporcionaram a descoberta de novos alvos possíveis para o tratamento do câncer. Neste contexto, como o mastoparano mantém conservado um importante motivo, possivelmente, correlacionado com os efeitos biológicos e o peptídeo da β-caseína também possui esse motivo de lisina, lisina e isoleucina (KKI), o presente trabalho busca validar experimentalmente o emprego desses peptídeos como agentes terapêuticos ou adjuvantes, visando aumentar a eficácia do tratamento e diminuindo a incidência de efeitos adversos.

2.OBJETIVOS

2.1 Objetivo geral

O principal objetivo do presente trabalho foi avaliar os efeitos antitumorais *“in vitro*” e *“in vivo”* do mastoparano isolado do veneno de vespa e do INKKI em modelo de melanoma experimental.

3.MATERIAIS E MÉTODOS

3.1 Obtenção dos peptídeos

O mastoparano foi adquirido comercialmente da Peptide2.0. Os peptídeos (INKKI) e seus análogos (NKKII, INAAI, INDDI, ANKKI, INRRI e INKKY) foram sintetizados em fase sólida pelo método Fmoc (N-(9-fluorenil-metoxicarbonil). Após a fase de síntese a solução teve seu pH ajustado para 4 utilizando-se ácido acético e carregada em um cartucho Sep-Pak C18 (Water Associates) equilibrado com água acidificada. Em seguida foram eluídos com acetonitrila 60% em água acidificada, concentrados em centrífuga a vácuo e purificados por cromatografia líquida de fase reversa, utilizando-se uma coluna preparativa (Aquapore RP 300 C8, 150 x 10 mm, BrownleeTM). O peptídeo INKKI marcado com FITC foi adquirido comercialmente da Peptide2.0 (Chantilly, VA, USA).

3.2 Culturas de linhagens não tumorigênicas

A linhagem de melanócito murinho melan-A foi fornecida por Mary C.S. Armelin (Departamento de Bioquímica, do Instituto de Química da Universidade São Paulo). A linhagem de queratinócitos humanos HaCaT foi gentilmente cedida pela Dra. Norma Yamanouye (Laboratório de Farmacologia do Instituto Butantan, São Paulo/Brasil). As células foram cultivadas em garrafas de cultura de 75 cm² em meio de cultura (DEMEN), suplementado com 10% de soro fetal bovino (SFB) inativado, 10 mM de HEPES, 24 mM de bicarbonato, 40 µg/mL de sulfato de gentamicina e mantidos em estufa contendo atmosfera úmida com 5% de CO_2 a 37℃. Antes das células atingirem a confluência de 100%, foram subcultivadas para ampliação e congelamento em solução contendo 10% de DMSO em SFB e estocadas em nitrogênio líquido (MATSUO et al., 2011).

3.3 Culturas de Linhagens Tumorais

As linhagens tumorais de melanoma murino B16F10-Nex2, melanoma humano A2058, leucemia de células T JurKat, adenocarcinoma de mama humano de linhagens MCF-7, MDA-MB-231 e SKBR-3, carcinoma de células escamosas uterino SiHa e glioblastoma humano U87 foram obtidas pelo Instituto Ludwig para o Câncer e Pesquisa, São Paulo, Brasil. As células foram cultivadas em garrafas de cultura de 75 cm² em meio de cultura (RPMI - 1640), suplementado com 10% de SFB inativado, 10 mM de HEPES, 24 mM de bicarbonato, 40 mg/mL de gentamicina e mantidos em estufa contendo atmosfera úmida com 5% de CO_2 a 37℃. Antes das células atingirem confluência foram subcultivadas para ampliação e congelamento em solução contendo 10% de DMSO em SFB, estocadas em nitrogênio líquido (MATSUO et al., 2010

3.4 Preparo da solução de MTT

A solução de Brometo de 3-[4,5-dimetiltiazol-2-il]-2,5-difeniltetrazólio (MTT) foi obtida pela diluição de 50 mg do pó em 10 mL de PBS (5 mg/mL). A solução foi armazenada ao abrigo da luz e em geladeira.

3.5 Avaliação da viabilidade celular após o tratamento com o mastoprano, do INKKI e de seus análogos. Determinação da concentração inibitória (IC_{50}).

Para a avaliação da viabilidade celular foi utilizado o teste colorimétrico do MTT [3-(4,5-dimetiltiazol-2-1)2,5-difenil tetrazólio brometo]. As diversas linhagens tumorais e normais foram plaqueadas em triplicata na concentração de 10^4/poço em placas de 96 poços e cultivadas por 24 horas em estufa contendo 5% de CO_2 a 37℃. Após o período de incubação as células foram tratadas com concentrações de 15,6 a 500 µM do mastoparano, do INKKI e seus análogos (NKKII, INAAI, INDDI, AIKKI e INRRI) e incubadas por 24 horas.

Após incubação foram adicionados 5µl de MTT (5mg/mL) às células e incubadas por 3 horas. Após este período foram adicionados 100 µL de SDS 30% e as placas foram deixadas overnight e então foi realizada a quantificação da absorbância foi mensurada em comprimento de onda de 570 nm por espectrofotometria (Spectramax-M2, Software Molecular Pro 5.4, Sunnyvale, CA, EUA). A viabilidade celular foi expressa com valores de percentagem em comparação com as células não tratadas.

3.6 Método de exclusão por azul de Tripan

Foi preparada inicialmente uma solução estoque do corante a 0,4 % da seguinte maneira: 400 mg do corante azul de Tripan foram adicionados a 90 mL de água bidestilada (Milli-Q) contendo 810 mg de NaCl e 60 mg de K_2HPO_4. Em seguida, o volume da solução foi ajustado para 100 mL com água bidestilada (Milli-Q). A solução foi aquecida até solubilização completa e o pH ajustado para 7,2 com auxílio da solução de NaOH 1 N. Essa solução estoque foi diluída à concentração de 0,2 %, com água bidestilada (Milli-Q) e armazenada em geladeira.

3.7 Avaliação das alterações morfológica das culturas de melanoma murino B16F10-Nex2

A morfologia celular foi avaliada em culturas de melanoma murino B16F10 após o tratamento com o mastoparano 500 µM e INKKI 500 µM. Após obtenção da confluência, 10^4/poço de células de melanoma murino B16F10-Nex2 foram plaqueadas em triplicata. Com objetivo de correlacionar à morfologia celular com viabilidade celular após o tratamento, as células foram acondicionadas em diferentes temperaturas (37℃ e 4 ℃). Após o tratamento a mor fologia foi acompanhada e microfotografada nos tempos de 0, 8 e 24 horas utilizando microscópio óptico invertido Nikon (MATSUO et al., 2010).

3.8 Efeitos do INKKI e do peptídeo scramble sobre a proliferação celular

Os efeitos do INKKI e seu scramble sobre a proliferação celular foram avaliados em linhagem tumoral de melanoma murino B16F10-Nex2. As células foram plaqueadas com concentração de 10^3 cel/poço em placas de 96 poços e incubadas por 4 horas em estufa contendo 5 % de CO_2 a 37℃. Após o período de incubação as células foram tratadas com 500 µM do INKKI e scramble e incubadas por até 72 horas. A cinética do crescimento celular foi quantificada através da contagem das células viáveis utilizando o método de exclusão do azul de Tripan nos tempos de 24, 48 e 72 horas.

3.9 Inibição da adesão celular em cultura de melanoma murino B16F10-Nex2 tratadas com o INKKI e scramble

A adesão celular foi avaliada em cultura de melanoma murino B16F10-Nex2. Foram empregadas uma monocamada de células B16F10-Nex2, o matrigel e o poliestireno da placa de 96 poços como substratos para a aderência celular. O preparo da monocamada celular foi iniciado no dia anterior ao tratamento, onde as células foram plaqueadas na concentração de 10^5 cel/poço com o objetivo de obter a confluência celular. No dia do tratamento, matrigel foi plaqueado em placas de 96 poços e incubados por 2 horas em estufa contendo 5% de CO_2 a 37℃ para a polimerização. Após os tempos de incubação da monocamada celular e do matrigel, as células B16F10 na concentração de 10^4 células/poço foram pré-tratadas com 500 µM de INKKI e scramble. O controle negativo foi padronizado com o meio RPMI e o veículo utilizado para diluir os peptídeos. Após o pré-tratamento, as células foram plaqueadas sobre os substratos previamente preparados e sobre a superfície de poliestireno da placa de 96 poços e incubadas por 4 horas em estufa contendo 5 % de CO_2 a 37℃. Após o período de incubação os poços foram lavados com PBS e as células aderentes foram tripsinizadas e quantificadas utilizando o método de exclusão do azul de tripan e contadas em câmara de Neubauer.

3.10 Estudo do efeito inibitório da migração celular em cultura de melanoma murino B16F10-Nex2 tratadas com o INKKI e scramble

A avaliação da migração celular foi padronizada em células de melanoma murino B16F10-Nex2. As células foram plaqueadas na concentração de $2{,}5\text{x}10^5$ células/poço e incubadas por 24 horas em estufa contendo 5% de CO_2 a 37℃. Após obtenção da confluência foi realizado um "risco" no centro de cada poço com auxílio de uma ponteira para micropipetas P1000. Em seguida os poços foram lavados com PBS e as células tratadas com 500 µM de INKKI e scramble. O controle negativo foi padronizado com o meio RPMI e o veículo utilizado para diluir os peptídeos. As imagens foram adquiridas nos tempos de 0, 4, 8 e 24 horas e a quantificação da migração foi determinada pela área percorrida pelas células e expressas em porcentagem utilizando o Software Wimasis Image Analisys.

3.11 Inibição da invasão celular *in vitro* em cultura de células B16F10-Nex2 tratadas com o INKKI e Scramble

Para o ensaio de invasão em matrigel foi utilizado o sistema *BioCoat Matrigel Chambers* (BD Biosciences) em placa de 24 poços e poros de 8 µm. Durante a preparação do sistema, o matrigel foi diluído em PBS gelado, adicionado no compartimento interno do transwell e incubado por 30 minutos a 37 ℃ e 5% CO_2. Após a polimerização do matrigel, as células de melanoma B16F10-Nex2 foram plaqueadas no compartimento interno do transwell com concentração de $2{,}5\text{x}10^5$ em meio RPMI sem adição de SFB e tratadas com 500 µM de INKKI e scramble. O meio RPMI suplementado com 10% de SFB foi utilizado como agente quimiotático. Foram plaqueados 500 µL desse meio completo no compartimento externo ao transwell. O controle negativo foi padronizado com o meio RPMI e veículo utilizado para diluir os peptídeos. O sistema foi incubado por 24 horas em estufa contendo 5% de CO_2 a 37℃.

Após 24 horas as células que migraram através do matrigel foram fixadas com glutaraldeído 5% diluído em PBS, lavado 3x com água destilada e então coradas com Giensa. Após nova lavagem com água destilada para retirada do excesso do corante, o compartimento interno do Transwell foi limpo com haste de algodão. As células que invadiram foram contadas sobre lupa com aumento de 4x.

3.12 Análise das fases do ciclo celular das células B16F10-Nex2 tratadas com o INKKI e scramble

Para o estudo das fases do ciclo celular do ciclo celular as células de melanoma murino B16F10-Nex2 foram plaqueadas em placas de 12 poços na concentração de $2x10^5$ cel/poço. Para sincronização, as células B16F10 foram plaqueadas com meio RPMI sem adição de SFB. Após 24 horas de incubação o meio sem SFB foi aspirado e as células foram tratadas com 500 µM de INKKI e scramble diluídos em meio RPMI suplementado com 10% de SFB e incubado por mais 24 horas em estufa contendo 5% de CO_2 a 37℃. O controle negativo foi padronizado com o meio RPMI e veículo utilizado para diluir os peptídeos. Após o período de incubação do tratamento, 10^6 células B16F10-Nex2 foram tripsinizadas e centrifugadas a 240 *g* por 5 minutos. O pellet foi ressuspenso em 300 µL de HSF (0.1% DE Triton X-100, 0.1% de citrato de sódio e 50 µg/mL de Iodeto de Propídeo, 10 µg/mL de RNAse (Sigma) e incubados a 4℃ por 1 hora na ausência de luz. Os dados foram adquiridos em citometria de fluxo (BD FACSCanto II, Franklin Lakes, NJ, EUA). Para a determinação da porcentagem de células em cada fase do ciclo, utilizou-se o algoritmo Dean Jett-Fox, do software FlowJo (TreeStar Inc., Ashland, OR, EUA).

3.13 Preparação do extrato do lisado celular das células B16F10-Nex2 tratadas com o INKKI e scramble

As células B16F10-Nex2 na concentração de 10^6 foram tratadas com 500 µM do INKKI e scramble e incubadas por mais 24 horas em estufa contendo 5% de CO_2 a 37℃. O controle negativo foi padronizado com o meio RPMI e o veículo utilizado para diluir os peptídeos. Após a incubação, as células foram lavadas com PBS e lisadas adicionando 100 µL de tampão de amostra de SDS 1x (62.5 mM Tris-HCl, pH 6.8 at 25℃, 2% w/v SDS, 10% glicerol, 50 mM DTT, 0 .01% w/v azul de bromofenol). O lisado foi transferido para tubos de microcentrífugas na presença de gelo. As amostras foram sonicadas por 15 segundos, e desnaturadas a 95℃ por 5 minutos, centrifugadas a 240 *g* por 10 min e armazenadas a -20℃.

3.14 Análise da sinalização celular induzida pelos peptídeos

Para análise dos mediadores do ciclo e migração celular, foi padronizado o ensaio de Western blotting a partir dos lisados celulares obtidos da cultura das células de melanoma B16F10-Nex2 tratadas com os peptídeos, conforme descrito acima. As proteínas de cada amostra foram separadas por eletroforese em gel de SDS-PAGE 10% e em tampão contendo 2,5 mM de Tris-HCl (pH 8,0), 19 mM de glicina e 0,3 mM de SDS. A seguir as amostras foram transferidas para membranas de nitrocelulose (Protran, Schleicher e Schuell, EUA) em tampão contendo 1,2 mM de Tris-HCl (pH 8,0), 9,6 mM de glicina e 20% de metanol. A eficácia das transferências foi verificada através da coloração das membranas com o corante Ponceau S (Sigma), seguida por bloqueio em solução contendo 5% de leite em pó desnatado (Nestlé, Brasil) diluído em PBS. Após o bloqueio foram realizadas 03 (três) lavagens de 10 minutos com TTBS (20 mM Tris-HCl (pH 7,6), 150 mM de NaCl e 0,1% de Tween 20 (pH 7,6)) por 2 horas. Após as lavagens as membranas foram incubadas por 24 horas, a 4℃ sob agitação constant e com os seguintes anticorpos primários: anti-ciclina D1 mouse, anti-ciclina D3 mouse, anti-ciclina A mouse, anti-NFκ-B rabbit, anti-fosfo Akt (Thr308) rabbit, anti-β-Cadenina rabbit, anti-c-Raf, anti-fosfo c-Ras, anti-fosfo p38 (Thr 180/Tyr182) rabbit, anti-fosfo MAPK rabbit, anti-fosfo GSK3β (Ser 9) rabbit; anti-N-Caderina rabbit, anti-Src rabbit, anti-fosfo Src (Tyr 416) rabbit, anti-FAK rabbit, anti-fosfo FAK (Tyr 925) rabbit e anti-fosfo FAK (Tyr 397) rabbit. Todos os anticorpos primários foram adquiridos da Cell Signaling Technology (Beverly, MA). Após a incubação com os anticorpos primários, as membranas foram lavadas com TTBS por 30 minutos e incubadas por 1 hora a temperatura ambiente sob agitação com o anticorpo secundário conjugado com IgG horseradish peroxidase, adquirido da Sigma-Aldrich (St. Louis, MO). Após a incubação com o anticorpo secundário, as membranas foram lavadas com TTBS e adicionado o substrato quimioluminescente Luminata^{TM} e as membranas foram reveladas e analisadas em sistema Fotodocumentador ImageQuant LAS4000 (GE). Todas as bandas foram normalizadas pela da banda da beta-actina.

3.15 Preparação de células da medula óssea de camundongos C57BL/6 e diferenciação de macrófago

Células frescas de medula óssea de camundongos C57BL/6 foram utilizadas para obtenção de macrófagos, por meio de sua incubação com sobrenadante de meio condicionado de células L929, como fonte de fator estimulante de colônia granulócito/macrófago (GM-CSF) conforme descrito por Fischer, et al (1988). As células foram suspendidas em 10 mL de meio de diferenciação de medula óssea, o qual consiste de RPMI-1640 (Gibco, Grand Island, NY, EUA) suplementado com 20% SFB, 30% de sobrenadante de meio condicionado de células L929, 100 U/mL de penicilina, 100 µg/mL de estreptomicina e 2nM de l-glutamina (Sigma-Aldrich, St. Louis, MO, EUA). As células foram semeadas em placa de Petri Optilux (BD Biosciences, Franklin Lakes, NJ) e incubadas em uma atmosfera de 5% de CO_2 a 37 ℃. Após 4 dias, 10 mL de meio fresco foram adicionados, seguindo-se incubação adicional de 3 dias foi procedida. Para a obtenção dos macrófagos, o sobrenadante das culturas foi descartado e as células aderidas (macrófagos) foram lavadas com 15 mL de PBS estéril. Em seguida, as células foram centrifugadas a 240 *g* por 5 min, resuspensas em 10 mL de RPMI-1640 e utilizadas nos experimentos descritos.

3.16 Ensaio de ativação de macrófagos por dosagem de óxido nítrico (NO)

Para estudar a resposta da imunidade inata mediada pelos peptídeos que apresentaram potencial protetor *in vivo*, foi analisada a produção de NO induzido em macrófagos derivados de medula óssea. Os macrófagos derivados de medula óssea foram isolados de fêmur de camundongos sacrificados por deslocamento cervical. As patas traseiras foram dissecadas e cada fêmur isolado em solução salina estéril. As extremidades de cada fêmur foram removidas e com o auxílio de uma seringa de 10 mL estéril, a medula óssea foi obtida em placa de petri estéril pela adição de 10 mL de meio L (50% RPMI, 30% sobrenadante de cultura de células L929, 20% SFB) no interior de cada fêmur. As placas foram incubadas a 37 ºC e 5% de CO_2 por 7 (sete) dias para diferenciação das células progenitoras em macrófagos. Após o período de incubação, $5x10^5$ macrófagos foram plaqueados em placas de 24 poços e incubados por 6 h a 37 ℃ e 5% CO_2. Após o período de incubação, os macrófagos foram tratados com o INKKI nas concentrações de 100 a 0.1 µM e em seguida, os macrófagos foram ativados com IFN-γ (100 U/mL) e LPS (200 ng/mL) e incubados por até 72 h a 37 ℃ e 5% CO_2. Alíquotas de 100 µL do sobrenadante de cultura foram obtidas e quantificadas com 100 µL de reagente de Griess nos pontos de 24 h, 48 h e 72 h a 550 nm em leitora de placas.

3.17 Avaliação da internalização do peptídeo INKKI por microscopia confocal em linhagem de melanoma murino B16F10-Nex2

Os efeitos biológicos desencadeados através do tratamento pelos diversos compostos estão diretamente correlacionados com sua localização, seja na superfície celular, no citoplasma ou no núcleo. Determinar a localização e tráfego do peptídeo foi um importante passo que trouxe evidências sobre o mecanismo de ação. A localização foi avaliada por microscopia confocal em células de melanoma murino B16F10-Nex2 na presença de 500 µM do INKKI marcado com FITC (verde). As células obtidas da cultura foram cultivadas na concentração de 10^4 em lamínulas redondas e incubadas por 1 e 24 horas a 37 ℃ . Após o tratamento, as células foram lavadas com PBS e fixadas com formaldeído 2% por 30 minutos a temperatura ambiente. Logo em seguida as células foram permeabilizadas com 0,1% de Triton X-100 por 30 minutos. As células foram lavadas novamente com PBS e incubadas com 10 µg/mL de 4’,6-diamidino-2-fenilindol (DAPI, Invitrogen, Carlsbad, CA, EUA) por 10 minutos a temperatura ambiente. As células B16F10-Nex2 duplamente marcadas com o INKKI FITC e DAPI foram adquiridas utilizando o microscópio Carl Zeiss LSM780, 488nm argônio com aumento de 40 e 60x.

3.18 Análise da condensação da cromatina

Células de melanoma murino B16F10-Nex2 na concentração de 10^4/poço foram cultivadas em placa de 96 poços e incubadas com 165 µM de mastoparan por 18 horas. Em seguida, as células foram lavadas com PBS, fixadas por 30 minutos a temperatura ambiente com formaldeído 2% e coradas com 10 µg/mL de DAPI

(Invitrogen, Carlsbad, CA, EUA), por 10 minutos para avaliação da cromatina. Após esse período as células foram observadas em microscópio de fluorescência empregando objetiva de 20 e 40x. As analises de fluorescência foram conduzidas em microscópio Olympus BX-51 e filtros com comprimento de onda de excitação de 340 nm e de emissão de 450 nm objetiva de 40X. As imagens foram analisadas com software ImagJ (HTTP://rsb.info.nih.gov/ij/).

3.19 Degradação de DNA

Células B16F10-Nex2 na concentração de 5 x 10^5/poço foram plaqueadas em placas de 6 poços e incubadas por 6 horas a 37℃. A pós o período de incubação, as células foram tratadas com 165 µM de mastoparano e incubadas por 3 horas a 37 ℃. O DNA foi isolado após lise das células em tamp ão TELT (50nM Tris-HCl pH 8,0, Triton X-100 0,4%, 2,5 mM EDTA pH 9,0 e 2,5 M de LiCl). O lisado foi centrifugado por 20 min (240 g) a 4 ℃. O tampão fenol equilibra do (1:1 v/v) foi adicionado, seguido por centrifugação e adição de clorofórmio (1:1 v/v) para a formação da fase aquosa. Os tubos foram centrifugados (15 min, 240 g, 4 ℃), a fase aquosa foi coletada e o DNA foi precipitado com acetato de sódio 3 M, pH 7,0 e etanol absoluto (1:0,1:2,5 v/v) após incubação a -80 ° por 20 min. O DNA foi precipitado e diluído em 50 µg/mL de RNAse-A (Invitrogen, Carlsbad, CA, EUA). O DNA extraído foi submetido a eletroforese em gel de Agarose 1% com brometo de etídio (0,5 µg/mL) em tampão TBE (2 nM de EDTA, 90 nM Tris-HCl, 90 nM de ácido bórico, pH 8,0) a 100v. O maracador de peso molecular de mil pares de bases (1Kb) (Gibco, Grand Island, NY, EUA) foi utilizado para comparação dos tamanhos das bandas obtidas. Após a eletroforese, o DNA foi fotografado e analisadas em sistema Fotodocumentador ImageQuant LAS4000 (GE) após exposição a luz ultravioleta (UV).

3.20 Determinação dos efeitos pró-apoptóticos através do teste da Anexina V

As proporções de células apoptóticas foram detectadas utilizando o teste que marca a externalização da fosfatidilserina exposta na superfície extracelular da membrana plasmática, marcado com Anexina V (Boehringer-Mannheim GmbH, Mannheim-Germany) e Isotiocianato de fluoresceína-FITC (Sigma®). As células também foram marcadas com iodeto de propídeo-ficoeritrina-PE (Sigma®) o que permite a identificação da população que apresentou perda da integridade da membrana plasmática. A concentração de 5 x 10^5 células de melanoma murino B16F10-Nex2 foram tratadas e incubadas por 12 horas com o mastoparano a 165 µM. Após o período de incubação as células foram separadas com tripsina 2% e lavadas com PBS a 37℃, centrifugadas a 834 *g* por 10 minutos a 4℃. As células foram incubadas com 4µg/mL anexina V e 1,8µg/µL de PI por 1 hora a 37ºC, centrifugadas a 240 *g* por 10 minutos a 4℃ e ressuspensas em 400µL de tampão de ligação fornecido pelo fabricante. Foram analisados 10.000 eventos para cada amostra citômetro FACSCanto II (BD Bioscience, Franklin, NJ, EUA) e analisadas utilizando o software FlowJo (TresStar Inc., Ashland, OR, EUA).

3.21 Análise ultraestrutural por Microscopia Eletrônica de Transmissão

Após 3 e 12 horas de tratamento com 165 µM de mastoparano, as células de melanoma murino B16F10-Nex2 foram lavadas 2 vezes com PBS e fixadas com glutaraldeído 2,5%, paraformaldeído 4% e tampão fosfato 0.1M pH 7.2, por 2 horas à 4ºC. As células foram descoladas da placa de 6 poços com um *cellscraper* e centrifugadas a 240 *g* por 10 minutos. Posteriormente, as células foram fixadas em tetróxido de ósmio a 1% (diluído em tampão fosfato) por 30 minutos. As células foram lavadas novamente, desidratadas em acetona e embebidas em Epon. As secções foram contrastadas com acetato de uranila por 30 minutos e citrato de chumbo por 5 minutos. As grades contendo as células foram analisadas em um Microscópio Eletrônico de Transmissão Jeol 1200 EXII (Tókio, Japão).

3.22 Avaliação do aumento nos níveis de ânion superóxido intracelular induzido pelo mastoparano

A produção de ânion superóxido foi determinada através do ensaio com dihidroetídio (DHE, Invitrogen, Carlsbad, CA, EUA), que quando oxidado pelo radical ânion superóxido, é convertido em etídio e emite fluorescência em vermelho. As células de melanoma murino B16F10-Nex2 na concentração de 5 x 10^4 foram cultivadas em placas de 24 poços e tratadas com 165 µM de mastoparano e incubadas com 3 e 6 horas a 37 ℃ e 5% CO_2. O controle positivo foi padronizado utilizando 5 mM H_2O_2 (peróxido de hidrogênio) a 37 ℃ por 40 min. A ana lise por microscopia por fluorescência foi analisadas em no microscópio Olympus BX-51, com objetiva de 40X. As imagens foram analisadas com software ImagJ (HTTP://rsb.info.nih.gov/ij/).

3.23 Avaliação do efeito de N-acetilcisteína (NAC) na morte celular induzida pelo mastoparano

As células de melanoma murino B16F10-Nex2 (10^4/poço) foram cultivadas em placas de 96 poços na presença ou ausência de 4 mM de NAC por 4 horas. Logo após esse período, as células foram tratadas com concentrações de 15,6 a 500 µM do mastoparano e incubadas por 24 horas.

Após incubação foram adicionados 5µl de MTT (5mg/mL) às células e incubadas por 3 horas. Após este período foram adicionados 100 µL de SDS 30% e as placas foram deixadas overnight e então foi realizada a quantificação da absorbância foi mensurada em comprimento de onda de 570 nm por espectrofotometria (Spectramax-M2, Software Molecular Pro 5.4, Sunnyvale, CA, EUA). A viabilidade celular foi expressa com valores de percentagem em comparação com as células não tratadas.

3.24 Análise do potencial de membrana mitocondrial ($\Delta\psi m$)

O corante catiônico lipofílico tetrametilrodamina éster etílico (TMRE) entra na célula na forma de um éster que é subsequentemente hidrolisado e convertido a tetrametilrodamina, o qual dependendo do potencial de membrana mitocondrial pode ser reversivelmente acumulado na matriz mitocondrial carregada negativamente. Para análise do $\Delta\psi m$ após o tratamento com 165 µM de mastoparano, 10^5 células B16F10-Nex2 foram incubadas por 1 e 3 horas em placa de cultura de 12 poços a 37 ℃ e 5% CO_2. Após o período incubação, as células foram lavadas com PBS e incubadas com 20 nM de TMRE (Molecular Probes, OR, EUA) por 10 minutos a 37 ℃. As células foram coletadas com solução PBS/tripsina 0,02%/EDTA 0,02% e a fluorescência foi mensurada em FACSCanto II (BD Bioscience, Franklin, NJ, EUA) e analisadas empregando os softwares FACSDiva (BD Bioscience, Franklin, NJ, EUA) e FlowJo (TresStar Inc., Ashland, OR, EUA).

3.25 Determinação da cascata de sinalização da apoptose ativada pela via mitocondrial intrínseca induzida pelo mastoparano

A análise dos mediadores da via mitocondrial intrínseca de apoptose, foi padronizada pelo ensaio de Western blotting a partir dos lisados das células de melanoma B16F10-Nex2 tratadas com 165 µM de mastoparano e incubado por 3 e 12 horas. As proteínas de cada amostra foram separadas por eletroforese em gel de SDS-PAGE 10% e em tampão contendo 2,5 mM de Tris-HCl (pH 8,0), 19 mM de glicina e 0,3 mM de SDS. A seguir as amostras foram transferidas para membranas de nitrocelulose (Protran, Schleicher e Schuell, EUA) em tampão contendo 1,2 mM de Tris-HCl (pH 8,0), 9,6 mM de glicina e 20% de metanol. A eficácia das transferências foi verificada através da coloração das membranas com o corante Ponceau S (Sigma), seguida por bloqueio em solução contendo 5% de leite em pó desnatado (Nestlé, Brasil) diluído em PBS. Após o bloqueio foram realizadas 03 (três) lavagens de 10 minutos com TTBS (20 mM Tris-HCl (pH 7,6), 150 mM de NaCl e 0,1% de Tween 20 (pH 7,6)) por 2 horas. Após as lavagens as membranas foram incubadas por 24 horas, a 4℃ sob agitação constante com os seguintes anticorpos primários: anti-β actina rabbit, anti-pró caspase 3 rabbit, anti-caspase 3 clivada rabbit, anti-pró caspase 8 rabbit, anti-caspase 8 clivada rabbit, anti-pró caspase 9 rabbit, anti-caspase 9 clivada rabbit, anti-pró caspase 12 rabbit, anti-caspase 12 clivada rabbit, anti-PARP clivado rabbit, anti-fosfo Bad (Ser 112) rabbit, anti-Bcl-XL rabbit, anti-Bim rabbit, anti-Bak rabbit, anti-citocromo c rabbit, anti-VDAC rabbit e anti-PBB1 rabbit. Todos os anticorpos primários foram adquiridos da Cell Signaling Technology (Beverly, MA). Após a incubação com os anticorpos primários, as membranas foram lavadas com TTBS por 30 minutos e incubadas por 1 hora a temperatura ambiente sob agitação com o anticorpo secundário conjugado com IgG horseradish peroxidase, adquirido da Sigma-Aldrich (St. Louis, MO). Após a incubação com o anticorpo secundário, as membranas foram lavadas com TTBS e adicionado o substrato quimioluminescente Luminata^{TM} e as membranas foram reveladas e analisadas em sistema Fotodocumentador ImageQuant LAS4000 (GE). Todas as bandas foram normalizadas pela da banda da beta-actina.

3.26 Atividade Enzimática Caspase 3

3.26.1 Preparo do tampão de lise para ensaio de atividade enzimática

A solução utilizada para extração das proteínas e também como meio reacional para medição da atividade de caspases foi composta pelo tampão HEPES 20 mM, NaCl 100 mM, EDTA 1mM, sacarose 10% e o detergente CHAPS 0,1%.

3.26.2 Ensaio de atividade enzimática da Caspase 3

A caspase-3 é uma enzima efetora comum as vias intrínseca e extrínseca da apoptose. O aumento da atividade enzimática caracteriza a apoptose caspase dependente (COHEN, 1997). As células de melanoma murino B16F10-Nex2 foram tratadas e incubadas por 6 horas com o mastoparano 165 µM. Após o período de incubação, a atividade desta enzima foi mensurada através do ensaio fluorimétrico, onde o peptídeo Asp-Glu-Val-Asp (DEVD), substrato específico para caspase-3, ligados ao fluoróforo 7-amino-4-trifluorometil cumarina (AFC) são incubados por 2 horas a uma concentração final de 70 µM com o extrato das células lisadas, adicionado de DTT a uma concentração final de 10 mM. As caspases ativadas clivam a ligação peptídeo-AFC liberando o fluoróforo, que é então dosado por fluorimetria, em comprimentos de onda de 400nm para excitação e 505 para emissão (VON EULER et al., 2002; PERCHELLET et al., 2004).

3.27 Modelo *in vivo* de estudo

3.27.1 Declaração de ética

Este estudo foi realizado de acordo com os princípios em pesquisa com animais aprovado pelo Comitê de Ética para Experimentação Animal da Universidade Federal de São Paulo (UNIFESP) (processo número CEP1234/2011).

3.27.2 Implantes das células tumorais e delineamento animal

Diferentes grupos de camundongos das linhagens C57BL/6 e NOD/SCID/γ_c^{null} foram mantidos no biotério do Departamento de Biologia Celular, Unidade de Oncologia Experimental da Universidade Federal de São Paulo, com aproximadamente 25 g, idade aproximada de seis a oito semanas, dieta de água e ração*.* As suspensões celulares obtidas da cultura de melanoma murino B16F10 foram desprendidas com PBS-EDTA. Em seguida as células foram centrifugadas, lavadas por 3 vezes com PBS e ressuspensas com meio RPMI sem adição de SFB. A concentração celular foi ajustada por contagem em câmara de Neubauer, sendo a viabilidade celular superior a 97%. Nos animais de linhagem C57BL/6 foi injetado o volume final de 100 µL de células B16F10 subcutaneamente na concentração de 10^5 por animal e no plexo retro-orbital $5x10^5$ por animal. Para indução das metástases pulmonares nos animais NOD/SCID/γ_c^{null} foram injetados $5x10^4$ de células B16F10 por animal.

3.27.3 Avaliação dos efeitos antitumorais em modelo singênico de melanoma dorsal

A progressão tumoral foi acompanhada após o 12º dia do implante tumoral e os animais foram eutanasiados por deslocamento cervical quando apresentaram volume tumoral de 3000 mm^3. A eficácia do tratamento no modelo descrito foi acompanhada pelas análises macroscópicas dos tumores dorsais, taxa de sobrevida animal e volume tumoral. O tamanho dos tumores foram avaliados de dois em dias com ao auxílio de um paquímetro digital e o volume foi mensurado em milímetros cúbicos (mm^3) através da equação $V=(0.52xD1^2xD2)$, onde D1 e D2 correspondem ao menor e maior diâmetros em milímetros, respectivamente.

3.27.4 Avaliação da atividade antimetastática em modelo de metástase pulmonar

Os efeitos antimetastáticos foram quantificados após o 14º dia do implante. Os pulmões dos animais eutanasiados foram inspecionados e as colonizações metastáticas (micros e macros nódulos metastáticos) foram quantificados em lupa com magnitude de 20x.

3.28 Delineamento experimental

3.28.1 Inibição do crescimento do melanoma cutâneo em animais tratados com o INKKI e scramble

Após o implante das células tumorais, foram delineados 03 (três) grupos experimentais com 05 (cinco) animais cada grupo. O tratamento teve início após os tumores atingirem 100mm^3. O grupo controle foi tratado com PBS (veículo) e os grupos experimentais foram tratados com 2,5 mg/Kg com o INKKI e scramble por 5 dias consecutivos através da via intraperitoneal.

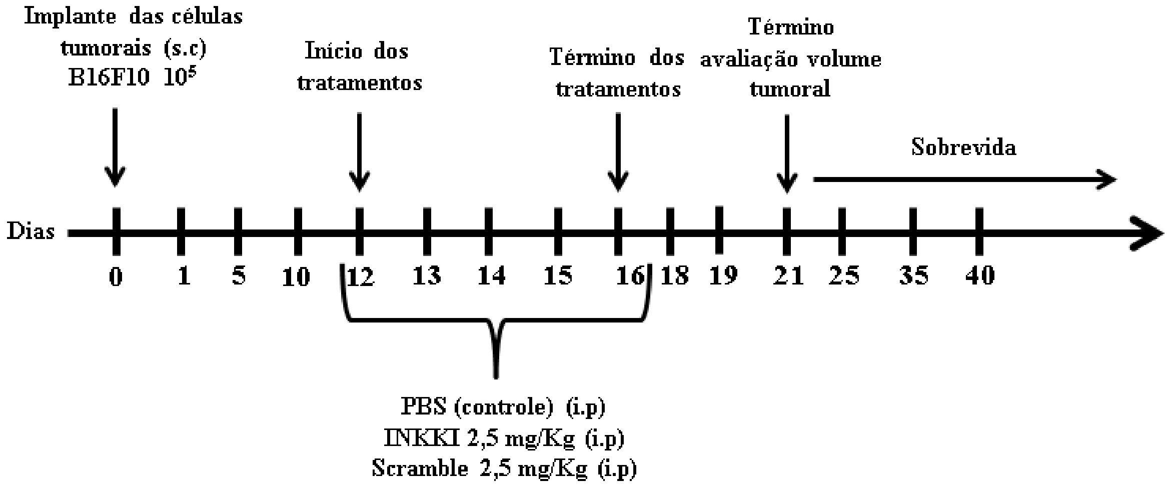

3.28.2 Efeitos antimetastáticos em animais C57BL6 tratados com o INKKI e scramble

Foram delineados 03 (três) grupos experimentais com 05 (cinco) animais cada grupo. Após 24 horas da inoculação, o grupo controle foi tratado com PBS (veículo) e os grupos experimentais foram tratados com 2,5 mg/Kg com o INKKI e scramble durante 5 (cinco) dias consecutivos após a inoculação, através da via intraperitoneal. Os pulmões foram inspecionados no 14° dia após a inoculação das células B16F10 para a quantificação dos nódulos metastáticos.

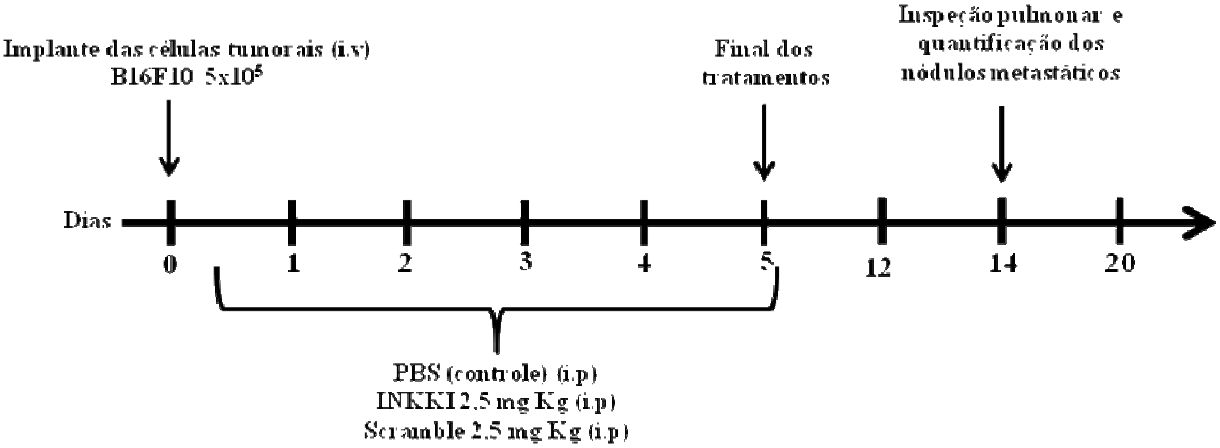

3.28.3 Efeitos antimetastáticos em animais imunocomprometidos NOD/SCID/γ_c^{null} tratados com o INKKI

Foram delineados 02 (dois) grupos experimentais com 05 (cinco) animais cada grupo. Após 24 horas da inoculação, o grupo controle foi tratado com PBS (veículo) e o grupo experimental foi tratado com 2,5 mg/Kg com o INKKI durante 5 (cinco) dias consecutivos após a inoculação, através da via intraperitoneal. Os pulmões foram inspecionados no 14° dia após a inoculação das células B16F10 para a quantificação dos nódulos metastáticos.

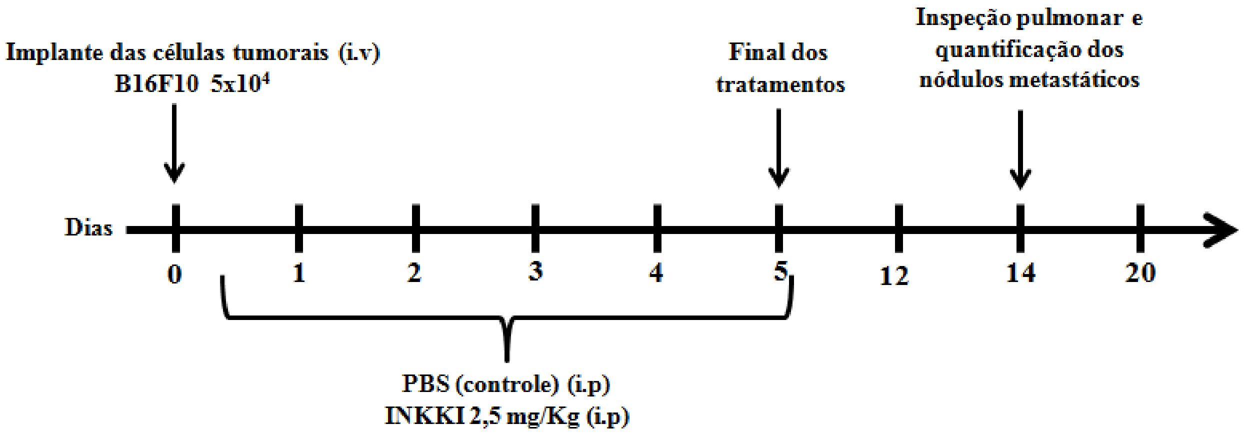

3.28.4 Efeito antitumoral do mastoparano em modelo singênico de melanoma murino.

Foram delineados 02 (dois) grupos experimentais com 05 (cinco) animais cada grupo. Após os tumores dos animais atingiram 100 mm^3, foi iniciado o tratamento sendo que o grupo controle foi tratado com PBS (veículo) e o grupo experimental foi tratado com 5 mg/kg com o mastoparano por 5 dias consecutivos através da via peri-tumoral.

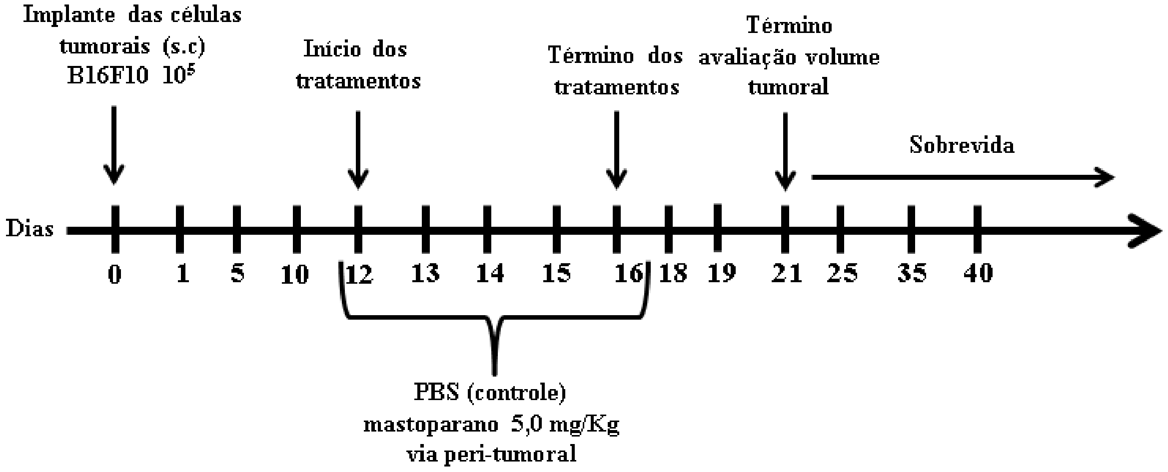

3.29 Análise Estatística

As taxas de sobrevida dos camundongos foram submetidas ao teste estatístico de Kaplan-Meyer seguido do teste de log-rank. Os outros dados foram analisados pela distribuição (Gaussiana ou Normal), seguido do teste t student para a comparação entre os dois grupos utilizando o Software Graph Prism. Para a comparação entre três ou mais grupos os dados foram analisados pelo método de variância ANOVA seguido de teste comparativo múltiplo de Tukey-Kramer utilizando o Software Graph Prism. Os valores foram expressos em média ± desvio padrão (DP) de três experimentos independentes, considerando-se como valores significantes *p<0,05; ** p<0,01; ***p<0,001.

4.RESULTADOS

4.1 Avaliação da viabilidade do mastoparano e INKKI em células de melanoma B16F10, melanócitos melan-A e queratinócitos HaCaT

O estudo dos efeitos sobre a viabilidade celular foi o primeiro delineamento realizado para obtenção da IC_{50} que possibilitou a utilização desses valores para os estudos dos possíveis mecanismos antitumorais. A viabilidade das células tratadas com o mastoparano e INKKI foi avaliada nas linhagens não tumorigênicas de melanócitos melan-A e queratínócitos HaCaT e tumoral de melanoma murino B16F10-Nex2. Os resultados obtidos após o tratamento e incubação por 24 horas mostraram que o mastoparano é um potente agente citotóxico para as células de melanoma murino B16F10-Nex2 nas concentrações de 62,5 a 500 µM com o IC_{50} (165 µM). Em células de melanócitos murinos melan-A e queratinócitos humano HaCaT, o mastoparano exibiu menor citotoxicidade em relação à linhagem de B16F10-Nex2, mostrando-se tóxico entre as concentrações de 250 e 500 µM em ambas as linhagens com o IC_{50} de 411,5 µM e 428 µM, respectivamente (Figura 4). O INKKI reduziu a viabilidade em linhagens de B16F10-Nex2 nas concentrações de 250 e 500 µM com o IC_{50} (386,70 µM). A citotoxicidade foi confirmada através do método de exclusão utilizando azul de tripan, onde a quantificação foi realizada através da contagem das células não marcadas com o corante em câmara de neubauer. O INKKI não apresentou toxicidade em células não tumorigênicas (Figura 5).

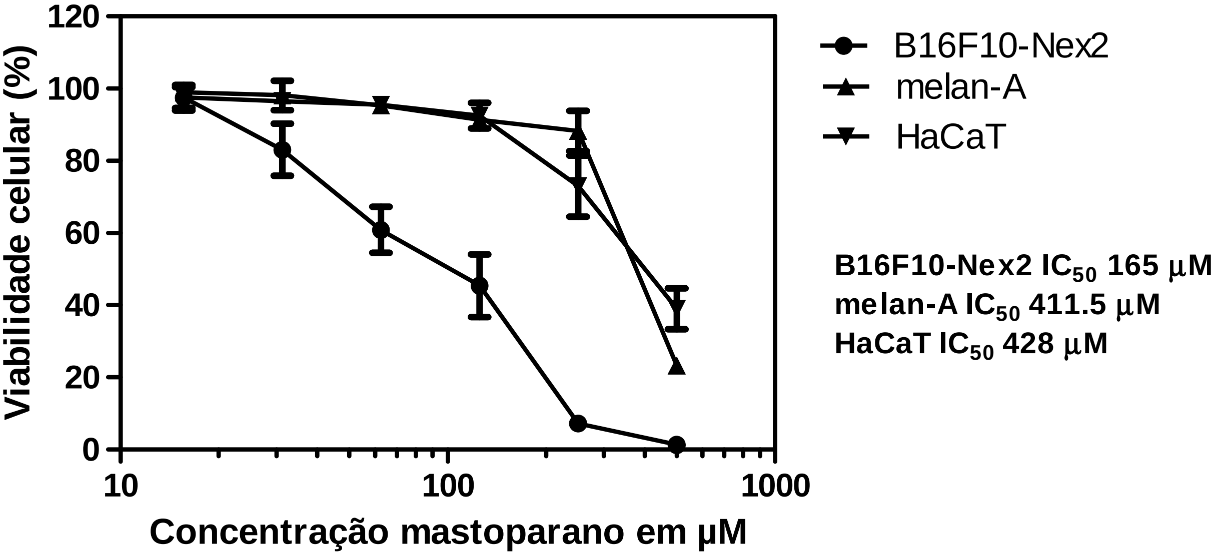

Figura 4. Avaliação da viabilidade após o tratamento com o mastoparano pelo método colorimétrico MTT. As células de melanoma murino B16F10-Nex2, melanócitos melan-A e queratinócitos HaCaT na densidade de 10^4 foram plaqueadas em placas de 96 poços, tratadas com diferentes concentrações do mastoparano e incubados durante de 24 horas. A curva mostra a correlação do efeito dose-resposta expressa em média ± DP de três experimentos independentes.

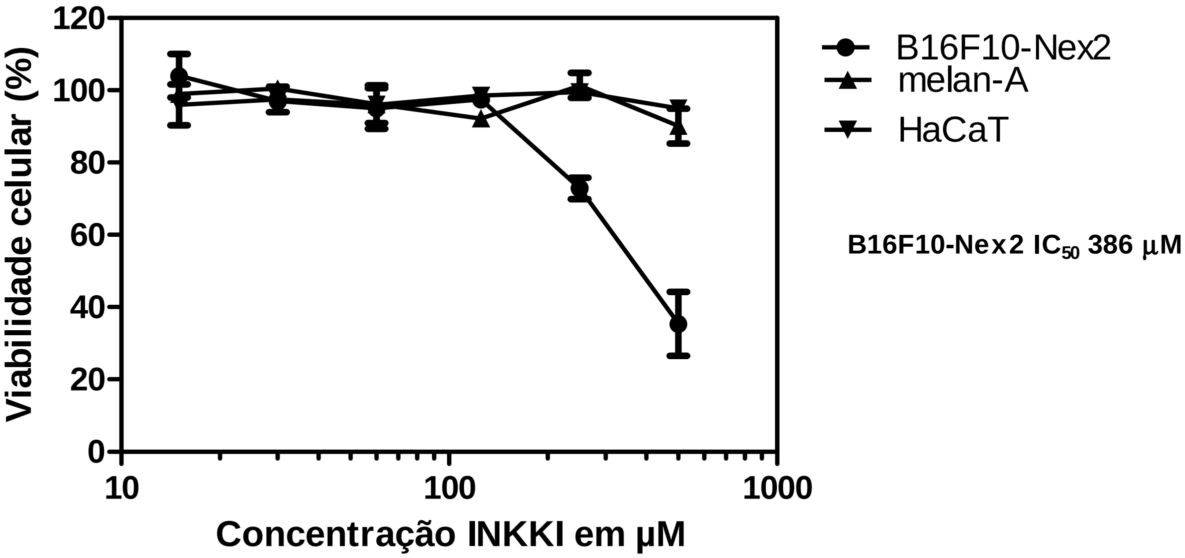

Figura 5. Avaliação da viabilidade após o tratamento com o INKKI pelo método colorimétrico MTT. As células de melanoma murino B16F10-Nex2, melanócitos Melan-A e queratinócitos HaCaT na densidade de 10^4 foram plaqueadas em placas de 96 poços, tratadas com diferentes concentrações do INKKI e incubados durante de 24 horas. A curva mostra a correlação do efeito dose-resposta expressa em média ± DP de três experimentos independentes.

4.2 Avaliação dos efeitos citotóxicos do mastoparano e INKKI em linhagens tumorais

A avaliação da citotoxicidade em diversas linhagens tumorais, além de fornecer significativas informações sobre a efetividade de compostos candidatos a agentes antitumorais, também é um protocolo amplamente utilizado e preconizado pelo National Cancer Institute (http://www.cancer.gov). A citotoxicidade do mastoparano e INKKI foi determinada em linhagens tumorais humanas. Após o tratamento e incubação, os dados mostraram que o mastoparano induziu morte celular *in vitro* em todas as linhagens tumorais testadas, de maneira dose dependente e exibiu diferentes graus de citotoxicidade (Figura 6). O INKKI não apresentou efeito sobre as linhagens de MDA-MB-231 e SiHa, uma vez que não foi possível estabelecer uma correlação do efeito dose-resposta e por apresentar IC_{50} maior que a dose máxima empregada no delineamento experimental. Os resultados mostraram que o INKKI apresentou efeito nas demais linhagens tumorais de maneira dose dependente e exibiu diferentes graus de efetividades (Figura 7). Após obter os dados da toxicidade, foi possível estabelecer as IC_{50} dos tratamentos com o mastoparano e INKKI, sendo que a viabilidade das células em 50% variou de 77.9 µM a 432,5 µM e de 87,53 µM a 486 µM, respectivamente (Tabela 2).

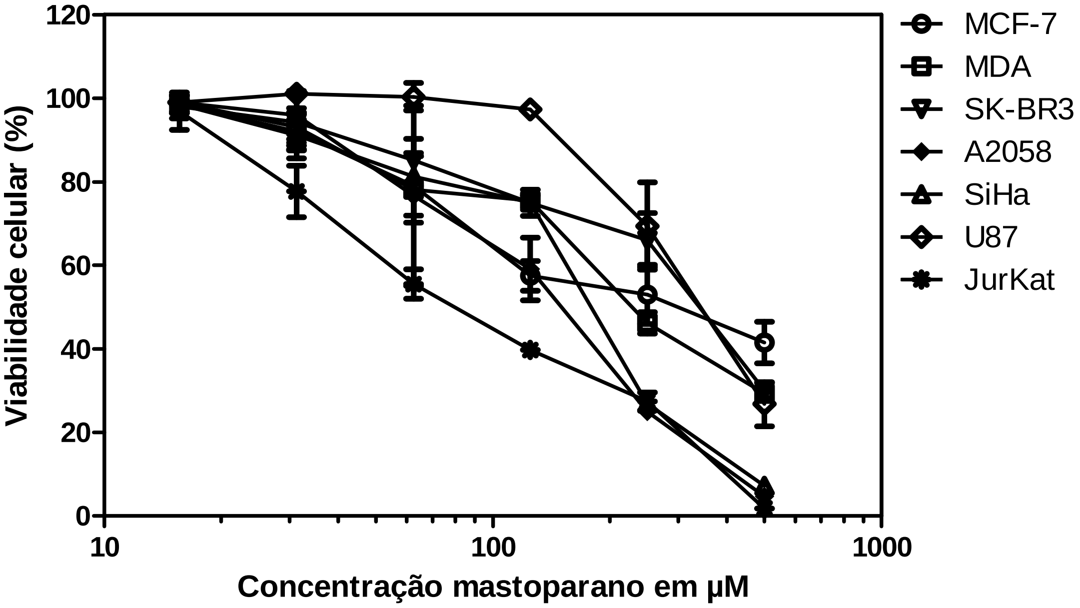

Figura 6. Avaliação da citotoxicidade após o tratamento com o mastoparano pelo método colorimétrico MTT. As diversas linhagens tumorais na densidade de 10^4 foram plaqueadas em placas de 96 poços, tratadas com diferentes concentrações do mastoparano e incubados durante de 24 horas. A curva mostra a correlação do efeito dose-resposta expressa em média ± DP de três experimentos independentes.

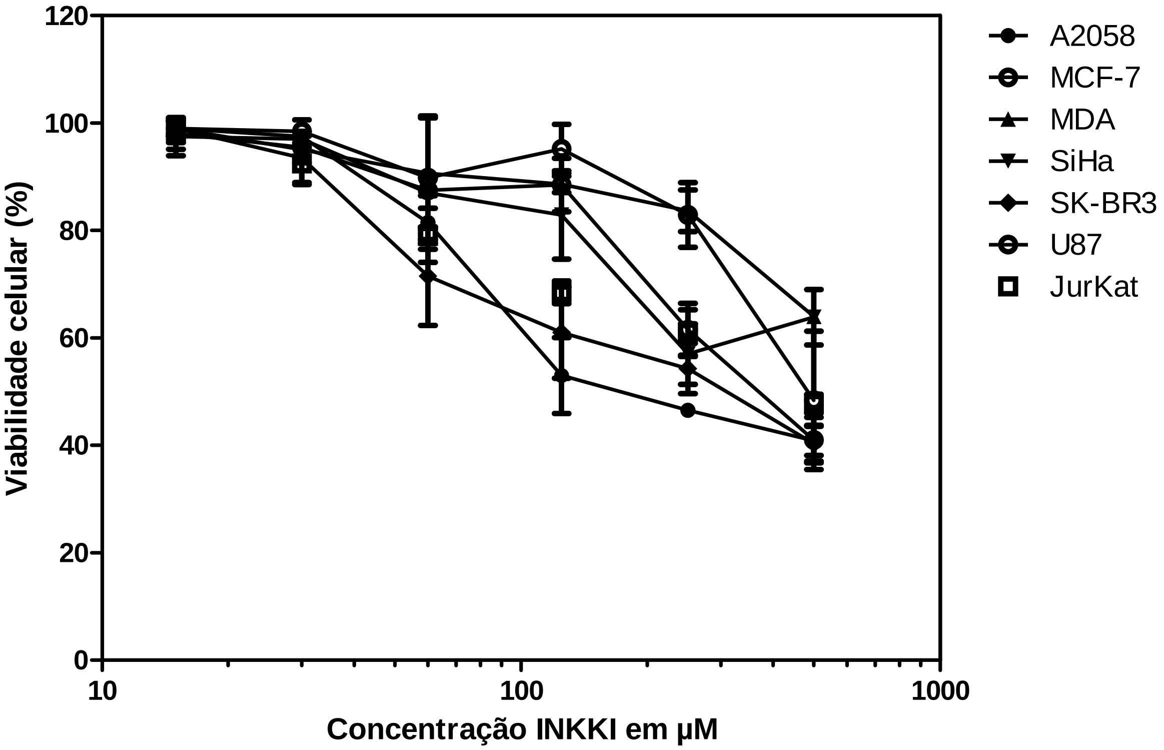

Figura 7. Avaliação da citotoxicidade após o tratamento com INKKI pelo método colorimétrico MTT. As diversas linhagens tumorais na densidade de 10^4 foram plaqueadas em placas de 96 poços, tratadas com diferentes concentrações do INKKI e incubados durante de 24 horas. A curva mostra a correlação do efeito dose-resposta expressa em média ± DP de três experimentos independentes.

Tabela 2. Atividade citotóxica do mastoparano e INKKI em células tumorais

	IC_{50} (µM)* DP (µM)	
Linhagem Celular	mastoparano	INKKI
A2058	140 ± 9,2	87,53 ± 7,25
MCF-7	432,5 ± 10,9	319,01 ± 12,5
MDA-MB-231	251,25 ± 11,5	> 500
SiHa	172,1 ± 8,8	> 500
SK-BR3	320,3 ± 12,5	232,73 ± 11,15
U87	311,7 ± 8,9	486 ± 13,9
Jurkat	77,9 ± 6,7	452,60 ± 9,50

***Valores de IC_{50}, definido como a concentração do peptídeo que induz a inibição de 50% das células observada após 24 horas de tratamento, foram estimados a partir de uma curva dose resposta.**

4.3 Estudo da viabilidade celular correlacionada com as características bioquímicas após o tratamento com os peptídeos análogos ao INKKI

O ensaio de viabilidade celular com os peptídeos análogos ao INKKI foi delineado com o objetivo de correlacionar os possíveis efeitos sobre a viabilidade com as características bioquímicas dos peptídeos. Os efeitos dos peptídeos análogos ao INKKI foram avaliados em linhagens tumorais de melanoma murino B16F10-Nex2. Os resultados obtidos após o tratamento e incubação por 24 horas mostraram que somente o peptídeo análogo ANKKI na concentração de 500 µM apresentou significativa redução na viabilidade celular ($*p < 0.05$). Não foi possível estabelecer a correlação do efeito dose-resposta (Figura 8A). Os demais peptídeos análogos não apresentaram efeitos citotóxicos (Figuras 8B, Figura 9 A e B e Figura 10 A e B).

Esses dados da citotoxicidade foram confirmados através do método de exclusão utilizando azul de tripan, onde a quantificação foi realizada através da contagem das células não marcadas com o corante em câmara de Neubauer.

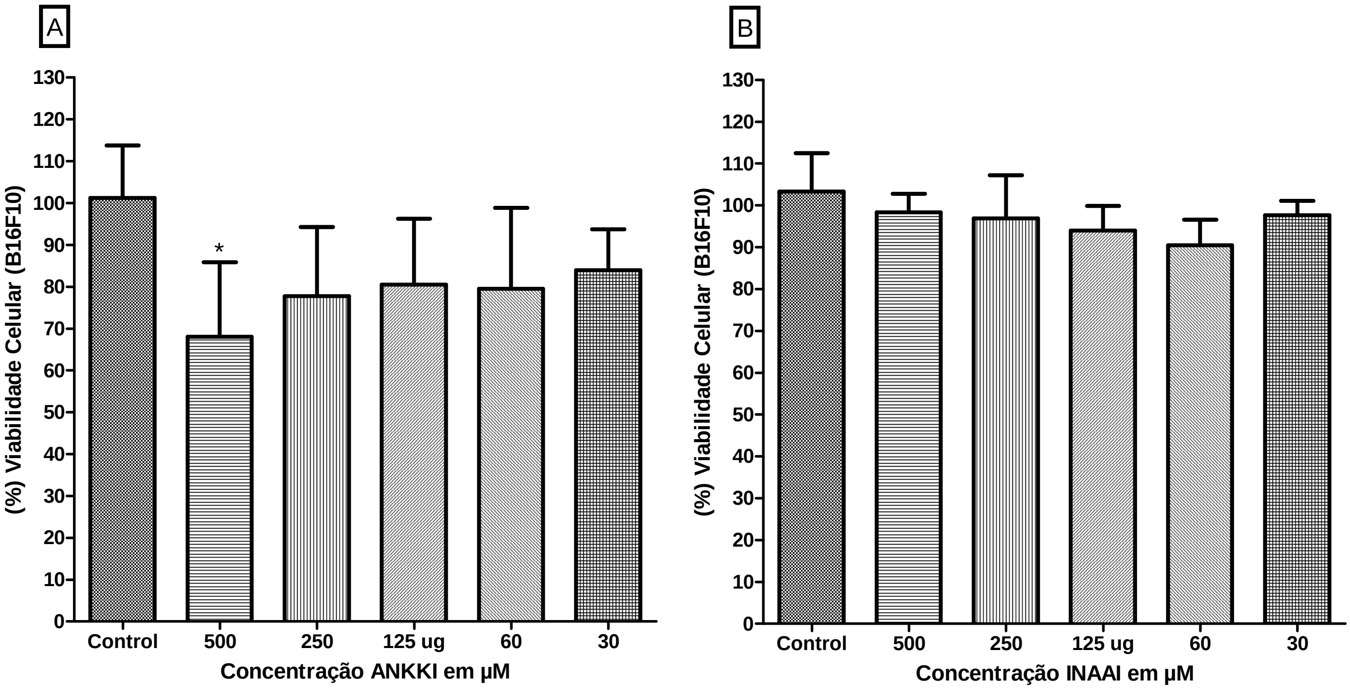

Figura 8. Avaliação da viabilidade celular após o tratamento com os análogos ao INKKI pelo método colorimétrico MTT. As células de melanoma murino B16F10-Nex2 na densidade de 10^4 foram plaqueadas em placas de 96 poços, tratadas com diferentes concentrações dos análogos ao INKKI e incubados durante de 24 horas. A e B mostram que somente o peptídeo ANKKI, apresentou um discreto efeito sobre a viabilidade celular. Os dados foram confirmados através do método de exclusão utilizando azul de tripan, onde a quantificação foi realizada através da contagem das células não marcadas com o corante em câmara de Neubauer.

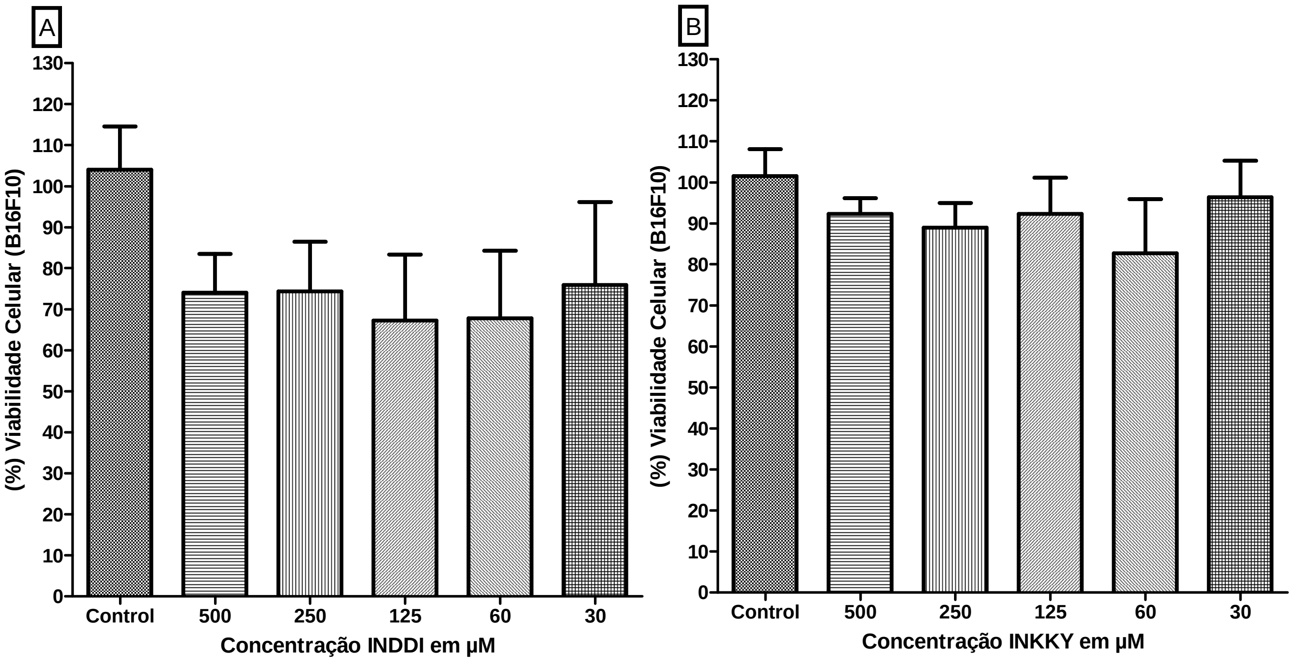

Figura 9. Avaliação da viabilidade celular após o tratamento com os análogos ao INKKI pelo método colorimétrico MTT. As células de melanoma murino B16F10-Nex2 na densidade de 10^4 foram plaqueadas em placas de 96 poços, tratadas com diferentes concentrações dos análogos ao INKKI e incubados durante 24 horas. A e B mostram que ambos os peptídeos análogos ao INKKI (INDDI e INKKY), não apresentaram significativos efeitos sobre a viabilidade celular. Os dados foram confirmados através do método de exclusão utilizando azul de tripan, onde a quantificação foi realizada através da contagem das células não marcadas com o corante em câmara de Neubauer.

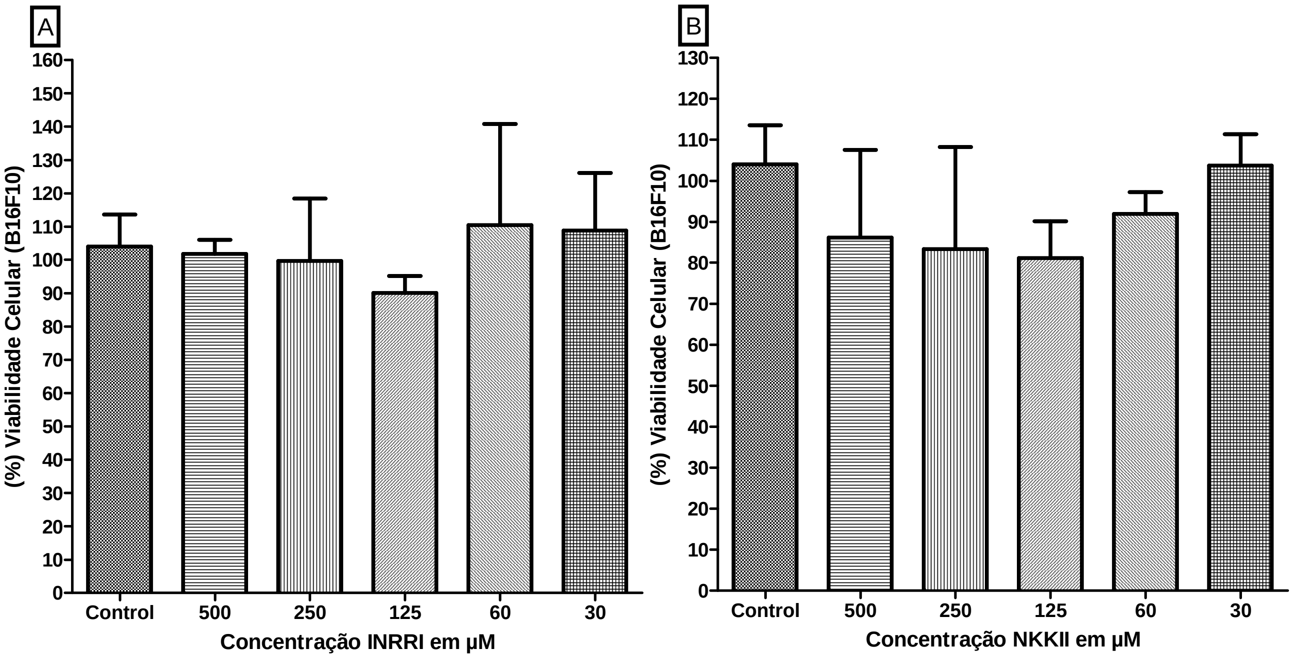

Figura 10. Avaliação da viabilidade celular após o tratamento com os análogos ao INKKI pelo método colorimétrico MTT. As células de melanoma murino B16F10-Nex2 na densidade de 10^4 foram plaqueadas em placas de 96 poços, tratadas com diferentes concentrações dos análogos ao INKKI e incubados durante 24 horas. A e B mostram que ambos os peptídeos análogos ao INKKI (INRRI e NKKII), não apresentaram significativos efeitos sobre a viabilidade celular. Os dados foram confirmados através do método de exclusão utilizando azul de tripan, onde a quantificação foi realizada através da contagem das células não marcadas com o corante em câmara de Neubauer.

4.4 Avaliação dos aspectos morfológicos das células de melanoma murino B16F10-Nex2 cultivadas a 4 ℃ e 37 ℃ e tratadas co m o mastoparano e INKKI.

A análise dos aspectos morfológicos, tais como, perda da adesão e comunicação celular, retraimento do citoplasma, formas arredondadas e perda refringência, fornecem importantes indícios sobre o tipo de efeito biológico desencadeado em resposta ao tratamento com os peptídeos. As diferentes condições experimentais de temperatura também fornecem informações importantes sobre o efeito biológico. As culturas celulares de melanoma murino B16F10-Nex2 foram plaqueadas em placas de 96 poços, incubadas com o mastoparano a 500 µM, mantidas em estufa contendo 5% de CO_2 a 4℃ e 37℃ e acompanhadas por 0, 8 e 24 horas. Os resultados mostraram que em ambas as condições de temperatura, o mastoparano foi capaz de induzir, desde o tempo inicial de 15 minutos até a oitava hora do tratamento, significativas modificações morfológicas como perda de adesão, retraimento do citoplasma e perda de refringência (Figura 11).

O delineamento experimental para avaliar os aspectos morfológicos das células tratadas com o INKKI 500 µM seguiu as mesmas especificações do ensaio com o mastoparano, ou seja, cultivadas em placas de 96 poços e mantidas em estufa contendo 5% de CO_2 a 4 ℃ e 37 ℃ e acompanhadas por 0, 8 e 24 horas. Os resultados mostraram que o INKKI não apresentou modificações morfológicas nas culturas mantidas a 4 ℃ durante as 24 horas de acompanhamento (Figura 12). As culturas mantidas a 37 ℃ apresentaram significativas alterações morfológicas desde a 8ª hora do tratamento. Essas modificações foram caracterizadas pela perda da comunicação celular e principalmente pelas formas arredondadas. Porém, apesar das mudanças morfológicas, as células permaneceram viáveis durante as 24 horas do tratamento. As principais características que suportam essa hipótese é a manutenção da refringência, integridade da membrana plasmática e núcleo celular bem delimitado, ou seja, as células estavam brilhantes e sem aparência de morte celular (Figura 13).

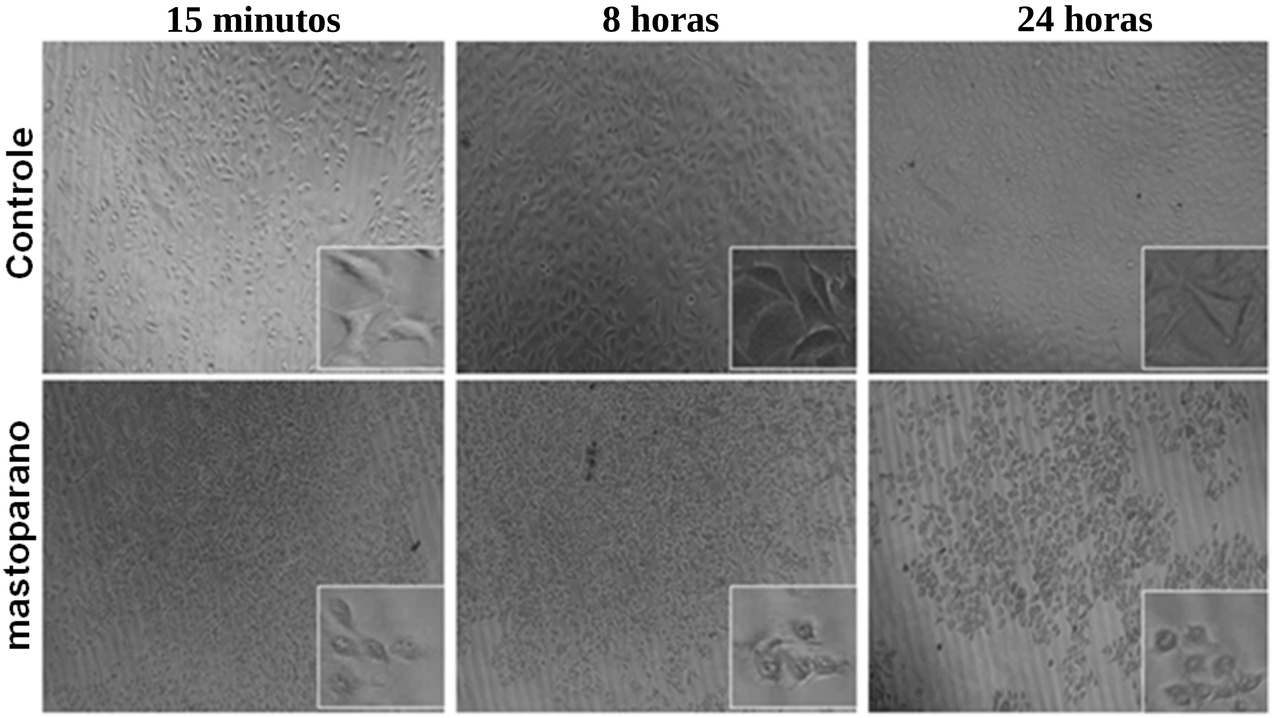

Figura 11. Fotomicrografia da microscopia óptica invertida das células de melanoma murino B16F10 mantida a 37 ℃ e tratadas com o mastoparano. As fotomicrografias mostram em destaque, os aspectos morfológicos das culturas de melanoma murino B16F10-Nex2 controle e tratadas com o mastoparano 500 µM, acompanhada por 24 horas e mantidas a 37 ℃. Foram observadas alterações na morfologia característica de morte celular, como perda de adesão, retraimento do citoplasma e perda de refringência, desde a 0 até a 24ª hora do tratamento.

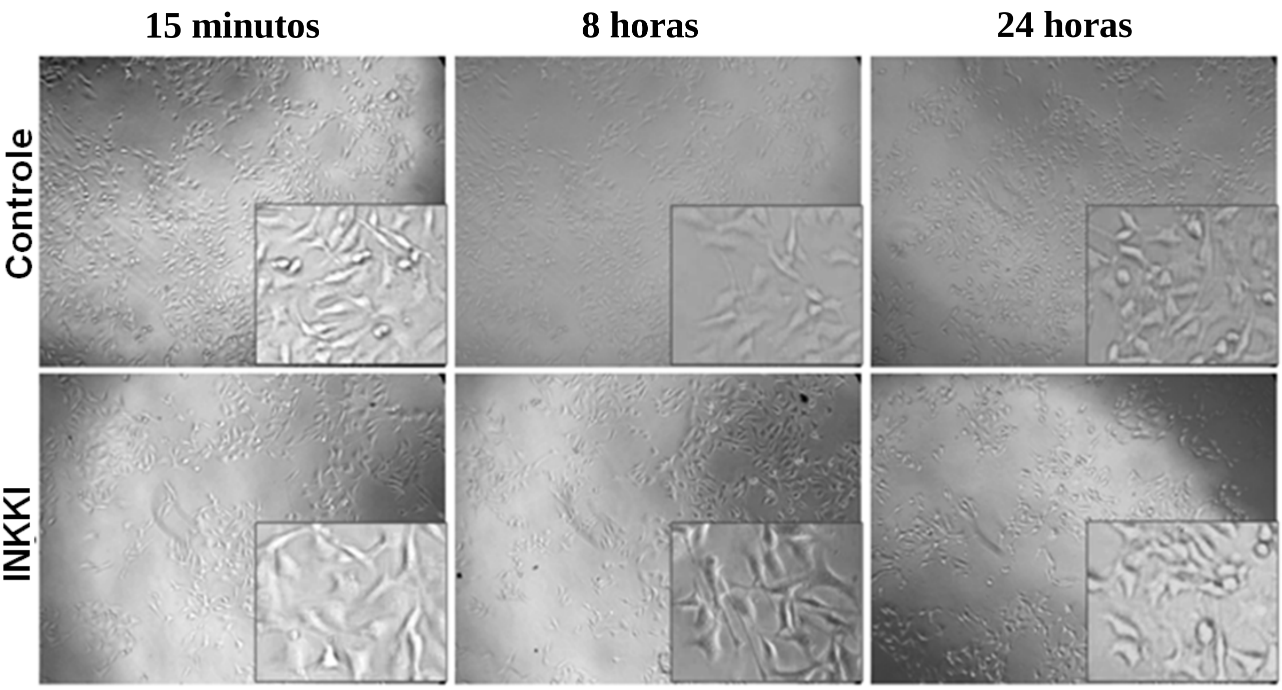

Figura 12. Fotomicrografia da microscopia óptica invertida das células de melanoma murino B16F10 mantidas a 4 ℃ e tratadas com o INKKI. As fotomicrografias mostram em destaque, os aspectos morfológicos das culturas de melanoma murino B16F10-Nex2 controle e tratadas com o INKKI 500 µM, acompanhada por 24 horas e mantidas a 4 ℃. Não foram observadas significativas alterações morfológicas tanto no controle quanto nas células tratadas durante as 24 horas de tratamento.

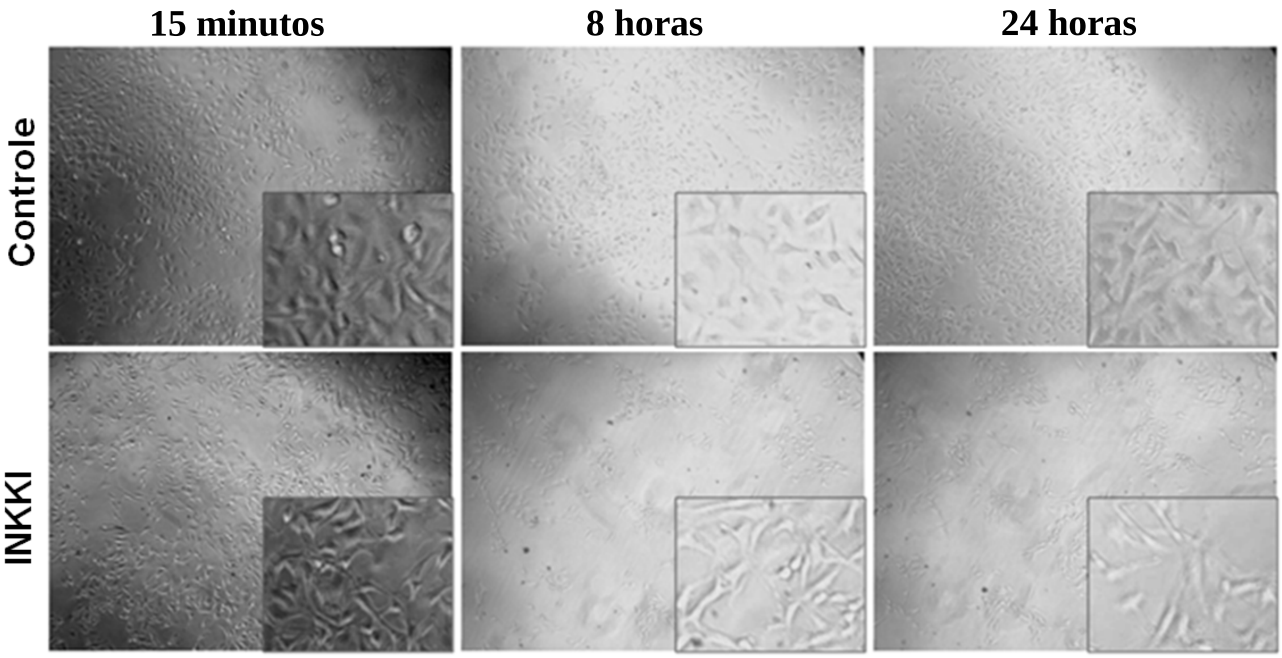

Figura 13. Fotomicrografia da microscopia óptica invertida das células de melanoma murino B16F10 mantidas a 37 ℃ e tratadas com o INKKI. As fotomicrografias mostram em destaque, os aspectos morfológicos das culturas de melanoma murino B16F10-Nex2 controle e tratadas com o INKKI 500 µM, acompanhada por 24 horas e mantidas a 37 ℃. A partir da 8ª hora, foram observadas significativas alterações morfológicas com perda da comunicação celular e presença de formas arredondadas. Apesar destas alterações, as células aparentemente estavam viáveis, caracterizadas pela refringência.

4.5 Efeitos sobre a proliferação em células de linhagens de melanoma murino B16F10-Nex2 após o tratamento com o INKKI e scramble

A avaliação da proliferação celular fornece importantes dados sobre os possíveis efeitos relacionados com o ciclo celular. Os efeitos antiproliferativos foram avaliados em linhagens tumorais de melanoma murino B16F10-Nex2. Os resultados mostraram que ao longo das 72 horas de incubação o tratamento com 500 µM de INKKI apresentou uma progressiva redução do número de células em relação ao controle negativo e scramble. Nas primeiras 24 horas, os dados mostraram que houve uma inibição da proliferação de 37,6% e 35,65% em comparação ao controle negativo e scramble, respectivamente. Após 48 horas de incubação, o tratamento com INKKI foi capaz de inibir a proliferação em 55,64% e 43,70% em comparação ao controle negativo e scramble, respectivamente. Após 72 horas, foi possível verificar que houve um aumento na inibição da proliferação em 78,34% e 74% em comparação ao controle negativo e scramble, respectivamente. Não foi possível prolongar o tempo de incubação por 96 horas, uma vez que o controle negativo atingiu a confluência com 72 horas (Figura 14).

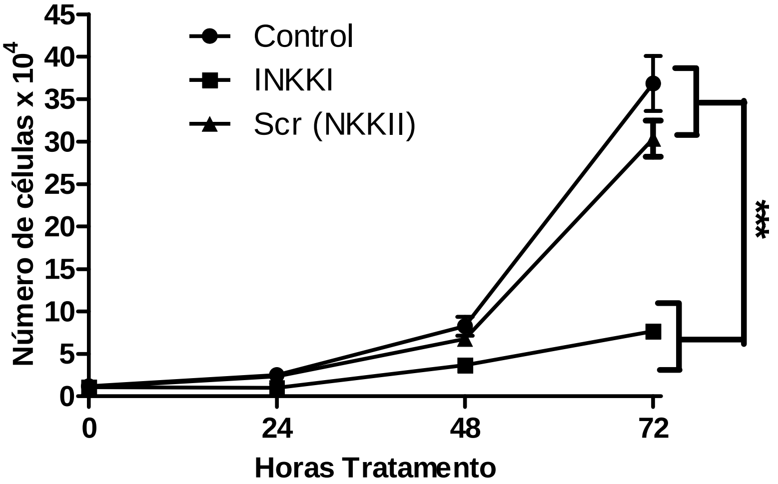

Figura 14. Avaliação sobre a proliferação celular após o tratamento com o INKKI e scramble. As células de melanoma murino B16F10-Nex2 na densidade de 10^3 foram plaqueadas em placas de 96 poços, tratadas com 500 µM de INKKI e incubadas por 72 horas. Após os tempos de incubação de 24, 48 e 72 horas as células foram quantificadas pelo método de exclusão do azul de tripan em câmara de Neubauer. Os dados mostraram que INKKI foi capaz de inibir a proliferação de forma progressiva ao longo do tratamento. A curva mostra a cinética de proliferação expressa em média ± DP de três experimentos independentes e a análise estatística realizada pelo o teste One-Way ANOVA seguido pelo teste de Tukey-Kramer (*** p<0,001).

4.6 Inibição da adesão celular em culturas de B16F10-Nex2 tratadas com o INKKI e scramble

Estudos sobre a adesão celular em linhagens tumorais apresentam importantes indícios de possíveis efeitos sobre microambiente tumoral e/ou formação de metástases. Esses dados podem contribuir para a geração dos futuros delineamentos experimentais, como por exemplo, estudos *in vivo* antimetastáticos. Os efeitos sobre a adesão foram avaliados em linhagens tumorais de melanoma murino B16F10-Nex2 cultivadas sobre a monocamada celular, matrigel e superfície de poliestireno da placa de 96 poços. Após 24 horas de incubação com 500 µM de INKKI e scramble, a adesão foi quantificada. Os resultados mostraram que o INKKI foi capaz de inibir a adesão sobre a monocamada celular em 43% e 31% comparando com controle negativo e o scramble, respectivamente (Figura 15). A avaliação sobre o matrigel mostrou que o INKKI foi capaz de inibir a adesão em 50% e 45%, comparando com o controle negativo e o scramble, respectivamente (Figura 16). Por fim, os dados apresentados após a incubação sobre o poliestireno da placa de 96 poços mostraram que o INKKI inibiu a adesão celular em 40% e 34,5%, comparando com o controle negativo e o scramble, respectivamente (Figura 17).

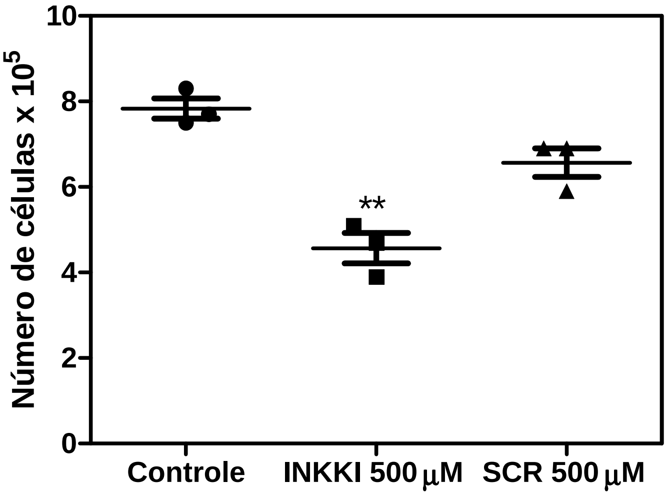

Figura 15. Inibição da adesão sobre o monolayer celular após o tratamento com o INKKI e scramble. As células de melanoma murino B16F10-Nex2 na densidade de 10^4 foram plaqueadas sobre o monolayer celular em placas de 96 poços, tratadas com 500 μM de INKKI e incubadas por 4 horas. Após os tempos de incubação as células foram quantificadas pelo método de exclusão do azul de tripan em câmara de Neubauer. Os dados mostraram que o INKKI foi capaz de inibir significativamente a adesão sobre o monolayer celular e a análise estatística foi realizada aplicando o teste One-Way ANOVA seguido pelo teste de Tukey-Kramer (** $p<0.01$).

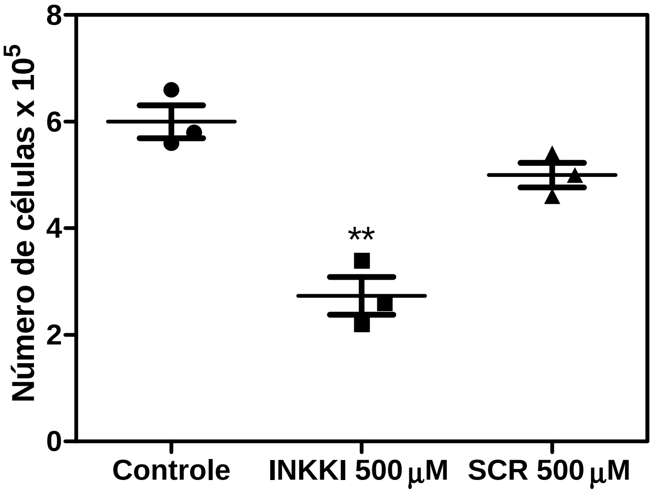

Figura 16. Inibição da adesão sobre o matrigel após o tratamento com o INKKI e scramble. As células de melanoma murino B16F10-Nex2 na densidade de 10^4 foram plaqueadas sobre o matrigel em placas de 96 poços, tratadas com 500 µM de INKKI e incubadas por 4 horas. Após os tempos de incubação as células foram quantificadas pelo método de exclusão do azul de tripan em câmara de Neubauer. Os dados mostraram que o INKKI foi capaz de inibir significativamente a adesão sobre o matrigel e a análise estatística foi realizada aplicando o teste One-Way ANOVA seguido pelo teste de Tukey-Kramer (** $p<0.01$,** $p<0.01$).

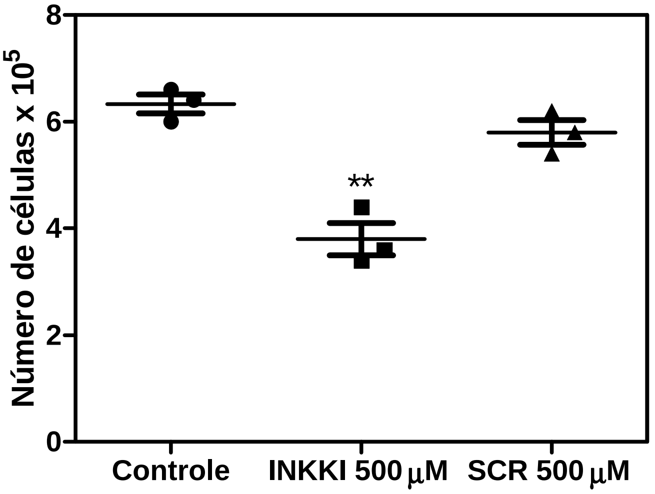

Figura 17. Inibição da adesão sobre a superfície de poliestireno da placa de 96 poços após o tratamento com o INKKI e scramble. As células de melanoma murino B16F10-Nex2 na densidade de 10^4 foram plaqueadas sobre o poliestireno da placas de 96 poços, tratadas com 500 µM de INKKI e incubadas por 4 horas. Após os tempos de incubação as células foram quantificadas pelo método de exclusão do azul de tripan em câmara de Neubauer. Os dados mostraram que o INKKI foi capaz de inibir significativamente a adesão sobre o poliestireno e a análise estatística foi realizada aplicando o teste One-Way ANOVA seguido pelo teste de Tukey-Kramer (** $p<0.01$)

4.7 Inibição da migração em células de linhagem B16F10-Nex2 após tratamento com o INKKI e scramble.

A migração celular *in vitro* fornece indícios sobre o comportamento das linhagens tumorais frente ao tratamento com os peptídeos. É importante enfatizar que os dados gerados desse experimento também podem promover futuros planejamentos para avaliação antimetastática *in vivo*. Os efeitos inibitórios da migração foram avaliados em linhagens tumorais de melanoma murino B16F10-Nex2. Os resultados mostraram que ao final das 24 horas de incubação, os poços que receberam o tratamento de 500 µM de INKKI ainda apresentaram espaços a serem percorridos pelas células, enquanto que o controle negativo atingiu 100% de confluência, indicando que o peptídeo exibiu efeito inibitório significativo sobre migração celular (Figura 18). A quantificação da inibição da migração celular foi mensurada através da área percorrida pelas células. Os resultados mostraram que o INKKI foi capaz de inibir a migração em 51,9% e 44,26% em comparação ao controle negativo e ao peptídeo scramble, respectivamente (Figura 19).

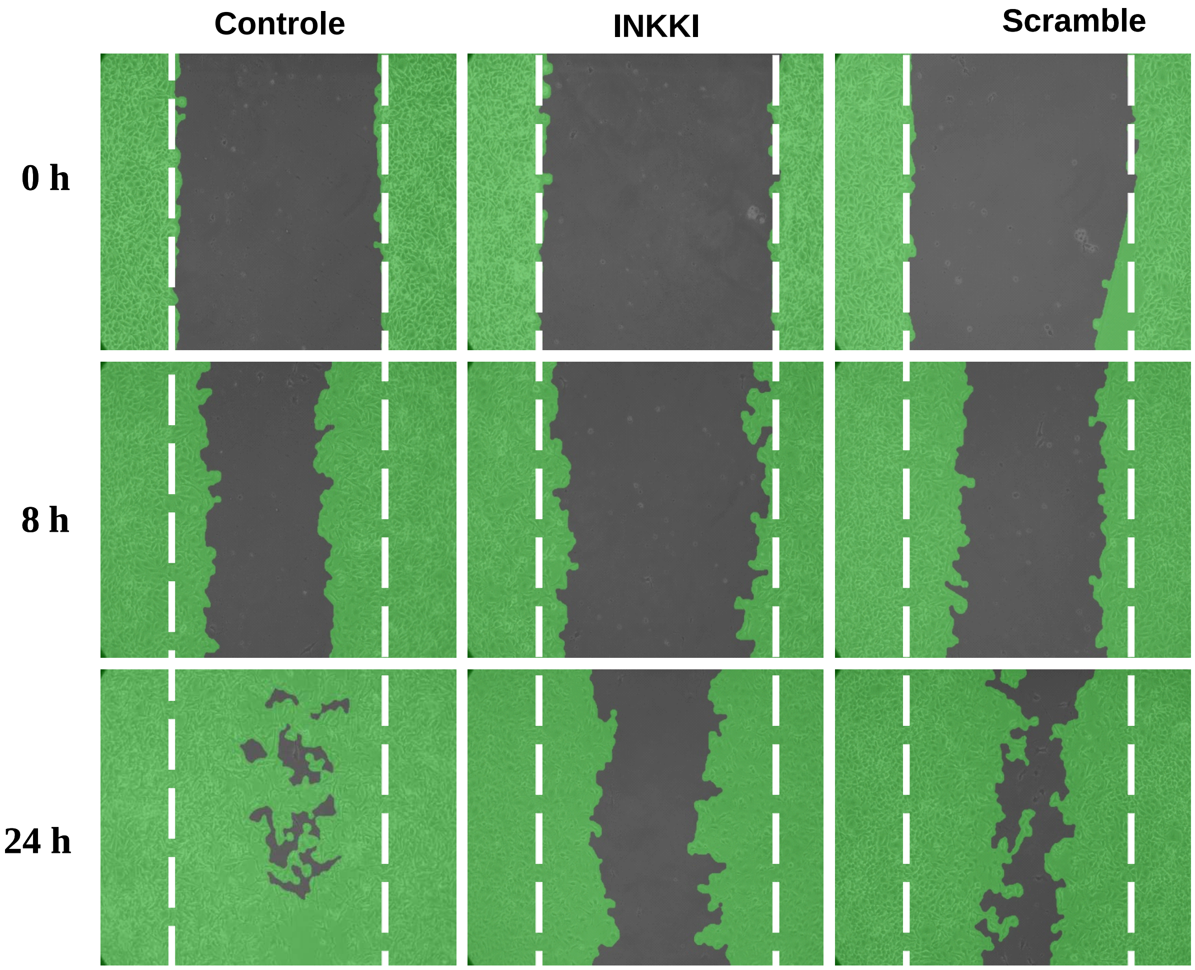

Figura 18. Avaliação da inibição da migração celular após tratamento com INKKI e scramble. As células de B16F10-Nex2 foram plaqueadas na concentração de 2,5x10^5 em placas de 12 poços, tratadas com 500 µM de INKKI e incubadas por 24 horas. Ao longo do período de incubação, as células foram fotodocumentadas e as imagens analisadas através do Software Wimasis Image. As imagens mostraram que, em comparação ao controle negativo, as células tratadas com o INKKI não foram capazes de atingir a confluência ao final da incubação. Analisando as distâncias percorridas pelas células, ficou evidente que os poços tratados com o INKKI apresentam menores áreas percorridas do que o Scramble. As imagens foram adquiridas por microscopia óptica com magnitude de 10x.

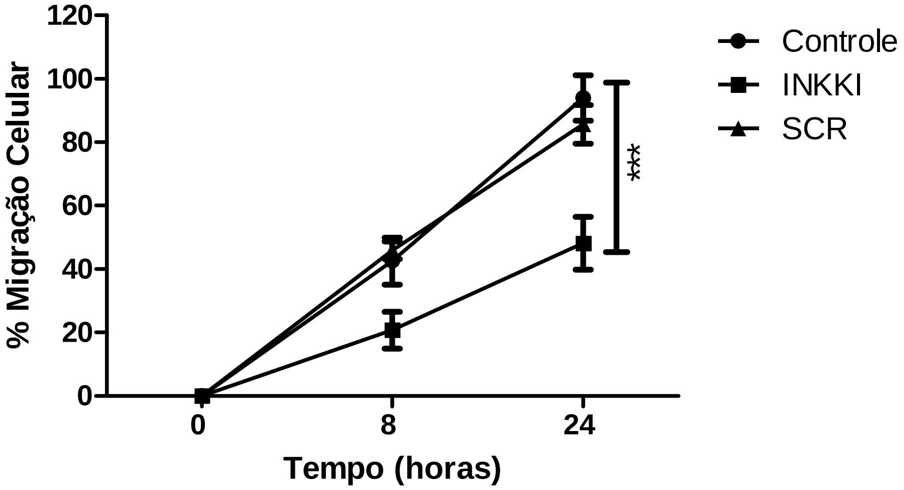

Figura 19. Quantificação do efeito inibitório da migração celular após o tratamento com o INKKI e scramble. As células de B16F10-Nex2 foram plaqueadas na concentração de 2,5x10^5 em placas de 12 poços, tratadas com 500 µM de INKKI e incubadas por 24 horas. As culturas foram fotodocumentadas nos tempos de 0, 8 e 24 horas. A quantificação foi realizada através da área percorrida pelas células. Os dados mostraram que o INKKI foi capaz de inibir a migração celular em comparação ao controle e scramble. A curva mostra a área percorrida na placa de cultura expressa em média ± DP de três experimentos independentes e a análise estatística foi realizada aplicando o teste One-Way ANOVA seguido pelo teste de Tukey-Kramer (*** $p<0.001$).

4.8 Efeitos sobre a invasão celular após o tratamento com o INKKI e scramble

A invasão celular é uma importante característica associada à metástase. O estudo dos efeitos do tratamento com o INKKI e scramble sobre a invasão forneceu importantes evidências para futuros delineamentos experimentais antimetastáticos *in vivo*. Os efeitos sobre a invasão celular foram avaliados em linhagens tumorais de melanoma murino B16F10-Nex2. Os resultados mostraram que após 24 horas de incubação e tratamento com 500 µM de INKKI, houve uma significativa redução na invasão celular. Esses dados estão representados na Figura 20 A, onde ficou evidente a redução no número de células que invadiram o lado oposto do Transwell, em comparação com o controle negativo e Scramble. Esses dados foram quantificados através da contagem do número das células que ultrapassaram o matrigel. Os resultados mostraram que o tratamento com o INKKI foi capaz de inibir a invasão celular em 66,87% e 53,38% em comparação ao controle negativo e scramble, respectivamente (Figura 20 B).

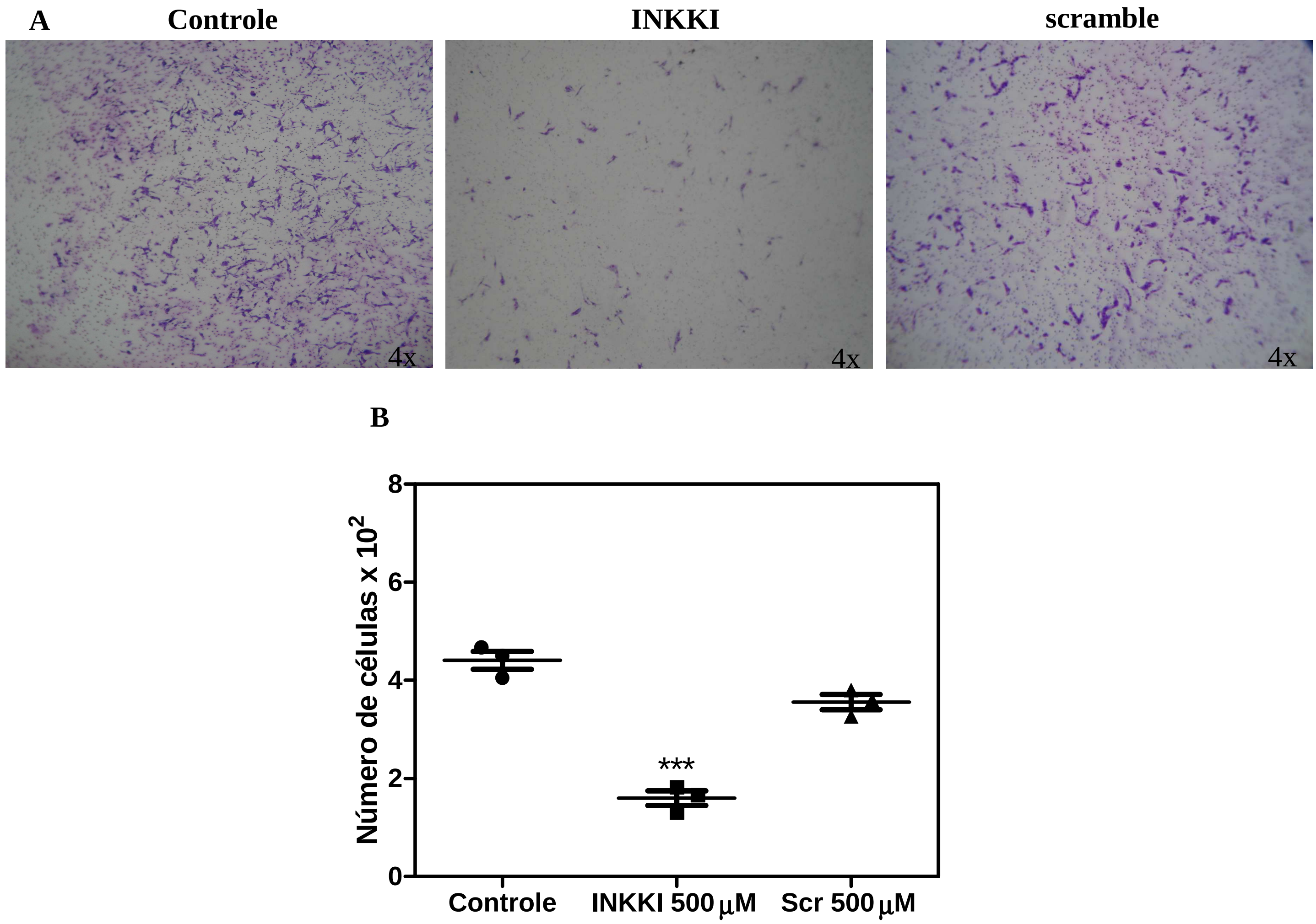

Figura 20. Ensaio de invasão celular em linhagens de melanoma murino B16F10-Nex2 após o tratamento com o INKKI e scramble. A figura **(A)** exibe em destaque o número de células de melanoma murino B16F10-Nex2 que migraram pelo matrigel, evidenciando a diferença entre o tratamento com o INKKI, o controle negativo e scramble após 24 horas de incubação. Após o tempo de incubação as células foram coradas, quantificadas e os dados mostraram que o INKKI foi capaz de inibir significativamente a invasão das células tumorais e a análise estatística foi realizada aplicando o teste One-Way ANOVA seguido pelo teste de Tukey-Kramer (*** $p < 0.001$).

4.9 Avaliação das fases do ciclo celular das células B16F10-Nex2 tratadas com o INKKI e scramble

A redução do numero total de células B16F10-Nex2 após o tratamento com o INKKI, sugeriu uma possível atividade moduladora sobre a proliferação. Desse modo, foi determinada a porcentagem de células em cada fase do ciclo celular após o tratamento com o INKKI, Scramble e controle não tratado. Os resultados mostraram que o INKKI na concentração de 500 µM foi capaz de reduzir significativamente a proliferação das células B16F10-Nex2, demonstrada pela diminuição da porcentagem de células nas fases S e G2/M e aumento das células em G0/G1. O tratamento com o INKKI levou uma redução de 65,17%, e 40,26% das células nas fases S e G2/M, respectivamente. Por outro lado, o INKKI aumentou a proporção da população celular em 36% na fase G0/G1, ambas em comparação ao controle negativo sem o tratamento. Em comparação ao peptídeo Scramble, o INKKI aumentou a porcentagem de células em G0/G1 em 33,86% e reduziu a proporção da população em 61.85% e 61,36% nas fases S e G2/M, respectivamente (Figura 21 A e B).

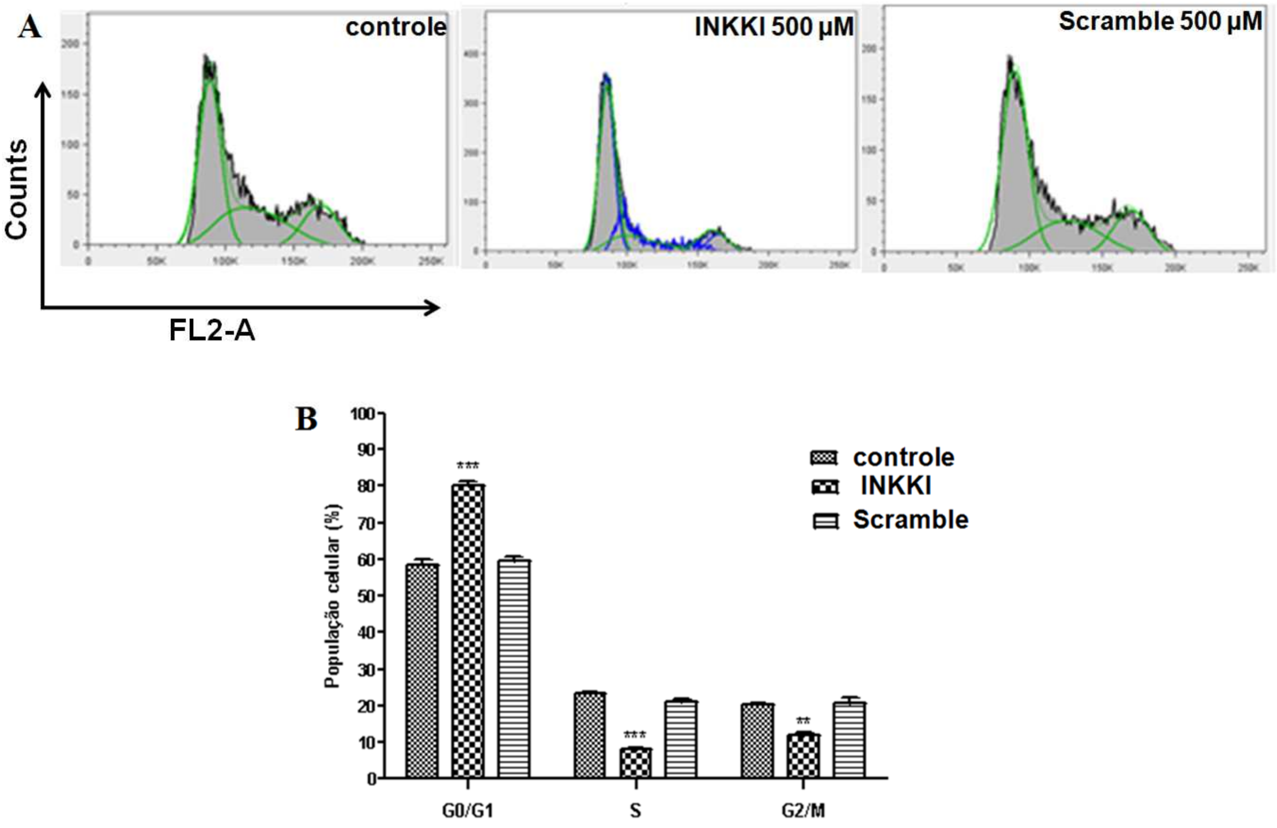

Figura 21. Indução da parada da fase G0/G1 do ciclo celular das células B16F10-Nex2 após o tratamento com o INKKI e Scramble. As células B16F10-Nex2 foram plaqueadas na concentração de $2,5x10^5$ em placas de 12 poços, tratadas com 500 µM de INKKI e incubadas por 24 horas **(A)** O histograma representa o número de eventos em função da fluorescência marcada com a incorporação do Iodeto de Propídeo (PI). **(B)** Representa a distribuição da porcentagem das fases do ciclo celular após o tratamento com os peptídeos. Os dados mostraram que o INKKI induziu significativamente a parada do ciclo celular na fase G0/G1 e consequentemente, reduziu o número de células nas fases S e G2/M (** p< 0.01, *** p< 0.001).

4.10 Efeitos sobre os mediadores envolvidos na regulação do ciclo celular e migração celular após o tratamento com o INKKI e scramble pelo método de Western blotting

Para entender o mecanismo de ação do INKKI sobre a parada do ciclo celular em cultura de melanoma B16F10-Nex2, as proteínas envolvidas no controle do ciclo foram avaliadas por Western blotting. As células B16F10-Nex2 na concentração de 10^6 foram tratadas com 500 µM do INKKI e scramble e incubadas por mais 24 horas. Após o período de incubação foi possível observar que as células tratadas com o INKKI apresentaram significativas alterações morfológicas caracterizadas pela perda da confluência, prolongamentos citoplasmáticos e diminuição da adesão intercelular (Figura 22).

A primeira proteína analisada foi a ciclina D1. Os dados mostraram que o tratamento das células B16F10-Nex2 com 500 µM do INKKI induziu a inibição da expressão de ciclina D1, corroborando com os dados obtidos com a análise do ciclo celular, onde foi possível mostrar o amento na proporção da população celular na fase G0/G1. O estudo com a Ciclina D3 mostrou que houve uma discreta redução dos níveis de expressão em comparação ao controle negativo e o peptídeo Scramble.

Analisando a via de sinalização upstream da ciclina D1, o INKKI mostrou ser capaz de reduzir significativamente os níveis de importantes mediadores correlacionados com a via da MAPK/Erk1-2 que controlam a progressão do ciclo celular. Os resultados mostraram significativa redução nos níveis de expressão do NFκ-B, bem como da β-Catenina e Erk1-2 quando comparado com o controle negativo e peptídeo Scramble. Esses dados corroboram efetivamente com os efeitos biológicos descritos anteriormente através da análise da expressão da ciclina D1 e do ciclo celular. Somando aos dados anteriores, também foi possível observar que os níveis de expressão de fosfo-c-Raf (Ser 338) e fosfo-AKT também apresentaram significativa redução, enquanto que, o c-Raf não fosforilado apresentou o mesmo nível de expressão quando comparado com o controle e scramble. Além disso, o INKKI também foi capaz de induzir o aumento da expressão da p38. Todos os dados foram padronizados com a β-actina (Figura 23 A e B).

Agregando aos resultados obtidos com a via de sinalização do ciclo celular, foram avaliados os principais mediadores correlacionados com a migração celular.

Os dados obtidos da análise por Western blotting mostraram que as células tratadas com o INKKI apresentaram uma significativa redução nos níveis de fosfo Src (Tyr 416), GSK3β, fosfo FAK (Tyr 925), fosfo FAK (Tyr 397) e um aumento na expressão de Src, quando comparadas com o controle e o peptídeo scramble. Os níveis de FAK apresentaram discreta redução da expressão entre os tratamentos com o controle, INKKI e scramble. A N-caderina é uma importante molécula de adesão que esta diretamente envolvida no processo de migração celular. As células tratadas com o INKKI apresentaram significativa redução nos níveis de expressão de N-caderina (Figura 24).

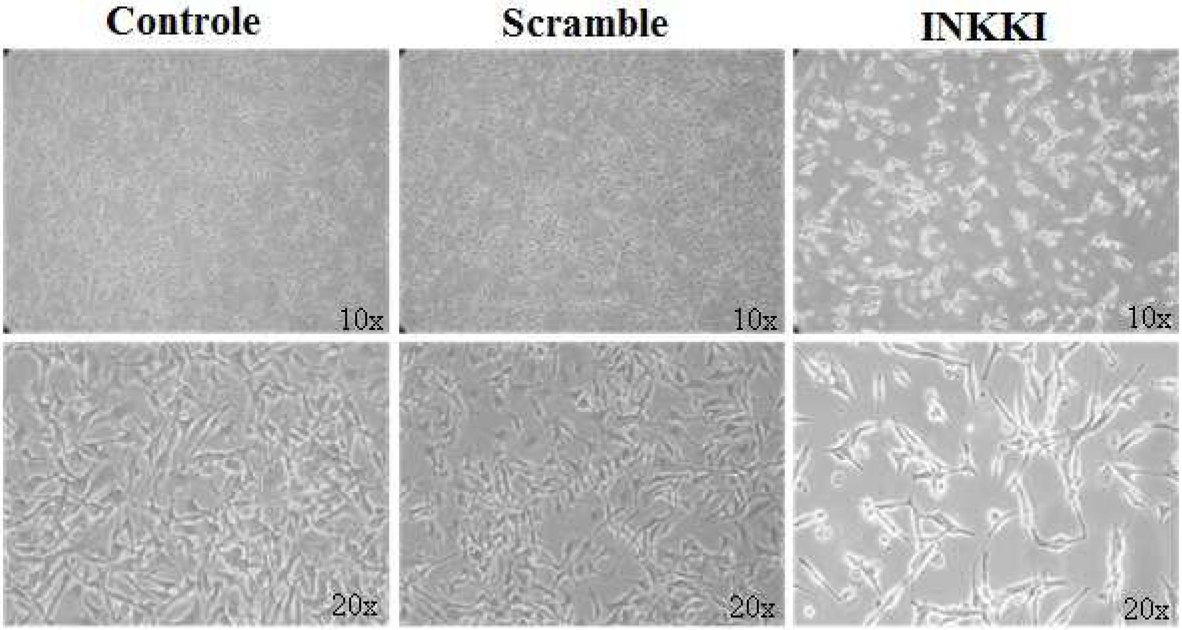

Figura 22. Alterações morfológicas das células B16F10-Nex2 após 24h de tratamento com o INKKI e scramble. As células B16F10-Nex2 foram plaqueadas na concentração de 10^6 em placas de 6 poços, tratadas com 500 μM de INKKI e incubadas por 24 horas. Após a incubação foi possível observar as significativas alterações na morfologia celular. As células tratadas com o INKKI apresentaram prolongamentos citoplasmáticos, perda de confluência e adesão intercelular, além da significativa diminuição do número de células.

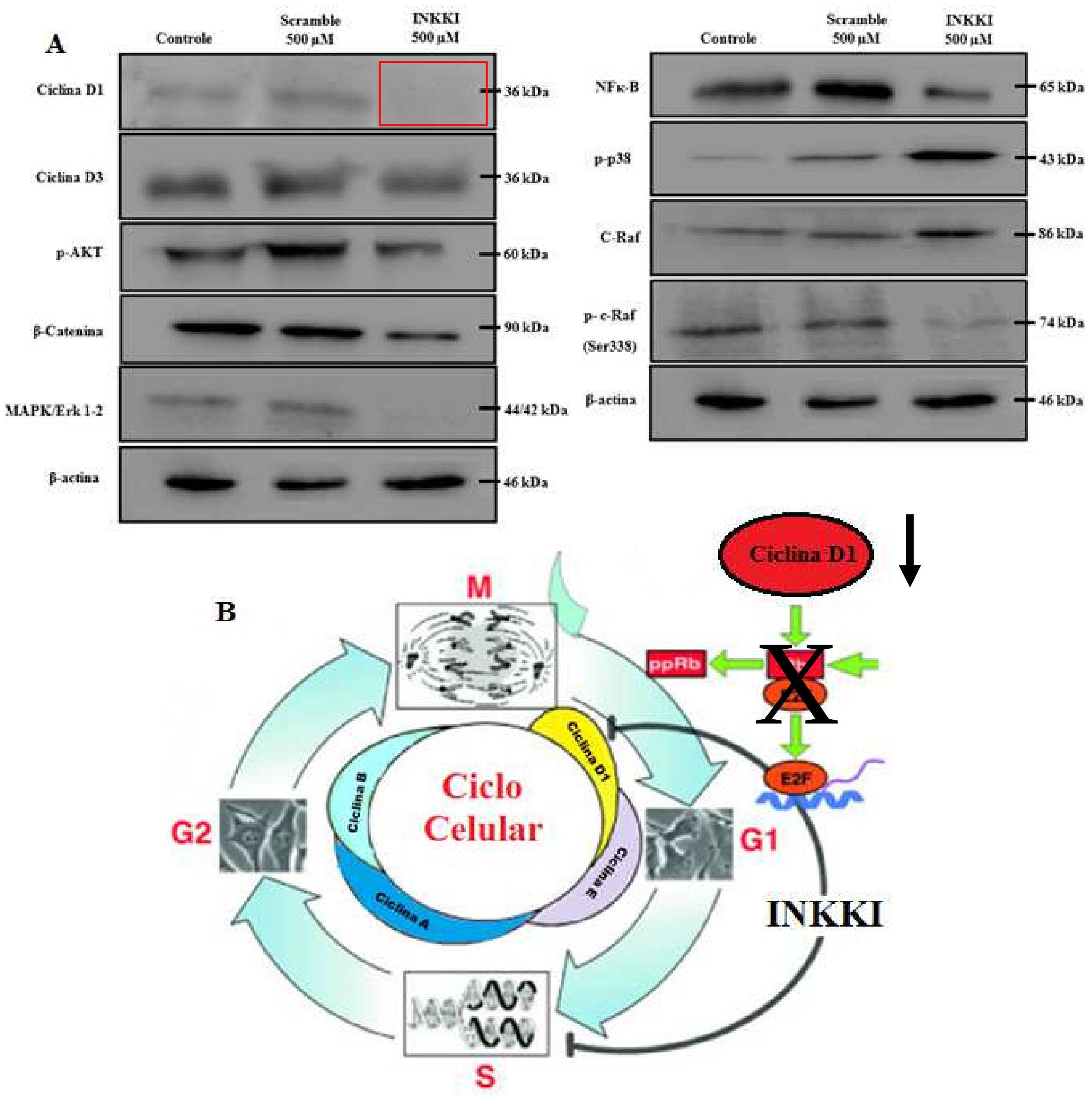

Figura 23. Efeitos do tratamento das células B16F10-Nex2 com o INKKI e scramble sobre os níveis de expressão de ciclinas D1 e D3, p-AKT, MAPK, β-Catenina, p38, c-Raf, Phosp-c-Raf (Ser338) e NFκ-B. (A) As células B16F10-Nex2 foram plaqueadas na concentração de 10^6 em placas de 6 poços, tratadas com 500 µM de INKKI e incubadas por 24 horas. Após a incubação foram realizados Western Blottings para checagem da expressão de Cilina D1, Ciclina D3, AKT, MAPK, β-Catenina e NFκ-B, todos os anticorpos diluídos na proporção de 1:1000 e normalizados pela quantificação da β-actina. Os resultados mostraram inibição da expressão de Ciclina D1 e MAPK e redução nos níveis de expressão da β-Catenina, Phosp-c-Raf (Ser338) e NFκ-B, enquanto que houve um aumento na expressão de p-p38. **(B)** Esquema representativo da parada do ciclo celular induzida pelo INKKI inibindo a expressão da ciclina D1 e acumulo das células na fase G0/G1. Adaptada: (Gaurisankar; Tanya, 2008).

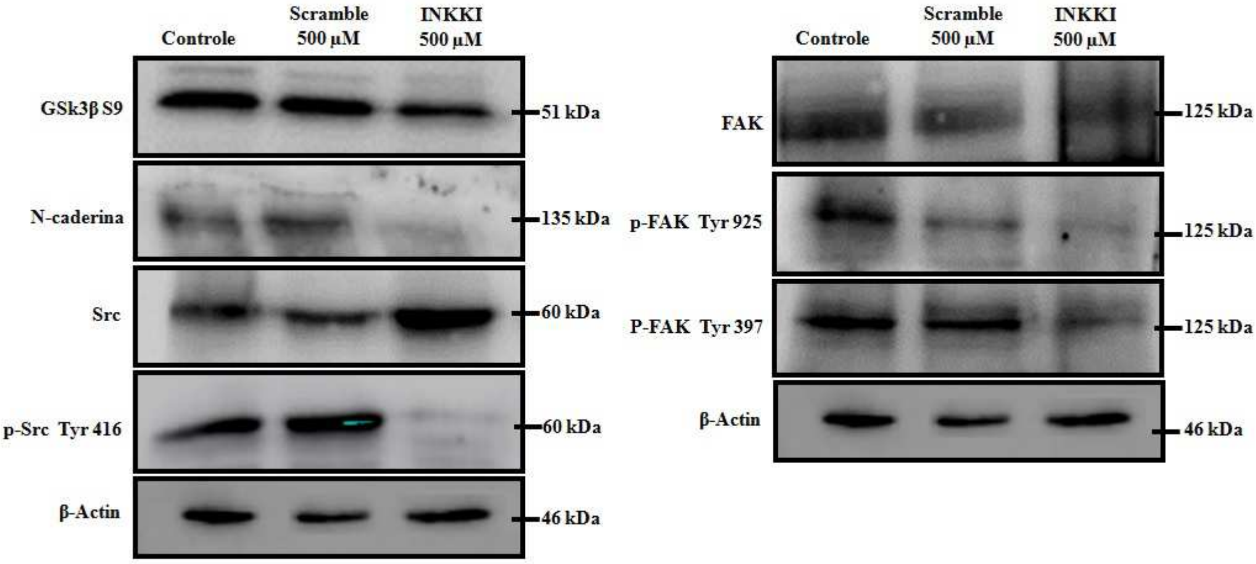

Figura 24. Efeitos do tratamento das células B16F10-Nex2 com o INKKI e scramble sobre os níveis de expressão de GSk3β, N-caderina, Src, fosfo Src (Tyr 416), FAK, fosfo FAK (Tyr 925), fosfo FAK (Tyr 397) e β-actina. As células B16F10-Nex2 foram plaqueadas na concentração de 10^6 em placas de 6 poços, tratadas com 500 µM de INKKI e incubadas por 24 horas. Após a incubação foram realizados western blotting para checagem da expressão GSk3β, E-caderina, Src, fosfo Src (Tyr 416), FAK, fosfo FAK (Tyr 925) E fosfo FAK (Tyr 397), todos os anticorpos diluídos na proporção de 1:1000 e normalizados pela quantificação da β-actina. Os resultados mostraram inibição da expressão de Ciclina D1 e MAPK e redução nos níveis de expressão da GSk3β, E-caderina, fosfo Src (Tyr 416), fosfo FAK (Tyr 925) E fosfo FAK (Tyr 397), enquanto que houve um aumento na expressão de Src.

4.11 Avaliação da internalização por microscopia confocal das células de melanoma murino B16F10-Nex2 tratados com INKKI marcado com FITC

A determinação da localização e o tráfego celular do INKKI fornecem importantes evidências quanto ao mecanismo de ação, onde é possível observar se o peptídeo encontra-se ligado na superfície da membrana celular, se é internalizado e disperso pelo citoplasma ou se está localizado no núcleo celular. A internalização foi avaliada através de ensaios de microscopia confocal. As células de melanoma murino B16F10-Nex2 foram incubadas por 1 e 24 horas com o INKKI marcado com FITC (verde) na concentração de 500 µM. Após ambos os períodos de incubação, os dados mostraram que o INKKI foi capaz de internalizar apresentando ampla distribuição citoplasmática. Além da localização citoplasmática, o núcleo celular foi marcado com DAPI (azul) e foi possível observar que o INKKI apresentou uma co-localização nuclear em ambos os tempos de incubação (Figura 25). Outro importante dado obtido neste ensaio foi a Série-Z e reconstrução tridimensional das células B16F10-Nex2. As fotomicrografias mostraram que o INKKI não se localizou na membrana celular sendo totalmente internalizado (Figuras 26 e 27).

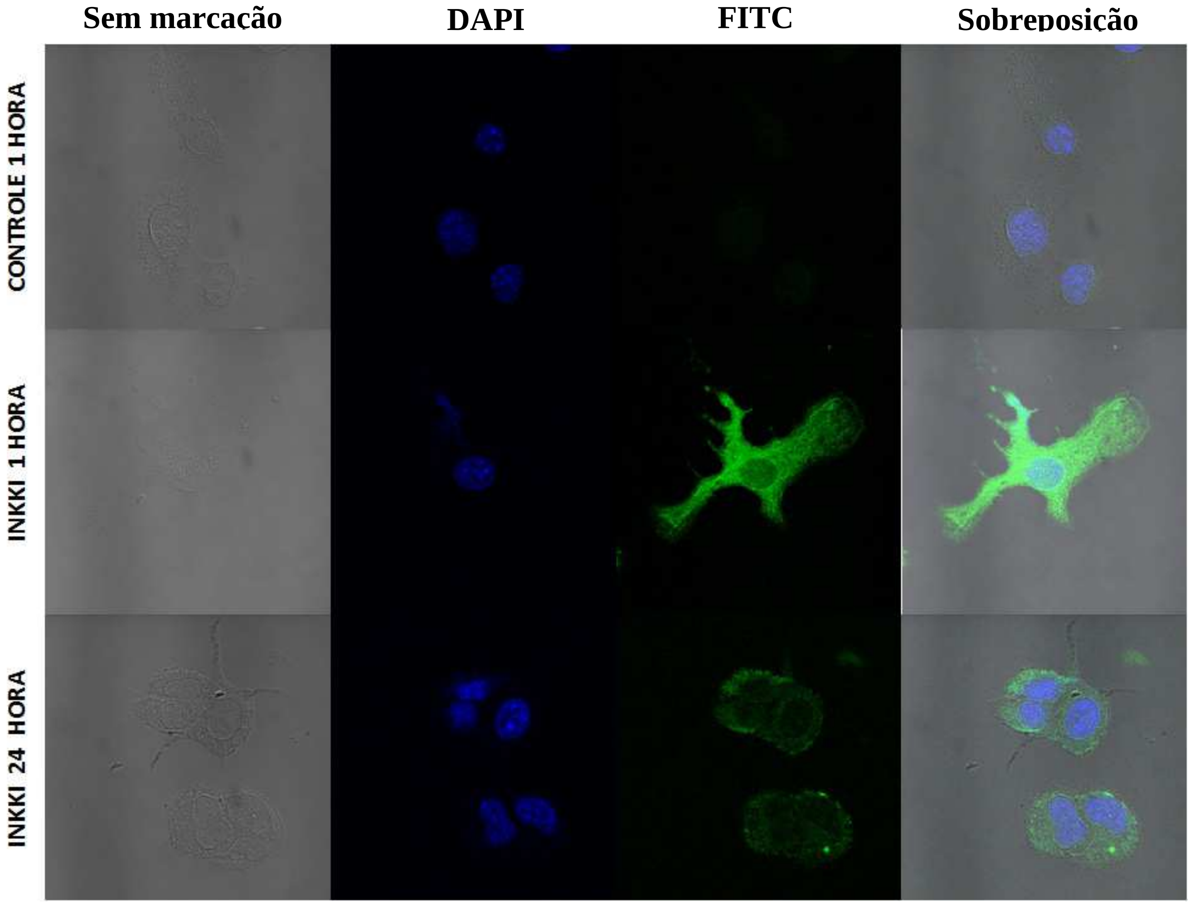

Figura 25. Imagens de microscopia confocal das células de melanoma murino B16F10-Nex2 tratados com INKKI marcado com FITC (verde) e DAPI (azul). As células B16F10-Nex2 foram incubadas com 500 µM de INKKI marcado com FITC e DAPI pelos períodos de 1 e 24 horas. Após o período de incubação foi possível observar que o peptídeo foi internalizado e amplamente distribuído pelo citoplasma. A co-localização entre o FITC e o DAPI mostrou que o peptídeo também foi encontrado na região nuclear das células (aumento 60x).

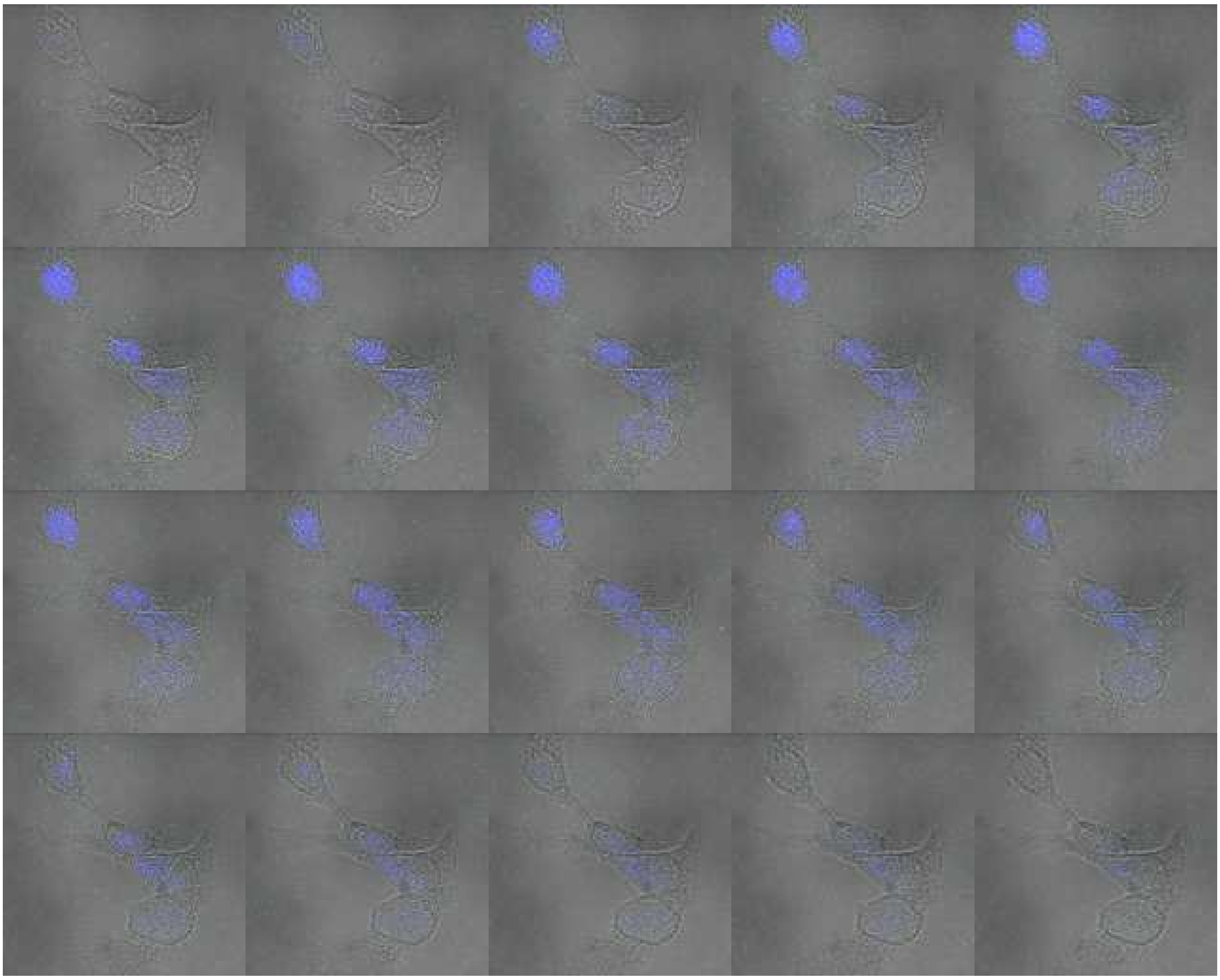

Figura 26. Imagens de microscopia confocal da Série-Z e reconstrução tridimensional das células B16F10 das células controle de melanoma murino B16F10-Nex2 marcadas com FITC (verde) e DAPI (azul). As células B16F10-Nex2 foram incubadas com FITC e DAPI pelos períodos de 1 e 24 horas. Após o período de incubação foi possível observar que somente a região nuclear apresentou marcação com DAPI (aumento de 40x).

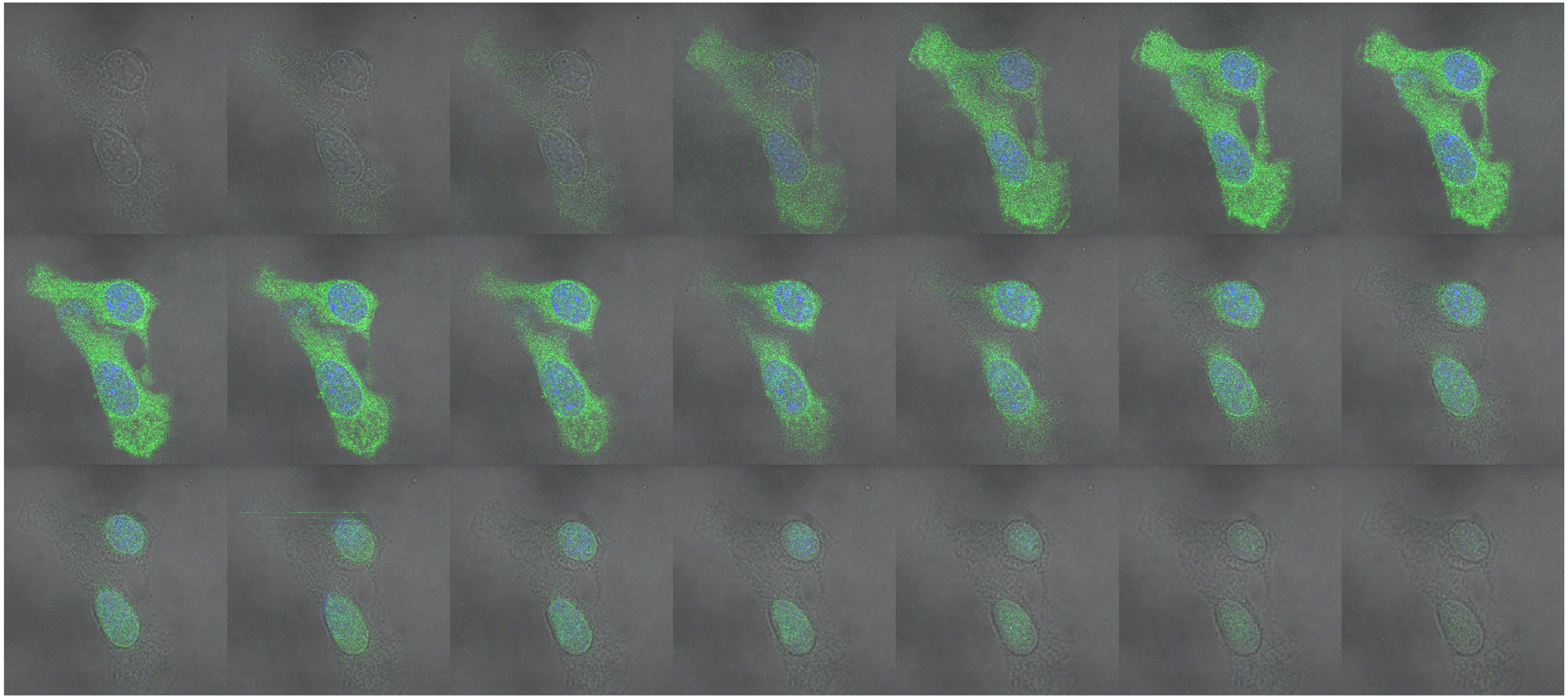

Figura 27. Imagens de microscopia confocal da Série-Z e reconstrução tridimensional das células de B16F10-Nex2 tratadas com INKKI e marcadas com FITC (verde) e DAPI (azul). As células B16F10-Nex2 foram tratadas com 500 µM de INKKI marcado com FITC e DAPI pelo período de 1. Após o período de incubação foi possível observar que o INKKI não encontra-se localizado na superfície da membrana celular, sendo amplamente distribuído pelo citoplasma e co-localizado na região nuclear (aumento 40x).

4.12 Efeitos antimetastáticos em animais tratados com o INKKI e scramble (NKKII)

A habilidade das células tumorais de invadirem outros órgãos distantes do foco primário é um evento clínico de ocorrência letal em muitas neoplasias. Os principais sítios de invasão dos tumores metastáticos são o pulmão e o fígado. Para avaliar o efeito antimetastático, as células viáveis de melanoma murino B16F10-Nex2 foram injetadas endovenosamente pelo plexo retro-orbital $5x10^5$ células nos camundongos C57BL/6. Após 24 horas da inoculação, os camundongos foram tratados com 2,5 mg/Kg por animal durante 5 dias. Após o 14º dia os nódulos pulmonares foram quantificados. Os resultados mostraram que o INKKI foi capaz de inibir a formação de nódulos metastáticos pulmonares em 74% e 63,06% em comparação ao controle negativo tratados com solução fisiológica e ao seu análogo Scramble, respectivamente (Figura 28 A e B).

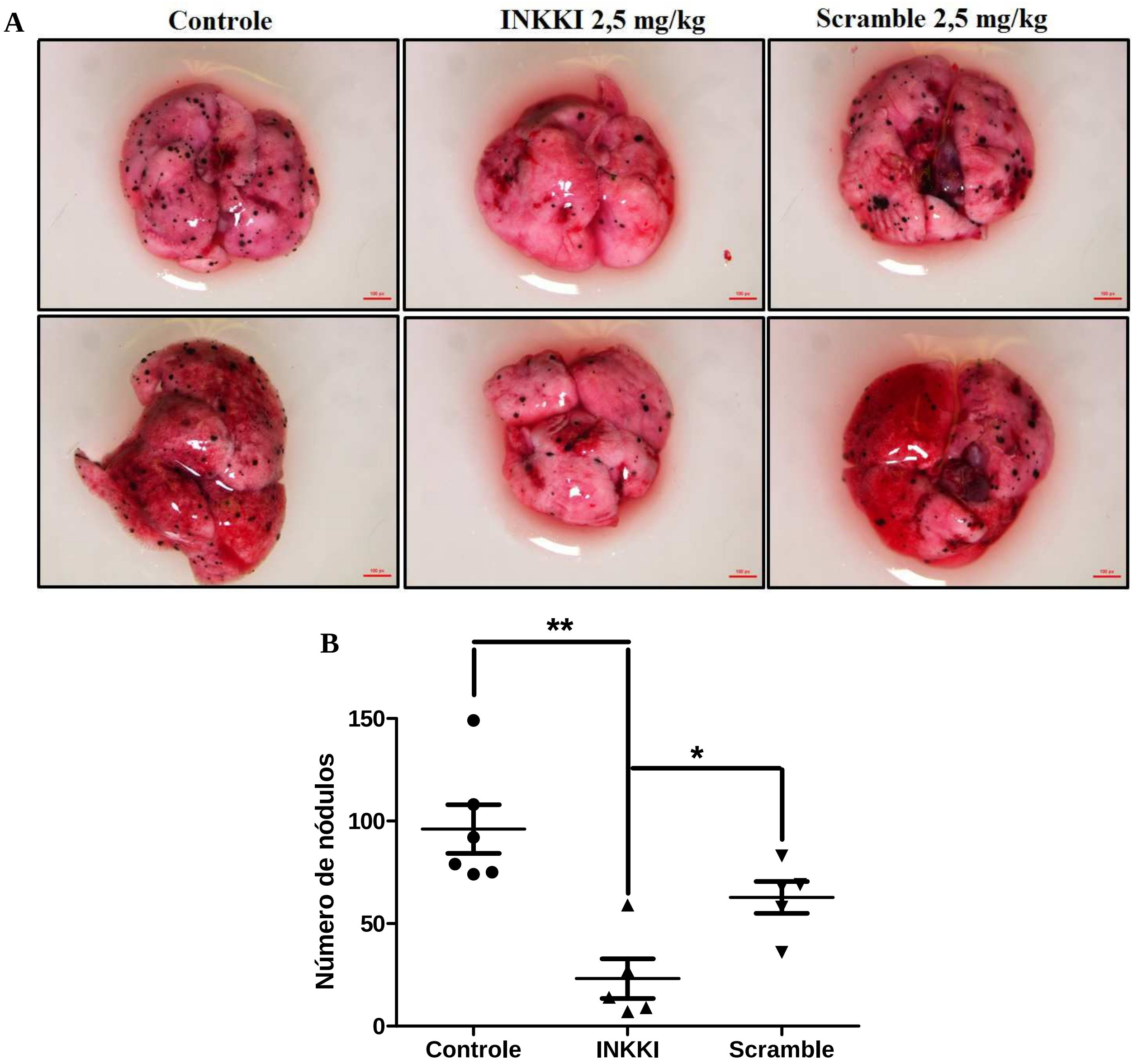

Figura 28. Aspectos macroscópicos e análise quantitativa da inibição da formação de nódulos metastáticos induzidos em camundongos de linhagem C57BL/6 após o tratamento com o INKKI e scramble. As células B16F10-Nex2 foram injetadas pelo plexo retro-orbital nos animais para indução da formação metastática. Após 24 horas da indução, os animais foram tratados durante 5 dias pela via intraperitoneal e no 14º dia os nódulos metastáticos foram quantificados. **A)** Aspectos macroscópicos dos pulmões mostraram que os animais tratados com o INKKI apresentaram menor número de nódulos metastáticos em comparação ao controle e scramble. **B)** As quantificações dos nódulos mostraram que INKKI apresentou significativa redução no número de metástases pulmonar. Para cada experimento foram utilizados 5 animais por grupos e a análise estatística foi realizada aplicando o teste One-Way ANOVA seguido pelo teste de Tukey-Kramer (* $p < 0.05$, ** $p < 0.01$).

4.13 Atividade antitumoral sobre o melanoma cutâneo em animais tratados com o INKKI e scramble

Os modelos experimentais *in vivo* apresentam significativa importância para obtenção da prova de conceito de compostos candidatos a agentes antitumorais. Um dos modelos mais empregado em estudos de atividade antitumoral é o melanoma dorsal. Este modelo permite o desenvolvimento e a avaliação de novas drogas e procedimentos terapêuticos. A inoculação subcutânea deste tumor provoca o desenvolvimento de um nódulo hipodérmico que se torna palpável em torno de uma a duas semanas, sendo facilmente mensurado, evoluindo para um tumor sólido, podendo chegar a grandes dimensões. Para avaliar os efeitos protetores 10^5 células de melanoma murino B16F10-Nex2 foram injetadas subcutaneamente nos flancos direitos dorsais dos camundongos de linhagem C57BL/6. Os animais foram tratados com 2,5 mg/Kg de INKKI e scramble e o volume tumoral foi mensurado até que os animais atingissem o volume máximo de 3000 mm^3. Os dados mostraram que o INKKI foi capaz de inibir o crescimento tumoral em 76,42% e 61,09% em comparação aos animais controles tratados com solução salina e ao peptídeo Scramble, respectivamente (Figura 29).

Outro importante parâmetro avaliado simultaneamente ao desenvolvimento tumoral é a taxa de sobrevida. Esse aspecto fornece importantes informações sobre a resposta frente ao tratamento com drogas antitumorais, uma vez que muitos agentes quimioterápicos disponíveis para o melanoma não apresentam aumento na expectativa de vida do paciente. A taxa de sobrevida foi avaliada de acordo com as condições experimentais descritas acima. Os resultados mostraram que o tratamento com o INKKI foi capaz de aumentar a taxa de sobrevida dos animais portadores de tumores dorsais em 65,5% e 54,8% em comparação ao controle negativo tratado com o veículo (solução salina) e ao scramble (Figura 30).

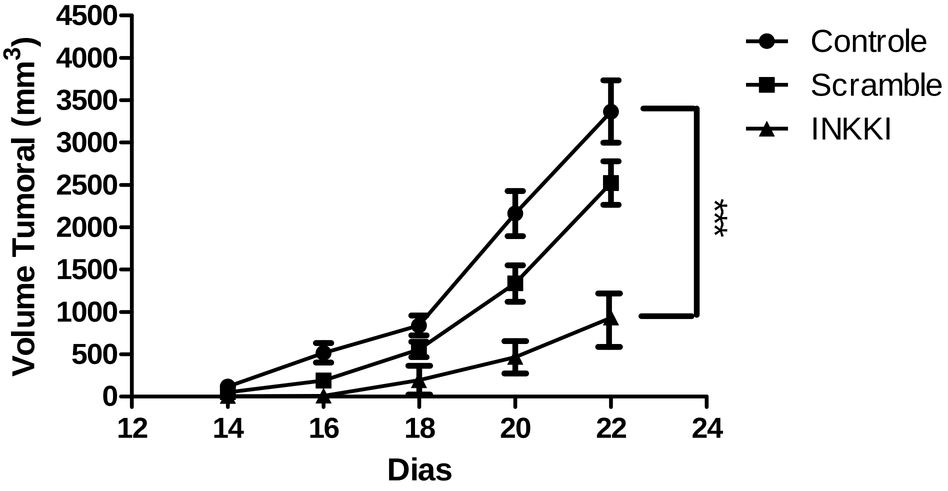

Figura 29. Atividade antitumoral sobre o melanoma cutâneo induzidos em camundongos de linhagem C57BL/6 após o tratamento com o INKKI e scramble. As células de melanoma murino B16F10-Nex2, na concentração de 5x10^5 células de foram injetadas subcutaneamente em camundongos de linhagem C57BL/6. Os animais foram tratados com 2,5 mg/Kg com o INKKI e scramble e o volume tumoral foi mensurado até que os animais atingissem o volume máximo de 3000 mm^3. Os dados mostram que o INKKI apresentou significativo efeito protetor em comparação ao controle negativo tratado com solução salina e ao scramble. Para cada experimento foram utilizados 5 animais por grupos e a análise estatística foi realizada aplicando o teste One-Way ANOVA seguido pelo teste de Tukey-Kramer (* p< 0.05, ** p< 0.01 e *** p< 0.001).

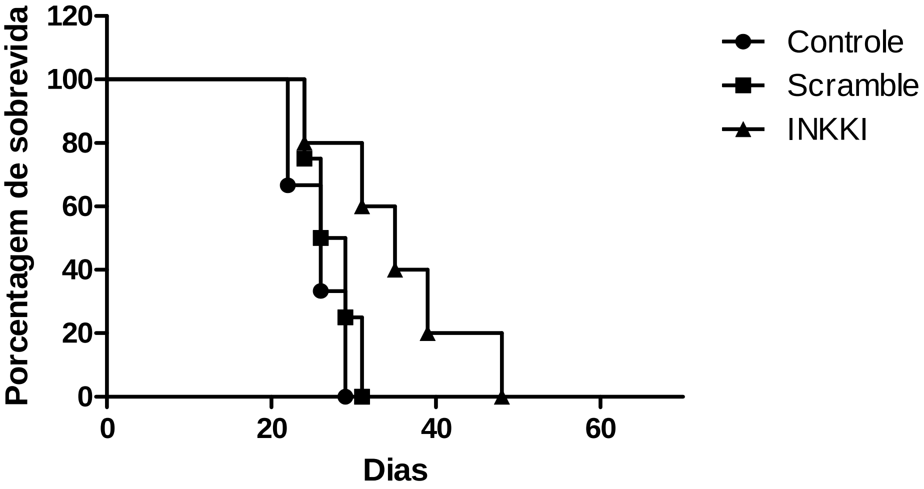

Figura 30. Avaliação da taxa de sobrevida dos animais portadores de melanoma cutâneo tratados com o INKKI e scramble. As células de melanoma murino B16F10-Nex2, na concentração de 5x10^5 células foram injetadas subcutaneamente e tratadas com solução fisiológica e 2,5 mg/Kg com INKKI e scramble. A terapia intraperitoneal começou após os tumores atingirem 100mm^3 e foi prolongada durante 5 dias. Os dados mostraram que o INKKI proporcionou um aumento na taxa de sobrevida em comparação ao controle negativo tratado com solução fisiológica e ao scramble. Para cada experimento foram utilizados 5 animais por grupos e a análise estatística foi realizada pelo método Kaplan-Meyer (***p<0,001 e ** p< 0.01).

4.14 Efeitos antimetastáticos em animais imunodeficientes NOD/SCID/γ_c^{null} tratados com o INKKI

O estudo dos efeitos antitumorais decorrentes da ação direta dos compostos candidatos a agentes antitumorais ou os efeitos protetores deles mediados através da ativação do sistema imunológico fornece importante dado para determinação do mecanismo de ação *in vivo*. Para determinar o envolvimento do sistema imunológico nos efeitos protetores *in vivo*, as células de melanoma B16F10-Nex2 foram injetadas pelo plexo retro-orbital 5×10^4 células nos camundongos imunodeficientes NOD/SCID/γ_c^{null}. Após 24 horas da inoculação, os camundongos foram tratados com 2,5 mg/Kg de INKKI, por animal, através da via intraperitoneal e durante 5 dias. Após o 14º dia os nódulos metastáticos pulmonares foram quantificados. Os resultados mostraram que o INKKI não exerceu efeito direto sobre a inibição das metástases pulmonares, onde foi possível observar que em ambos os grupos experimentais os animais apresentaram mais do que 500 nódulos por pulmão, não estabelecendo diferença estatística entre eles (Figura 31).

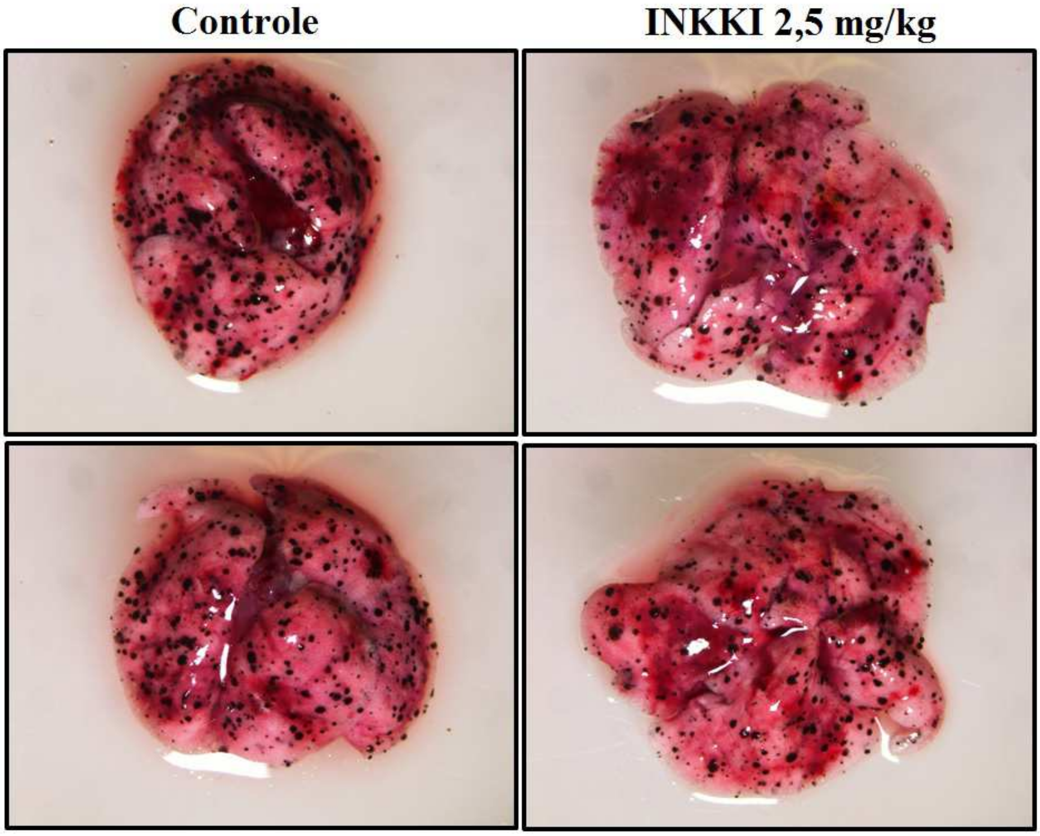

Figura 31. Aspectos macroscópicos e análise quantitativa formação de nódulos metastáticos induzidos em camundongos imunodeficientes de linhagem NOD/SCID/γ_c^{null} após o tratamento com o INKKI. As células B16F10-Nex2 foram injetadas pelo plexo retro-orbital nos animais para indução da formação metastática. Após 24 horas da indução, os animais foram tratados durante 5 dias e no 14º dia os nódulos metastáticos foram quantificados. Aspectos macroscópicos dos pulmões mostraram que os animais tratados com o INKKI não apresentaram diferença significativa do número de nódulos metastáticos em comparação ao controle. As quantificações dos nódulos pulmonares mostraram que os animais controles e tratados com INKKI apresentaram mais de 500 nódulos metastático por pulmão.

4.15 Ensaio de ativação de macrófagos

O sistema imunológico apresenta uma estreita correlação com o controle e o desenvolvimento tumoral. A avaliação da participação da imunidade inata mediada pelos peptídeos que apresentaram atividade antitumoral *in vivo*, foi analisada a produção de NO induzido em macrófagos naive. Os macrófagos foram obtidos da medula, estimulado sua diferenciação e tratados com o INKKI nas concentrações de 100 a 0,1 µM. Os macrófagos foram ativados com IFN-γ (100 U/mL) e LPS (200 ng/mL) e incubados por até 72 horas. Os resultados obtidos mostraram que durante todo o período de incubação, o INKKI não foi capaz de ativar os macrófagos (Figuras 32, 33 e 34). Esse resultado sugere que os efeitos antimetastáticos e protetor *in vivo* não são mediados diretamente pela ativação de macrófagos naive.

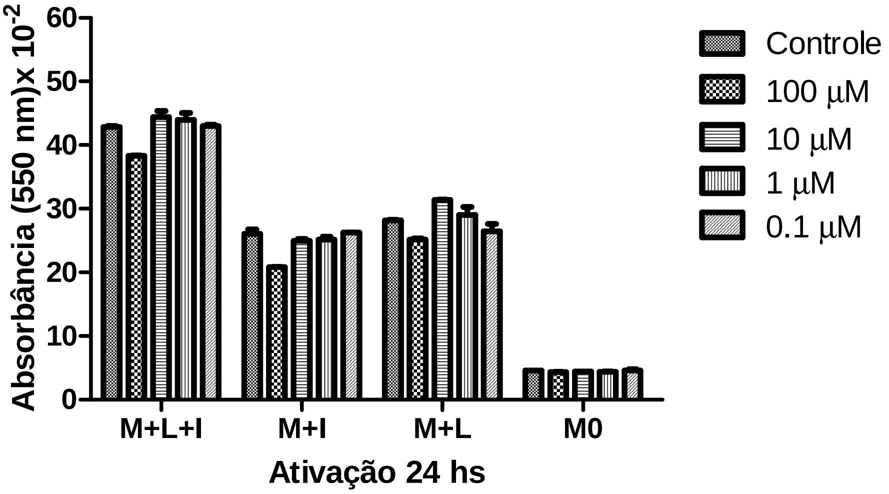

Figura 32. Efeitos sobre a ativação de macrófagos após o tratamento com o INKKI. A cultura de macrófagos foi obtida da medula óssea. Após a obtenção os macrófagos foram diferenciados, tratados com o INKKI e ativados como descrito a seguir: M+L+I (macrófago + LPS + IFN-γ + peptídeo); M+I (macrófago + IFN-γ + peptídeo); M+L (macrófago + LPS + peptídeo); e M0 (macrófago + peptídeos). Após 24 horas de incubação foi quantificada a produção de NO. Os dados mostraram que o peptídeo INKKI não foi capaz de ativar os macrófagos.

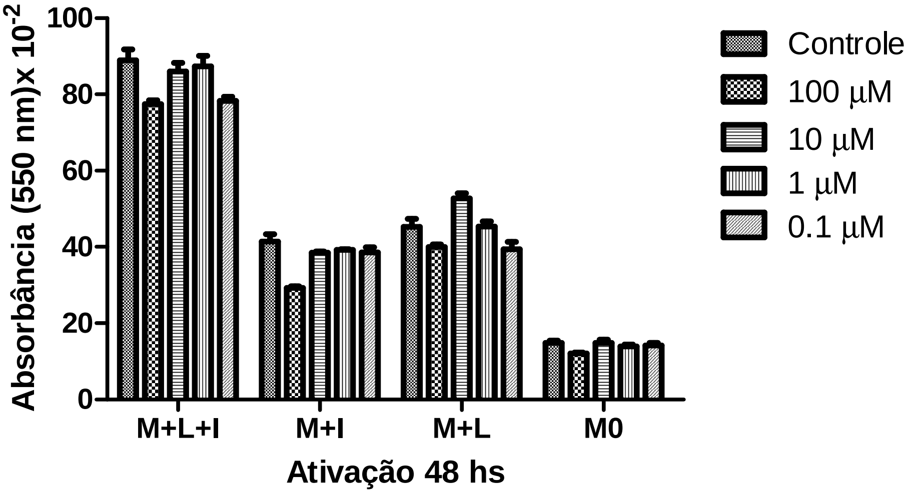

Figura 33. Efeitos sobre a ativação de macrófagos após o tratamento com o INKKI. A cultura de macrófagos foi obtida da medula óssea. Após a obtenção os macrófagos foram diferenciados, tratados com o INKKI e ativados como descrito a seguir: M+L+I (macrófago + LPS + IFN-γ + peptídeo); M+I (macrófago + IFN-γ + peptídeo); M+L (macrófago + LPS + peptídeo); e M0 (macrófago + peptídeos). Após 48 horas de

incubação foi quantificada a produção de NO. Os dados mostraram que o peptídeo INKKI não foi capaz de ativar os macrófagos.

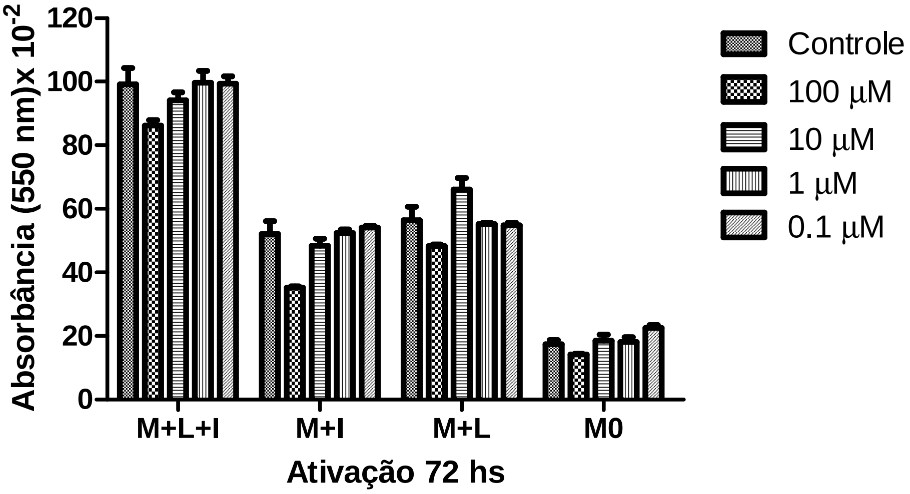

Figura 34. Efeitos sobre a ativação de macrófagos após o tratamento com o INKKI. A cultura de macrófagos foi obtida da medula óssea. Após a obtenção os macrófagos foram diferenciados, tratados com o INKKI e ativados como descrito a seguir: M+L+I (macrófago + LPS + IFN-γ + peptídeo); M+I (macrófago + IFN-γ + peptídeo); M+L (macrófago + LPS + peptídeo); e M0 (macrófago + peptídeos). Após 72 horas de incubação foi quantificada a produção de NO. Os dados mostraram que o peptídeo INKKI não foi capaz de ativar os macrófagos.

4.16 Determinação das proporções da população celular em apoptose pelo teste de Anexina V

Uma das características da apoptose é a perda da polaridade de membrana, acompanhada pela translocação da fosfatidilserina (PS) a partir do interior de folhetos da membrana externa expondo PS para o ambiente externo. A proteína de ligação de fosfolipídios, anexina V, liga-se a células quando expostas externamente, enquanto a coloração PI ocorre somente após perda da integridade da membrana. Os resultados obtidos mostraram que houve significativo aumento das porcentagens das populações das células B16F10-Nex2 controles (tratadas somente com o veículo) de 7,06% para 44,8% tratadas com o mastoparano e marcadas com anexina V positiva. Simultaneamente, também foi possível observar um aumento das células de B16F10 duplamente marcadas com anexina V e PI nas proporções de 7,6% controle para 19,1% tratadas com o mastoparano. (Figura 35 A e B).

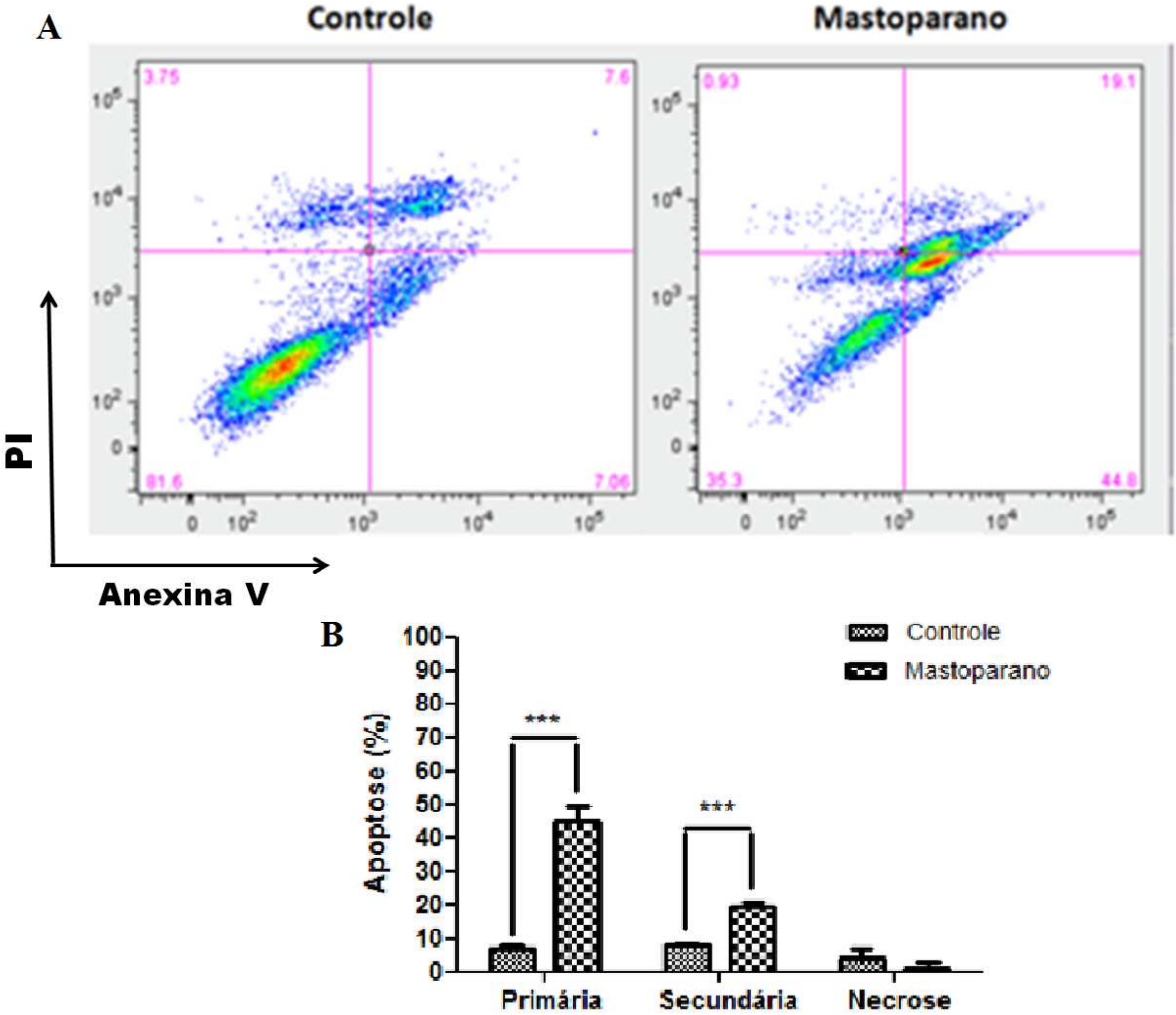

Figura 35. Avaliação morte celular pelo teste de Anexina V/PI por citometria fluxo. (A) Dot plots representando a distribuição da marcação na população celular. (B) Gráfico de barras representando a quantificação da porcentagem de marcação distribuída pela população celular. Os dados representam os efeitos apoptóticos/necróticos após os tratamentos com o 165 µM de mastoparano, comparado com o controle sem o peptídeo, em culturas de células tumorais de linhagem de melanoma murino B16F10-Nex2 e determinadas por citometria de fluxo após 12 horas de tratamento. O mastoparano foi capaz de aumentar significativamente a proporção de morte por apoptose na população celular (*** $p< 0.001$).

4.17 Indução da despolarização do potencial de membrana mitocondrial (*ψm*)

O estudo dos efeitos do mastoparano durante o processo de apoptose via alterações do potencial elétrico mitocondrial foram avaliados através da utilização do corante catiônico lipofílico TMRE nas células de melanoma. Os dados mostraram que o mastoparano foi capaz de reduzir significativamente a intensidade da fluorescência, sugerindo que o tratamento com este peptídeo resultou na dissipação do ΔΨm. O dano mitocondrial durante o processo de apoptose induzida pelo mastoparano em células B16F10-Nex2 foi demonstrado pela redução em 42,8% e 49,7% do acumulo do corante lipofílico catiônico TMRE na organela após o período de 1 e 3 horas de incubação, respectivamente, implicando em limiar de permeabilidade reduzida (Figura 36).

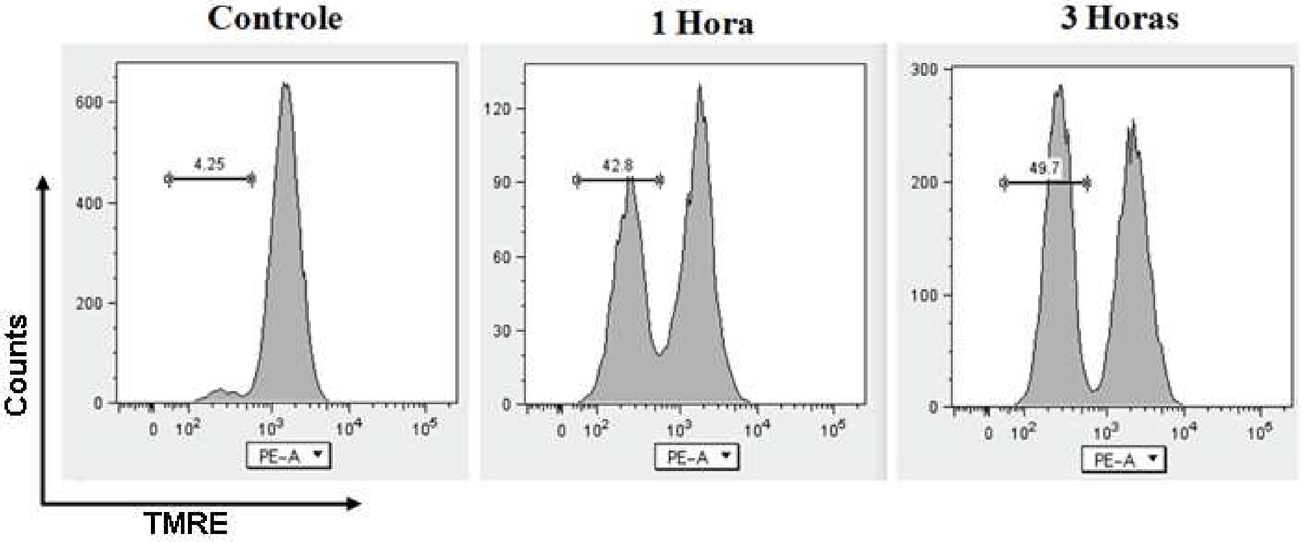

Figura 36. Perda do potencial mitocondrial transmembrana (ΔΨm) em células tratadas com mastoparano. As células de melanoma murino B16F10-Nex2 foram tratadas com 165 µM do mastoparano pelos períodos indicados e recolhidos para a determinação do ΔΨm utilizando TMRE por citometria de fluxo. Os histogramas representativos do acúmulo do TMRE em células não tratadas (controle) e tratadas com o mastoparano por 1 e 3 horas.

4.18 Análise da integridade do DNA após tratamento com o mastoparano

O desenvolvimento de novos agentes antitumorais fundamenta-se na capacidade desses compostos de inibirem a proliferação e induzirem morte celular. O padrão de bandas formadas durante a degradação do DNA fornece importantes informações do tipo de morte celular. Desta forma, análise através da eletroforese em gel de agarose mostrou que o mastoparano na concentração de 165 µM incubado por 3 horas proporcionou a degradação de DNA em células de melanoma murino B16F10-Nex2 com formação padrão de bandas característico de apoptose (Figura 37).

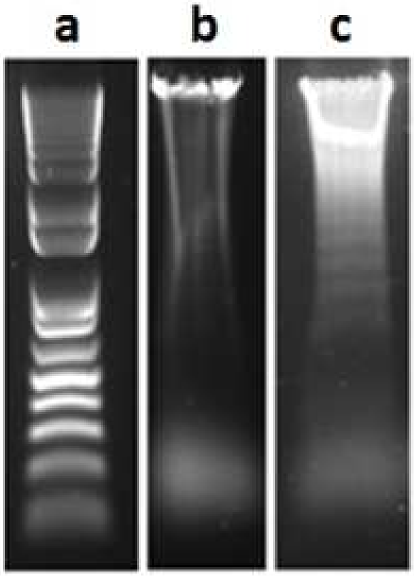

Figura 37. Fragmentação do DNA induzida por mastoparano em células B16F10-Nex2. As células foram incubadas com o mastoparano na concentração 165µM por 3h. Os extratos nucleares foram obtidos e a fragmentação do DNA foi analisada por eletroforese em gel de agarose 1,0%, corado com brometo de etídio, como descrito nos materiais e métodos. a) padrão de 1Kb; b) controle (células não tratadas); c) células tratadas com o mastoparano. Os dados mostram que as células tratadas com o mastoparano apresenta a formação do padrão de fragmentação característica de apoptose.

4.19 Determinação de alterações morfológicas características de apoptose em células induzidas pelo mastoparano

O processo de morte celular induzida por apoptose apresenta significativas modificações morfológicas. Para estudar as características morfológicas da apoptose desencadeada pelo mastoparano em células B16F10-Nex2, foram empregadas a marcação com DAPI e mensurado por microscopia de fluorescência. A densidade da cromatina foi avaliada em células cultivadas em placa de 96 poços na presença de 165 µM de mastoparano. Após a incubação foi adicionado DAPI e os resultados mostraram que o mastoparano induziu significativas alterações morfológicas, onde é possível observar a fragmentação e condensação nuclear (núcleos picnóticos). O percentual de núcleos apoptóticos foi de 65,87 % em células de melanoma incubadas com o mastoparano (Figura 38 A e B).

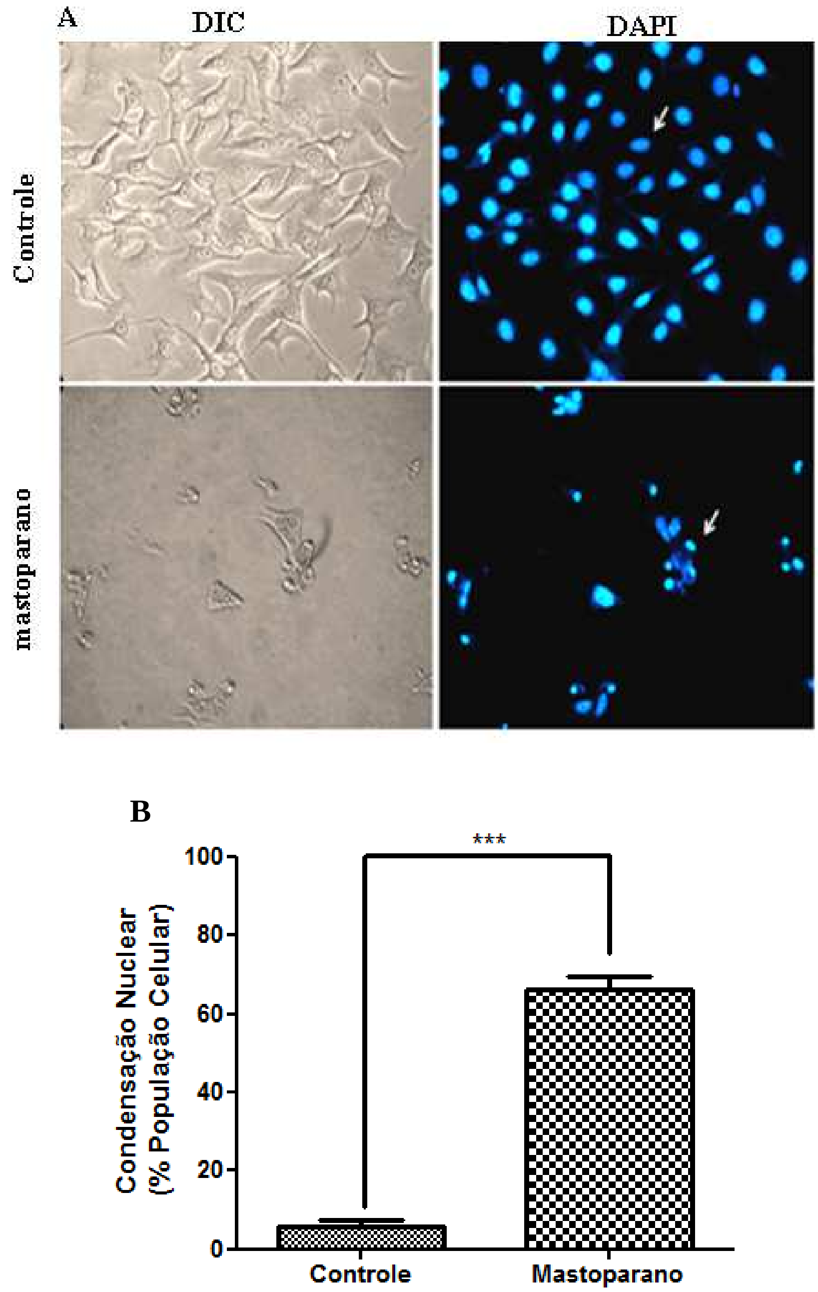

Figura 38. Alterações morfológicas características de apoptose induzidas pelo mastoparano em células de melanoma murino B16F10-Nex2. As células de melanoma foram cultivadas na concentração de 10^4 em placa de 96 e tratadas com 165 µM de mastoparano e incubadas por 18 horas. (A) As modificações morfológicas correlacionadas com o estado da cromatina foi avaliada após a marcação nuclear com DAPI. Nota-se a presença de condensação da cromatina após o tratamento com o mastoparano (seta branca). (B) Quantificação da percentagem de células marcadas com DAPI. As células positivas para a coloração foram visualizadas em microscópio de fluorescência e expressa em porcentagem do total de células contadas de células controle (aumento 20x) e a análise estatística foi realizada aplicando o test t de student utilizando o Software Graph Prism (***p<0,001 e ** p< 0.01).

4.20 Geração de Espécie Reativas do Oxigênio (ROS) induzida pelo mastoparano

O aumento de liberação de espécies reativas do oxigênio (ROS) pode desencadear uma cascata de eventos que conduzem a apoptose. A avaliação da geração de ROS pode contribuir de forma significativa para a compreensão do mecanismo de morte celular proporcionado pelo mastoparano. Para avaliar a geração de ROS as células de melanoma murino B16F10-Nex2 foram tratadas com 165 µM de mastoparano e incubadas por 3 e 6 horas. Após a incubação as células B16F10-Nex2 foram coradas com dihidroetídio (DHE) por 30 minutos a 37 ℃ em temperatura ambiente e sua conversão em etídio foram mensuradas em microscopia confocal. Após a aquisição das imagens foi possível observar que o mastoparano aumentou significativamente a intensidade da fluorescência de etídio de 12% na população controle para 44% e para 74,76% na população tratada e incubada por 6 horas (Figura 39 A e B).

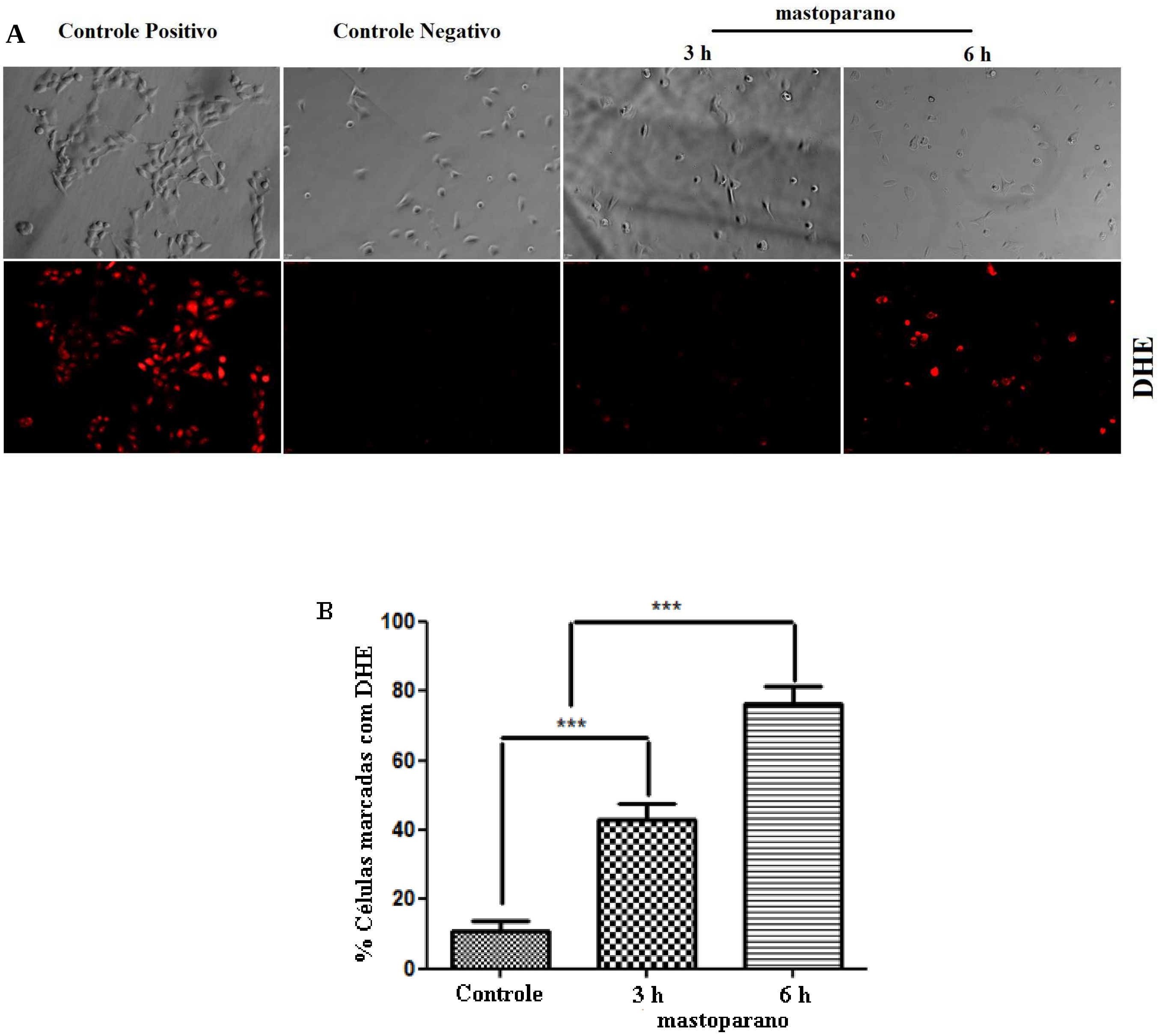

Figura 39. Geração de espécies reativas do oxigênio (ROS) pelo mastoparano em células de melanoma murino B16F10-Nex2. (A) Células de melanoma B16F10-Nex2 não tratadas (controle negativo) e tratadas com 165 µM de mastoparano por 3 e 6 horas foram incubadas com o corante fluorescente DHE (5 µM) para detecção da produção de ânion superóxidos. (B) Quantificação da percentagem de células marcadas com DHE. As células positivas para a coloração foram visualizadas em microscópio de fluorescência e expressa em porcentagem do total de células contadas de células controle e a análise estatística foi realizada aplicando o test t de student utilizando o Software Graph Prism (***$p<0,001$ e ** $p< 0.01$).

4.21 Efeitos sobre a viabilidade celular em culturas de B16F10-Nex2 pré-incubadas com o antioxidante N-acetilcistína (NAC) após tratamento com o mastoparano

A liberação de espécies reativas de oxigênio (ROS) pode desencadear uma cascata de eventos que conduz a apoptose. A N-acetilcisteína é conhecida como um importante agente inibidor da produção de ROS. A avaliação da citotoxicidade do mastoparano na presença e ausência de NAC foi mensurada pelo método MTT em células de melanoma murino B16F10-Nex2. Os resultados obtidos após o tratamento mostraram que o mastoparano na presença de NAC apresentou menor toxicidade quando comparado com o tratamento na ausência do NAC. As células pré-tratadas com o NAC apresentaram significativo aumento na IC_{50} de 165 µM NAC^- para 295 µM NAC^+ (Figura 40). Esses dados mostram que a geração de ROS é um importante evento envolvido no processo de morte celular induzidas pelo mastoparano.

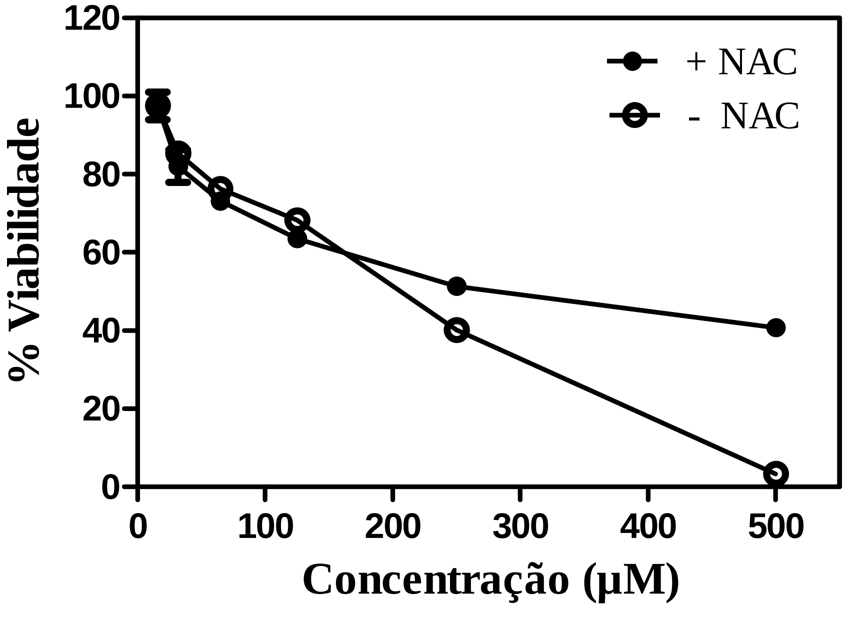

Figura 40. Avaliação da citotoxicidade do mastoparano na presença e ausência de N-acetilcisteína (NAC). As células de melanoma murino B16F10-Nex2 na densidade de 10^4 foram plaqueadas em placas de 96 poços, tratadas com diferentes concentrações do mastoparano na presença e ausência de NAC e incubados durante de 24 horas. Os dados exibiram que as células tratadas com o mastoparano na presença do antioxidante foram mais resistentes aos efeitos citotóxicos. A curva mostra a correlação do efeito dose-resposta expressa em média ± DP.

4.22 Avaliação da atividade enzimática da caspase 3 após o tratamento com o mastoparano

Umas das principais alterações funcionais foram avaliadas em linhagens de melanoma murino B16F10-Nex2 após o tratamento com o mastoparano por fluorimetria. Neste experimento foi avaliado a atividade da caspase 3, uma importante cisteíno proteinase executora, comum as vias intrínseca e extrínseca. A atividade enzimática de caspase-3 foi mensurada após o tratamento com 165 µM de mastoparano. Após o período de incubação, a análise por fluorimetria indicou que o mastoparano foi capaz de aumentar significativamente a atividade da caspase 3 quando comparado com o controle sem o tratamento (Figura 41).

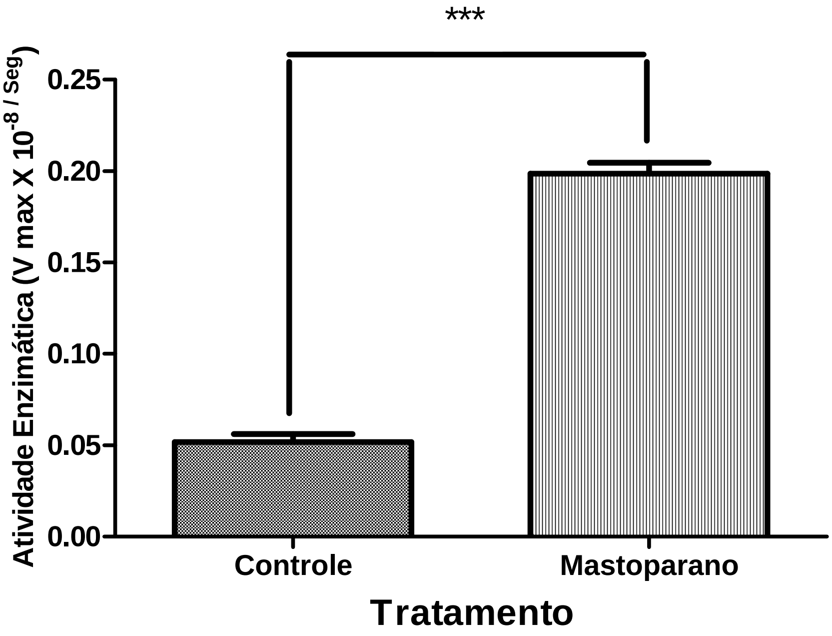

Figura 41. Avaliação da atividade enzimática da caspase 3 em culturas de melanoma murino B16F10-Nex2 após o tratamento com o mastoparano. As barras do histograma indicam o aumento da atividade da caspase 3 após os tratamentos com o mastoparano 165 µM comparado o controle sem o tratamento determinada por fluorimetria após 6 horas de tratamento. Os tratamento com o mastoparano foi capaz de aumentar significativamente a atividade da caspase 3 e a análise estatística foi realizada aplicando o test t de Student utilizando o Software Graph Prism (***p<0,001 e ** p< 0.01).

4.23 Análise do mecanismo de ação da apoptose via mitocondrial intrínseca induzidos pelo tratamento com o mastoparano por Western Blotting

Para entender o mecanismo de ação desencadeado pelo mastoparano induzindo apoptose através da via mitocondrial intrínseca em cultura de melanoma B16F10-Nex2, foram avaliados os principais mediadores pró e anti-apoptóticos por Western blotting. As células B16F10-Nex2 na concentração de 10^6 foram tratadas com 165 µM do mastoparano e incubadas por 3 e 12 horas. Após o período de incubação foi possível observar significativas modificações morfológicas que caracterizam a apoptose, tais como, retraimento citoplasmático com manutenção da integridade de membrana plasmática, condensação nuclear e formação de corpos apotóticos (Figura 42).

A apoptose está associada com a ativação específica através do processamento proteolítico das caspases iniciadoras 8, 9 e 12 e da caspase efetora 3. Os resultados mostraram que o mastoparano nos tempos de 3 e 12 horas de incubação, foi capaz de reduzir as pró-caspases 3, 9 e 12 e aumento nos níveis de suas formas clivadas (ativas) (Figura 43 A). Não foi possível detectar o alterações nos níveis da pró-caspase 8 ou caspase 8 clivada (dados não mostrados). Adicionalmente, foi detectado aumento nos níveis da poli (ADP-ribose) polimerase (PARP) clivado, resultante da clivagem específica do PARP pela forma ativa da caspase 3. Esses resultados indicam que a morte celular induzida pelo mastoparano está associada com a ativação das caspases iniciadoras 9 e 12 e efetora 3 (Figura 43 B).

Além da despolarização da membrana mitocondrial e a clivagem da pro-caspase 9 em sua forma ativa, a via intrínseca da apoptose também envolve a perturbação da permeabilidade da membrana mitocondrial, no qual libera importantes fatores pró-apoptóticos para o citoplasma e consequentemente, desencadeando a ativação da via das caspases. Neste contexto, as proteínas da família da Bcl-2 apresentam uma importante regulação no balanço entre os membros pró-apoptóticos, anti-apoptóticos e sobrevida celular. Sobre a avaliação da expressão da família Bcl-2 em células B16F10 tratadas com o mastoparano, foi possível observar que houve significativa redução da expressão do BCL-XL e Bad fosforilado. Somando a esses resultados, também ficou evidente que o mastoparano induziu, de maneira tempo dependente, o aumento nos níveis de fatores pró-apoptóticos tais como o Bim e Bak (Figura 44 A).

Consistentemente com a despolarização da membrana mitocondrial e a modulação de proteínas pró-apoptóticas, foi possível observar significativo aumento nos níveis de citocromo c nas células tratadas com o mastoparano. Adicionalmente, o tratamento com o mastoparano resultou na significativa diminuição dos níveis e PHB-1 e dos canais aniônicos dependente de voltagem (VDAC), no qual pode explicar a morfologia anormal das cristas mitocondriais e perda da integridade de membrana mitocondrial (Figura 44 A). Sendo assim, ficou evidente que o mastoparano exibiu importante efeito na perturbação da permeabilidade mitocondrial, liberando fatores pró-apoptóticos para o citoplasma e consequentemente, acionamento da via das caspases durante a apoptose (Figura 44 B).

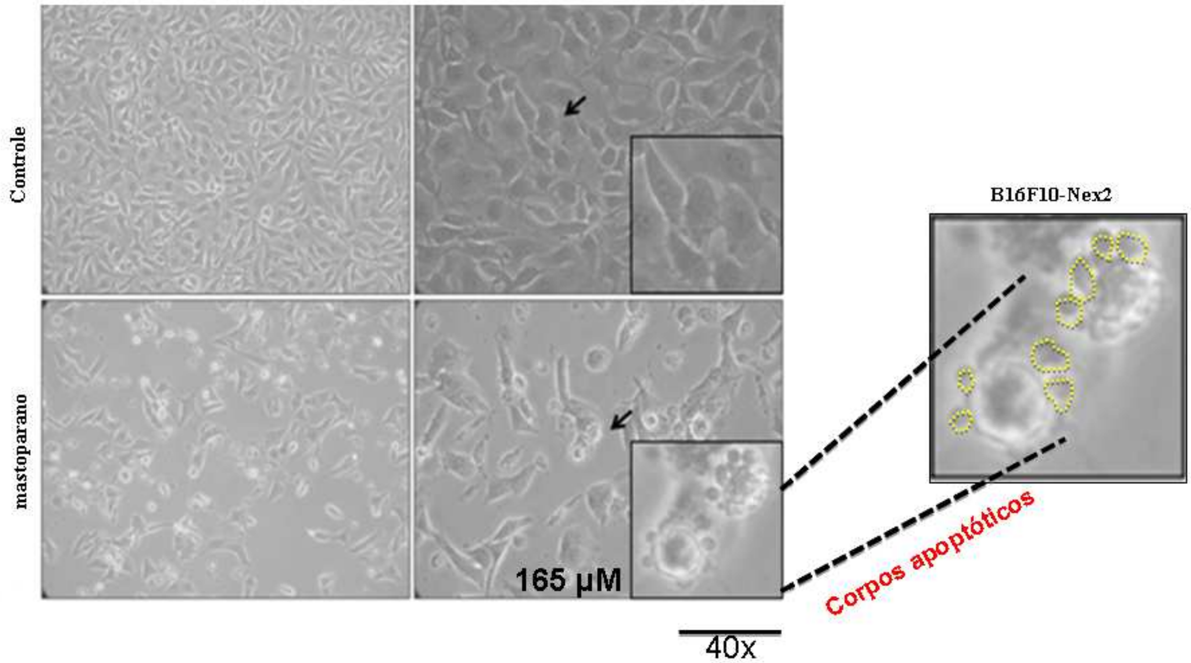

Figura 42. Alterações morfológicas das células B16F10-Nex2 após 12h de tratamento com o mastoparano. As células B16F10-Nex2 foram plaqueadas na concentração de 10^6 em placas de 6 poços, tratadas com 165 µM de mastoparano e incubadas por 12 horas. Após a incubação foi possível observar significativas alterações na morfologia celular. As células tratadas com o mastoparano exibiram retraimento do citoplasma, formas arredondadas, manutenção da integridade da membrana plasmática e a formação de corpos apoptóticos.

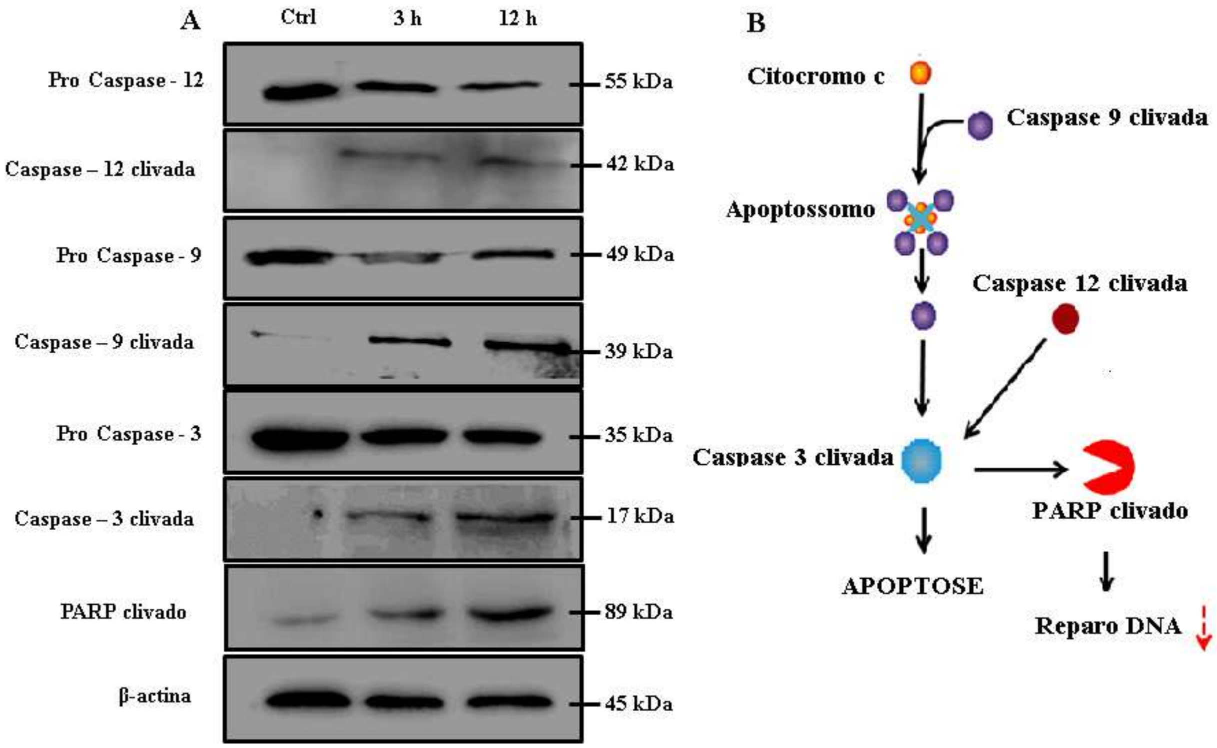

Figura 43. Avaliação dos efeitos apoptóticos do tratamento das células B16F10-Nex2 com o mastoparano sobre os níveis de expressão da via de ativação das caspases. As células de B16F10-Nex2 foram plaqueadas na concentração de 10^6 em placas de 6 poços, tratadas com 165 µM de mastoparano e incubadas por 3 e 12 horas. Após a incubação, os mediadores foram estudados por western blottings para checagem da expressão das pró-caspase 3, 9, 12, caspases clivadas 3, 9, 12 e PARP clivado. Todos os anticorpos foram diluídos na proporção de 1:1000 e normalizados pela quantificação da β-actina. **A)** Os resultados mostraram redução dos níveis de pró-caspase 3, 9 e 12 e consequentemente aumento nos níveis das caspases 3, 9, 12 clivadas e PARP clivado. **B)** Esquema de ativação da sinalização da apoptose caspase dependente. O citocromo c pode ser liberado para o citoplasma através da perturbação da permeabilidade da membrana mitocondrial. No citoplasma forma o complexo com Apaf-1 e pró-caspase-9, que na presença de dATP, cliva e ativa a caspase-9. A ativação da caspase-9 pode decompõe e ativa a pró-caspase-3, levando a clivagem da PARP, que por sua vez, não irá induzir o reparo de DNA. A consequência da ativação desses eventos é a condução da morte celular por apoptose caspase dependente.

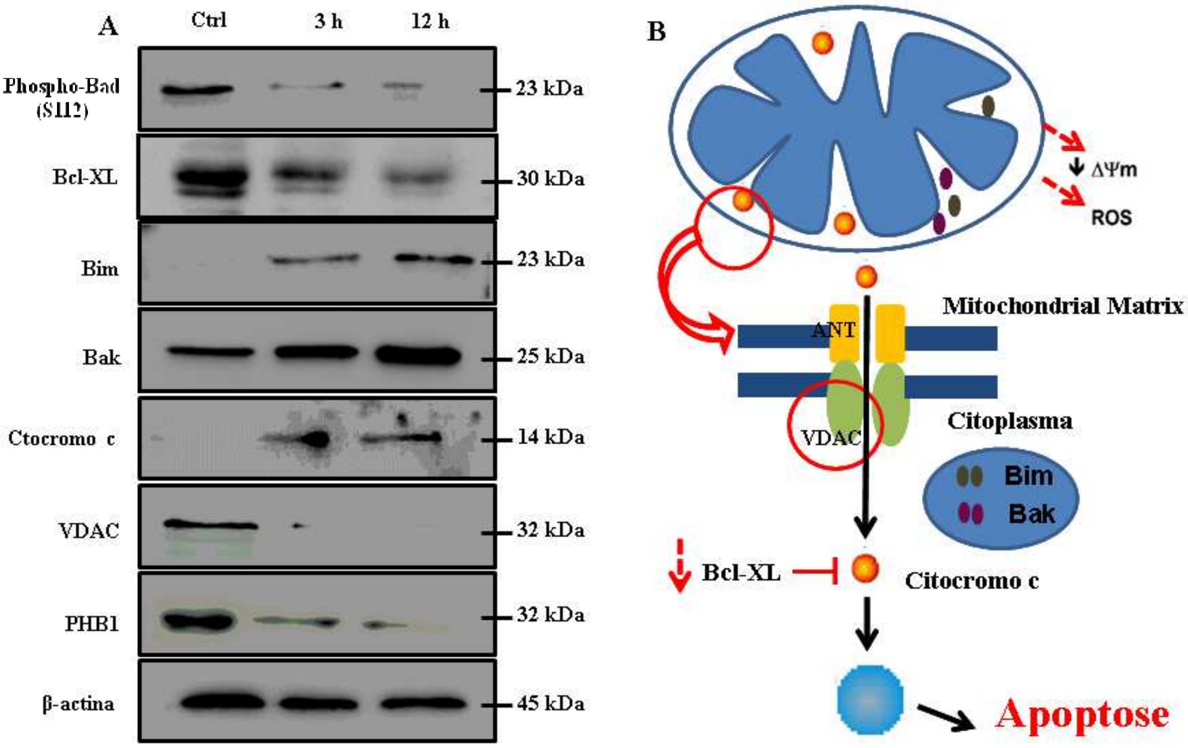

Figura 44. Avaliação dos efeitos apoptóticos do tratamento das células B16F10-Nex2 com o mastoparano sobre os níveis de expressão da via intrínseca mitocondrial. As células de B16F10-Nex2 foram plaqueadas na concentração de 10^6 em placas de 6 poços, tratadas com 165 µM de mastoparano e incubadas por 3 e 12 horas. Após a incubação, os mediadores foram estudados por western blottings para checagem dos níveis do fosfo-Bad (Ser 112), Bcl-XL, Bim, Bak, citocromo c,VDAC e PHB1. Todos os anticorpos foram diluídos na proporção de 1:1000 e normalizados pela quantificação da β-actina. **A)** Os resultados mostraram redução dos níveis de fosfo-Bad (Ser 112), VDAC e PHB1 e consequentemente aumento nos níveis Bim, Bak e citocromo c. **B)** Esquema de ativação da sinalização da apoptose através da via mitocondrial intrínseca. A geração de espécie reativa de oxigênio pode perturbar os poros de transição mitocondrial caracterizado pela redução dos níveis de VDAC e PHB1. A perturbação da permeabilidade mitocondrial mobiliza o influxo de fosfo-Bad (Ser 112) para a mitocondria, reduz a expressão de proteína anti-apoptótica Bcl-XL e aumenta os níveis de fatores pró-apoptóticos tais como Bim, Bak e citocromo c, ativando as caspases e conduzindo para a apoptose via mitocondrial.

4.24 Avaliação ultraestrutural dos efeitos morfológicos induzidos pelo mastoparano em células B16F10-Nex2

As análises ultraestruturais das células B16F10-Nex2 tratadas com 165 µM foram realizadas para correlacionar os efeitos moleculares com as alterações morfológicas. Nas células não tratadas as membranas citoplasmáticas apresentaram microvilosidades regulares e polimorfismo celular. Foi possível observar nucléolo visível na maioria das secções e numerosas mitocôndrias distribuídas ao longo do citoplasma (Figura 45). O Complexo de Golgi está composto em lamelas dispondo morfologicamente de cisternas preservadas, localizado na porção cis em relação ao núcleo e adjacente com o retículo endoplasmático (RE). O RE apresenta estruturas variadas, formadas em longos filamentos, com cisternas planas e portando numerosos ribossomos adjacente ao microtúbulo (Figura 46). As mitocôndrias apresentam-se de forma pleomórfica com cristas septadas e separadas por membrana interna e externa (Figura 47).

As células B16F10-Nex2 tratadas com o 165 µM de mastoparano apresentaram significativas alterações ultraestruturais características da apoptose tais como condensação da cromatina, dilatação da membrana nuclear e aumento da porosidade do envoltório nuclear, que supostamente ocorre em resposta à liberação de endonucleases que permeiam os poros do envelope nuclear, induzindo clivagem de substratos nucleares (Figura 48). As análises ultraestruturais das mitocondriais das células B16F10-Nex2 tratadas com o mastoparano mostraram que as modificações da bioenergética mitocondrial estão relacionadas com as alterações ultraestruturais observadas. As mitocôndrias exibem vários graus de condensação com deformidades nas cristas e invaginações citoplasmáticas apresentando descontinuidade entre a membrana externa. É possível observar algumas características associadas à redução do potencial elétrico mitocondrial tais como perda da eletrodensidade, aumento de volume e ruptura da membrana externa (Figura 48).

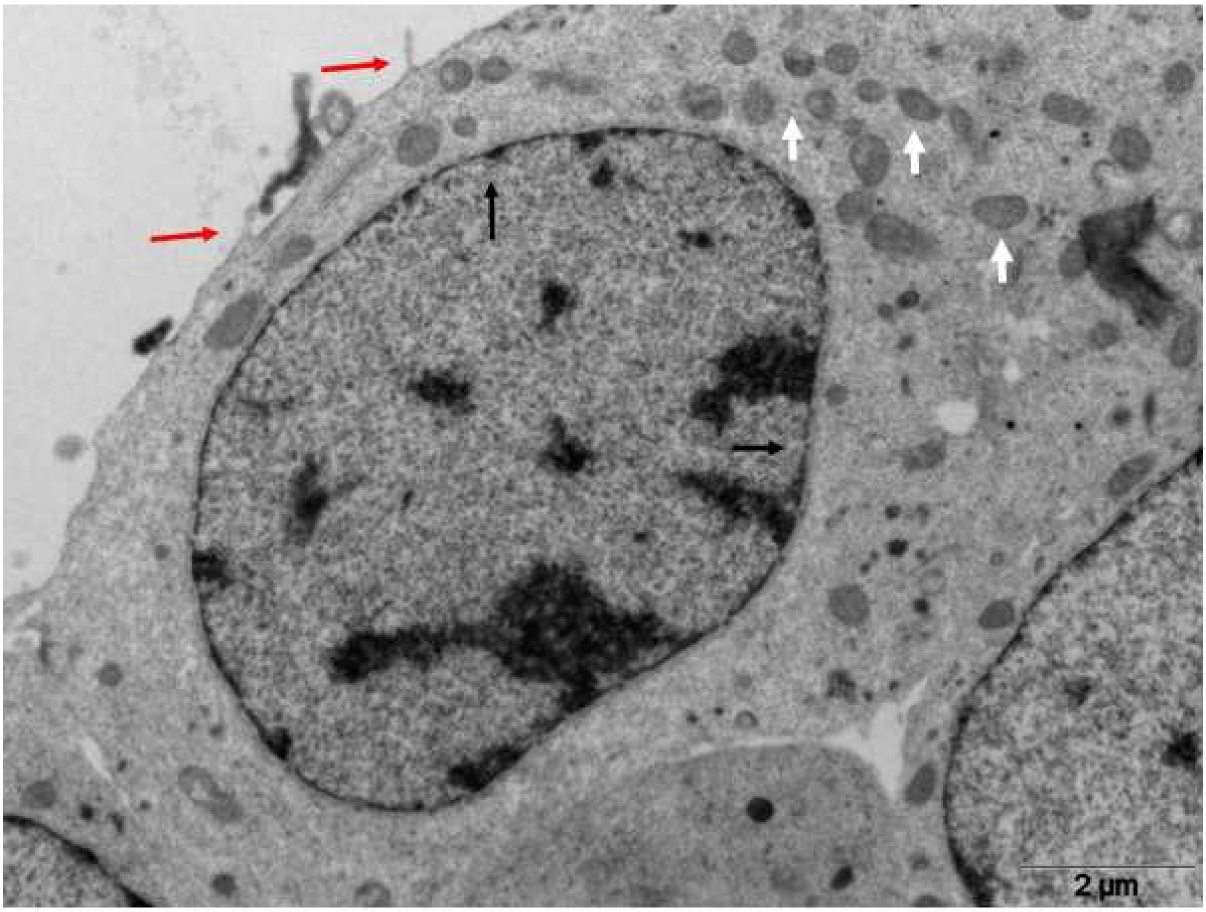

Figura 45. Fotomicrografia eletrônica das células B16F10-Nex2 sem tratamento. Nas células não tratadas observam-se microvilosidades salientes na superfície celular (setas vermelhas), com o núcleo suavemente contornado com a heterocromatina (setas pretas) e presença de numerosas mitocôndrias (setas brancas) distribuídas ao longo do citoplasma.

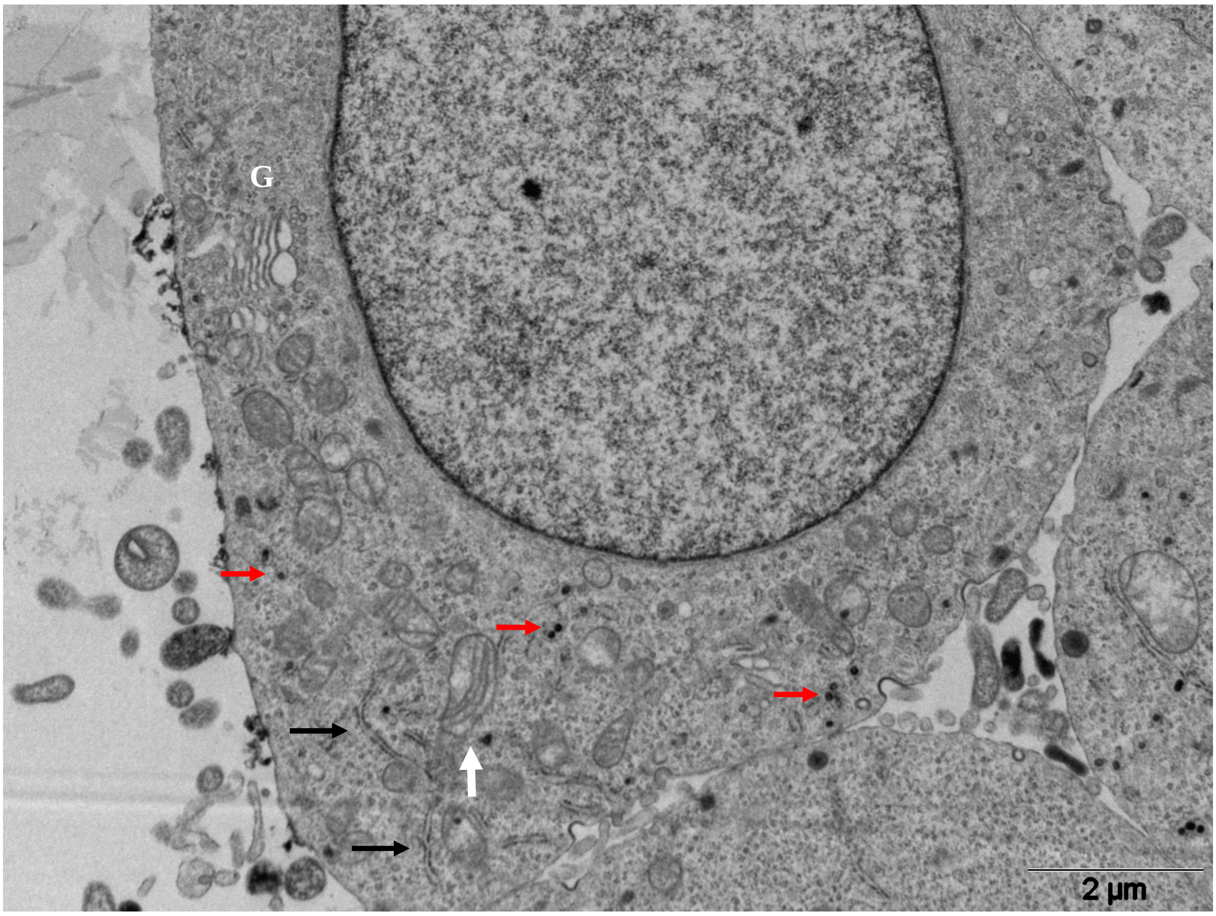

Figura 46. Análises ultraestruturais das organelas das células B16F10-Nex2 controle. Observam-se diversas vesículas melanocíticas distribuídas amplamente pelo citoplasma (setas vermelhas). Diversas organelas, tais como, retículo endoplasmático rugoso (setas pretas), complexo de golgi (G) e mitocôndrias (setas brancas) apresentam morfologias bem definidas e ausência de modificações estruturais.

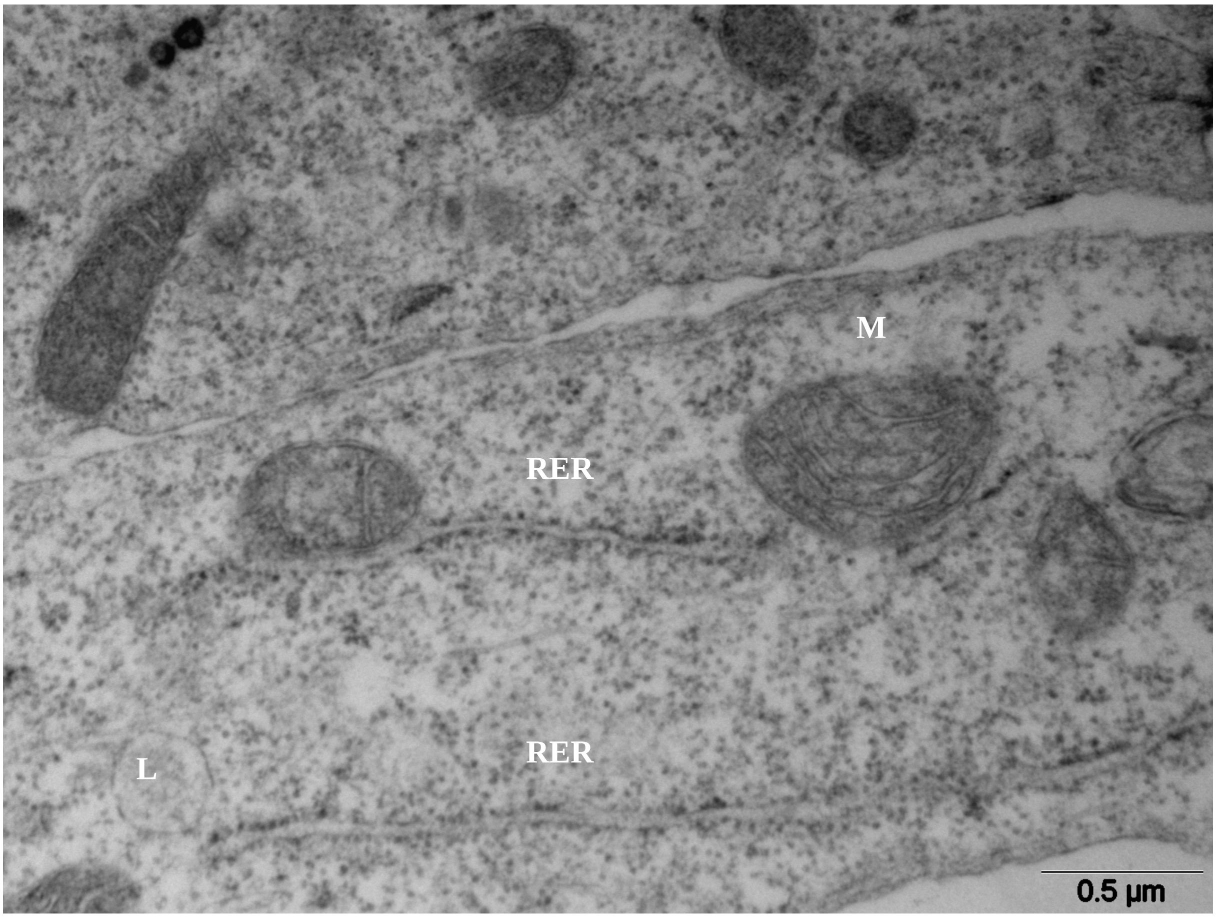

Figura 47. Análises ultraestruturais das mitocôndrias e reticulo endoplasmático rugoso das células B16F10-Nex2 não tratadas com o mastoparano. A população de mitocôndria (M) nas células não tratadas apresentam-se em formas pleomórficas sem modificações estruturais. Nota-se que as cristas mitocondriais estão bem delimitadas, sem alterações na ultraestrutura da membrana externa ou interna. O lisossomo (L) e retículo endoplasmático rugoso (RER) apresentam formas bem definidas e ausência de anomalias estruturais.

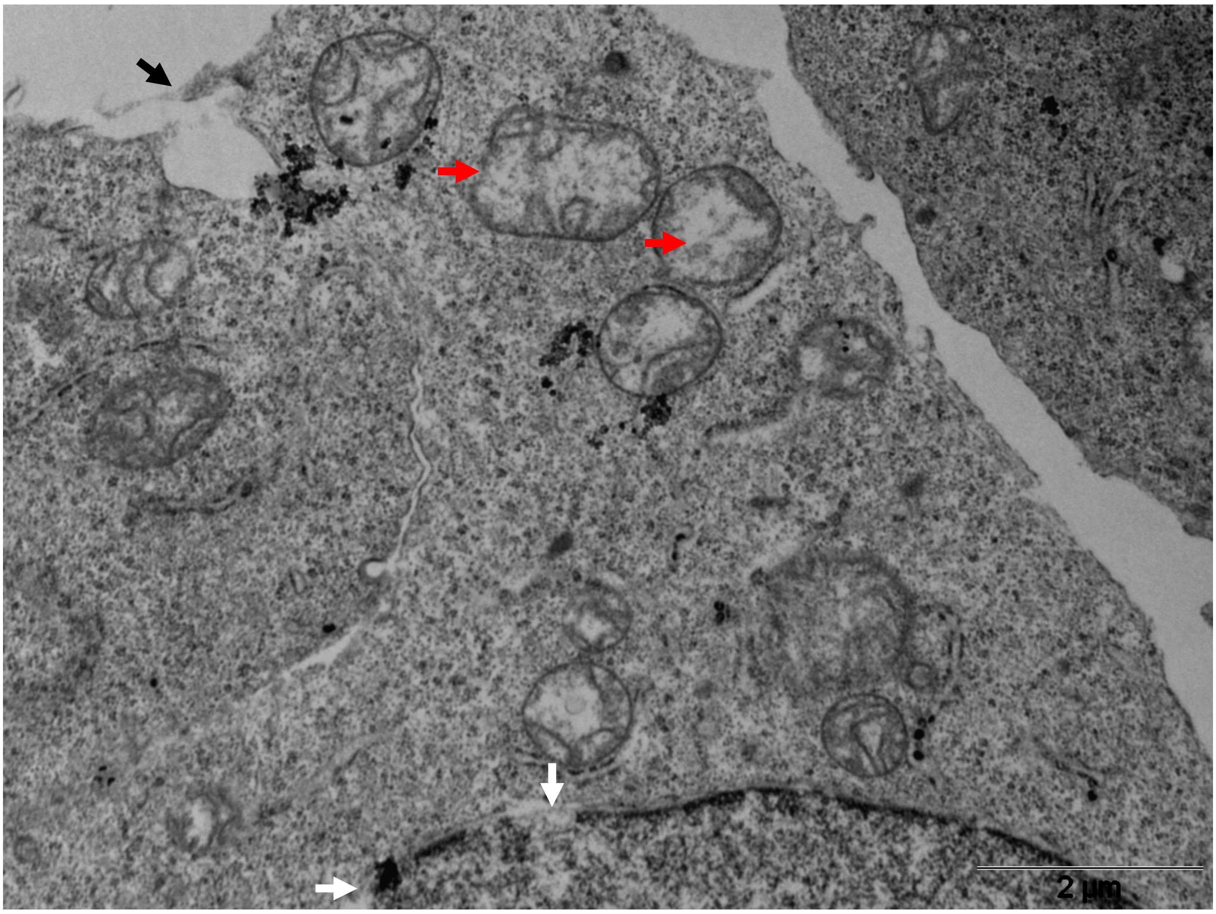

Figura 48. Análises das ultraestruturas das células B16F10-Nex2 tratadas com mastoparano. A eletromicrografia das células tratadas com mastoparano apresentam características morfológicas típicas da apoptose, tais como, perda de integridade de membrana (seta preta) e aumento da porosidade do envoltório nuclear (setas brancas). As mitocôndrias apresentaram redução de eletrodensidade correspondente à redução do potencial elétrico mitocondrial, amento do volume mitocondrial, perda da integridade das cristas mitocondriais e ruptura da membrana mitocondrial (setas vermelhas)

4.25 Efeito antitumoral sobre o melanoma cutâneo em animais tratados com o mastoparano

A inoculação subcutânea das células melanoma murino induz o desenvolvimento de um nódulo hipodérmico que se torna palpável em torno de uma a duas semanas, sendo facilmente mensurado, evoluindo para um tumor sólido, podendo chegar a grandes dimensões. Para avaliar os efeitos terapêuticos 10^5 células de melanoma murino B16F10-Nex2 foram injetadas subcutaneamente nos flancos direitos dorsais dos camundongos de linhagem C57BL/6. Após os tumores atingirem 100 mm^3, os animais foram tratados com 5 mg/Kg de mastoparano, pela via peritumoral e o volume tumoral foi mensurado até que os animais atingissem o volume máximo de 3000 mm^3. Os dados mostraram que o mastoparano foi capaz de inibir o crescimento tumoral em 70,29% em comparação aos animais controles tratados com solução salina (Figura 49).

A taxa de sobrevida é um importante parâmetro amplamente utilizado para avaliar a eficácia terapêutica antitumoral, uma vez que diversos agentes quimioterápicos utilizados na clínica oncológica disponíveis para o melanoma apresentam discreto aumento na expectativa de vida do paciente. A taxa de sobrevida foi avaliada de acordo com as condições experimentais descritas acima. Os resultados mostraram que o tratamento com o mastoparano foi capaz de aumentar a taxa de sobrevida dos animais portadores de tumores dorsais em 28,26% (P<0.007), em comparação ao controle negativo tratado com solução salina e ao scramble (Figura 50).

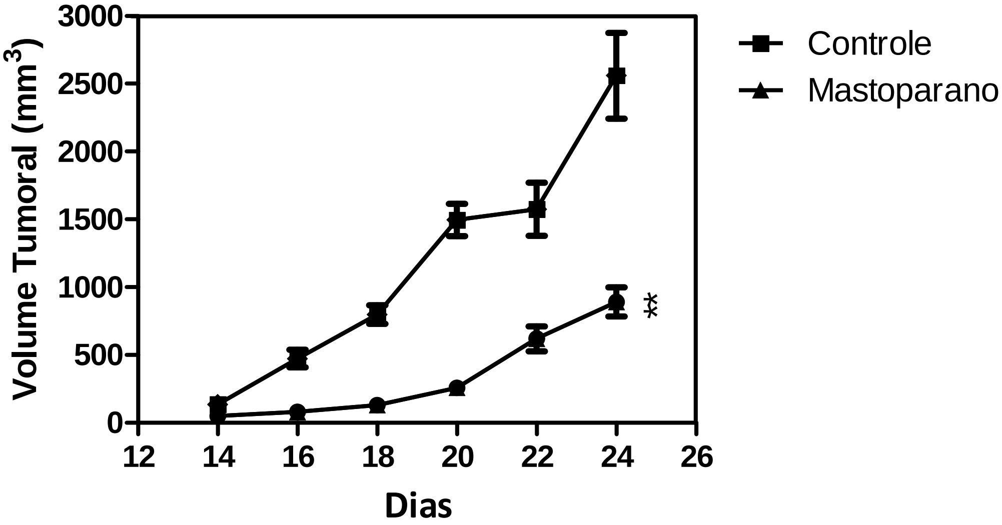

Figura 49. Efeito antitumoral sobre o melanoma cutâneo induzidos em camundongos de linhagem C57BL6 após o tratamento com mastoparano. As células de melanoma murino B16F10-Nex2, na concentração de 10^5 células de foram injetadas subcutaneamente em camundongos de linhagem C57BL/6. Após os tumores atingirem 100 mm^3, os animais foram tratados com 5 mg/Kg com o mastoparano, pela via peritumoral e o volume tumoral foi mensurado até que os animais atingissem o volume máximo de 3000 mm^3. Os dados mostram que o mastoparano apresentou significativo efeito protetor em comparação ao controle negativo tratado com solução salina. Para cada experimento foram utilizados 5 animais por grupos e a análise estatística foi realizada aplicando utilizando o Software Graph Prism (***p<0,001 e ** p< 0.01).

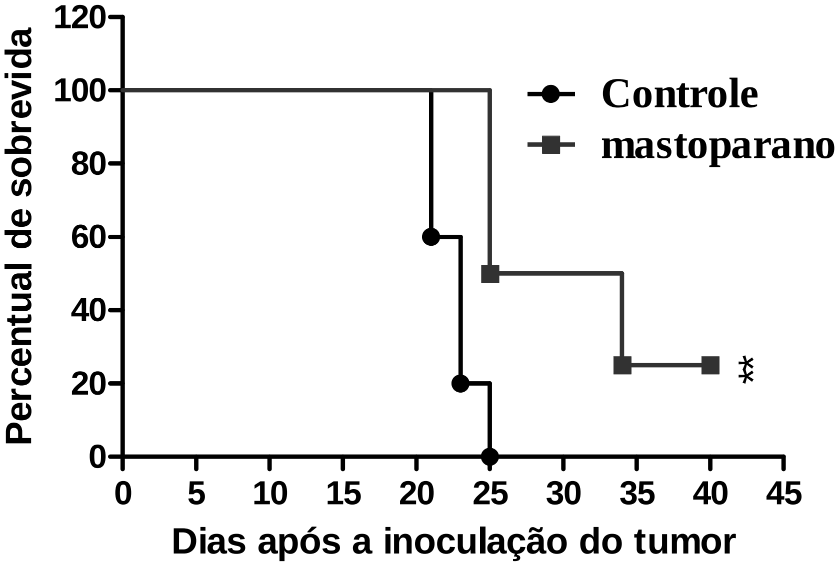

Figura 50. Avaliação da taxa de sobrevida dos animais portadores de melanoma cutâneo tratados com o mastoparano. Os animais foram injetados subcutaneamente com 10^5 células e tratadas com solução fisiológica ou 5 mg/Kg de mastoparano. Terapia peritumoral iniciou após os tumores atingirem 100 mm^3 e foi prolongada durante 5 dias. Os dados mostraram que o mastoparano proporcionou um aumento na taxa de sobrevida em comparação ao controle negativo tratado com solução fisiológica. Para cada experimento foram utilizados 5 animais por grupos e a análise estatística foi realizada pelo método Kaplan-Meyer (***p<0,001 e ** p< 0.01).

5. DISCUSSÃO

Ao longo dos anos, diversos estudos mostraram uma grande variedade de novos compostos candidatos a agentes antitumorais obtidos de várias fontes naturais ou sintéticas. Os peptídeos cada vez mais podem se tornar promissores candidatos ao desempenho dessas atividades, uma vez que apresentam ações em diversos sistemas biológicos celulares. Esses peptídeos podem ser obtidos de diversas fontes tais como de toxinas animais, de microrganismos ou até mesmo de proteínas endógenas que em determinadas condições fisiológicas podem gerar fragmentos menores com ações específicas denominadas como criptídeos (LEBRUN; PIMENTA, 2007).

Trabalhos descritos anteriormente relataram que peptídeos com caráter catiônicos, apresentam significativos efeitos antitumorais específicos. A eficácia desses efeitos antitumorais pode variar de acordo com a linhagem tumoral. Também é possível verificar que alguns peptídeos antitumorais não apresentam os mesmos efeitos em linhagens normais. A literatura atribui essa seletiva atividade antitumoral a diferenças na composição das membranas das células, na área de superfície e na fluidez das bicamadas lipídicas (LEUSCHNER; HANSEL, 2004; MADER et al., 2005).

As células tumorais também apresentam modificações no âmbito molecular, uma vez que é observado mudanças no grau de glicolisação membrana. O número de glicoproteínas presentes na membrana é aumentado devido à ativação das glicosiltransferases, que catalisam a biossíntese das glicoproteínas. O aumento da expressão destas moléculas aniônicas contribui para que as células tumorais apresentem membranas mais eletronegativas quando comparado com as células normais (HOSKIN; RAMAOOTHY, 2008).

Outro trabalho relacionou diversos peptídeos com características catiônicas e efeitos antitumorais. Os primeiros peptídeos de origem humana com efeitos antitumorais foram os HNP-1 (α-defensina) e LL-37. Os peptídeos BMAP-28 e lactoferricina B, obtidos de outras fontes, tais como originados da caseína bovina, também apresentaram atividade antitumoral. A melitina é um polipeptídeo catiônico composto por 26 resíduos de aminoácidos, originário do veneno de abelhas *Apis* *melífera*, cujo seus efeitos sobre células tumorais foram amplamente discutidos pela literatura (HOSKIN; RAMAOOTHY, 2008).

Outros peptídeos como as catelicidinas, cecropinas, defensinas e a magainina 2 foram citotóxicos em células tumorais de leucemia humana, linfoma, e em células tumorais de mama, pulmão, ovário, útero e carcinoma de células escamosas orais (MADER; HOSKIN, 2006).

Nossos resultados mostraram que o INKKI não apresentou efeito citotóxico em linhagens de células não tumorigênicas murinas e humanas (melanócitos murino melan-A e queratinócitos humano HaCaT). Em contrapartida, apresenta significativo efeito sobre linhagens tumorais murinas e humanas (melanoma murino B16F10, melanoma humano A2058, leucemia de células T JurKat, adenocarcinoma de mama humano de linhagens MCF-7 e SKBR-3, e glioblastoma humano U87). Esses dados sugerem ação específica nessas linhagens. As linhagens de adenocarcinoma de mama humano MDA-MB-231 e carcinoma de células escamosas uterino SiHa, apresentaram maior resistência ao tratamento com o INKKI. A resistência ao tratamento também é encontrados em diversos quimioterápicos comercialmente utilizados na terapia antineoplásica. Esta resistência ocorre ou porque as populações celulares desenvolvem nova codificação genética (mutação) ou porque são estimuladas a desenvolver tipos celulares resistentes ao ser expostas às drogas, o que lhes permite enveredar por vias metabólicas alternativas, através da síntese de novas enzimas (ROTTENBERG; BORST, 2012).

O mastoparano, embora com efetividade distinta, apresentou efeito citotóxico tanto em linhagens não tumorigênicas como tumorais. Esses dados sugerem que os peptídeos, mesmo exibindo um importante motivo homólogo, apresentam distintos efeitos biológicos.

Durante a realização dos ensaios de viabilidade celular nas linhagens de melanoma murino B16F10-Nex2 foi possível observar que 500 µM do mastoparano induziu importantes modificações morfológicas logo nos primeiros tempos de incubação. O INKKI, na mesma concentração, apresentou diferente comportamento quando comparado com o mastoparano, onde só foi possível determinar as diferenças na morfologia após longos períodos de incubação. De acordo com essa observação, foi delineado um segundo experimento com o objetivo de avaliar as mudanças morfológicas das células de melanoma murino submetidas a diferentes condições de temperatura para cultivo celular.

Essas diferentes condições de temperatura para o cultivos celular podem influenciar na sinalização celular e ou na permeabilidade de membrana. A apoptose e a proliferação são um dos exemplos de eventos celulares que depende da temperatura para o desencadeamento dos seus efeitos, uma vez que diversos mediadores dependem da ação enzimática para a transdução do sinal. Consequentemente, a ação de diversas enzimas depende de uma temperatura ideal para desempenhar suas funções (MATSUO et al., 2010; CARUSO-NEVES et al., 2005).

A permeabilidade de membrana é outro importante evento dependente da temperatura. A passagem de substâncias através da membrana celular e das paredes dos capilares depende fortemente da difusão, onde o deslocamento destas moléculas e íons é dependente de sua energia térmica. Variações na temperatura alteram a estrutura das membranas celulares podendo comprometer as atividades enzimáticas associadas às membranas e os processos de transporte. O conjunto de alterações das propriedades químicas e físicas das membranas resulta, em última análise, em mudanças na fluidez (QUINN, 1988). A diminuição da temperatura pode comprometer sua flexibilidade, devido a alterações na configuração dos seus lipídeos e proteínas, podendo limitar a sua estabilização (QUINN, 1988). Os aspectos morfológicos das culturas de melanoma murino B16F10-Nex2 cultivadas a 4 e 37 ℃, sugerem que o mastoparano nas concentrações de 500 µM apesentou efeito citotóxico em ambas as temperaturas. Esses dados sugerem que o peptídeo não depende exclusivamente dos mecanismos de transporte de membrana para desencadear seus efeitos biológicos, uma vez que as células apresentaram perda de adesão, retraimento do citoplasma e perda de refringência.

Esses efeitos sobre a membrana celular estão de acordo com o descrito pela literatura, onde diversos trabalhos mostraram que os mastoparanos agem sobre a membrana formando poros e consequentemente, internalizados. Essa característica inclui o mastoparano no grupo de peptídeos chamados de peptídeos penetradores de células (*CPP – cell penetrated peptide*) (De SOUZA; 2006).

A anfipaticidade caracteriza-se pela tendência que uma sequencia possui para formar domínios hidrofílicos e/ou hidrofóbicos bem estruturados, em faces opostas. Os mastoparanos possuiem esses domínios muito bem caracterizados e podem causar perturbações nas membranas, levando a um aumento da permeabilidade, facilitando a formação de poros, conduzindo a um desequilíbrio dos eletrólitos intracelulares e à morte da mesma (PFEIFFER et al., 1995; HIRAI et al., 1979; YEAMAN; YOUNT, 2003). Matsuzaki et al., (1999) demonstraram que o aumento na permeabilidade da célula está relacionado com o fato das membranas citoplasmáticas dos mamíferos geralmente serem compostas por fosfolipídios que apresentam carga líquida zero, no entanto, em algumas condições fisiopatológicas, as cargas das membranas se alteram tornando-as eletronegativas (aniônicas). Como os mastoparano são policatiônicos, há uma atração eletrostática entre eles e as superfícies carregadas negativamente, facilitando sua inserção na região hidrofóbica da membrana. Durante sua inserção, ocorre uma mudança conformacional nas intermediações da membrana e os mastoparanos podem adotar como orientação o eixo da hélice em paralelo à membrana e/ou com o eixo em perpendicular à membrana. Contudo, o exato mecanismo da formação de poros e ou ruptura da membrana ainda não está muito bem definido. (HORI et. al., 2001; SATO; FEIX, 2006).

Embora alguns peptídeos apresentem alta homologia entre si, podem desencadear diferentes efeitos nos diversos sistemas biológicos. Esses diferentes efeitos podem estar correlacionados com a substituição de resíduos de aminoácidos, grupos funcionais ou radicais ligados à cadeia peptídica (KOROLEVA; MIASOEDOV, 2012). Apesar do peptídeo INKKI apresentar o motivo (KKI) homólogo ao mastoparano, ficou claro que esses dois peptídeos apresentaram significativas diferenças entre os fenômenos biológicos desencadeados *in vitro* em linhagens de melanoma murino B16F10-Nex2.

Conforme demonstrado anteriormente, as células tratadas com o INKKI apresentaram significativas alterações morfológicas quando comparado ao tratamento com o mastoparano. Os dados obtidos da cultura mantidas a 4 ℃, mostraram que as células tratadas com o INKKI não sofreram mudanças morfológicas durante todo o tempo de incubação. Em contraste, as culturas mantidas a 37 ℃ apresentaram significativas alterações morfológicas já a partir da 8ª hora de incubação, onde foi possível observar perda da comunicação celular, aumento do volume, manutenção de integridade de membrana e núcleo celular íntegro e bem delimitado. Apesar destas alterações, a viabilidade celular foi confirmada através do método de exclusão com azul de tripan e mostraram-se viáveis, sugerindo uma ação citostática. Esses dados sugerem que a ação desse peptídeo necessita de sua internalização ou acoplamento a algum tipo de receptor de superfície para o desencadeamento de sua sinalização intercelular, uma vez que necessitou da temperatura adequada para desencadear a atividade biológica.

A literatura traz que a superfície das células tumorais apresentam diversas modificações, tais como aumento de microvilosidades na superfície. Essas alterações podem aumentar a superfície de contato e facilitar a ligação ou a internalização de peptídeos (HOSKIN; RAMAOOTHY, 2008). A localização do peptídeo foi avaliada através da microscopia confocal do INKKI marcado com FITC. Para visualizar uma possível colocalização com o núcleo, essas células foram marcadas com DAPI e após 1 e 24 horas de incubação, as imagens foram adquiridas em microscópio confocal. Os dados confirmaram as evidências obtidas anteriormente no ensaio da cultura a 4 e 37 ℃, onde foi possível observar que o peptídeo é internalizado e amplamente distribuído pelo citoplasma já na primeira hora de incubação. Após as 24 hora de incubação é possível observar que as células exibiram as mesmas alterações morfológicas apresentadas nos ensaios anteriores, que o INKKI também está presente no núcleo e que há uma diminuição da fluorescência do peptídeo, sugerindo uma possível degradação após o desencadeamento do efeito.

Os estudos da morfologia e dos fenômenos encontrados após o tratamento com o mastoparano e INKKI forneceram importantes evidências quanto aos distintos efeitos desencadeados por esses peptídeos. Esses dados preliminares proporcionaram os diferentes delineamentos experimentais aplicados aos dois peptídeos. Como o mastoparano apresentou alta toxicidade, todos os experimentos foram direcionados para o estudo dos possíveis mecanismos de morte celular. Em contrapartida, como o INKKI apresentou características citostáticas, os ensaios utilizados no estudo desse peptídeo foram direcionados no sentido de avaliar a proliferação, adesão e migração celular.

Após a análise desses resultados e somando com os da literatura, foi possível planejar, desenhar e delinear peptídeos análogos com o objetivo de estabelecer uma correlação entre a estrutura e a atividade do INKKI. Foram propostas algumas modificações/substituições de aminoácidos nas sequências dos análogos com o objetivo de obter dados para propor uma correlação das características bioquímicas e biofísicas dos peptídeos com os efeitos encontrados *in vitro*. Os resultados apresentados revelaram que a substituição de dois resíduos de lisina por dois de ácido áspartico (INDDI), conferindo assim uma característica eletronegativa ao peptídeo, ou a substituição dois resíduos de duas lisinas por alanina (INAAI) conferindo assim uma característica apolar não foram capazes de induzirem efeitos sobre as culturas de células de melanoma murino B16F10-Nex2. Outra substituição manteve as mesmas características catiônicas do peptídeo, contudo, com resíduos diferentes, onde os dois resíduos de lisinas foram substituídos por dois de arginina (INRRI). Esse análogo também não demonstrou efeito biológico. A substituição do resíduo isoleucina (ramificado) por alanina (linear) na porção N-terminal (ANKKI) mostrou discreto efeito citostático, porém com menor intensidade ao peptídeo líder INKKI, sugerindo que o efeito do peptídeo não está relacionado unicamente com a presença das cargas positivas na molécula, mas também com a estrutura do aminoácido envolvido, no caso a isoleucina. Outra substituição foi delineada pensando em substituir um resíduo alifático por um resíduo aromático na porção C-terminal (INKKY) onde novamente não se observou efeito o que sugere que a presença de aminoácidos ramificados nas extremidades da molécula pode não ser importante para seu efeito. Por fim, o último delineamento dos análogos simplesmente embaralhou as sequências (Scramble) (NKKII) com o objetivo de verificar se a possível conformação espacial poderia influenciar na atividade antitumoral do INKKI e também não apresentou efeitos biológicos.

Os dados mostrados sugerem que a atividade antitumoral desses peptídeos não esteja correlacionada somente com uma única característica, ou seja, é dependente somente da carga ou depende somente conformação espacial. Os efeitos biológicos dependem de um conjunto de características para o seu desencadeamento (DO, et al., 2014; TORFOSS, et al., 2012). A avaliação da citotoxicidade dos análogos ao peptídeo INKKI pelo método do MTT, mostrou que somente o peptídeo ANKKI apresentou atividade citostática, porém, não foi possível determinar a IC_{50}. Os demais peptídeos não apresentaram efeitos citotóxicos. Esses dados sugerem que somente a característica catiônica não foi suficiente para desempenhar a atividade antitumoral, pois, aqueles peptídeos que apresentaram substituições, contudo, mantiveram as mesmas características catiônicas, não desempenharam as atividades citotóxicas em células de B16F10. Outra forte evidência está relacionada com o Scramble (NKKII), pois, o fato de embaralhar a sequência, foi suficiente para que esse análogo não desencadeasse seus efeitos antitumorais, mesmo mantendo as mesmas características bioquímicas. Esses dados são prévios e necessitam ser confirmados.

Os resultados obtidos da citotoxicidade indicaram que o INKKI apresentou significativo e seletivo efeito sobre as linhagens tumorais. Conforme descrito anteriormente, foi possível observar que após o tratamento, as células tratadas não apresentavam características de toxicidade. Ao obsevar a morfologia não foi possível constatar células no sobrenadante, células em processo de injúria ou mesmo debri celular. Esses aspectos fizeram com que fosse proposta uma possível ação sobre crescimento e proliferação celular. Sendo assim, os delineamentos experimentais foram direcionados para avaliar a ação do INKKI e Scramble sobre a proliferação, invasão, migração, adesão e ciclo celular em células de melanoma B16F10-Nex2.

Uma das primeiras e principais características das células tumorais é a perda do controle sobre a proliferação celular. A capacidade de proliferação das células tumorais é mais acelerada do que as células normais (BOCKSTAELE, et al., 2006). Como os dados anteriores sugeriram uma possível correlação da ação do INKKI com a velocidade de crescimento celular, inicialmente foram avaliados os efeitos antiproliferativos do INKKI e Scramble sobre as células tumorais B16F10-Nex2. A cinética de crescimento foi acompanhada durante 72 horas após o tratamento e a contagem do número total de células mostra que houve inibição significativa da proliferação celular.

Após a obtenção dos dados da cinética de crescimento, onde ficou caracterizado que o peptídeo foi capaz de reduzir a proliferação, o próximo passo foi analisar os efeitos dos peptídeos sobre a progressão do ciclo celular. O controle do ciclo celular compreende a uma série de mecanismos coordenados que controlam a replicação do DNA e divisão celular (Sheppard; McArthur, 2013). Os dados mostraram que o INKKI foi capaz de reduzir significantemente a proliferação das células B16F10-Nex2 conforme demonstrado pela diminuição da porcentagem de células na fase S e aumento das células em G0/G1.

A transição entre as fases do ciclo celular é controlada através da mudança na atividade específica das ciclinas dependentes de cinases (CDKs). Para avaliar os possíveis mediadores envolvidos com a atividade antiproliferativa, foi padronizada a análise por Western blotting, uma vez que os efeitos da inibição do INKKI sugerem a ação sobre algumas proteínas envolvidas na transição das fases G0/G1 para S do ciclo celular.

O primeiro complexo formado com a finalidade de fosforilar a proteína Rb e dar início ao processo de progressão do ciclo celular são constituídos pelas ciclina D1 e D3/ complexadas com suas respectivas cinases dependentes de ciclina 4/6 (CDK4/CDK6) (LI et al., 2006; MASAMHA; BENBROOK, 2009; VAN RIGGELEN; FELSHER, 2010).

O tratamento com INKKI inibiu a expressão da proteína ciclina D1, e apresentou uma discreta inibição da expressão da cilina D3. A inibição da expressão da ciclina D1, consequentemente impedirá sua complexação com as CDK4/CDK6 (LI et al., 2006), que por sua vez, não permitirá que ocorra a fosforilação da proteína Rb (CARNERO, 2002; NEGANOVA et al., 2008). Consequentemente a célula para em G0/G1 e impede que o ciclo progrida para a fase S (LI et al., 2006).

A partir dos dados obtidos da análise da expressão das ciclinas, os próximos mediadores analisados foram aqueles upstream da via de sinalização da MAPK/Erk 1-2. A primeira proteína analisada foi a β-catenina citoplasmática. Essa proteína pode ser considerada um dos elementos reguladores da proliferação e invasão de células epiteliais. Quando há β-catenina livre no citoplasma, esta molécula transloca para o núcleo, onde ativa os fatores de transcrição da família de LEF/Tcf, induzindo a transcrição de genes que controlam o ciclo celular (Myc e ciclina D1), ou ainda, a transcrição de enzimas proteolíticas como as metaloproteinases (TSUI et al., 2012).

A β-catenina também exerce papel no controle da proliferação, apoptose e também está aumentada em alguns tipos de câncer (TSUI et al., 2012). Dados recentes mostraram que moléculas de adesão suprime o crescimento de células de carcinoma de cólon por inibir a via de sinalização β-catenina/Wnt (SYED, et al., 2011). Nossos resultados corroboram com os dados obtidos pela literatura, onde foi possível verificar que o INKKI foi capaz de reduzir os níveis de expressão da β-catenina em células tumorias, proporcionando parada do ciclo celular em G0/G1.

As cascatas de MAPK (Mitogen-Activated Protein Kinase) são vias relacionadas a diversos fenômenos celulares através de eventos de fosforilação. Elas estão presentes em todos os eucariotos e controlam processos como a proliferação, expressão gênica, diferenciação e apoptose (CANO; MAHADEVAN, 1995; COHEN, 1997). Esse tipo de cascata é formado, basicamente, por uma proteína G ligada à membrana e, no citoplasma, conduzindo para uma sinalização downstreans e consequentemente proliferação (CANO; MAHADEVAN, 1995; COHEN, 1997).

A família da MAPK pode ser subdividida em quatro subgrupos tais como a ERK, ativada principalmente por estímulos mitogênicos, a p38 e JNK (c-Jun N-terminus Kinase), ativadas principalmente por estímulos de stress e citocinas inflamatórias (RINCON et al., 2000; KYRIAKIS; AVRUCH, 2012) e ERK5, ativada por EGF (Epidermal Growth Factor) e NGF (Neuronal Growth Factor), stress osmótico e oxidativo (SCHAEFFER; WEBER, 1999; KYRIAKIS; AVRUCH, 2012).

Trabalhos anteriores mostraram que a ativação da ERK está correlacionada com a progressão maligna de carcinomas (LICATO et al., 1997). Também foi observado um aumento da atividade da ERK em diversos tipos de tumores humanos, tais como de rim, mama, pâncreas, cólon, pulmão e ovário. A cascata Raf/MEK/ERK, assim como a da PI3K, é uma das efetoras da atividade oncogênica da Ras (STOKOE et al, 1994; RODRIGUEZ-VICIANA et al, 1997; TOLKACHEVA; CHAN, 2000), embora o Ras possa ter efeito oncogênico independentemente da ativação da Raf (SHIELDS et al, 2000). Em células de tumores, a via da ERK se encontra usualmente ativada. Um fator envolvido na invasividade dos tumores é o gene do ativador da uroquinaseplasminogênio (uPA), cuja síntese é aumentada pela ativação de ERK (SIMON et al, 1996). A progelatinase B, outra proteína correlacionada com invasão tumoral, também pode ser positivamente regulada pela ERK (REDDY et al, 1999). Os diversos fatores de transcrição ativados pela ERK estão diretamente ligados à proliferação e crescimento celular, por exemplo, através do aumento da expressão de ciclinas, reguladores positivos do ciclo celular (LIU et al, 1996; GILLE; DOWNWARD, 1999). Assim, existe um uso potencial destas vias como alvos de terapias para o tratamento de cânceres, através do desenvolvimento de inibidores específicos (SEBOLT-LEOPOLD, 2000). Interessantemente, nossos dados mostraram que o INKKI foi capaz de inibir a expressão de ERK1/2 e fosfo-c-

Raf (Ser338) o que está de acordo com resultados anteriores, onde o houve uma parada na fase G0/G1 do ciclo.

Outra importante proteína envolvida na sinalização que conduz a progressão e a parada do ciclo celular é o NFκ-B. O NFκ-B é um fator de transcrição, descoberto em 1986, que pode ser induzido por uma variedade de sinais como citocinas, fatores de crescimento, tirosina kinases, Ras/MAPK e pAkt (CARLSEN et al., 2004). O aumento da expressão de membros da família do receptor do fator de crescimento epitelial, receptor do fator de insulina, receptor do fator de necrose tumoral também podem ser responsáveis pela ativação do NFκ-B. A sua capacidade de realizar a transcrição genética só é possível quando localizado no núcleo celular. No citosol ele é incapaz de regular a transcrição. Nossos resultados mostraram que o INKKI foi capaz de reduzir discretamente a expressão da NFκ-B, correlacionando assim, a cascata de sinalização descrita anteriormente.

A via p38 MAPK pode ser ativada em resposta a diversos estímulos tais como citocinas inflamatórias, patógenos e estresse ambiental. A proteína p38 é altamente conservada e considerada essencial na regulação da sobrevivência celular, diferenciação e apoptose. (PARK et al., 2011). A via da p38 é ativada em resposta a estresse celular e envolve sinais que suprimem a proliferação, através da modulação das proteínas p53 e p73 ou promovem a apoptose, sendo assim referida com uma importante sinalizadora de supressão tumoral (MUTHUSAMY; PIVA, 2010). Em câncer de pele, existem fortes indícios que corroboram o papel supressor tumoral de p38, e os quimioterápicos mais utilizados clinicamente apresentam efeito antiproliferativo em células de melanoma mediado por ativação de p38 (LOPEZ-BERGAMI, 2011). Corroborando com a literatura, os dados mostraram que o INKKI aumentou significativamente a expressão de fosfo p38 em células de melanoma murinho B16F10-Nex2.

Os resultados obtidos da cinética de crescimento celular proporcionaram os próximos delineamentos *in vitro* correlacionados com a migração, adesão e invasão celular. A invasão de células tumorais aos tecidos adjacentes é um processo comum na progressão tumoral e os primeiros passos para a indução de metástase. A migração celular, através da polimerização da actina, é um dos primeiros eventos necessários para que sejam desencadeados os efeitos invasivos das células tumorais. No processo de invasão celular as células tumorais migram para o compartimento estromal, onde tem livre acesso aos vasos sanguíneos e linfáticos (VIGNJEVIC; MONTAGNAC, 2008).

Ao penetrar nas paredes dos vasos (processo chamado de intravasão) estas células são carregadas pelo sistema circulatório para locais distantes. Ao ficarem presas a capilares as células tumorais escapam e penetram no tecido circundante, um fenômeno chamado de extravasamento, que pode ocorrer de diferentes maneiras (através da proliferação dentro do lúmen do vaso ou forçando mecanicamente as células do endotélio, possivelmente degradando-o, num processo similar à diapedese) (VIGNJEVIC; MONTAGNAC, 2008).

Os ensaios de invasão e migração fornecem importantes evidências das possíveis atividades antitumorais apresentadas pelos compostos candidatos a agentes antitumorais. Essas informações auxiliam no planejamento de futuros delineamentos experimentais *in vivo*. Apesar de não evidenciar um mecanismo específico de ação, esse ensaio é importante etapa para obtenção do sucesso em descobertas de novas drogas. Interessantemente o INKKI apresentou um significativo efeito inibitório da invasão e migração em células tumorais.

O principal mecanismo de invasão e migração em células está correlacionado com os níveis de expressão de importantes mediadores celulares. A família de FAK (cinase de adesão focal) apresenta um importante papel durante a execução desses eventos celulares. Essa tirosina cinase citoplasmática é amplamente expressa e composta por diferentes domínios, o que permite sua participação em diferentes vias de sinalização, envolvendo receptores de fatores de crescimento e moléculas que participam da via das integrinas. Também podem regular a dinâmica dos complexos presentes nas adesões focais, influenciam no movimento celular remodelando o citoesqueleto seu tunover de adesão focal, exercendo o efeito sobre a proliferação celular por regular a progressão no ciclo celular da fases G1 para S, aumentando a expressão de ciclina D1 (REA et al., 2013; KALLERGI et al., 2007; DERAMAUDT et al., 2011).

Sequência de eventos inter e intracelulares resultam na auto-fosforilação na tirosina 397 de FAK. A fosforilação nesse sítio, além de aumentar a unidade catalítica, também desempenha um importante papel na fosforilação de proteínas associadas ao complexo focal. A fosforilação na tirosina 397 também gera um sítio de alta afinidade que reconhece o domínio SH2 da família das Src quinases e leva ao recrutamento e ativação de Src através da formação de um complexo de duas cinases (FAK-Src). A ativação desse complexo desempenha um papel central para a regulação das vias que controlam o processo de metástases, migração e sobrevida celular (DERAMAUDT et al., 2011).

A fosforilação da tirosina 925 é outro importante evento celular que está correlacionado com a migração celular através da alteração da dinâmica de FAK para FAs (adesão focal). O aumento no turnover de FAK para FAs contribui para a estabilização do Fas. Essa diminuição de FAK pode alterar o recrutamento de cruciais efetores dos FAs para desmontarem o FA. Trabalhos anteriores mostraram que a redução nos níveis das fosforilações das tirosinas 397 e 925 está correlacionada com a diminuição da migração celular. Nossos dados sugerem que a redução da migração e invasão induzidas pelo tratamento com o peptídeo INKKI está diretamente correlacionada com a via de sinalização das cinases de adesão focal, uma vez que as células apresentaram significativa redução nos níveis de fosfo FAK 397 e 925, Src, Src fosforilada no sítio 416 (DERAMAUDT et al., 2011; JOBIN et al., 2012; JIANFEI et al., 2006).

Nos tecidos, quando há interação entre células e formação das junções aderentes, mediados por E-caderinas, as moléculas de β-catenina são recrutadas para a região submembranar. Direciona-se assim o pool citoplasmático de β-catenina para uma função associada à organização do citoesqueleto. As células então parariam de proliferar. Há formas alternativas de controlar-se o pool citoplasmático de β-catenina, como por exemplo, estimulando-se sua degradação (SYED, et al., 2011).

Uma das vias de degradação da β-catenina está diretamente correlacionada com os níveis de fosfo GSK3β (S9). O peptídeo INKKI induziu significativa redução da expressão da fosfo GSK3β (S9) e β-catenina. Esses dados sugerem uma estreita correlação entre o desbalanceamento nos níveis dessas proteínas com os resultados da migração, invasão e análise do ciclo celular. A redução nos níveis de fosfo GSK3β (S9) sugere que a β-catenina esteja sendo fosforilada, sofrendo ubiquitinação, sendo degradada pelo proteossomo, impedindo que seja translocada para o núcleo celular e induzindo parada no ciclo celular (JOBIN, et al., 2012). Além de impedir a expressão de fatores de transcrição, com sua degradação, a β-catenina deixa de ser recrutada para a região submembranar inibindo a transdução do sinal para as moléculas de adesão (SYED, et al., 2011).

Para as células tumorais invadirem os tecidos adjacentes e formarem metástases à distância, elas devem ter a habilidade de formar interações transientes ora com as proteínas da matriz extracelular, ora com as outras células, como células do estroma, células endoteliais e plaquetas. Entre as moléculas de adesão célula-célula alteradas estão as caderinas e as CAMs (moléculas de adesão celular), proteínas pertencentes à superfamília das imunoglobulinas; entre as moléculas que regulam as interações entre células e a matriz extracelular estão as integrinas (PAREDES et al., 2012).

As caderinas são moléculas de adesão dependentes de Ca^{2+} que mediam à interação homotípica célula-célula, inicialmente identificadas nas junções aderentes. As caderinas são uma superfamília de pelo menos 30 diferentes moléculas, cuja expressão é controlada (PAREDES, et al., 2012).

A perda funcional de E-caderina também está associada ao desenvolvimento de melanomas. Melanócitos encontram-se frequentemente na camada basal da epiderme, onde interage com queratinócitos, formando a chamada unidade de pigmentação da pele. A perda de expressão de E-caderina parece ser um passo crítico na progressão de melanomas, permitindo que as células tumorais sejam liberadas da epiderme e invadam a derme. Ao deixar de expressar E-caderina, as células de melanoma passam a expressar altos níveis de N-caderina, potencializando as interações com fibroblastos e células endoteliais que também expressam N-caderina. Esta mudança no padrão de expressão de caderinas ocorre durante a progressão tumoral e já foi documentada *in vitro* e *in vivo* e foi confirmado com a redução dos níveis de N-caderina após o tratamento com o INKKI (PAREDES et al., 2012).

Os dados obtidos no ensaio de adesão mostraram que o INKKI apresentou diferentes resultados de acordo com o substrato utilizado. Interessantemente, o resultado mais expressivo foi obtido quando as células utilizaram o Matrigel como substrato, simulando o ambiente de matriz extracelular. O INKKI exibiu uma redução de 50% no número de células aderentes, em comparação ao controle negativo tratados com o veículo utilizado para diluir os peptídeos. No monolayer celular e na superfície de poliestireno da placa, o INKKI apresentou uma redução de 43% e 40%, respectivamente, em comparação ao controle negativo. Esses dados sugerem uma possível correlação da atividade antitumoral com as famílias de proteínas envolvidas, uma vez que a capacidade de migração pela matriz extracelular é mediada por moléculas da superfamília das integrinas. Esses dados estão completamente de acordo com os experimentos anteriores, onde foi possível verificar que o INKKI também inibiu a invasão e migração celular e reduziu os níveis de expressão da N-caderina (PAREDES et al., 2012).

O modelo *in vivo* representa um importe passo para obtenção de prova de conceito com o objetivo de confirmar a atividade anticâncer observada em cultura de células, superando as limitações dos modelos *in vitro*. Todos os dados obtidos *in vitro*, trouxeram importantes evidências da atividade antitumoral do INKKI. Essas informações proporcionaram o planejamento dos experimentos *in vivo*, onde foram avaliados diferentes parâmetros. O primeiro correlacionou com a atividade antimetastáticas induzidos em camundongos de linhagem C57BL6. O segundo correlacionou com o crescimento dos tumores dorsais e taxa de sobrevidas dos camundongos de linhagem C57BL6 tratados com o INKKI. Por fim, foi delineado modelo em animais imunodeficientes de linhagen NOD/SCID/γ_c^{null} com objetivo de avaliar o efeito direto do peptídeo ou se esse efeito é dependente da ativação do sistema imunológico.

Um dos modelos mais utilizados em estudos de atividade antitumoral é o melanoma murino, onde é composto por neoplasia altamente maligna, que tem origem no melanoblasto da pele e apresenta boa similaridade com a neoplasia humana (VAN DYKE; JACKS, 2002). Este modelo permite o desenvolvimento e a avaliação de novas drogas e procedimentos terapêuticos (TIETZE; CHIN, 2000). A inoculação subcutânea deste tumor induz o desenvolvimento de um nódulo hipodérmico que se torna palpável em torno de uma a duas semanas, sendo facilmente mensurado. Esse nódulo evolui para um tumor sólido, podendo chegar a grandes dimensões.

As células de melanoma murino B16F10-Nex2 constituem uma ferramenta experimental muito utilizada para o estudo do melanoma, cujo crescimento se dá tanto *in vitro* como *in vivo*, sendo desenvolvido em camundongos C57BL/6. Esta linhagem foi estabelecida por Fidler (1973) oriunda de melanoma de ocorrência natural em camundongos C57BL/6 que por meio de seleção progressiva, obteve o isolamento de variantes com diferentes graus de potencial metastático. Tais células quando inoculadas por via subcutânea apresentam a capacidade de multiplicação neoplásica sem propiciar o desenvolvimento de metástase, enquanto que quando inoculadas via endovenosa desenvolvem nidação em parênquima pulmonar formando nódulos macroscópicos na superfície dos pulmões passíveis de serem quantificados (PETER et al., 2001; NAKAMURA et al., 2002; ZHAO et al.,2001).

O melanoma metastático também representa um modelo muito empregado no estudo de compostos candidatos a agentes tumorais. Nossos resultados mostraram que o INKKI foi capaz de apresentara significativo efeito antitumoral sobre o melanoma metastático, reduzindo a quantidade de nódulos apresentados nos pulmões de camundongo C57BL/6. Similarmente, o INKKI apresentou o mesmo efeito antitumoral nos tumores dorsais dos camundongos C57BL/6.

Após o INKKI mostrar significativa atividade antitumoral *in vivo*, foi questionado o possível envolvimento do sistema imunológico no desencadeamento do efeito protetor *in vivo*. Para avaliar o possível envolvimento do INKKI com o sistema imunológico, foi delineado o modelo utilizando animais imunodeprimidos de linhagens NOD/SCID/γ_c^{null}. Esses animais apresentam órgãos linfoides com um décimo do seu tamanho normal. Timo, linfonodos e o baço estão completamente destituídos de linfócitos, são totalmente deficientes de linfócitos T e B e suas células esplênicas não respondem a estímulos de mitose para células B ou T, por esta razão, não rejeitam transplantes (FOSTER et al., 1983). Sendo assim, esse modelo apresenta-se como uma importante ferramenta de estudo para avaliação do efeito direto do composto candidato a agente antitumoral. Interessantemente, os resultados mostraram que o INKKI não foi capaz de apresentar o efeito protetor antimetastático. Esses dados sugerem que o INKKI depende da ativação do sistema imunológico para desencadear seu efeito protetor *in vivo*.

Paralelamente aos delineamentos experimentais empregados na avaliação da atividade citostática do INKKI, foram propostos os estudos sobre as vias de morte celular induzida pelo tratamento com o mastoparano. A literatura aponta que esse peptídeo pode desencadear diversos efeitos biológicos em distintas linhagens de células (ROCHA, 2010; ARMSTRONG 2006; YAMADA et al., 2005). A efetividade do mastoparano e o tipo de efeito dependem diretamente de sua concentração durante os tratamentos. A concentração do peptídeo na superfície da membrana também contribui para a suscetibilidade, uma vez que ao atingir um razão limite entre a concentração de peptídeo e lipídio (P/L), acaba provocando sua imersão na membrana plasmática (DEBER; LI, 1995). Após o estabelecimento da correlação dose resposta com o mastoparano em linhagens de melanoma murino B16F10-Nex2, os ensaios para o estudo dos efeitos pró-apoptóticos foram padronizados utilizando a IC_{50} de 165 µM.

O exato mecanismo de citotoxicidade induzido pelo mastoparano em células de melanoma não está bem estabelecido pela literatura. Em outras células tumorais, alguns trabalhos relataram que o mastoparano pode desencadear o efeito pró-apoptótico (ROCHA, 2010; ARMSTRONG 2006; YAMADA et al., 2005). Nossos resultados mostraram que o mastoparan foi capaz de induzir citotoxicidade em linhagens de melanoma com significativas mudanças morfológicas características de apoptose, tais como perda de refringência, retração citoplasmática e formação de corpos apoptóticos (KROEMER, 2002).

A morte celular representa um processo altamente heterogêneo que pode seguir através da ativação de distintas cascatas bioquímicas. Os critérios morfológicos nem sempre são os mais precisos ou suficientes para a diferenciação do processo de indução de morte celular. Para complementar a caracterização do tipo de morte celular, foi padronizado o ensaio que marca um importante evento bioquímico correlacionado com a externalização da fosfatidilserina. Conforme a literatura relata, os resultados obtidos pelo teste de Anexina V/PI apresentam uma boa correlação com os achados morfológicos. Desta forma, a quantificação desse evento permitiu sugerir que o mastoparano induziu o aumento da permeabilidade da membrana plasmática, demonstrando que o principal evento envolvido no efeito desencadeado pelo peptídeo está correlacionado com a apoptose (KROEMER, 2002).

A apoptose é um evento de morte celular ativo controlado por uma rede de genes. Esse processo é essencial durante o desenvolvimento, bem como exibe um importante papel ligado a doenças patogênicas incluindo o câncer. Esse evento é caracterizado pela condensação nuclear e fragmentação cromossomal do DNA sem induzir reação inflamatória (FRIEDLANDER, 2003; KERR et al., 1972).

A degradação do DNA durante a apoptose inicialmente é regulada pela formação de fragmentos com tamanho que varia de 50 a 300 Kilobases (Kb)

(OBERHAMMER et al., 1993; WALKER et al., 1999). As endonucleases atacam as regiões de ligação entre a dupla fita de DNA, onde ocorrem às clivagens internucleossomal, que resulta na formação de fragmentos de 180 a 200 pares de base e seus múltiplos. Na eletroforese em gel de agarose, corada com brometo de etídio, estes fragmentos apresentam um padrão de bandas característico quando visualizados em luz UV (OBERHAMMER et al., 1993).

Em contraste, os eventos de clivagem do DNA durante a necrose são randômicos e mostram degradação das histonas, produzindo uma mancha difusa na eletroforese de DNA. Os fragmentos de DNA necrótico são maiores, e significantemente em menor número do que os fragmentos do DNA apoptóticos (ALLEN et al., 1997). Os dados mostraram que o mastoparano foi capaz de formar bandas com padrões característicos de apoptose, corroborando com os dados morfológicos e bioquímicos.

Além da formação de bandas de degradação de DNA característica de apoptose, o mastoparano induziu significativamente a condensação da cromatina. Esses aspectos morfológicos do núcleo complementam as informações para a caracterização da morte por apoptose. Assim, os mecanismos envolvidos na morte celular caracterizados pelos critérios morfológicos baseados nas análises da condensação da cromatina marcadas com DAPI e analisadas por microscopia de fluorescência, sugerem que o principal efeito do tratamento com o mastoparano é característico de apoptose (ROGALIŃSKA, 2002).

Após a obtenção de dados que demostraram a ação pró-apoptótica do mastoparano sobre a linhagem de melanoma murino B16F10-Nex2, a próxima etapa foi definir e estudar a sinalização celular através da avaliação da cascata de ativação das caspases e outros mediadores correlacionados com a indução da apoptose. A morte celular por apoptose pode ocorrer por duas distintas vias, no qual a primeira inclui a ativação pelos ligantes e seus respectivos receptores na superfície celular. A segunda via é caracterizada pela ativação da via de morte através da mitocôndria (ARMSTRONG, 2006). Para o desencadeamento dos eventos apoptóticos, é necessário que haja à participação de cisteínos proteases. Essas enzimas podem ser divididas em iniciadores, caspase-8, -9 e -12 e executoras, caspase-3, -6 e -7. Essas caspases são responsáveis pelas alterações morfológicas no núcleo e citoplasma, devido à clivagem de proteínas como laminina nuclear e a actina

(MASHIMA et al., 1999). A análise das principais caspases envolvidas no processo de morte induzidos pelo mastoparano, mostrou significativo aumento nos níveis das formas ativas das caspases iniciadoras 9 e 12. Consequentemente, aumentou os níveis da caspase efetora 3, que por sua vez cliva o PARP em sua forma ativa. As somatórias de todas essas informações mostram que a apoptose induzida pelo mastoparano é caspase dependente.

A via mitocondrial intrínseca desempenha um importe papel durante o processo de morte por apoptose. Diversos trabalhos mostram que a mitocôndria pode ser considerada como um importante alvo para o planejamento e desenvolvimento de novos compostos para a terapia antitumoral (ARMSTRONG, 2006). Diferentes modelos têm sido propostos para explicar como as mitocôndrias liberam os fatores apoptogênicos. A redução do potencial de membrana mitocondrial ($\Delta m\Psi$) é um importante evento que contribui para esclarecer do possível envolvimento da mitocôndria durante o processo de apoptose (KROEMER, 2002; ARMSTRONG, 2006). A análise morfométrica das mitocôndrias das células de melanoma murino e a avaliação do potencial elétrico indicaram que o tratamento com o mastoparano induziu apoptose com efetiva participação da mitocôndria. A análise das imagens adquiridas através da microscopia de transmissão mostraram que o mastoparano foi capaz de causar significativas mudanças morfológicas, caracterizadas pela perda das cristas mitocondriais, aumento do volume mitocondrial, redução da eletrodensidade e perda da integridade de membrana. Esses dados estão relacionadas com a inibição da função mitocondrial, abertura e remodelação das cristas mitocondriais, após estímulos apoptóticos, que culminam na liberação do citocromo c, AIF, HTrA2/Omi, endonuclease G, OPA1 e o Smac/Diablo (van GURP et al., 2003). Esses resultados foram confirmados pelo estudo das proteínas de integridade de membrana mitocondrial PHB1 e poro de transição mitocondrial VDAC (MERKWIRTH et al, 2008; SCHLEICHER et al, 2008). O tratamento com o mastoparano mostrou significativa redução nos níveis dessas proteínas, confirmando assim, a participação da mitocondria na transdução do sinal através da perturbação do poro de transição mitocondrial e desencadeando o efeito pró-apoptotico (ARMSTRONG, 2006).

A hiperpolarização da membrana mitocondrial é considerada um evento precoce durante o processo de morte celular por apoptose, seguida posteriormente da perda do potencial de membrana mitocondrial (KROEMER, et al., 2007; NAGY et al., 2003; ZOROV et al., 2006). A hiperpolarização da membrana mitocondrial pode resultar em um estado mais reduzido de transportadores de elétrons responsáveis pela transferência de um único elétron ao oxigênio para produzir principalmente o radical ânion superóxido (ZOROV et al., 2006). Esse radical é um precursor das maiorias dos demais ROS, também envolvidos na propagação das reações da cadeia oxidativa (TURRENS, 2003). A geração de espécie reativa de oxigênio gerada por esse colapso elétrico mitocondrial traz drásticas consequências para as células tumorais. Dados da literatura mostram que a geração das espécies reativas de oxigênio tornam as células tumorais mais sensíveis, podendo conduzir a morte celular (KARDEH, et al., 2014; IVANOVA, et al., 2013). Interessantemente, nossos dados mostraram que o mastoparano é capaz de modular a geração de espécie reativas de oxigênio e que esse fenômeno desempenha um importante papel na indução da morte celular, uma vez que as células pré-incubadas com o antioxidante N-acetil cisteína, apresentaram maior resistência ao peptídeo.

Interessantemente, mastoparan foi capaz de proporcionar o colapso do potencial de membrana mitocondrial mensurado com o corante fluorescente lipofílico TMRE através da despolarização do potencial de membrana mitocondrial a partir da 1 hora de incubação. A permeabilização mitocondrial, bem como o escape de proteínas normalmente confinadas a mitocôndria, pode aumentar a liberação de ROS e determinar as características catabólicas da morte celular (FULDA; KROEMER, 2011; ARMSTRONG, 2006).

Os poros formados na membrana mitocondrial interna podem ser desencadeados por diversos fatores incluindo alteração da concentração iônica celular (SOKOLOVE; KINNALLY, 1996; BELIZÁRIO et al, 2007). Outro importante fator está correlacionado com a sobrecarga de Ca_2^+ que pode levar à formação de edema mitocondrial e à liberação de proteínas mitocondriais através do aumento da permeabilidade da membrana externa (GU et al., 2011). Este evento, é responsável pela translocação do citocromo c para o citoplasma, promovendo à formação de um complexo chamado apoptossomo, que em conjunto com a proteína adaptadora citoplasmática Apaf-1 e o ATP, induzem a auto-clivagem da pró-caspase-9, ativando a forma ativa da caspase-3. O mastoparan foi capaz de aumentar os níveis dessas proteínas como o citocromo c (Raf, 1998), que uma vez no citoplasma, ativa a pró-caspase-9, posteriormente a caspase-3, que a cliva o PARP em PARP clivado, desencadeando toda a cascata de eventos que conduzirá a apoptose, condensação e fragmentação do DNA e produção de corpos apoptóticos (CASCIOLA-ROSEN et al, 1996; DALLA LIBERA et al, 1999; HILDER et al, 2005; MANCINI et al, 1998).

As vias que levam à ativação das caspases variam de acordo com o estímulo apoptótico, que podem direcionar as células a distintas ações após o estímulo de morte. A família da proteína Bcl-2, incluindo a Bcl-2 e Bcl-XL, controla e direciona os sinais apoptótico da via intrínseca. Essas proteínas impedem a liberação do citocromo c das mitocôndrias. Nos diferentes tratamentos das células de melanoma murino com o mastoparan os níveis de expressão das proteínas Bcl-XL e fosfo Bad (S112) apresentaram significativa redução quando comparada ao controle, demonstrando maior suscetibilidade na liberação do citocromo c (DEWSON; KLUCK, 2009; BELIZÁRIO et al., 2007; ZHANG et al., 2009). Somando a esses dados, foi possível observar que o peptídeo aumentou os níveis das proteínas pró-apoptótica Bim e Bak e consequente desencadeamento do sinal apoptótico. Essas proteínas podem se translocar para a membrana da mitocôndria modificando a permeabilidade da membrana externa, induzindo a liberação de proteínas pró-apoptóticas (KROEMER, 2002). Todos esses dados estão de acordo com as análises ultraestruturais das células de melanoma tratadas com o mastoparano, demonstrando assim, que esse peptídeo é um agente indutor de apoptose através da via mitocondrial intrínseca (ZHANG et al., 2012).

Por fim, nosso resultado mais importante com o mastoparano foi avaliado sobre a regressão dos tumores sólidos dorsais. Os dados mostraram que o mastoparan na concentração de 5 mg/Kg exibe efeito terapêutico apresentando significativa redução do volume tumoral. Após o término do período experimental dos tratamentos com os animais portadores dos tumores sólidos, os animais tratados com o mastoparano mostraram aumento no período de sobrevida global, com estimativa superior a 28 %, mesmo após a descontinuidade do tratamento. Diante desses resultados, o mastoprano pode ser considerado um importante composto candidato a agente antitumoral.

6. CONCLUSÕES

Após o desenvolvimento do trabalho foi possível concluir que:

- Os peptídeos INKKI e mastoparano, apesar de conservarem o mesmo motivo (KKI), apresentam efeitos distintos *in vitro*. O peptídeo INKKI demonstrou significativo efeito citostático enquanto que o mastoparano foi citotóxicos em células de melanoma murino B16F10;
- O peptídeo INKKI foi capaz de apresentar efeitos antiprolifertivo através da redução da expressão de mediadores correlacionados com a via do MAPK/ERK, proporcionado um aumento na proporção de células na fase G0/G1.
- O INKKI apresenta ações inibindo a migração e invasão celular envolvendo a via de sinalização da FAK/Src;
- Os estudos *in vivo* mostraram que o INKKI apresenta significativo efeito protetor nos modelos metastáticos e dorsais. Esse efeito *in vivo* depende da ativação do sistema imunológico, uma vez que o peptídeo não apresentou diminuição do número de nódulos metastáticos em modelo imunodeficientes de linhagem NOD/SCID/γ_c^{null};
- O mastoparan apresentou significativo efeito citotóxico, induzindo apoptose em linhagens de melanoma murinho B16F10;
- Os dados mostraram que o mastoparano é capaz de induzir apoptose através da via mitocondrial intrínseca, mediada pela geração de espécie reativa de oxigênio e perturbação dos poros de transição mitocondrial;
- Os estudos em modelo de melanoma dorsal mostraram que o mastoparano exibiu significativo efeito terapêutico com aumento da sobrevida em animais portadores de tumores.

REFERÊNCIAS*

ALBERTO, J. A; WAINSTEIN,T.; FRANCISCO, A. Conduta para o melanoma cutâneo. **Verol. Bras. Cir**. v. 31, n. 3, p.204-214, 2004.

ALLEN, R. T. HUNTER, W. J.; AGRAWAL, D. K. Morphological and biochemical characterization and analysis of apoptosis. **J. Pharmacol. Toxicol. Methods.** v. 37, n. 4, p. 215-228, 1997.

ALONSO, S.R; ORTIZ, P; POLLAN, M. Progression in cutaneous malignant melanoma is associated with distinct expression profiles: a tissue microarray-based study. **Am. J. Pathol**. v. 164, n. 1, p.193-203, 2004.

ARGIOLAS, A.; PISANO, J. J. Facilitation of phospholipase A2 activity by Mastoparans, a new class of mast cell degranulating peptides from wasp venom. **J. Biol. Chem.** v. 258, n. 22, p. 13697-13702, 1983.

ARMSTRONG, J.S. Mitochondria: a target for cancer therapy. **Br. J. of Pharmacol.** v. 147, n. 3, p. 239–248, 2006.

AZEVEDO, R.A.; FERREIRA, A.K.; AUADA, A.V.V. PASQUALOTO, K.F.P MARQUES-PORTO, R. MARIA, D.A.; LEBRUN, I. Antitumor effect of cationic INKKI peptide from bovine β-casein on melanoma B16F10. **J. Cancer Therapy**. v.3, p. 237-244, 2012.

BELIZÁRIO, J. E.; ALVES, J.; OCCHIUCCI, J. M.; GARAY-MALPARTIDA, M.; SESSO, A. A mechanistic view of mitochondrial death decision pores. **Braz. J. Med. Biol. Res.** v.40, n.8, p.1011-24, 2007.

BOCKSTAELE, L.; COULONVAL, K.; KOOKEN, H.; PATERNOT. S.; ROGER, P. P. Regulation of cdk4. **Cell Div**. v. 8, n. 1, p. 1-16, 2006.

CANO, E.; MAHADEVAN, L.C. Parallel signal processing among mammalian MAPKs. **Trends. Biochem. Sci**. v. 20, n. 3, p.117-22, 1995.

CARLSEN, H. Molecular imaging of the transcription factor NF-kappaB, a primary regulator of stress response. **Mutat. Res**. v. 551, n. 1-2, p. 199-211, 2004.

CARNERO, A. Targeting the cell cycle for cancer therapy. **Br. J. Cancer**. v. 87, n. 2, p. 129-133, 2002.

***De Acordo com:**
ASSOCIAÇÃO BRASILEIRA DE NORMAS TÉCNICAS. NBR 6023: Informação e documentação: referências: elaboração. Rio de Janeiro, 2002.

CARUSO-NEVES, C.; KWON, S. H.; GUGGINO, W. B. Albumin endocytosis in proximal tubule cell is modulated by angiotensin II through an AT2 receptor-mediated protein kinase B activation. **PNAS.** v. 102, n°48, p. 17513-17518, 2005.

CASCIOLA-ROSEN, L.; NICHOLSON, D. W.; CHONG, T.; ROWAN, K. R.; THORNBERRY, N. A.; MILLER, D. K.; ROSEN, A. Apopain/CPP32 cleaves proteins that are essential for cellular repair: A fundamental principle of apoptotic death. **J. Exp. Med.** v.183, n.5, p.1957-1964, 1996.

CHUANG, C. C.; HUANG, W. C.; YU, H. M.; WANG, K. T.; WU, S. H. Conformation of *Vespa basalis* mastoparan-B in trifluoroethanol-containing aqueous solution. **Biochim. Biophys. Acta.** v.1292, n.1, p.1-8, 1996.

CLARK, W. H. J R.; ELDER, D. E; GUERRY, D; EPSTEIN, M.N; GREENE, M.H AND VAN HORN, M. A study of tumor progression: the precursor lesions superficial spreading and nodular melanoma. **Hum. Pathol.** v.15, n. 12, p. 1147-1165, 1984.

CLARK, W. H. Tumor progression and the nature of cancer. **Br. J. Cancer**. v. 64, n. 4, p. 631-644, 1991.

COHEN, G. M. Caspases: the executioners of apoptosis. **Biochem. J**. v. 15, n. 326, p.1-16, 1997.

DALLA LIBERA, L.; ZENNARO, R.; SANDRI, M.; AMBROSIO, G.B.; VESCOVO, G. Apoptosis and atrophy in rat slow skeletal muscles in chronic heart failure. **Am. J. Cell. Physiol.** v. 277, n.5, p.982-986, 1999.

DANILENKO, M.; WORLAND, P.; CARLSON, B.; SAUSVILLE, E. A.; SHARONI, Y. Selective effects of mastoparan analogs: separation of G-protein-directed and membrane perturbing activities. **Biochem. Biophys. Res. Commun**. v. 196, n.3, p.1296-302, 1993.

DEBER, C. M.; LI, S. C. Peptides in membranes: helicity and hydrophobicity. **Biopolymers**. v. 37, n. 5, p. 295-318, 1995.

De SOUZA, B. M. **Estrutura e função de mastoparanos dos venenos de vespas**. Rio Claro, 2006.115p. Tese (Doutorado em Biologia Celular e Molecular) – Instituto de Biociencias de Rio Claro-SP, Universidade Estadual Paulista Julio de Mesquita Filho.

DERAMAUDT, T. B.; DUJARDIN, D.; HAMAD,I A.; NOULET, F.; KOLLI, K.; DE MEY, TAKEDA, J. K.; RONDE, P. FAK phosphorylation at Tyr-925 regulates cross-talk between focal adhesion turnover and cell protrusion. **Mol. Bio. Cell.**. v.22, n. 7, p. 964-975, 2011.

DEWSON, G.; KLUCK, R.M. Mechanisms by which Bak and Bax permeabilize mitochondria during apoptosis. **J. Cell. Sci**. v. 122, n. 16, p.2801-2808, 2009.

DO, N.; WEINDL, G.; GROHMANN, L.; SALWICZEK, M.; KOKSCH, B.; KORTING, H.C.; SCHÄFER-KORTING, M. Cationic membrane-active peptides - anticancer and antifungal activity as well as penetration into human skin. **Exp. Dermatol**. v. 23, n. 5, p. 326-331, 2014.

ELLERHORST, J.A; NADERI, A. A; JOHSON, M.K; PELLETIER,P; PRIETO,V.G; DIWAN, A. H;JOHSON, M.M; GUNN,D.C; YEKELL, S; GRIMM, E. A. Expression of thyrotropion-releaseing hormone by human melanoma and nevi. **Clin. Cancer. Res**. v. 10, n. 6, p. 5531-5536, 2004.

ENGELS, W. , VAN HAASTER, C. M.; VLEEMING, W.; VAN DER VUSSE, G.J. Antigen-evoked mast cell degranulation in the isolated rat heart: no effect on subsequent ischemia-reperfusion induced damage. **Inflamm. Res**. v. 46, n.2, p.40-45, 1997

FIAT, A.M. MIGLIORE-SAMOUR, D.; JOLLES, P.; DROUET, L.; BAL DIT SOLLIER, C.; CAEN, J. Biologically active peptides from milk proteins with emphasis on two examples concerning antithrombotic and immunomodulating activities. **J. Dairy. Sci**. v.76, n. 1, p. 301-310, 1993.

FIAT, A. M.; JOLLÈS, P. Caseins of various origins and biologically active casein peptides and oligosaccharides: Structural and physilogical aspect. **Mol. Cell. Biochem**. v. 87, n. 1, p. 5-30, 1989.

FOSTER, H. SMALL, D.; FOX, G. **The Mouse in Biomedical Research**. New York: Academic Press, 1983.

FRIEDLANDER, R. M. Apoptosis and caspases in neurodegenerative diseases. **N. Engl. J Med.** v. 348, n.14, p. 1365-1375, 2003.

FULDA, S. KROEMER, G. Mitochondrial as therapeutic targets for the treatment of malignant disease. **Antioxid. Redox. Signal.** v.15, n. 12, p. 2937-2949, 2001.

GAURISANKAR, S.A.; TANYA, D.A.S. Anti cancer effects of curcumin: cycle of life and death. **Cell. Div**. v. 3, n.14, p. 1-14, 2008.

GILLE, H.; DOWNWARD, J. Multiple ras effector pathways contribute to G(1) cell cycle progression. **J. Biol. Chem**. v. 274, n. 31, p. 22033-2240, 1999.

GRAY-SCHOPFER, V; WELLBROCK, C.; RICHARD MARAIS. Melanoma biology and new targeted therapy. **Nature**. v. 22, n. 445, p. 851-857, 2007.

GU X, YAO, Y.; CHENG, R.; ZHANG, Y.; DAI, Z.; WAN, G.; YANG, Z.; CAI, W.; GAO, G.; YANG, X. Plasminogen K5 activates mitochondrial apoptosis pathway in endothelial cells by regulating Bak and Bcl-x(L) subcellular distribution. **Apoptosis**. v. 16, n. 8, p.846-855, 2011.

HENRIQUES, O. B.; de DEUS, N. R.; SANTOS, R. A. S. Bradikinin potentiating peptides isolated from alpha-casein tryptic hydrolysate**. Biochem. Pharmacol**. v. 36, n. 1, p. 182-184, 1987.

HIGASHIJIMA, T.; BURNIER, J.; ROSS, E. M. Regulation of Gi and G0 by mastoparan related peptides and hydrophilic amines. **J. Biol. Chem**. v. 265, n. 24, p.14176-86, 1990.

HIRAI, Y. YASUHARA, T.; YOSHIDA, H.; NAKAJIMA, T.; FUJINO, M.; KITADA, C. A new mast cell degranulating peptide "mastoparan" in the venom of *Vespula lewisii*. **Chem. Pharm. Bull**. v.27, n. 8, p. 1942-1944, 1979.

HILDER, T. L.; CARLSON, G .M.; HAYSTEAD, T. A. J.; KREBS, E. G.; GRAVES, L. M. Caspase-3 dependent cleavage and activation of skeletal muscle phosphorylase b kinase. **Mol. Cell. Biochem.** v.275, n.1-2, p.233-242, 2005.

HO, C. L.; HWANG, L. L.; LIN, Y. L.; CHEN, C. T.; YU, H. M.; WANG, K. T. Cardiovascular effects of mastoparan B and its structural requirements. Amsterdam, **Eur. J. Pharmacol**. v. 259, n. 3, p.259-64, 1994.

HORI, Y.; Demura, M.; Iwadate, M.; Ulrich, A. S.; Niidome, T.; Aoyagi, H.; Asakura, T. Interaction of mastoparan with membranes studied by 1H-NMR spectroscopy in detergent micelles and by solid-state 2H-NMR spectroscopy in oriented lipid. **Eur. J. Biochem.** v. 268, n. 2, p. 3029, 2001.

HOSKIN D. W.; RAMAMOORTHY, A. Studies on anticancer activities of antimicrobial peptides. **Biochim. Biophys. Acta.** v. 1778, n. 2, p. 357–375, 2008.

HSU, M.; ANDL, T.; LI,G; MEINKOTH, J. L.; HERLYN, M. Cadherin repertorie determines partner-especific gap junctional communication during melanoma progression. **J. Cell. Sci**. v.113, n 9, p.1535-1542, 2000.

INSTITUTO NACIONAL DO CÂNCER (INCA). Disponível em: http://www2.inca.gov.br/wps/wcm/connect/inca/portal/home. Acessado em 05/05/2014.

IVANOVA, P. T.; CERDA, B. A.; CHIFRE, D.M.; COHEN, J. S.; MCLAFFERTY, F.W.; BROWN, H. A. Electrospray ionization mass spectrometry analysis of changes in phospholipids in RBL- 2H3 mastocytoma cells during degranulation. **PNAS**. v. 98, n. 13, p. 7152-7157, 2001.

IVANOVA, D.; BAKALOVA, R.; LAZAROVA, D.; GADJEVA, V.; ZHELEV Z. The impact of reactive oxygen species on anticancer therapeutic strategies. **Adv. Clin. Exp. Med**. v. 22, n. 6, p. 899-908, 2013.

JIANFEI, Q.; Wang, J.; Romanyuk, O.; Siu, C. H. Involvement of Src Family Kinases in N-Cadherin Phosphorylation and β-Catenin Dissociation during Transendothelial Migration of Melanoma Cells. **Mol. Biol. Cell**. v. 17, p. n. 3, p. 1261–1272, 2006.

JOBIN, K. J.; PARAISO, K. H.; REBECCA, V. W.; CANTINI, L. P.; ABEL, E. V.; PAGANO, N.; MEGGERS, E.; MATHEW, R.; KREPLER, C.; IZUMI, V.; FANG, B.; KOOMEN, J. M.; MESSINA, J.L.; HERLYN, M.; SMALLEY, K. S. GSK3b Inhibition Blocks Melanoma Cell/Host Interactions by Downregulating N-Cadherin Expression and Decreasing FAK Phosphorylation. **J. Invest. Dermatol**. v.132, n. 12, p. 2818–2827, 2012.

KALLERGI, G.; AGELAKI, S.; MARKOMANOLAKI, H.; GEORGOULIAS, V.; STOURNARAS, C. Activation of FAK/PI3K/Rac1 Signaling Controls Actin Reorganization and Inhibits Cell Motility in Human Cancer Cells. **Cell. Physiol. Biochem.** v.20, n. 6, p. 977-986, 2007.

KATSU, T.; KUROKO, M.; MORIKAWA, T.; SANCHIKA, K.; YAMANAKA, H.; SHINODA, S.; FUJITA, Y. Interaction of wasp venom mastoparan with biomembranes. **Biochim. Biophys. Acta.** v. 1027, n. 2, p. 185-190, 1990.

KARDEH, S.; ASHKANI-ESFAHANI, S.; ALIZADEH, A.M. Paradoxical action of reactive oxygen species in creation and therapy of cancer. **Eur. J. Pharmacol**. v. 26, n. 35, p.150-168, 2014.

KAWAHARA, T.; KATAYAMA, D.; OTANI, H. Effect of β-casein (1-28) on proliferative responses and secretory functions of human immunocompetent cell lines. **Biosci. Biotechonol. Biochem**. v. 68, n. 10, p. 2091-2095, 2004.

KERR, J. F.; WYLLIE, A. H.; CURRIE, A. R. Apoptosis: a basic biological phenomenon with wideranging implications in tissue kinetics. **Br. J. Cancer.** v.26, n.4, p. 239-57, 1972.

KITAZAWA, H.; Yonezawa, K.; Tohno, M.; Shimosato, T.; Kawai, Y.; Saito, T.; Wang, J. M. Enzimatic digestion of the milk protein β-casein releases potent chemotactic peptide (s) for monocytes and macrophages. **Int. Immunopharmacol**. v. 7, n. 9, p. 1150-1159, 2007.

KONNO, K.; HISADA, M.; ITAGAKI, Y.; NAOKI, H.; KAWAI, N.; MIWA, A.; YASUHARA, T.; TAKAYAMA, H. Isolation and structure of pompilidotoxins (PMTXs), novel neurotoxins in solitary wasp venoms. **Biochem. Biophys. Res. Commum.** v.250, n 3, p. 612-616, 1998.

KOROLEVA, S. V.; MIASOEDOV, N. F. Dynamic hierarchy of regulatory peptides. Structure of the induction relations of regulators as the target for therapeutic agents. **Usp. Fiziol. Nauk**. v.43, n.3, p. 38-47, 2012.

KROEMER, G. Introduction: mitochondrial control of apoptosis. **Biochemie**. v. 84, n. 2-3, p.103-104, 2002.

KROEMER, G.; GALLAZZI, L.; BRENNER, C. Mitochondrial membrane permeabilization in cell death. **Physiol. Rev.** v. 87, n. 1, p. 99-163, 2007.

KUMOSINSKI, T.F.; Brown, E. M.; Farrell, H. M. Three-dimensional molecular modeling of bovine caseins: An energy-minimized β-casein structure. **J. Dairy.** v. 76, n. 4, p. 931-945, 1993.

KYRIAKIS, J. M.; AVRUCH, J. Mammalian MAPK signal transduction pathways activated by stress and inflammation: a 10-year update. **Physiol. Rev**. v. 92, n. 2, p. 689-737, 2012.

LAHOV, E.; REGELSON, W. Antibacterial and immustimulating casein-derived substances from milk casecedin, isracidin peptides. **Food. Chem. Toxicol**. v.34, n. 1, p. 131-145, 1996.

LEBRUN, I.; CAVALLARO, V.; JULIANO, L.; JULIANO, M. A.; DE SOUSA E SILVA, M. C. Effects of ‘casoparan’, a peptide isolated from casein hydrolysates with mastoparan-like properties. **Mediators. Inflamm**. v.13, n. 4, p. 263-268, 2004.

LEBRUN, I.; LEBRUN, F. L.; HENRIQUES, O. B.; CARMONA, A. K.; JULIANO, L.; CAMARGO, A. C. Isolation and characterization of a new bradykinin potentiating octapeptide from gama-casein. **J. Physiol. Pharmacol**. v. 73, n. 1, p. 85-91, 1995.

LEUSCHNER, C.; HANSEL, W. Membrane disrupting lytic peptides for cancer treatments. **Curr. Pharm. Des.** v. 10, n. 19, p. 2299-2310, 2004.

LI, G.; FUKUNAGA, M.; HERLYN, M. Reversal of melanocytic malignancy by keratinocytes is an E-cadherin-mediated process overriding h-catenin signaling. **Experimental. Cell. Research**. v. 297, n. 1, p. 142–151, 2004.

LI, GANG.; HERLYN, M. Dinamics of intercellular communication during melanoma development. **Mol. Med. Today**. v. 6, n. 4, p. 163-169, 2000.

LI, Z.; WANG, C.; PRENDERGAST, G. C.; PESTELL, R. G. Cyclin D1 functions in cell migration. **Cell Cycle**. v. 5, n. 21, p. 2440-2442, 2006.

LICATO, L.L. KEKU, T. O.; WURZELMANN, J. I.; MURRAY, S. C.; WOOSLEY, J. T.; SANDLER, R. S.; BRENNER, D. A. *In vivo* activation of mitogen-activated protein kinases in rat intestinal neoplasia. **Gastroenterology**. v. 113, n. 5, p. 1589-1598, 1997.

LIU, N.; LUCIBELLO, F.C.; ZWICKER, J.; ENGELAND, K.; MÜLLER, R. Cell cycle-regulated repression of B-myb transcription: cooperation of an E2F site with a contiguous corepressor element. **Nucleic Acids Res**. v. 24, n. 15, p. 2905-2910, 1996.

LOPEZ-BERGAMI, P. The role of mitogen-and-stress-activated protein kinase pathways in melanoma. **Pigment. Cell. Melanoma. Res.** v. 24, n. 5, p. 902-921, 2011.

LORENZI, C. C. B. **Estudo estrutural de mastoparanos isolados de vespas solitárias**. São José do Rio Preto, 2002. 115p. Dissertação (Mestrado em Biofísica Molecular) – Instituto de Biociências, Letras e Ciências Exatas, Universidade Estadual Paulista.

MADER, J. S.; SALSMAN, J.; CONRAD, D. M.; HOSKIN, D. W. Bovine lactoferricin selectively induces apoptosis in human leukemia and carcinoma cell lines. **Mol. Cancer. Ther**. v. 4, n. 4, p. 612–624, 2005.

MADER, J. S.; HOSKIN, D. W. Cationic antimicrobial peptides as novel cytotoxic agents for cancer treatment. **Expert. Opin. Investig. Drugs**. v.15, n. 8, p. 933-946, 2006.

MASAMHA, C. P.; BENBROOK, D. M. Cyclin D1 degradation is sufficient to induce G1 cell cycle arrest despite constitutive expression of cyclin E2 in ovarian cancer cells. **Cancer. Res**. v. 69, n. 16, p. 6565-6572, 2009.

MASHIMA, T.; NAITO, M.; TSURUO, T. Caspase-mediated cleavage of cytoskeletal actin plays a positive role in the process of morphological apoptosis. **Oncogene**. v.18, n. 15, p. 2423-2430, 1999.

MANCINI, M.; NICHOLSON, D. W.; ROY, S.; THORNBERRY, N. A.; PETERSON, E. P.; CASCIOLA-ROSEN, L. A.; ROSEN, A. The caspase-3 precursor has a cytosolic and mitochondrial distribution: implications for apoptotic signaling. .**J Cell. Biol**. v. 140, n. 6, p.1485-1495, 1998.

MATSUO, A. L.; TANAKA, A. S.; JULIANO, M. A.; RODRIGUES, E. G.; TRAVASSOS, LR. A novel melanoma-targeting peptide screened by phage display exhibits antitumor activity. **J. Mol. Med.** v.88, n. 12, p. 1255-1264, 2010.

MATSUO, A. L.; FIGUEIREDO, C. R.; ARRUDA, D. C.; PEREIRA, F. V.; SCUTTI, J. A.; MASSAOKA, M. H.; TRAVASSOS, L. R.; Sartorelli, P.; Lago, J. H. α-Pinene isolated from *Schinus terebinthifolius* Raddi (Anacardiaceae) induces apoptosis and confers antimetastatic protection in a melanoma model. **Biochem. Biophys. Res. Commum.** v. 411, n. 2, p. 449-454, 2011.

MATSUZAKI, K.; YONEYAMA, S.; MURASE, O.; MIYAJIMA, K. Transbilayer transport of ions and lipids coupled with mastoparan X translocation. **Biochemistry.** v.35, n. 25, p.8450-6, 1996.

MATSUZAKI, K.; SUGISHITA, K.; MIYAJIMA, K. Interactions of an antimicrobial peptide, Magainin 2, with lipopolysaccharideo containing liposomes as a model for outer membranes of Gram-negative Bacteria. **FEBS. Lett**. v. 449, p. 221-224, 1999.

MARUYAMA, S.; SUZUKI, H. A peptide inhibitor of angiotensin I-converting enzyme in the tryptic hydrolysate of casein. **Agric. Biol. Chem**. v. 46, n. 5, p. 1393-1394, 1982.

MENDES, M. A.; DE SOUZA, B. M.; MARQUES, M. R.; PALMA, M. S. Structural and biological characterization of two novel peptides from the venom of the neotropical social wasp *Agelaia pallipes pallipes*. **Toxicon**. v. 44, n. 1, p.67-74, 2004.

MEISEL, H. Biochemical properties of regulatory peptides derived from milk proteins. **Biopolymers.** v. 43, n. 2, p. 119-128, 1997.

MELLOR, I. R.; SANSOM, M. S. Ion-channel properties of mastoparan, a 14-residue peptide from wasp venom, and of MP3, a 12-residue analogue. **Proc. R. Soc. Lond. B. Biol**. v.239, n.1296, p.383-400, 1990.

MERKWIRTH, C.; DARGAZANLI, S.; TATSUTA, T.; GEIMER, S.; LÖWER, B.; WUNDERLICH, F. T.; VON KLEIST-RETZOW, J. C.; WAISMAN, A.; WESTERMANN, B.; LANGER, T. Prohibitins control cell proliferation and apoptosis by regulating opa1-dependent cristae morphogenesis in mitochondria. **Genes. Dev.** v. 22, n. 4, p.476-488, 2008.

MUTHUSAMY, V.; PIVA, T.J. The UV response of the skin: a review of the MAPK, NFkappaB and TNFalpha signal transduction pathways. **Arch Dermatol Res**. v. 302, n. 1, p. 5-17, 2010.

NAKAJIMA, T.; UZU, S.; WAKAMATSU, K.; SAITO, K.; MIYAZAWA, T.; YASUHARA, T.; TSUKAMOTO, Y.; FUJINO, M. Amphiphilic peptides in wasp venom. **Biopolymers**. v.25, p.115-21, 1986.

NAKAMURA, K.; YOSHIKAWA, N.; YAMAGUCHI, Y.; KAGOTA, S.; SHINOZUKA, K.; KUNITOMO, M. Characterization of mouse melanoma cell lines by their mortal malignancy using an experimental metastatic model. **Life Sci**. v. 70, n. 7, p. 791-78, 2002.

NAGY, G.; KONCZ, A.; PERL, A. T cell activation-induced mitochondrial hyperpolarization is mediated by Ca^{2+} and redox-dependent production of nitric oxide. **J. Immunol.** v. 171, n. 10, p. 5188-5197, 2003.

NEGANOVA, I.; ZHANG, X.; ATKINSON, S.; LAKO, M. Expression and functional analysis of G1 to S regulatory components reveals an important role for CDK2 in cell cycle regulation in human embryonic stem cells. **Oncogene**. v. 28, n. 1, p. 20-30, 2009.

OBERHAMMER, F.; WILSON, J. W.; DIVE, C.; MORRIS, I. D.; HICKMAN, J. A.; WAKELING, A. E.; WALKER, P. R.; SIKORSKA, M. Apoptotic death in epithelial cells: cleavage of DNA to 300 and/or 50 kb fragments prior to or in the absence of internucleosomal fragmentation. **Embo. J.** v.12, n.9, p. 3679-3684, 1993.

OTANI, H.; WATANABE, T.; TASHIRO, Y. Effects of bovine β-casein (1-28) and its chemically synthesized partial fragments on proliferative responses and immunoglobulin production in mouse spleen cell culture. **Biosci. Biotechonol. Biochem.** v. 65, n. 11, p. 2489-2495, 2001.

PARK, K. R.; NAM, D.; YUN, H. M.; LEE, S. G.; JANG, H. J.; SETHI, G.; CHO, S. K.; AHN, K. S. β-Caryophyllene oxide inhibits growth and induces apoptosis through the suppression of PI3K/AKT/Mtor/s6k1 pathways and ROS-mediated MAPKs activation. **Cancer. Lett**. v.31, n. 2, p. 178-188, 2011.

PAREDES, J.; FIGUEIREDO, J.; ALBERGARIA, A.; OLIVEIRA, P.; CARVALHO, J.; RIBEIRO, A. S.; CALDEIRA, J.; COSTA, A. M.; SIMÕES-CORREIA, J.; OLIVEIRA, M. J.; PINHEIRO, H.; PINHO, S. S.; MATEUS, R.; REIS, C. A.; LEITE, M.; FERNANDES, M. S.; SCHMITT, F.; CARNEIRO, F.; FIGUEIREDO, C.; OLIVEIRA, C.; SERUCA, R. Epithelial E- and P-cadherins: role and clinical significance in cancer. **Biochim. Biophys. Acta**. v.1826, n.2, p. 297-311, 2012.

PERCHELLET, E. M.; WANG, Y.; WEBER, R. L.; SPERFSLAGE, B. J.; LOU, K.; CROSSLAND, J.; HUA, D. H.; PERCHELLET, J. P. Synthetic 1,4-anthracenedione analogs induce cytochrome c release, caspase-9, -3, and -8 activities, poly(ADP-ribose) polymerase-1 cleavage and internucleosomal DNA fragmentation in HL-60 cells by a mechanism which involves caspase-2 activation but not Fas signaling. **Biochem. Pharmacol**. v. 67, n. 3, p.523-537, 2004.

PETER, I.; MEZZACASA, A.; LEDONNE, P.; DUMMER, R.; HEMMI, S. Comparative analysis of immunocritical melanoma markers in the mouse melanoma cell lines B16, K1735 and S91-M. **Melanoma. Res**. v. 11, n. 1, p. 21-30, 2001.

PIMENTA, D. C.; LEBRUN I. Cryptides: buried secrets in proteins. **Peptides**. v. 28, n. 12, p.2403-2410, 2007.

PFEIFFER, C.; STEIN, J.; SOUTHWOOD, S.; KETELAAR, H.; SETTE, A.; BOTTOMLY, K. Altered peptide ligands can control CD4 T lymphocyte differentiation *in vivo*. **J. Exp. Med.** v. 181, n. 3, p. 1569-1574, 1995.

QUINN, P. J. Effects of temperature on cell membranes. **Symp. Soc. Exp. Biol**. v. 42, p. 237-58, 1988.

REA, K.; SENSI, M.; ANICHINI, A.; CANEVARI, S.; TOMASSETTI, A. EGFR/MEK/ERK/CDK5-dependent integrin-independent FAK phosphorylated on serine 732 contributes to microtubule depolymerization and mitosis in tumor cells. **Cell. Death. Dis**. v. 4, n. 3, p. 1-12, 2013.

REDDY, K.B.; KRUEGER, J. S.; KONDAPAKA, S. B.; DIGLIO, C. A. Mitogen-activated protein kinase (MAPK) regulates the expression of progelatinase B (MMP-9) in breast epithelial cells. **Int. J. Cancer**. v. 82, n. 2, p. 268-273, 1999.

RINCÓN, M.; FLAVELL, R. A.; DAVIS, A. R. A JNK e p38 MAP quinase vias de sinalização nas células T mediadas por respostas imunes. **Free .Radic. Biol. Med**. v. 28, n. 9, p. 1328-1337, 2000.

ROCHA T. Inflammation and apoptosis induced by mastoparan Polybia-MPII on skeletal muscle. **Toxicon.** v. 55, n. 7, p. 1213–1221, 2010.

ROBERTS, P. R.; ZALOGA, G. P. Dietary bioactive peptides. **New. Horiz**. v. 2, n. 2, p. 237-243, 1994.

RODRIGUEZ-VICIANA, P.; WARNE, P. H.; KHWAJA, A.; MARTE, B. M.; PAPPIN, D.; DAS, P.; WATERFIELD, M. D.; RIDLEY, A. DOWNWARD, J. Role of phosphoinositide 3-OH kinase in cell transformation and control of the actin cytoskeleton by Ras. **Cell**. v. 89, n. 3, p. 457-67, 1997.

ROBERTS, D .L.; ANSTEY, A. V.; BARLOW, R. J.; COX, N. H.; NEWTON BISHOP, J. A.; CORRIE, P. G.; EVANS, J.; GORE, M. E.; HALL, P. N.; KIRKHAM, N. U.K. guidelines for the management of cutaneous melanoma**. Br. J. Dermatol**. v. 146, n. 1, p.7-17, 2002.

ROGALIŃSKA, M. Alterations in cell nuclei during apoptosis. **Cell. Mol. Biol. Lett**. v. 7, n. 4, p. 995-1018, 2002.

ROTTENBERG, S.; BORST, P. Drug resistance in the mouse cancer clinic. **Drug Resist Updat**. v.15, n. 1-2, p. 81-89, 2012.

SATO, H.; FEIX, J. B. Peptide–membrane interactions and mechanisms of membrane destruction by amphipathic -helical antimicrobial peptides. **Biochim. Biophys. Acta.** v. 1758, n. 9, p. 1245–1256, 2006.

SCHAEFFER, H. J.; WEBER, M. J. Mitogen-activated protein kinases: specific messages from ubiquitous messengers. **Mol. Cell. Biol**. v. 19, n. 4, p. 2435-2444, 1999.

SCHWRZ, G.; BLOCHMANN, U. Association of the wasp venom peptide mastoparan with electrically neutral lipid vesicles. **FEBS. Letters**. v.318, n.2, p.172-6, 1993.

SCHLEICHER, M.; SHEPHERD, B. R.; SUAREZ, Y.; FERNANDEZ-HERNANDO, C.; YU, J.; PAN, Y.; ACEVEDO, L. M.; SHADEL, G. S.; SESSA, W. C. Prohibitin-1 maintains the angiogenic capacity of endothelial cells by regulating mitochondrial function and senescence. **J. Cell. Biol**. v.180, n. 1, p.101-112, 2008.

SEBOLT-LEOPOLD, J.S. Development of anticancer drugs targeting the MAP kinase pathway. **Oncogene**. v. 19, n. 56, p. 6594-6599, 2000.

SHEPPARD, K.E.; MCARTHUR, G.A. The cell-cycle regulator CDK4: an emerging therapeutic target in melanoma. Clin. Cancer. Res. v. 1, n. 19, p. 5320-5328, 2013.

SHIELDS, J. M.; PRUITT, K.; MCFALL, A.; SHAUB, A.; DER, C. J. Understanding Ras: 'it ain't over 'til it's over'. **Trends. Cell. Biol**. v. 10, n. 4, p. 147-154, 2000.

SIMON, M. M.; PAVLIK, P.; HARTIG, A.; BINDER, M.; RUIS, H.; COOK, W. J.; DENIS, C. L.; SCHANZ, B. A C-terminal region of the Saccharomyces cerevisiae transcription factor ADR1 plays an important role in the regulation of peroxisome proliferation by fatty acids. **Mol Gen Genet**. v. 249, n. 3, p. 289-296, 1995.

SOKOLOVE, P. M.; KINNALLY, K. W. A mitochondrial signal peptide from Neurospora crassa increases the permeability of isolated rat liver mitochondria. **Arch Biochem Biophys**. v. 336, n. 1, p. 69-76, 1996.

SOUZA, N; SONIA, R. P; FISCHER, FRIDA, M; Suntanning and risk of cutaneous melanoma: a literature review. **Rev. Sau. Pub.** v. 38, n. 4, p. 1-11, 2004.

SLOMINSKI, A.; TOBIN, D. J.; SHIBAHARA, S.; WORTSMAN, J. Melanin pigmentation in mammalian skin and its hormonal regulation. **Physiol. Rev**. v. 84, n. 1, p. 1155-1228, 2004.

STANLEY, P. L. L.; GERSHENWALD, J. E.; SOONG, S. J.; SCHADENDORF, D.; TARHINI, A. A.; AGARWALA, S.; HAUSCHILD, A.; SOON, C. W.; DAUD, A.; KASHANI-SABET, M. Cutaneous Melanoma: A Model to Study Cancer Metastasis. **J. Surg. Oncol.** v.103, n. 6, p.538–549, 2011.

STOKOE, D.; Macdonald, S. G.; Cadwallader, K.; Symons, M.; Hancock, J. F. Activation of Raf as a result of recruitment to the plasma membrane. **Science**. v. 264, n. 5164, p. 1463-147, 1994.

SYED, D.N.; AFAQ, F.; MADDODI, N.; JOHNSON, J. J.; SARFARAZ, S.; AHMAD, A.; SETALURI, V.; MUKHTAR, H. Inhibition of human melanoma cell growth by the dietary flavonoid fisetin is associated with disruption of Wnt/β-catenin signaling and decreased Mitf levels. **J. Invest. Dermatol**. v. 131, n.6, p.1291-1299, 2011.

TIETZE, M. K.; CHIN, L. Murine models of malignant melanoma. **Mol. Med. Today**. v. 6, n. 10, p. 408-410, 2000.

TØRFOSS, I.J.; AUSBACHER, D.; BRANDSDAL, B.O.; FLATEN, G.E.; ANDERSSEN, T.; CAVALCANTI-JACOBSEN, C.D.E. A.; HAVELKOVA, M.; NGUYEN, L.T.; VOGEL, H.J.; STRØM, M.B. Improved anticancer potency by head-to-tail cyclization of short cationic anticancer peptides containing a lipophilic β(2,2) -amino acid. **J. Pept. Sci.** v. 18, n. 10, p. 609-619, 2012.

TOLKACHEVA, T.; CHAN, A. M. Inhibition of H-Ras transformation by the PTEN/MMAC1/TEP1 tumor suppressor gene. **Oncogene**. v. 19, n. 5, p. 680-69, 2000.

TSUI, M. M.; TAI, W. C.; WONG, W. Y.; HSIAO, W. L. Selective G2/M arrest in a p53(Val135)-transformed cell line induced by lithium is mediated through an intricate network of MAPK and β-catenin signaling pathways. **Life. Sci**. v. 24, n. 91, p. 312-21, 2012.

TURRENS, J.F. Mitochondrial formation of reactive oxygen species. **J. Phusiol.** v. 552, n. 15, p. 335-344, 2003.

VAN GURP, M.; FESTJENS, N.; VAN LOO, G.; SAELENS, X.; VANDENABEELE, P. Mitochondrial intermembrane proteins in cell death. **Biochem. Biophys. Res. Commun**. v. 304, n. 3, p. 487-497, 2003.

VAN DYKE, T.; JACKS, T. Cancer modeling in the modern era: progress and challenges. **Cell**. v. 108, n. 2, p. 135-144, 2002.

Van RIGGELEN, J.; FELSHER, D. W. Myc and a Cdk2 senescence switch. **Nat Cell Biol**. v. 12, n. 1, p. 7-9, 2010.

VIGNJEVIC, D.; MONTAGNAC, G. Reorganisation of the dendritic actin network during cancer cell migration and invasion. **Semin. Cancer. Biol**. v. 18, n. 1, p.12-22, 2008.

VON EULER, H.; Söderstedt, A.; Thörne, A.; Olsson, J. M.; Yongqing, G. Cellular toxicity induced by different pH levels on the R3230AC rat mammary tumour cell line. An *in vitro* model for investigation of the tumour destructive properties of electrochemical treatment of tumours. **Bioelectrochemistry**. v.58, n.2, p.163-170, 2002.

YAMADA, Y.; SHINOHARA, Y.; KAKUDO, T.; CHAKI, S.; FUTAKI, S.; KAMIYA, H.; HARASHIMA, H. Mitochondrial delivery of mastoparan with transferrin liposomes equipped with a pH-sensitive fusogenic peptide for selective cancer therapy. **Int. J. Pharm.** v. 303, n. 13, p.1-7, 2005.

YEAMAN, M. R.; YOUNT, N. Y. Mechanism of antimicrobial peptide action and resistance. **Pharmacol. Rev.** v. 55, p. 27-55, 2003.

WAKAMATSU, K.; OKADA, A.; MIYAZAWA, T.; OHYA, M.; HIGASHIJIMA, T. Membrane-bound conformation of Mastoparan-X, a G-protein-activating peptide. **Biochemistry.** v. 31, n. 1, p. 5654-5660, 1992.

WALKER, P. R.; Leblanc, J.; Smith, B.; Pandey, S.; Sikorska, M. Detection of DNA fragmentation and endonucleases in apoptosis. **Methods.** v. 17, n. 4, p. 329-338, 1999.

ZHANG, F. M.; OTANI, H. Immunogenicity and antigenicity of casein phosphopeptides. **Milchwissenschaft Nurnberg.** v. 58, n. 1-2, p. 9-13, 2003.

ZHANG, S.; Li, G.; Ma, X.; Wang, Y.; Liu, G.; Feng, L.; Zhao, Y.; Zhang, G.; Wu, Y.; Ye, X.; Qin, B.; Lu, J. l. Norcantharidin enhances ABT-737-induced apoptosis in hepatocellular carcinoma cells by transcriptional repression of Mcl-1. **Cell. Signal**. v. 24, n. 9, p.1803-1809, 2012.

ZHANG, D.W.; Shao, J.; Lin, J.; Zhang, N.; Lu, B. J.; Lin, S. C.; Dong, M. Q.; Han, J. RIP3, an energy metabolism regulator that switches TNF-induced cell death from apoptosis to necrosis. **Science**. v. 325, n. 5938, p. 332-36, 2009.

ZHAO, W.; LIU, H.; XU, S. Correlation between the biological behavior and invasion potential in three mouse melanoma cell lines. **Zhonghua. Zhong. Liu. Za. Zhi.** v.23, n. 4, p. 301-304, 2001.

ZOROV, D. B.; JUHASZOVA, M.; SOLLOTT, S. J. Mitochondrial ROS-induced ROS release: an update and review. **Biochem. Biophys. Acta.** v. 1757, n. 5-6, p. 509-517, 2006.

ANEXO 1

PRODUÇÃO ACADÊMICA

TRABALHOS ACEITOS

Advanced Pharmaceutical Bulletin

Adv Pharm Bull, 2014, 4(x), x-x
doi: 10.5681/apb.2014.052
http://apb.tbzmed.ac.ir

Research Article

Antitumor Activity of *Kielmeyera Coriacea* Leaf Constituents in Experimental Melanoma, Tested *in Vitro* and *in Vivo* in Syngeneic Mice

Carlos Rogério Figueiredo[1]*, Alisson Leonardo Matsuo[1], Mariana Hiromi Massaoka[1], Natalia Girola[1], Ricardo Alexandre Azevedo[1], Aline Nogueira Rabaça[1], Camyla Fernandes Farias[1], Felipe Valença Pereira[1], Natalia Silva Matias[2], Luciana Pereira Silva[2], Elaine Guadelupe Rodrigues[1], João Henrique Guilardi Lago[3], Luiz Rodolpho Travassos[1], Regildo Márcio Gonçalves Silva[2]

[1] *Department of Microbiology, Immunology and Parasitology, Experimental Oncology Unit (UNONEX), Federal University of São Paulo (UNIFESP), São Paulo, Brazil.*

[2] *Department of Biological Sciences – Laboratory of Herbal Medicines, Universidade Estadual Paulista (UNESP- FLC/Assis), São Paulo, Brazil.*

[3] *Institute of Environmental, Chemical and Pharmaceutical Sciences, Federal University of São Paulo (UNIFESP), Diadema, São Paulo, SP, Brazil.*

Article info

Article History:
Received: 4 January 2014
Revised: 7 February 2014
Accepted: 19 February 2014
Available Online: 25 February 2014

Keywords:
- Cancer
- Cell cycle arrest
- Cell migration
- Cerrado
- Anti-tumor
- Cytotoxic

Abstract

Purpose: The antitumor activity of *Kielmeyera coriacea* (Clusiaceae), a medicinal plant used in the treatment of parasitic, as well as fungal and bacterial infections by the Brazilian Cerrado population, was investigated.

Methods: A chloroform extract (CE) of *K. coriacea* was tested in the murine melanoma cell line (B16F10-Nex2) and a panel of human tumor cell lines. Tumor cell migration was determined by the wound-healing assay and the *in vivo* antitumor activity of CE was investigated in a melanoma cell metastatic model. ^{1}H NMR and GC/MS were used to determine CE chemical composition.

Results: We found that CE exhibited strong cytotoxic activity against murine melanoma cells and a panel of human tumor cell lines *in vitro*. CE also inhibited growth of B16F10-Nex2 cells at sub lethal concentrations, inducing cell cycle arrest at S phase, and inhibition of tumor cell migration. Most importantly, administration of CE significantly reduced the number of melanoma metastatic nodules *in vivo*. Chemical analysis of CE indicated the presence of the long chain fatty compounds, 1-eicosanol, 1-docosanol, and 2-nonadecanone as main constituents.

Conclusion: These results indicate that *K. coriacea* is a promising medicinal plant in cancer therapy exhibiting antitumor activity both *in vitro* and *in vivo* against different tumor cell lines.

Introduction

Plant-derived compounds have received considerable attention in recent years because of their pharmacological properties, including cytotoxicity and chemotherapeutic activities in cancer. Brazilian Cerrado, the second largest biome in Brazil,[1] is the source of many species containing bioactive compounds assayed in different experimental models.[2,3] The Cerrado is one of the 25 important biodiversity hotspots in the World, with an exceptional concentration of rare endemic species.[4] Recent studies have described the biological activities of several plant extracts or isolated compounds from this tropical savanna ecoregion.[5-8]

Kielmeyera coriacea Mart. & Zucc. (Clusiaceae) is a medicinal plant derived from the Brazilian Cerrado, used by the native population in the treatment of several tropical diseases, including schistosomiasis, leishmaniasis, malaria, fungal and bacterial infections.[9] Recent studies have reported on the cytotoxic activity of *K. coriacea* Root and Bark extracts in tumor cells, such as HCT-8 (human colon carcinoma), HL-60 (human leukemia), SF-295 (glioblastoma) and MDA-MB-435 (melanoma).[8] Previous studies have shown the low toxicity of a dichlorometane extract of *K. coriacea* stems, suggesting a margin of safety for *in vivo* therapeutic doses.[10] It has also been reported that the dichloromethane fraction from stems of *K. coriacea* can be an important therapeutic alternative in the treatment of anxiety disorders by induction of antidepressant response in rats.[11,12]

We evaluated the *in vitro* and *in vivo* antitumor effects of different leaf extracts of *K. coriacea* on murine melanoma B16F10-Nex2. We also evaluated *K. coriacea* cytotoxicity in several human cancer cells. Our results indicate that the chloroform extract (CE) from leaves of *K. coriacea* inhibited murine melanoma B16F10-Nex2 cell growth with cell cycle arrest, cell migration *in vitro* and tumor-cell lung colonization *in vivo*. Analysis of CE using ^{3}H-

---

***Corresponding author:** Carlos Rogério Figueiredo, Tel: + 55 (11) 5084-2991, Fax: + 55 (11) 5571-5877, Email: c.figueiredo@unifesp.br

NMR (Nuclear magnetic resonance spectroscopy) as well as GC/MS (gas chromatography–mass spectrometry) indicated the presence of long-chain fatty alcohols (C_{20}, C_{22}, C_{26}), ketones (C_{17}, C_{19}) and an alkene (C_{22}) as the main compounds. The length of the alkyl chains may play an important role in eliciting the biological activity of these molecules.[13] Their unsuspected antitumor activity adds to several other properties of these compounds as insect repellents (USPatent 4774082), antiviral agents, neurotrophic factors, waxes for thermal insulation.[14-16]

Materials and Methods

Plant materials and extraction

Leaves of *K. coriacea* were collected in the Cerrado area in the city of Patos de Minas-MG, Brazil (17°30.27'34"S and 45°31.21'17"W) in August 2008, and 2009. The plant was identified by MSc. Alice F. Amaral and a voucher specimen was deposited at the Mandevilla Herbarium, Centro Universitario de Patos de Minas (UNIPAM), No. MGHM0632-7. Hydroalcoholic (HA) and ethyl acetate (EA) extracts were obtained from 50 g of powdered leaves macerated in 250 mL of ethanol (EtOH): H_2O 7:3 (v/v) for 3 h at 45°C. Chloroform (CE), hexane (HE) and heptane (HP) were used to obtain extracts from 20 g of powdered leaves. Triplicate extractions were carried out with 200-mL of each solvent with stirring for 2 h at room temperature. Stock solutions were prepared with the dry residues diluted in dimethylsulfoxide at 10 mg/ml. The yield of extraction of leaf plant compounds with chloroform was higher than with dichloromethane, therefore chloroform was chosen in the subsequent extractions.

Chemical analysis

^{1}H-NMR spectra were recorded at 300 MHz in a Bruker DPX300 spectrometer, using $CDCl_3$ as solvent and TMS (tetramethylsilane) as internal standard. GC–MS analysis was performed at 70 eV in a INCOS 50 Finnigan-Mat-quadrupole spectrometer, using a capillary column (DB-5) coated with crosslinked methyl silicone gum (50 m, 0.20 mm i.d., film thickness 0.33 □m). The temperature program was 100°C isothermal for 1 min, then 100–280°C at 10°C/min, and isothermal at 280°C for 20 min. The temperatures of injection and detection were 250 and 280°C, respectively.

Cell lineages and mice

The following cell lineages were used: murine melanoma (B16F10-Nex2), a subclone of B16F10, deposited at BCRJ no. 0342; human colon carcinoma (HCT); human cervical cancer (Siha); human melanoma (A2058, SKmel28 and MeWO) all obtained from the Ludwig Institute for Cancer Research (LICR), São Paulo branch. Cells were cultivated as previously described.[17]

In vitro cytotoxicity and proliferation assays

K. coriacea extracts and specifically CE, diluted in RPMI medium with 1% DMSO (10 to 40 µg/ ml) were incubated with B16F10-Nex2 cells or human tumor cells (10^4 cells) in 96-well plates in a final volume of 100 µL for 24 h for cell cytotoxicity assay. For cell proliferation assay, 5 x 10^3 B16F10-Nex2 cells were incubated with 20 and 10 µg/ml of CE in a final volume of 100 µL for 24 h, 48 h and 72 h. Positive controls were carried out with doxorubicin, and negative controls with 1% DMSO supplemented RPMI medium. Cell viability was quantified using the MTT-based Cell Proliferation Kit I (SIGMA). Readings were made in a plate reader at 570 nm. Alternatively, the Trypan Blue exclusion method was also used. All experiments were performed in triplicate.

Wound healing assay

B16F10-Nex2 cells ($3x10^5$) were seeded in 12-well plates and incubated over-night with a sublethal dose of CE (10 µg/ml). Wounds were made on tumor cell monolayers with a pipette tip, and images were captured at 0, 3, 8 and 24 h during cell migration and gap filling. Images of CE treated cells were compared with control cell images for quantification of cell migration ratio.

Cell cycle analysis

Tumor cells ($1x10^6$) were incubated with 20 µg/ml of CE for 24 hours. Cells were trypsinized and centrifuged at 1000 rpm for 5 minutes. Pellets were suspended in 1 ml of ethanol 70% for fixation and incubated in ice for 15 minutes. Cells were centrifuged at 1000 rpm for 5 min and suspended in 500 µL of PI (propidium iodide) solution containing 50 µg/ml PI, 0.1 mg/ml RNase A and 0.05% Triton X-100, for 40 min at 4 °C. Cells were pelleted and suspended in 500 µl phosphate-buffered saline (PBS) for analysis in a Facs CantoII flow cytometer (BD Biosciences). Data were analyzed with FlowJo software (Tree Star, Inc. Ashland, OR).

Melanoma metastasis assay

Mice were endovenously injected with $5x10^5$ B16F10-Nex2 cells in 100 µl of RPMI without bovine fetal serum (SFB) in the tail veins of syngeneic C57Bl6 mice. Three groups of 5 animals were challenged with tumor cells and daily treated with intraperitoneal (i.p.) doses of CE (0.1mg and 0.5 mg/100µl 1% DMSO-PBS) during fourteen consecutive days. After 15 days, the lungs were removed and inspected for metastatic colonization and their masses quantified.

Ethics statement

All necessary permits were obtained for the described field studies, granted by the State of São Paulo Research Support Foundation (FAPESP), Brazil. The Ethics Committee of Federal University of São Paulo approved the main Project submitted by the Experimental Oncology Unit, CEP 1234/2011.

Statistical analysis

The experiments were performed in triplicate and the values are expressed as means ± standard deviations (S.D.). Student's *t*-test was used for significance analyses, using GraphPad Prism 4.0 software (La Jolla, CA). $p<0.05$ was considered significant difference.

Results

Cytotoxicity study

The different *K coriacea* leaf organic extracts were tested in the various tumor cells. The chloroform extract (CE) was the most cytotoxic in B16F10-Nex2 cells with IC_{50} of 10.26 µg/ml (Table 1). CE cytotoxicity was also evaluated in different tumor cells and non- tumorigenic cell lines (Figure 1A), and IC_{50} values are shown in Table 2 after 24 h of incubation. The positive control was run with doxorubicin at IC_{50} 0.03 µg/ml in B16F10-Nex2 cells. We observed that CE induced tumor cell death at 40 µg/ml, as shown by Trypan Blue staining, suggesting a cytostatic effect of CE at concentrations lower than 40 µg/ml. B16F10-Nex2 cells incubated with subdoses of CE at 10 and 20 µg/ml, showed growth inhibition after 48 h and 72 h (Figure 1B), but the cells which showed morphological alterations did not stain with Trypan blue.

Table 1. Cytotoxic activity of different *K.coriacea* leaf extracts in B16F10-Nex2 cells *in vitro*.

K.coriacea **leaf extracts**	**IC_{50} (µg/ml)**
HA	> 100
EA	> 100
CE	10.26
HE	95.33
HP	> 100
Doxorubicin	0.03

HA – Hydroalcoholic extract / EA – Ethyl acetate extract / CE – Chloroform extract
HE – Hexane extract / HP – Heptane extract

CE interferes in the cell cycle of murine melanoma cells

The CE prolonged the S phase delaying the cell cycle kinetics in melanoma cells. Treated cells showed increased cytoplasmic area (Figure 2). This experiment was run with $1x10^6$ B16F10-Nex2 cells incubated with 20 µg/ml of CE for 24 h and cells were processed as described in methods. Interference in the cell cycle at sublethal concentrations explains the growth inhibition shown in Figure 1.

CE inhibits migration of murine melanoma cells

The migration of B16F10-Nex2 cells using the wound-healing assay was significantly inhibited after 8 and 24 h of incubation with 10 µg/ml of CE ($p < 0.05$) (Figure 3).

CE anti-metastatic activity in a syngeneic melanoma system

C57Bl6 mice were endovenously challenged with $1x10^6$ B16F10-Nex2 cells and intraperitoneally (i.p) treated with a daily dose of CE during 14 days. We observed that CE induced significant protection in mice treated with 0.5 mg ($p < 0.05$) rather than with 0.1 mg doses of CE (Figure 4A). The tumor mass values were calculated by subtracting the average mass value (20 mg) of normal lung from the lung mass values of treated animals (Figure 4B). Treated animals had no weight loss or other signs of toxicity during the experiment.

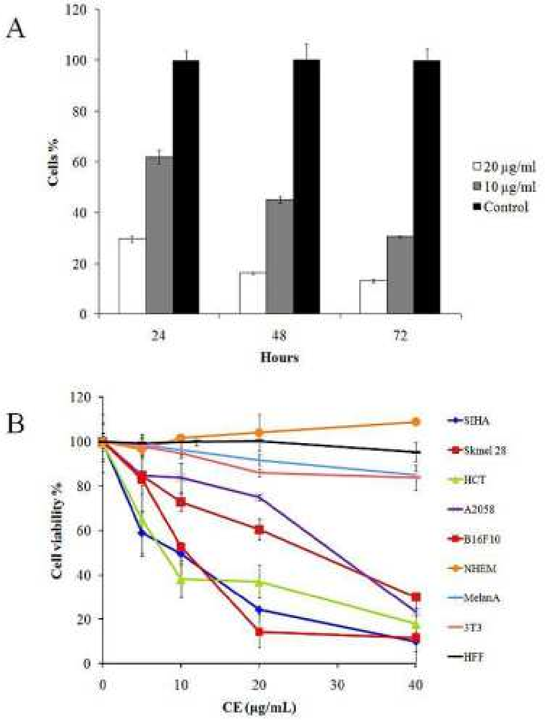

Figure 1. Cytotoxic effects of *K. coriacea* chloroform extract (CE). (A) B16F10-Nex2 cell growth after incubation with low concentrations of CE (10 and 20 µg/ml) compared to the untreated control, for 24, 48 and 72 hours; **(B)** Cytotoxic activity of CE in different cell lines. CE was incubated with 10^4 viable cells at concentrations ranging from 0 to 40 µg/ml for 24 h. Cell viability was determined by the MTT method.

Table 2. IC50 values obtained for CE in different cancer cell lines and non-tumorigenic cell lines.

Cell line	**-**	**IC_{50} (µg/ml)**	**SD**
Siha	Human cervix carcinoma	6.90	1.21
HCT	Human colon carcinoma	6.88	1.42
SKMel 28	Human melanoma	42.05	0.53
MeWo	Human melanoma	34.26	3.56
A2058	Human melanoma	26.80	3.54
B16F10-Nex2	Murine melanoma	10.26	0.68
3T3	Murine embryo fibroblast	> 100	2.90
Melan A	Murine melanocyte	> 100	3.28
NHEM	Normal human epidermal melanocyte	> 100	3.26
HFF	Human foreskin fibroblast	> 100	2,79

IC50 - half maximal inhibitory concentration
SD – Standard deviation

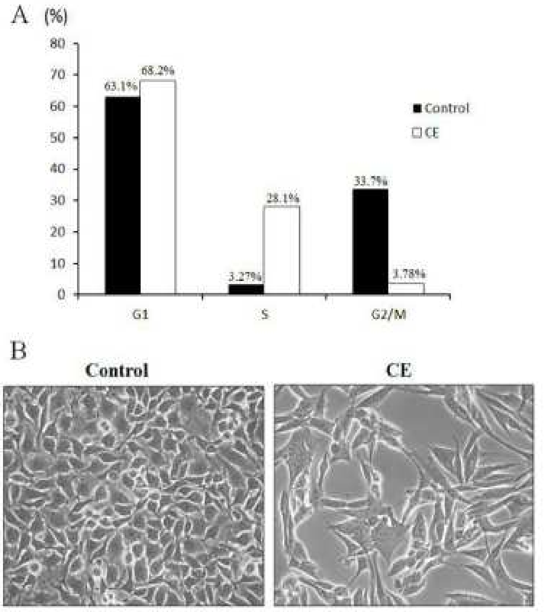

Figure 2. CE effects on melanoma cell cycle. (A) Cell cycle analysis of B16F10-Nex2 cells incubated with 20 µg/ml of CE for 24 h.; **(B)** Representative images of tumor cell morphology following CE treatment for 24h. Magnification, x200.

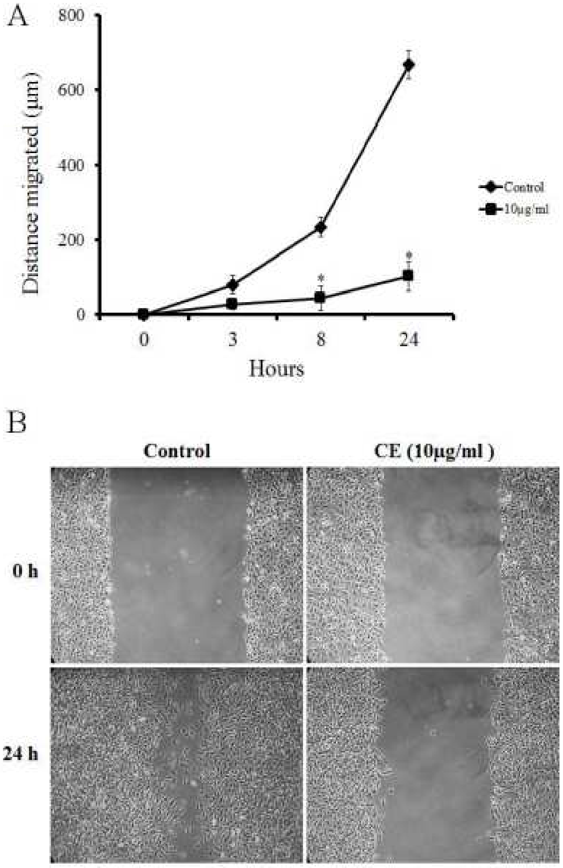

Figure 3. B16F10-Nex2 cell migration during incubation with CE at 10 µg/ml (A) Migration of tumor cells for 24 h. Statistical analysis was performed and data was plotted as the mean ± standard deviation (SD) (*$p < 0.05$ vs. control); **(B)** Migration of CE-treated tumor cells. Magnification, x100.

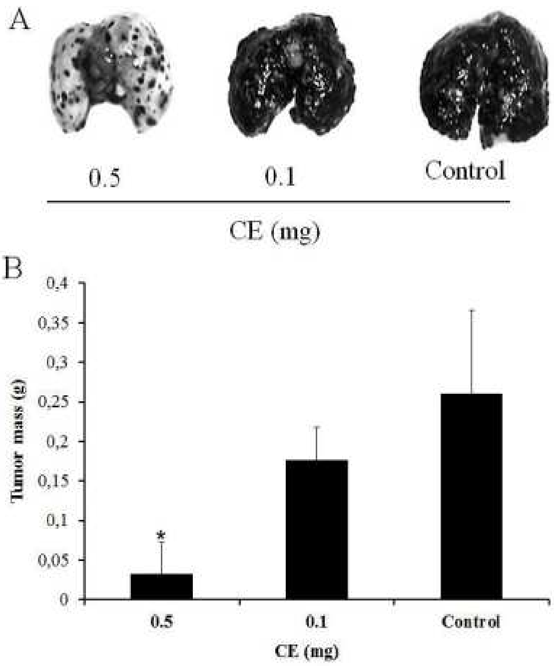

Figure 4. *In vivo* protection of CE against metastatic melanoma. (A) Representative mouse lungs after treatment with CE; **(B)** Tumor mass from mice treated with 0.1 mg and 0.5 mg of CE and vehicle (1% dimethylsulfoxide - DMSO in phosphate-buffered saline - PBS) intraperitoneally during 14 consecutive days (*$p < 0.05$ vs. control).

Chemical analysis of CE extract

The ^{1}H NMR spectrum of crude CE extract from *K. coriacea* showed an intense broad singlet at δ 1.2 and a deformed triplet at δ 0.8 (J = 7.0 Hz). These signals, associated with the presence of multiplets at δ 5- 6 ppm, indicated the occurrence of long side chain unsaturated hydrocarbon derivatives as major derivatives in this active group.[18] Additionally, several signals at δ 3-4 ppm as well as at δ 2-3 ppm were detected, which suggested the occurrence of alcohol and ketone derivatives as well. Aiming at the identification of these components, the crude extract was analyzed by GC-MS, which allowed the identification of six main fatty compounds (Table 3). ^{1}H NMR spectrum, GC and MS spectra of CE main compounds are shown in Figure 5. Compounds are grouped in three different classes: alkene: 1-docosene (16.59%); alcohols: 1-eicosanol (18.46%), 1-docosanol (19.80%), and 1-hexacosanol (13.38%); and ketones: 2-heptadecanone (11.63%) and 2-nonadecanone (20.12%). The characterization of these compounds was based on the mass spectra as well as on the retention times in a DB-5 column.

Discussion

CE cytotoxicity was evaluated since, according to the American National Cancer Institute, the IC_{50} limit for the cytotoxicity of a crude extract that requires further purification is 30 µg/ml.[19] Previous work has already demonstrated the antitumor potential of the hexane extract from the root bark of *K. coriacea*, particularly against MDA-MB-435 melanoma cells.[7-9] Our present data demonstrate the cytotoxic activity of *K coriacea* leaf extracts, showing that the chloroform extract (CE) is the most active *in vivo* and *in vitro* against melanoma and other human tumor cell lines.

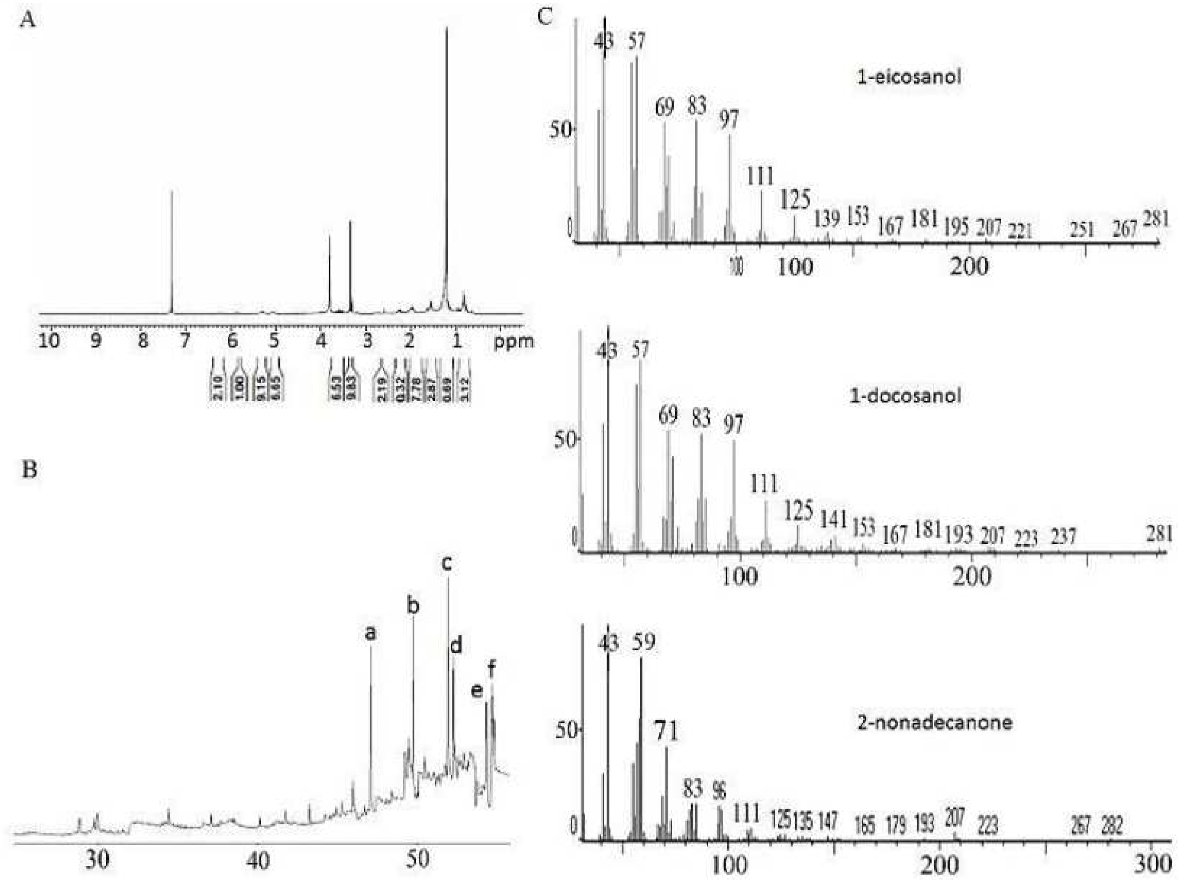

Figure 5. Analyses of CE chemical constituents. (A) ^{1}H NMR spectrum depicted an intense broad singlet at δ 1.2 and a deformed triplet at δ 0.8 ppm; **(B)** GC of CE chloroform extract showing peaks *a*: 1-docosene, *b*: 1-eicosanol, *c*: 1-docosanol, *d*: 2-heptadecanone, *e*: 2-nonadecanone, *f*: 1-hexacosanol); **(C)** MS spectra of the main compounds.

Table 3. Fatty compounds identified in CE.

Rt / min	Molecular formula		Relative amount (%)
47.1	$CH_3(CH_2)_{19}CH{=}CH_2$	(1-docosene)	16.59
49.8	$CH_3(CH_2)_{18}CH_2OH$	**(1-eicosanol)**	**18.46**
51.9	$CH_3(CH_2)_{20}CH_2OH$	**(1-docosanol)**	**19.80**
52.3	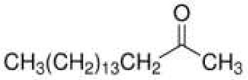 $CH_3(CH_2)_{13}CH_2C(=O)CH_3$	(2-heptadecanone)	11.63
54.4	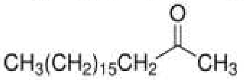 $CH_3(CH_2)_{15}CH_2C(=O)CH_3$	**(2-nonadecanone)**	**20.12**
54.7	$CH_3(CH_2)_{24}CH_2OH$	(1-hexacosanol)	13.4

High concentrations of CE (40 µg/ml) caused cytoplasmic swelling in B16F10-Nex2 melanoma cells, bleb formation and cell lysis thus suggesting both apoptosis and necrosis.[20] The genomic DNA in CE treated cells showed degradation in a ladder pattern (data not shown). Such morphological alterations were not observed at lower CE concentrations. CE was not significantly cytotoxic in non-tumorigenic cells, such as human and murine fibroblasts and melanocytes. The arrest in the S phase of tumor cells as observed in the present work, led to proliferation inhibition and apoptosis, as previously reported [21-24]

Cancer cells lack the growth control of normal cells, exhibiting unlimited self-sufficient replication.[25,26] For therapeutic effectiveness, drugs are being developed that act as biological modifiers, regulating the cell cycle and promoting cell death.[20] Plant derived compounds have been reported to induce cell cycle arrest and cell death in many tumor cell lines.[27-32] The present study reports on the delay of the cell cycle kinetics at the S phase, significantly reducing the G2/M phase, by *K. coriacea* leaf chloroform extract.

K. coriacea CE inhibited B16F10-Nex2 cell migration *in vitro* and protected against lung metastasis *in vivo.* Migration and invasion are essential steps in cancer cell metastasis.[33] Similar effects have been reported in many plant derived extracts and purified compounds that inhibit cancer cell migration.[34-38]

The previous analysis of hexane extracts from root and bark of *K. coriacea* described δ-tocotrienol, its dimeric derivative,[3] and xanthones in the dichloromethane fraction.[12] *K.coriacea* xanthones were shown to exert antimicrobial activities against *Staphylococcus aureus* at 50 µg/ml,[39] the plant pathogenic fungus *Cladosporium cucumerinum* and also *Candida albicans*.[40] A trypanocidal activity has also been described for *K.coriacea* xanthones.[41]

Presently, we show that the chloroform extract from leaves of *K. coriacea* have long-chain fatty compounds. The alkene 1-docosene, the alcohols 1-eicosanol, 1-docosanol and 1-hexacosanol, and the ketones 2-heptadecanone and 2-nonadecanone were identified. With chain lengths of C20 to C36,[42] these compounds constitute leaf cuticular waxes that may differ widely among species.[43,44] Genetic studies in *Arabidopsis* clarified the fatty acid elongation steps and the subsequent modification of the elongated products into primary alcohols, wax esters, secondary alcohols, and ketones, disclosing the enzymes involved in these pathways.[45] Fatty acid derivatives can act as signaling molecules, modulating normal and disease-related phenotypes in animals,[46] and display antimicrobial and anticarcinogenic activity [47]. One of these long chain hydrocarbon derivatives has already been characterized in plant extracts with antitumor activity, the 1-eicosanol, a component of the acetate fraction of *Leea indica* that inhibits growth of various cancer cell lines.[48]

Regarding ketones (C17, C19) and C22 alkene found in CE, there are still no data on the mechanism of action of these compounds against tumor cells. Apparently, the length of the alkyl group[13] and the hydrophobicity are related to their biological activities.[49] Previous work has shown that some long-chain fatty alcohols and their derivatives may act on mitochondria, inhibiting both tumor cell growth *in vitro* and the growth of B16 melanoma *in vivo.* [50-54] Regarding the long-chain fatty alcohols found in CE (eicosanol, docosanol and hexacosanol), they were found in plant extracts and fractions cytotoxic to tumor cell lines *in vitro.* [55] Recently, the activity of mixtures of long-chain alcohols (C26-C32), such as octacosanol, hexacosanol, heptacosanol, eicosanol and many others, derived most commonly from the wax of natural sources[56] and are similar to CE long-chain alcohols mixture has been studied. Antitumor properties have been described, such as inhibition of angiogenesis and metastasis *in vitro* and *in vivo*, by inhibition of matrix metalloproteinases activity (MMPs) and translocation of Nf-kB to nucleus.[57] Further studies are needed to clarify the mechanism of action of these compounds on tumor cells.

Conclusion

In the present work we describe the *in vitro* and *in vivo* antitumor activity of the chloroform extract (CE) of leaves from *K. coriacea* containing long-chain fatty alcohols, ketones and an alkene. The CE delayed the melanoma cell cycle with morphological alterations and inhibited tumor cell migration *in vitro.* CE growth inhibition *in vitro* was shown in murine melanoma B16F10-Nex2 and a few human tumor cell lineages. CE exerted *in vivo* protection effect using a syngeneic metastatic melanoma model with a significant reduction in the number of lung tumor nodules. It is still unclear whether any single fatty compound in the mixture, or a combination of constituents may reproduce the antitumor effects of the CE extract.

Acknowledgements

The authors thank FAPESP and CNPq for the financial support of this work.

Conflict of Interest

There is no conflict of interest to be reported.

References

1. Araujo JF, De Castro AP, Costa MM, Togawa RC, Junior GJ, Quirino BF, et al. Characterization of soil bacterial assemblies in Brazilian savanna-like vegetation reveals acidobacteria dominance. *Microb Ecol* 2012;64(3):760-70.
2. Badisa RB, Chaudhuri SK, Pilarinou E, Rutkoski NJ, Hare J, Levenson CW. Licania michauxii Prance root extract induces hsp 70 mRNA and necrotic cell death in cultured human hepatoma and colon carcinoma cell lines. *Cancer Lett* 2000;149(1-2):61-8.
3. De Mesquita ML, Araujo RM, Bezerra DP, Filho RB, De Paula JE, Silveira ER, et al. Cytotoxicity of delta-tocotrienols from Kielmeyera coriacea against cancer cell lines. *Bioorg Med Chem* 2011;19(1):623-30.
4. Myers N, Mittermeier RA, Mittermeier CG, Da Fonseca GA, Kent J. Biodiversity hotspots for conservation priorities. *Nature* 2000;403(6772):853-8.
5. Rios JL, Recio MC. Medicinal plants and antimicrobial activity. *J Ethnopharmacol* 2005;100(1-2):80-4.
6. Braga FG, Bouzada ML, Fabri RL, De OMM, Moreira FO, Scio E, et al. Antileishmanial and

antifungal activity of plants used in traditional medicine in Brazil. *J Ethnopharmacol* 2007;111(2):396-402.

7. Hiruma-Lima CA, Santos LC, Kushima H, Pellizzon CH, Silveira GG, Vasconcelos PC, et al. Qualea grandiflora, a Brazilian "Cerrado" medicinal plant presents an important antiulcer activity. *J Ethnopharmacol* 2006;104(1-2):207-14.
8. De Mesquita ML, De Paula JE, Pessoa C, De Moraes MO, Costa-Lotufo LV, Grougnet R, et al. Cytotoxic activity of Brazilian Cerrado plants used in traditional medicine against cancer cell lines. *J Ethnopharmacol* 2009;123(3):439-45.
9. Alves TM, Silva AF, Brandao M, Grandi TS, Smania E, Smania Junior A, et al. Biological screening of Brazilian medicinal plants. *Mem Inst Oswaldo Cruz* 2000;95(3):367-73.
10. Obici S, Otobone FJ, Da Silva Sela VR, Ishida K, Da Silva JC, Nakamura CV, et al. Preliminary toxicity study of dichloromethane extract of Kielmeyera coriacea stems in mice and rats. *J Ethnopharmacol* 2008;115(1):131-9.
11. Sela VR, Hattanda I, Albrecht CM, De Almeida CB, Obici S, Cortez DA, et al. Effect of xanthone from Kielmeyera coriacea stems on serotonergic neurons of the median raphe nucleus. *Phytomedicine* 2010;17(3-4):274-8.
12. Biesdorf C, Cortez DA, Audi EA. Assessment of anxiolytic and panicolytic effects of dichloromethane fraction from stems of Kielmeyera coriacea. *Phytomedicine* 2012;19(3-4):374-7.
13. Kubo I, Fujita K, Nihei K. Anti-Salmonella activity of alkyl gallates. *J Agric Food Chem* 2002;50(23):6692-6.
14. Treister NS, Woo SB. Topical n-docosanol for management of recurrent herpes labialis. *Expert Opin Pharmacother* 2010;11(5):853-60.
15. Borg J. The neurotrophic factor, n-hexacosanol, reduces the neuronal damage induced by the neurotoxin, kainic acid. *J Neurosci Res* 1991;29(1):62-7.
16. Greer S, Wen M, Bird D, Wu X, Samuels L, Kunst L, et al. The cytochrome P450 enzyme CYP96A15 is the midchain alkane hydroxylase responsible for formation of secondary alcohols and ketones in stem cuticular wax of Arabidopsis. *Plant Physiol* 2007;145(3):653-67.
17. Matsuo AL, Figueiredo CR, Arruda DC, Pereira FV, Scutti JA, Massaoka MH, et al. alpha-Pinene isolated from Schinus terebinthifolius Raddi (Anacardiaceae) induces apoptosis and confers antimetastatic protection in a melanoma model. *Biochem Biophys Res Commun* 2011;411(2):449-54.
18. Moreira IC, Roque NF, Contini K, Lago JHG. Sesquiterpenos e hidrocarbonetos dos frutos de *Xylopia emarginata* (Annonaceae). *Rev Bras Farmacognosia* 2007;17(1):55-8.
19. Suffness M, Pezzuto JM. Assays related to cancer drug discovery. In: Hostettmann K, editor. Methods in plant biochemistry: assays for bioactivity. London: Aacademic press; 1991.
20. Kroemer G, Galluzzi L, Vandenabeele P, Abrams J, Alnemri ES, Baehrecke EH, et al. Classification of cell death: recommendations of the Nomenclature Committee on Cell Death 2009. *Cell Death Differ* 2009;16(1):3-11.
21. Li L, Chen DB, Lin C, Cao K, Wan Y, Zhao XY, et al. hPNAS-4 inhibits proliferation through S phase arrest and apoptosis: underlying action mechanism in ovarian cancer cells. *Apoptosis* 2013;18(4):467-79.
22. Chen T, Wong YS. Selenocystine induces S-phase arrest and apoptosis in human breast adenocarcinoma MCF-7 cells by modulating ERK and Akt phosphorylation. *J Agric Food Chem* 2008;56(22):10574-81.
23. Yu YH, Kuo HP, Hsieh HH, Li JW, Hsu WH, Chen SJ, et al. Ganoderma tsugae Induces S Phase Arrest and Apoptosis in Doxorubicin-Resistant Lung Adenocarcinoma H23/0.3 Cells via Modulation of the PI3K/Akt Signaling Pathway. *Evid Based Complement Alternat Med* 2012;2012:371286.
24. Joe AK, Liu H, Suzui M, Vural ME, Xiao D, Weinstein IB. Resveratrol induces growth inhibition, S-phase arrest, apoptosis, and changes in biomarker expression in several human cancer cell lines. *Clin Cancer Res* 2002;8(3):893-903.
25. Hartwell LH, Kastan MB. Cell cycle control and cancer. *Science* 1994;266(5192):1821-8.
26. Vermeulen K, Van Bockstaele DR, Berneman ZN. The cell cycle: a review of regulation, deregulation and therapeutic targets in cancer. *Cell Prolif* 2003;36(3):131-49.
27. Zhang Y, Li Q, Ge Y, Chen Y, Chen J, Dong Y, et al. Silibinin triggers apoptosis and cell-cycle arrest of SGC7901 cells. *Phytother Res* 2013;27(3):397-403.
28. Geethangili M, Rao YK, Fang SH, Tzeng YM. Cytotoxic constituents from Andrographis paniculata induce cell cycle arrest in jurkat cells. *Phytother Res* 2008;22(10):1336-41.
29. Nadova S, Miadokova E, Mucaji P, Grancai D, Cipak L. Growth inhibitory effect of ethyl acetate-soluble fraction of Cynara cardunculus L. in leukemia cells involves cell cycle arrest, cytochrome c release and activation of caspases. *Phytother Res* 2008;22(2):165-8.
30. Du B, Zhong X, Liao X, Xu W, Zhou X, Xu S. A new antitumor arabinopyranoside from Laurencia majuscula induces G2/M cell cycle arrest. *Phytother Res* 2010;24(10):1447-50.
31. Kim SJ, Min HY, Lee EJ, Kim YS, Bae K, Kang SS, et al. Growth inhibition and cell cycle arrest in the G0/G1 by schizandrin, a dibenzocyclooctadiene lignan isolated from Schisandra chinensis, on T47D human breast cancer cells. *Phytother Res* 2010;24(2):193-7.

32. Lee EJ, Kim WJ, Moon SK. Cordycepin suppresses TNF-alpha-induced invasion, migration and matrix metalloproteinase-9 expression in human bladder cancer cells. *Phytother Res* 2010;24(12):1755-61.
33. Friedl P, Wolf K. Tumour-cell invasion and migration: diversity and escape mechanisms. *Nat Rev Cancer* 2003;3(5):362-74.
34. Lee SJ, Park K, Ha SD, Kim WJ, Moon SK. Gleditsia sinensis thorn extract inhibits human colon cancer cells: the role of ERK1/2, G2/M-phase cell cycle arrest and p53 expression. *Phytother Res* 2010;24(12):1870-6.
35. Wang HM, Chiu CC, Wu PF, Chen CY. Subamolide E from Cinnamomum subavenium induces sub-G1 cell-cycle arrest and caspase-dependent apoptosis and reduces the migration ability of human melanoma cells. *J Agric Food Chem* 2011;59(15):8187-92.
36. Yang EJ, Lee JS, Yun CY, Ryang YS, Kim JB, Kim IS. Suppression of ovalbumin-induced airway inflammatory responses in a mouse model of asthma by Mimosa pudica extract. *Phytother Res* 2011;25(1):59-66.
37. Mojzisova G, Mojzis J, Pilatova M, Varinska L, Ivanova L, Strojny L, et al. Antiproliferative and antiangiogenic properties of horse chestnut extract. *Phytother Res* 2013;27(2):159-65.
38. Kim EJ, Hong JE, Lim SS, Kwon GT, Kim J, Kim JS, et al. The hexane extract of Saussurea lappa and its active principle, dehydrocostus lactone, inhibit prostate cancer cell migration. *J Med Food* 2012;15(1):24-32.
39. Cortez DAG, Filho BAA, Nakamura CV, Filho BPD, Marston A and Hostettman K. Antibacterial Activity of a Biphenyl and Xanthones from *Kielmeyera coriacea*. *Pharma Biol* 2002;40(7):485-489
40. Cortez DAG, Young MCM, Marston A, Wolfender JL, Hostettmann K. Xanthones, triterpenes and a biphenyl from *Kielmeyera coriacea*. *Phytochemistry* 1998;47(7):1367–1374.
41. Caleare Ade O, Lazarin-Bidoia D, Cortez DA, Ueda-Nakamura T, Dias Filho BP, Silva Sde O, et al. Trypanocidal activity of 1,3,7-trihydroxy-2-(3-methylbut-2-enyl)-xanthone isolated from Kielmeyera coriacea. *Parasitol Int* 2013;62(5):405-11.
42. Pacini E, Guarnieri M, Nepi M. Pollen carbohydrates and water content during development, presentation, and dispersal: a short review. *Protoplasma* 2006;228(1-3):73-7.
43. Post-Beittenmiller D. Biochemistry and Molecular Biology of Wax Production in Plants. *Annu Rev Plant Physiol Plant Mol Biol* 1996;47:405-30.
44. Millar AA, Clemens S, Zachgo S, Giblin EM, Taylor DC, Kunst L. CUT1, an Arabidopsis gene required for cuticular wax biosynthesis and pollen fertility, encodes a very-long-chain fatty acid condensing enzyme. *Plant Cell* 1999;11(5):825-38.
45. Samuels L, Kunst L, Jetter R. Sealing plant surfaces: cuticular wax formation by epidermal cells. *Annu Rev Plant Biol* 2008;59:683-707.
46. Cury-Boaventura MF, Curi R. Regulation of reactive oxygen species (ROS) production by C18 fatty acids in Jurkat and Raji cells. *Clin Sci (Lond)* 2005;108(3):245-53.
47. Dembitsky VM. Natural neo acids and neo alkanes: their analogs and derivatives. *Lipids* 2006;41(4):309-40.
48. Yau Hsiung W, Abdul Kadir H. Leea indica Ethyl Acetate Fraction Induces Growth-Inhibitory Effect in Various Cancer Cell Lines and Apoptosis in Ca Ski Human Cervical Epidermoid Carcinoma Cells. *Evid Based Complement Alternat Med* 2011;2011:293060.
49. Hansch C, Dunn WJ, 3rd. Linear relationships between lipophilic character and biological activity of drugs. *J Pharm Sci* 1972;61(1):1-19.
50. Scolaro MJ, Gunnill LB, Pope LE, Khalil MH, Katz DH, Berg JE. The antiviral drug docosanol as a treatment for Kaposi's sarcoma lesions in HIV type 1-infected patients: a pilot clinical study. *AIDS Res Hum Retroviruses* 2001;17(1):35-43.
51. Holliday MW, Jr., Cox SB, Kang MH, Maurer BJ. C22:0- and C24:0-dihydroceramides confer mixed cytotoxicity in T-cell acute lymphoblastic leukemia cell lines. *PLoS One* 2013;8(9):e74768.
52. Setzer WN, Vogler B, Schmidt JM, Petty JL, Haber WA. Isolation of cupanioside, a novel cytotoxic and antibacterial long-chain fatty alcohol glycoside from the bark of Cupania glabra. *Planta Med* 2005;71(7):686-8.
53. Voutquenne L, Lavaud C, Massiot G, Sevenet T, Hadi HA. Cytotoxic polyisoprenes and glycosides of long-chain fatty alcohols from Dimocarpus fumatus. *Phytochemistry* 1999;50(1):63-9.
54. Matsunaga H, Saita T, Nagumo F, Mori M, Katano M. A possible mechanism for the cytotoxicity of a polyacetylenic alcohol, panaxytriol: inhibition of mitochondrial respiration. *Cancer Chemother Pharmacol* 1995;35(4):291-6.
55. Piovano M, Chamy MC, Garbarino JA, Tita B, Vitalone A, Di Fabio A, et al. Cytotoxic activity of the root extract from Myoschilos oblongum. *Fitoterapia* 2003;74(5):497-500.
56. Banerjee S, Ghoshal S, Porter TD. Activation of AMP-kinase by policosanol requires peroxisomal metabolism. *Lipids* 2011;46(4):311-21.
57. Thippeswamy G, Sheela ML, Salimath BP. Octacosanol isolated from Tinospora cordifolia downregulates VEGF gene expression by inhibiting nuclear translocation of NF-<kappa>B and its DNA binding activity. *Eur J Pharmacol* 2008;588(2-3):141-50.

PHCOG MAG. ORIGINAL ARTICLE

Pyrostegia venusta heptane extract containing saturated aliphatic hydrocarbons induces apoptosis on B16F10-Nex2 melanoma cells and displays antitumor activity *in vivo*

Carlos R. Figueiredo, Alisson L. Matsuo, Felipe V. Pereira, Aline N. Rabaça, Camyla F. Farias, Natália Girola, Mariana H. Massaoka, Ricardo A. Azevedo, Jorge A.B. Scutti, Denise C. Arruda, Luciana P. Silva[1], Elaine G. Rodrigues, João Henrique G. Lago[2], Luiz R. Travassos, Regildo M.G. Silva[1]

Departments of Microbiology, Immunology and Parasitology, Cell Biology Division and Experimental Oncology Unit (UNONEX), Federal University of São Paulo (UNIFESP), São Paulo, SP, [1]Department of Biological Sciences, Phytochemistry Laboratory, Universidade Estadual Paulista (UNESP), Assis, São Paulo State, [2]Institute of Environmental, Chemical and Pharmaceutical Sciences, Federal University of São Paulo (UNIFESP), Diadema, São Paulo, Brazil

Submitted: 19-08-2013 Revised: 25-09-2013 Published: ****

ABSTRACT

Background: *Pyrostegia venusta* (Ker. Gawl.) Miers (Bignoniacea) is a medicinal plant from the Brazilian Cerrado used to treat leucoderma and common diseases of the respiratory system. **Objective:** To investigate the antitumor activity of *P. venusta* extracts against melanoma. **Materials and Methods:** The cytotoxic activity and tumor induced cell death of heptane extract (HE) from *P. venusta* flowers was evaluated against murine melanoma B16F10-Nex2 cells *in vitro* and in a syngeneic model *in vivo*. **Results:** We found that HE induced apoptosis in melanoma cells by disruption of the mitochondrial membrane potential, induction of reactive oxygen species and late apoptosis evidenced by plasma membrane blebbing, cell shrinkage, chromatin condensation and DNA fragmentation, exposure of phosphatidylserine on the cell surface and activation of caspase-2,-3,-8,-9. HE was also protective against singeneyc subcutaneous melanoma HE compounds were also able to induce cell cycle arrest at G2/M phases on tumor cells. On fractionation of HE in silica gel we isolated a cytotoxic fraction that contained a mixture of saturated hydrocarbons identified by ^{1}H NMR and GC-MS analyses. Predominant species were octacosane ($C_{28}H_{58}$-36%) and triacontane ($C_{30}H_{62}$-13%), which individually showed significant cytotoxic activity against murine melanoma B16F10-Nex2 cells *in vitro* and a very promising antitumor protection against subcutaneous melanoma *in vivo*. **Conclusion:** The results suggest that the components of the heptane extract, mainly octasane and triacontane, which showed antitumor properties in experimental melanoma upon regional administration, might also be therapeutic in human cancer, such as in the mostly epidermal and slowly invasive melanomas, such as acral lentiginous melanoma, as an adjuvant treatment to surgical excision.

Access this article online
Website:
www.phcog.com
DOI:
***
Quick Response Code:

Key words: Apoptosis, cytotoxicity, melanoma, *Pyrostegia venusta,* saturated hydrocarbons

INTRODUCTION

Malignant melanoma is a very aggressive form of skin cancer, with a mortality rate that has increased in 2% annually since 1960, making it a worldwide public health risk and the fastest growing of all cancer types.[1] Melanomas are usually removed by resection but are very difficult to cure in the metastatic form. Several strategies and combinations of anticancer drugs have been used in an effort to improve the therapeutic effect on malignant melanomas.[2] Solid tumor cells develop resistance to antineoplasic drugs and multidrug resistance is a major cause of chemotherapy failures of human cancer.[3]

Address for correspondence:
Dr. Carlos R. Figueiredo, Department of Microbiology, Immunology and Parasitology, Experimental Oncology Unit (UNONEX), Federal University of São Paulo (UNIFESP). Rua Botucatu 862, 8º andar, Vila Clementino, São Paulo, SP 04023-062, Brazil.
E-mail: c.figueiredo@unifesp.br

Among skin cancers, the acral lentiginous melanoma (ALM) is a variant occurring on volar surfaces of hands, feet, subungual site, fingers or toes and is characterized by slow

Chromatin condensation analysis

B16F10-Nex2 cells (1×10^4) were cultivated on round coverslips, treated with 50 μg/ml of HE for 18 h, washed in PBS and fixed for 30 min at room temperature with 2% formaldehyde. The cells were washed in PBS and stained with 2μM Hoechst 33342 (Invitrogen) for 15 min and analyzed by fluorescence microscopy (Olympus BX-51 fluorescence microscope with immersion oil, at 60X magnification).

DNA fragmentation assay

DNA fragmentation of tumor cells was analyzed by the Terminal Deoxynucleotidyl Transferase dUTP Nick end Labeling (TUNEL) assay. 5×10^4 B16F10-Nex2 cells were incubated with 50μg/ml HE for 18 h and then processed and analyzed as previously described.[29] Combretastatin A4 (CA4) was used at 150 μM as positive controle of DNA fragmentation. Alternatively, DNA fragmentation was accessed by electrophoresis. 1×10^6 B16F10-Nex2 cells were incubated with 50μg/ml of HE at 37°C for 24 h and then genomic DNA were extracted from the cells, processed and analyzed as previously described.[30]

Annexin V and propidium iodide labeling

B16F10-Nex2 (3×10^5) cells were grown for 24 h in a 12-well plate and further incubated with 25 and 12μg/ml of HE or RPMI medium for 1 or 2 h at 37°C. The cells were harvested with cold PBS after three washes in the same buffer. Apoptotic cells were analyzed using the ApoScreen Annexin V-FITC kit according to the manufacturer's instructions (Southern Biotechnology, Birmingham, AL). Positive annexin V (AV) and propidium iodide cells were detected on an inverted fluorescence microscope (Olympus IX70) at 100X magnification.

Detection of caspase activity

The activity of caspases induced by HE was assessed using the *ApoTarget*™ Caspase Colorimetric Protease Assay Kit (Invitrogen, Carlsbad, CA) according to the manufacturer's protocol. 1×10^7 B16F10-Nex2 cells were seeded in 6-well plates and treated with 50 μg/ml of HE for 18 h. Briefly, cells were harvested and lysed in a lysis buffer for 10 min in ice. The lysate was centrifuged at 10,000*g* for 1 min, and 200 μg protein was incubated with 50 μl of the reaction buffer and 5 μl of the substrate, at 37°C for 2 h. The absorbance of the reaction mixture was quantified at 405 nm in a microplate reader (Spectramax M3, Molecular Devices).

N-acetylcysteine assay

B16F10-Nex2 cells (1×10^4) were seeded in 96-well plates for 6 h, pre-incubated with 10mM of N-acetylcysteine (NAC) for 2 h, washed twice in PBS and incubated with 50 μg/ml of HE for 18h at 37°C. In the control group, tumor cells were pre-incubated with RPMI. Cell viability was determined by Trypan blue (Gibco, Grand Island, NY) exclusion test.

Enhanced superoxide anion production

Enhanced superoxide anion production was detected by dihydroethidium (DHE) assay (Invitrogen) performed according to manufacturer's instructions. B16F10-Nex2 cells (5×10^4) were cultivated in 24-well plates and treated with 25 and 12 μg/ml of HE for 18 h. The cells were incubated with 5 μM DHE at 37°C for 30 min. For positive staining control, cells were treated with 5mM hydrogen peroxide for 30 min. Negative controls were treated with RPMI medium. The conversion of DHE to ethidium by oxidation was observed by fluorescence microscopy with an inverted fluorescence microscope (Olympus IX70) at 20X magnification.

Assessment of mitochondrial membrane potential ($\Delta\Psi m$)

B16F10-Nex2 (1×10^5) cells were grown for 24 h in a 12-well plate and were incubated with 25 and 12 μg/ml HE at 37°C for 18 h. Cells were gently washed in PBS and loaded with 20nM of tetramethylrhodamine ethyl ester (TMRE, Molecular Probes, OR) for 10 min at 37°C. Cells were immediately observed with the aid of an inverted fluorescence microscope (Olympus I x 70) at 20X magnification.

Cell cycle analysis

B16F10-Nex2 (3×10^5) cells were incubated with 25 μg/ml of HE for 24 h. Cells were washed three times in PBS and pelleted at 1,500 rpm for 5 min. Cells were suspended and fixed in 2.5 ml ethanol (70% in PBS) for 15 min in ice. Cells were pelleted and suspended in 500 μl of PI solution in PBS (50 μg/ml propidium iodide, 0.1mg/ml RNase A and 0.05% Triton X-100) for 40 min at 4°C. Cells were pelleted and suspended in 500μl PBS for flow analysis on a Facs CantoII flow cytometer (BD Biosciences). Data were analyzed by Flowjo software (Tree Star, Inc. Ashland, OR).

Peritumor treatment of subcutaneously grafted murine melanoma

Six-week-old male C57BL/6 mice obtained from the Center for Development of Experimental Models (CEDEME), Federal University of São Paulo (UNIFESP) (average weight of 25-28g), were subcutaneously injected with 5×10^4 B16F10-Nex2 tumor cells. Peritumor injections were given starting 24 h after tumor cell graft. Treated groups (5 animals per group) received daily doses of 400μg of HE or 500μg of alkanes and the control groups received 5% DMSO in PBS (HE control) or 0.1% hexane, 5% DMSO in PBS (alkanes control). The use of 5% DMSO as vehicle was based on previous *in vivo* protocols were carried out using protocols approved by the Ethics Committee for Animal Experimentation of Federal University of São Paulo, Brazil and the specific Project presented by the Experimental Oncology Unit, including the animal experiments herein reported, has been approved via doc by Ethics and Research Committee (CEP) under the number 1234/2011.

Plant material and extraction procedure

Flowers of Pyrostegia venusta (Miers) (Bignoniaceae) were collected at Patos de Minas county, Minas-MG (18°31’40.34”S e 46°32’19.75”W). The plant material was identified by MSc. Alice de Fátima Amaral and a voucher specimen was deposited in the Mandevilla Herbarium at the Centro Universitario de Patos de Minas (UNIPAM) under the number MGHM0430. The hydroalcoholic extract (HA) was obtained from 50g of powdered flowers macerated in 250mL of EtOH: H_2O 7:3 (v/v) for 3 h at 60°C. Chloroform (CE) or heptane (HE) extracts were obtained from 20g of powdered flowers extracted three times with 200mL of heptane or chloroform with stirring for 2 h at room temperature. The extracts were filtered, dried under pressurized nitrogen and stored at-20°C. The dry extracts were reconstituted with 100% (v/v) dimethylsulfoxide (DMSO) to prepare a stock solution at a concentration of 10 mg/ml., Bioguided fractionation of crude heptane extract (HE).

Part of a crude heptane extract (HE) from flowers of *P. venusta* (600mg) was subjected to silica gel column chromatography eluted with hexane containing increasing amounts of ethyl acetate (up to 100%), to give 54 samples that were pooled into five fractions (HEF1-HEF7) after Thin Layer Chromatography (TLC) analysis. The different fractions were tested for cytotoxicity using a murine melanoma (B16F10-Nex2) growth inhibition test. The cytotoxic potential of the heptane extract was detected only in the fraction pool HEF2 (12mg), therefore this was analyzed by ^{1}H NMR spectroscopy as well as GC-MS aiming at the identification of active compounds. The most abundant compounds found in HEF2, octacosane and triacontane were evaluated for their cytotoxic activity on tumor cells and were purchased from Santa Cruz Biotechnology, Inc (California, USA). Alkanes were diluted in Roswell Park Memorial Institute medium (RPMI-1640) with 0.1% n-hexane and 1% DMSO, vortexed and sonicated for 5 min for further incubation with 1 × 10^4 B16F10-Nex2 cells. Negative controls were performed with vehicle (0.1% n-hexane and 1% DMSO in RPMI-1640).

Nuclear magnetic resonance and GC-MS analysis

Silica gel (Merck 230-400 mesh) was used for column chromatography and silica gel 60 PF$_{254}$ (Merck) for analytical (0.25mm) TLC. Nuclear Magnetic Resonance (NMR) spectra were recorded at 200 MHz for ^{1}H nucleus on a Bruker AC200 spectrometer, using $CDCl_3$ as solvent and TMS (tetramethylsilane) as internal standard. GC-MS analysis was performed at 70 eV in an INCOS 50 Finnigan-Mat-quadrupole spectrometer, using a capillary column (DB-5) coated with crosslinked methyl silicone gum (50m, 0.20mm i.d., film thickness 0.33μm). The temperature program was 100°C isothermal for 1 min, then 100–280°C at 10°C/min, and isothermal at 280°C for 20 min. The temperature of injection and detection were 250 and 280°C, respectively.

Cell lines and culture

The following cell lines were used: human melanoma cell lines (SKMel 28 and A2058), originally provided by Dr. Alan N. Houghton of Memorial Sloan Kettering Cancer Center, NY; murine melanoma (B16F10-Nex2), a subclone of the B16F10 cell line obtained at the Experimental Oncology Unit (UNONEX), Federal University of São Paulo; human cervical cancer (HeLa), human umbilical vein endothelial cells (HUVEC), mouse fibroblasts (3T3) and human foreskin fibroblast (HF) cell lines were provided by Ludwig Institute for Cancer Research, São Paulo and Dr. Luiz F. Lima Reis, Hospital Sirio-Libanez, São Paulo, Brazil The U87-MG glioblastoma cell line was provided by Dr. Osvaldo K. Okamoto, University of São Paulo. Murine, syngeneic, colorectal adenocarcinoma cell (CT26) and murine pancreatic cells (PANC) were provided by Dr. Guillermo Mazzolini from the School of Medicine of Austral University, Derqui-Pilar, Buenos Aires, Argentina. Tumor cells were cultured at 37°C in a humidified atmosphere containing 5% CO_2, in RPMI 1640 medium (Invitrogen, Carlsbad, CA) supplemented with 10mM N-2-hydroxyethylpiperazine-N$_2$-ethanesulfonic acid (Hepes) (Sigma, St. Louis, MO), 24mM sodium bicarbonate (Sigma), 40mg/l gentamicin (Schering-Plough, São Paulo, Brazil), pH 7.2 and 10% fetal calf serum (Invitrogen). Human HF, mouse CT26 and 3T3 cells were maintained in DMEM supplemented as for the RPMI-1640 medium.

Cytotoxicity assay *in vitro*

P.venusta extracts and fractions were diluted in supplemented RPMI medium with 0.5% dimethyl sulfoxide (DMSO, SIGMA) and incubated with 5 × 10^3 or 1 × 10^4 murine and human tumor cells in 96-well plates. After a pre-incubation period (18 h), cell viability was assessed using the Cell Proliferation Kit I (MTT) (Boehringer Mannheim), a 3-(4,5-dimethylthiazol-2-yl)-2,5-diphenyltetrazolium bromide-based colorimetric assay. Readings were made in a plate reader at 570 nm. Alternatively, cell viability was accessed by the Trypan blue (Gibco, Grand Island, NY) exclusion test. All experiments were performed in triplicate.

Chromatin condensation analysis

B16F10-Nex2 cells (1 × 10^4) were cultivated on round coverslips, treated with 50 μg/ml of HE for 18 h, washed in PBS and fixed for 30 min at room temperature with 2% formaldehyde. The cells were washed in PBS and stained with 2μM Hoechst 33342 (Invitrogen) for 15 min and analyzed by fluorescence microscopy (Olympus BX-51 fluorescence microscope with immersion oil, at 60X magnification).

DNA fragmentation assay

DNA fragmentation of tumor cells was analyzed by the Terminal Deoxynucleotidyl Transferase dUTP Nick end Labeling (TUNEL) assay. 5 × 10^4 B16F10-Nex2 cells were incubated with 50μg/ml HE for 18 h and then processed and analyzed as previously described.[29] Combretastatin A4 (CA4) was used at 150 μM as positive controle of DNA fragmentation. Alternatively, DNA fragmentation was accessed by electrophoresis. 1 × 10^6 B16F10-Nex2 cells were incubated with 50μg/ml of HE at 37°C for 24 h and then genomic DNA were extracted from the cells, processed and analyzed as previously described.[30]

Annexin V and propidium iodide labeling

B16F10-Nex2 (3 × 10^5) cells were grown for 24 h in a 12-well plate and further incubated with 25 and 12μg/ml of HE or RPMI medium for 1 or 2 h at 37°C. The cells were harvested with cold PBS after three washes in the same buffer. Apoptotic cells were analyzed using the ApoScreen Annexin V-FITC kit according to the manufacturer's instructions (Southern Biotechnology, Birmingham, AL). Positive annexin V (AV) and propidium iodide cells were detected on an inverted fluorescence microscope (Olympus IX70) at 100X magnification.

Detection of caspase activity

The activity of caspases induced by HE was assessed using the *ApoTarget*™ Caspase Colorimetric Protease Assay Kit (Invitrogen, Carlsbad, CA) according to the manufacturer's protocol. 1 × 10^7 B16F10-Nex2 cells were seeded in 6-well plates and treated with 50 μg/ml of HE for 18 h. Briefly, cells were harvested and lysed in a lysis buffer for 10 min in ice. The lysate was centrifuged at 10,000*g* for 1 min, and 200 μg protein was incubated with 50 μl of the reaction buffer and 5 μl of the substrate, at 37°C for 2 h. The absorbance of the reaction mixture was quantified at 405 nm in a microplate reader (Spectramax M3, Molecular Devices).

N-acetylcysteine assay

B16F10-Nex2 cells (1 × 10^4) were seeded in 96-well plates for 6 h, pre-incubated with 10mM of N-acetylcysteine (NAC) for 2 h, washed twice in PBS and incubated with 50 μg/ml of HE for 18h at 37°C. In the control group, tumor cells were pre-incubated with RPMI. Cell viability was determined by Trypan blue (Gibco, Grand Island, NY) exclusion test.

Enhanced superoxide anion production

Enhanced superoxide anion production was detected by dihydroethidium (DHE) assay (Invitrogen) performed according to manufacturer's instructions. B16F10-Nex2 cells (5 × 10^4) were cultivated in 24-well plates and treated with 25 and 12 μg/ml of HE for 18 h. The cells were incubated with 5 μM DHE at 37°C for 30 min. For positive staining control, cells were treated with 5mM hydrogen peroxide for 30 min. Negative controls were treated with RPMI medium. The conversion of DHE to ethidium by oxidation was observed by fluorescence microscopy with an inverted fluorescence microscope (Olympus IX70) at 20X magnification.

Assessment of mitochondrial membrane potential ($\Delta\Psi m$)

B16F10-Nex2 (1 × 10^5) cells were grown for 24 h in a 12-well plate and were incubated with 25 and 12 μg/ml HE at 37°C for 18 h. Cells were gently washed in PBS and loaded with 20nM of tetramethylrhodamine ethyl ester (TMRE, Molecular Probes, OR) for 10 min at 37°C. Cells were immediately observed with the aid of an inverted fluorescence microscope (Olympus I x 70) at 20X magnification.

Cell cycle analysis

B16F10-Nex2 (3 × 10^5) cells were incubated with 25 μg/ml of HE for 24 h. Cells were washed three times in PBS and pelleted at 1,500 rpm for 5 min. Cells were suspended and fixed in 2.5 ml ethanol (70% in PBS) for 15 min in ice. Cells were pelleted and suspended in 500 μl of PI solution in PBS (50 μg/ml propidium iodide, 0.1mg/ml RNase A and 0.05% Triton X-100) for 40 min at 4°C. Cells were pelleted and suspended in 500μl PBS for flow analysis on a Facs CantoII flow cytometer (BD Biosciences). Data were analyzed by Flowjo software (Tree Star, Inc. Ashland, OR).

Peritumor treatment of subcutaneously grafted murine melanoma

Six-week-old male C57BL/6 mice obtained from the Center for Development of Experimental Models (CEDEME), Federal University of São Paulo (UNIFESP) (average weight of 25-28g), were subcutaneously injected with 5 × 10^4 B16F10-Nex2 tumor cells. Peritumor injections were given starting 24 h after tumor cell graft. Treated groups (5 animals per group) received daily doses of 400μg of HE or 500μg of alkanes and the control groups received 5% DMSO in PBS (HE control) or 0.1% hexane, 5% DMSO in PBS (alkanes control). The use of 5% DMSO as vehicle was based on previous *in vivo* protocols described in the literature.[31-33] Tumor size was measured daily for two weeks with a caliper, using the formula $V = 0.52 \times D1^2 \times D2$, where D1 and D2 are the short and long tumor diameters respectively, until the tumor volume reached a maximum of 3000mm^3, when the animals were sacrificed. The guidelines of the Animal Ethics Committee of Federal University of São Paulo (UNIFESP) were used for animal manipulation and experimental protocols (CEP 1234/2011).

Statistical analysis

All *in vitro* experiments were performed in triplicates. Student's *t* test was used for statistical analysis of *in vitro* and *in vivo* experiments. The IC$_{50}$ value and 95% confidence intervals were calculated using GraphPad Prism 5 (GraphPad Software Inc., San Diego, CA) and Instat Plus 3 (The University of Reading, United Kingdom). Gehan-Breslow-Wilcoxon Test was used for the *in vivo* statistics.

RESULTS

Cytotoxic effect of *P.venusta* extracts on murine melanoma cells

The *P.venusta* flower hydroalcoholic extract (HA) showed low cytotoxic effect on B16F10-Nex2 cells as indicated by IC$_{50}$ values higher than 100 μg/ml [Table 1]. Hydrophobic extracts, either in chloroform (CE) or heptane (HE) were also evaluated, and the HE extract showed the strongest cytotoxic activity in B16F10-Nex2 cells, with IC$_{50}$ value of 28.96 μg/ml, compared to CE with IC$_{50}$ of 70.93 μg/ml [Table 1]. Positive control was carried out with doxorubicin [Table 1], a well known antitumor compound.[34] Nontumor cells 3T3, HF and Huvec were less affected by HE extract than B16F10-Nex2 cells [Figure 1].

Evidence of apoptosis

Morphological changes on B16F10-Nex2 cells were observed after cell incubation with 50 μg/ml of HE for 18 h. Cellular blebs, likely apoptotic bodies and shrinkage of the cytoplasm were seen [Figure 2a]. Analysis of the genomic integrity, chromatin condensation and DNA fragmentation, was also examined as indicators of apoptosis.[7] Chromatin condensation was visualized in 30% of 1×10^4 B16F10-Nex2 cells treated with 50 μg/ml HE for 18 h and stained with Hoechst 33342 [Figure 2b].

Cleavage of chromosomal DNA into oligonucleosomal fragments was evaluated by electrophoresis gel of the tumor cell DNA extract after cell incubation with 50 μg/ml of HE for 24 h, and ladder fragmentation pattern was observed [Figure 2c]. Alternatively, the DNA fragmentation was assessed using TUNEL staining, resulting in 74% of TUNEL positive cells (green), compared to the negative control, which showed no TUNEL positive cells [Figure 2d].

Exposure of phosphatidylserine on the cell surface during apoptosis was also shown in HE treated cells as measured by the increased binding of Annexin V. After 18 h of cell incubation with 25 μg/ml of HE, 45% of the cells were at early apoptosis stage (Annexin $^+$PI$^-$) and 6% were at late apoptosis (Annexin $^+$PI$^+$), compared to the negative control. No primary necrosis (Annexin$^-$PI$^+$) was detected in treated cells [Figure 3a].

Treatment of B16F10-Nex2 cells with HE also rendered a significant increase in the activation of caspases 2, 3, 8 and 9 [Figure 3b], clearly defining the apoptotic response.

Enhanced superoxide anion production

Enhanced superoxide anion production in B16F10-Nex2 cells was observed after treatment with 12 and 25 μg/ml of HE for 18 h [Figure 4a]. About 60% of tumor cells treated with 25 μg/ml of HE showed enhanced superoxide anion production detected by dihydroethidium (DHE). In comparison, positive control cells incubated with 5mM of hydrogen peroxide for 30 min showed 65% DHE positive cells [Figure 4c]. Pre-incubation of B16F10-Nex2 cells with *N*-acetyl-L-cysteine (NAC) followed by incubation with HE increased cell viability by 30% ($P = 0.013$) compared to NAC-untreated cells [Figure 4d].

Table 1: IC$_{50}$ values of *P. venusta* extracts on B16F10-Nex2 cells *in vitro*

P.venusta extract	IC$_{50}$ (μg/ml)	SD (μg/ml)
HA (hydroalcoholic extract)	>100	-
CE (Chloroform extract)	70.93	±1.34
HE (heptane extract)	22.5	±1.08
^{a}Doxorrubicin	1.4	±0.30

^{a}Positive control

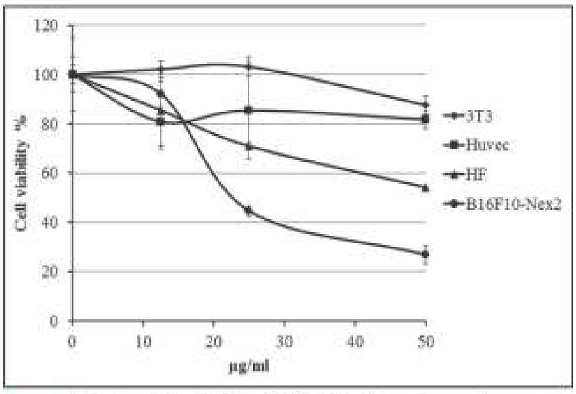

Figure 1: Cytotoxicity of HE in B16F10-Nex2 murine melanoma and nontumorigenic HUVEC, HF and 3T3 cells. Dose dependent activity of HE over 104 tumor cells in 18 h

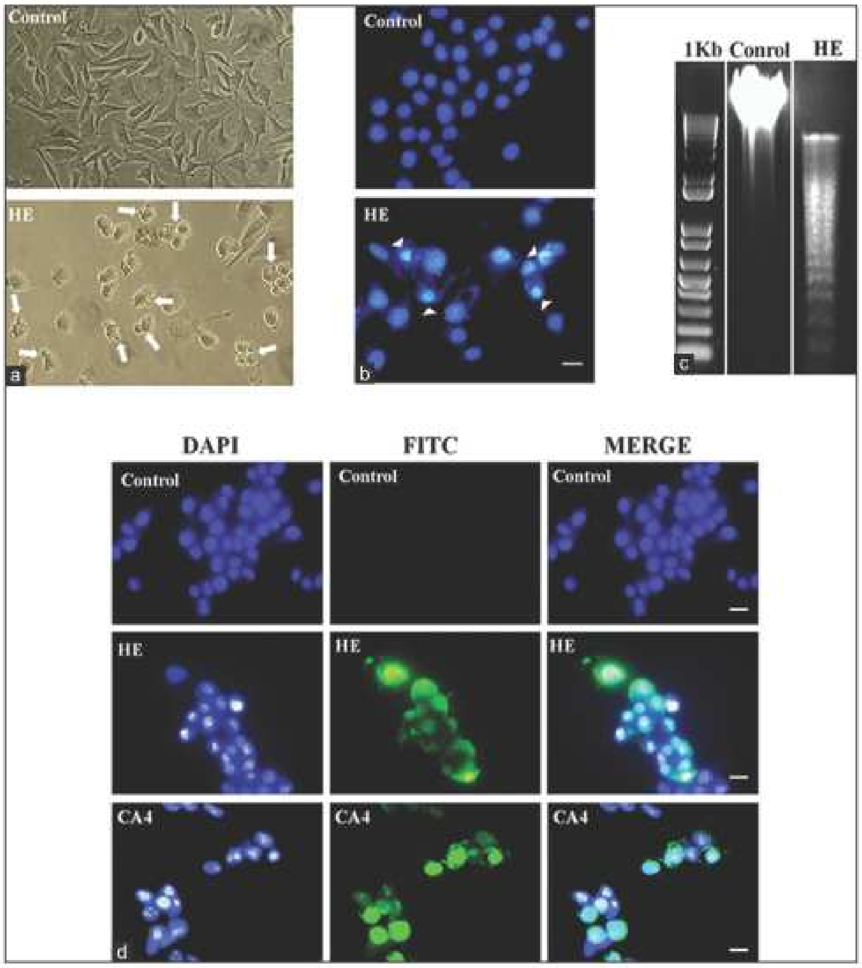

Figure 2 : Morphological evidence and DNA degradation in HE-treated apoptotic melanoma cells. (a) B16F10-Nex2 cell morphology after treatment with 50 μg/ml HE for 18 h. Apoptotic bodies' formation is indicated by white arrows; (b) Evaluation of chromatin condensation in HE treated cells. B16F10-Nex2 cells (104) were treated with 50μg/ml of HE for 18 h, labeled with Hoechst dye, and analyzed by fluorescence microscopy. Arrows indicate pronounced chromatin condensation in treated cells (Magnification 60x) Scale bar: 20μm; (c) Agarose gel electrophoresis of DNA fragmentation in B16F10-Nex2 cells induced by 50 μg/ml HE treatment for 24 h; (d) Fluorescence microscopy for DNA fragmentation. Melanoma cells (5 × 104) were treated with 50 μg/ml of HE and 150 μM of combretastatin A4 as positive apoptotic control for 24 h, and DNA fragmentation was detected using a TUNEL assay (green fluorescence). DAPI (blue) were used for total cell nuclei (Scale bar: 20 μm)

Inner mitochondrial membrane potential

B16F10-Nex2 cells were incubated with TMRE, a fluorescent probe used to measure $\Delta\Psi$m in mitochondria. In resting conditions, mitochondria appeared as elongated structures regularly distributed in the cell cytoplasm. HE-treated cells showed a significant breakdown of the mitochondrial membrane potential measured by the decrease in 91.6 and 60% of TMRE fluorescence in cells treated with 25 μg/ml and 12 μg/ml HE, respectively, compared to untreated control cells [Figure 4b and c].

HE induces G2/M cell cycle arrest in tumor cells

Treatment of tumor cells with 25 μg/ml of HE for 18 h increased the percentage of cells in G2/M phase with a significant reduction of the S phase [Figure 5a]. Positive control was carried out with CA4. The cell cycle arrest induced by HE was accompanied by morphological changes in the cell volume [Figure 5b].

In vivo antitumor activity of HE

The antitumor protective effect of HE was evaluated in C57Bl/6 mice challenged subcutaneously with 5×10^4 B16F10-Nex2 cells. Daily doses of 400 μg of HE were injected in 100 μl of vehicle (5% DMSO in PBS) at peripheral sites to the original cell grafting. Treatment resulted in a significant decrease in tumor volume as seen from the 14th day of treatment with a potent antitumor effect of HE compared to the vehicle treated

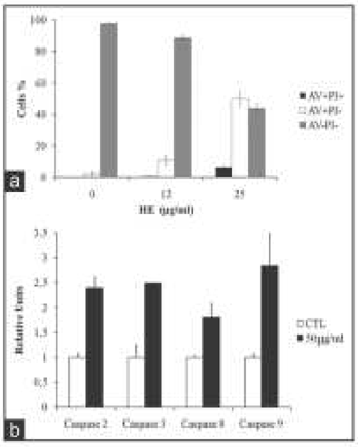

AQ1

Figure 3: Phosphatidyl serine surface expression and caspase activation. (a) Annexin V and propidium iodide labeling of B16F10-Nex2 (3 x 105) cells grown for 24 h in 12-well plate and incubated with 12 and 25 µg/ml of HE or RPMI medium for 18 h at 37 °C. Positive annexin V (AV) and propidium iodide cells were detected with an inverted fluorescence microscope at 10X magnification; (b) Activation of caspase-2, 3, 8 and 9 in HE treated melanoma cells. B16F10-Nex2 cells (107) were treated with 50 µg/ml of HE for 24 h, and the HE induced enzymatic activity of caspase-2, 3, 8 and 9 was evaluated by colorimetric assay

control [Figure 6]. In addition, no toxic effects, loss of weight, or alteration in animal behavior were observed during the treatment with HE.

Bioguided fractionation of HE extract and chemical analysis

The crude HE extract was subjected to a bioguided fractionation procedure, in which seven pooled fractions (HEF1, HEF2, HEF3, HEF4, HEF5, HEF6 and HEF7) were evaluated for their cytotoxic activity on murine melanoma cells *in vitro*. The cytotoxic acitivity on B16F10-Nex2 cells was restricted to pooled fraction HEF2 with IC_{50} of 28.48 µg/ml [Figure 7]. Cytotoxicity of HEF2 was also observed against several other tumor cell lines, as shown in Table 2.

Table 2: IC_{50} values of HEF2on different tumor cell lines *in vitro*

Cell lineage	IC_{50} (µg/ml)	SD (µg/ml)
A2058	62.04	±1.66
U87	48.60	±1.18
SIHA	38.48	±1.57
HCT	16.01	±0.63
SKmel28	10.76	±0.50
CT26	33.84	±0.35
B16F10-Nex2	28.48	±1.02
4T1	13.32	±0.23
PANC	8.36	±0.84

PANC: Pancreatic cells; SIHA: ???; HCT: ???; CT: ???; HEF: ???

AQ2

Table 3: Identification of saturated hydrocarbon derivatives and other compounds in group HEF2 from heptane extract from flowers of *Pyrostegia venusta*

Molecular formula	Identified compound	Relative amount/%
$C_6H_{12}O$	3-methyl-2-pentanone	1.13
$C_6H_{14}O$	3-methyl-3-pentanol	3.54
$C_6H_{14}O$	3-hexenol	0.83
$C_6H_{14}O$	4-methyl-2-pentanol	0.65
$C_5H_8O_2$	Allyl acetate	1.65
$C_7H_{14}O$	2,2-dimethylpentanal	4.79
$C_{24}H_{50}$	Tetracosane	6.92
$C_{26}H_{54}$	Hexacosane	7.23
$C_{27}H_{56}$	Heptacosane	2.72
$C_{28}H_{58}$	Octacosane	36.34
$C_{29}H_{60}$	Nonacosane	2.70
$C_{30}H_{62}$	Triacontane	12.72
$C_{32}H_{66}$	Dotriacontane	2.55

HEF: ???

AQ2

The ^1H NMR spectrum of HEF2 (in $CDCl_3$) depicted an intense singlet at δ 1.18 ppm, a multiplet at δ 1.51 ppm and a deformed triplet at δ 0.81 ppm ($J = 6.8$ Hz) [Figure 8a]. These signals, associated to the absence of signals at range of δ 5-6 ppm, characteristic of hydrogens linked at unsaturated sp^2 carbons, suggested the predominance of long side chain saturated hydrocarbons.[35,36] Analysis by GC-MS indicated that this fraction was composed by thirteen compounds [Table 3], which were identified as a mixture of hydrocarbons (71.18%): tetracosane ($C_{24}H_{50}$-6.92%), hexacosane ($C_{26}H_{54}$-7.23%), heptacosane ($C_{27}H_{56}$-2.72%), octacosane ($C_{28}H_{58}$-36.34%), nonacosane ($C_{29}H_{60}$-2.70%), triacontane ($C_{30}H_{62}$-12.72%), and dotriacontane ($C_{32}H_{66}$-2.55%) as well as by oxygenated derivatives in minor proportion (12.59%): 3-methyl-2-pentanone (1.13%), 3-methyl-3-pentanol (3.54%), 3-hexenol (0.83%), 4-methyl-2-pentanol (0.65%), allyl acetate (1.65%), 2,2-dimethylpentanal (4.79%). The characterization of these compounds was based on the comparison of recorded mass spectra with those available in the database as well as their retention times in a DB-5 column [Figure 8b], after co-injection of standards, as represented for octacosane [Figure 8c] and triacontane [Figure 8e].

In vitro cytotoxic activity of Octacosane and Triacontane

Since octacosane and triacontane were found in higher amounts in the HEF2 fraction, they were evaluated for cytotoxic activity on B16F10-Nex2 melanoma cells. Octacosane and triacontane were purchased from Santa Cruz Biotechnology, Inc (California, USA). Alkanes were incubated with 1 × 10^4 B16F10-Nex2 cells at different

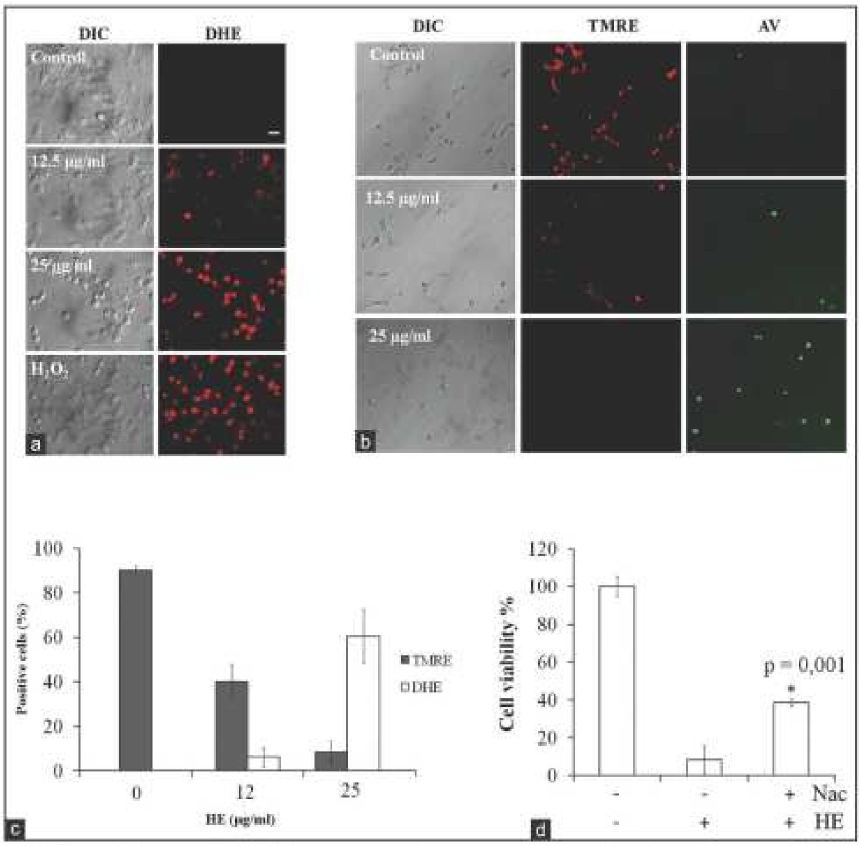

AQ1

Figure 4: Mitochondrial effects of HE treatment. (a) Representative images of superoxide anions' negative and positive cells treated with 12.5 and 25 μg/ml of HE for 18 h, and 5 mm of hydrogen peroxide (positive control) for 30 min. B16F10-Nex2 cells were stained with 5 μM of DHE (dihydroethidium). Scale bar: 20 μm; (b) Representative images of mitochondrial ΔΨm following HE treatment. B16F10-Nex2 cells were treated with negative control and with 12 and 25 μg/ml of HE for 18 h (original magnification, 20x). Positive apoptotic cells were stained with annexin V (original magnification, 10X). (c) Percentage of TMRE (tetramethylrhodamine ethyl ester) and DHE positive cells; (d) Protective effect of N-acetyl cysteine (NAC) on HE-treated cells. B16F10-Nex2 cells (104) were pretreated for 2 h with 10 mM NAC, washed and incubated with 50 μg/ml of HE at 37°C for 18 h

concentrations and we observed that both alkanes displayed strong cytotoxic activity on B16F10-Nex2 cells, with IC$_{50}$ values of 20.9 μg/ml and 41.08 μg/ml for triacontane and octacosane, respectively [Figure 9a]. We also observed that both alkanes induced similar morphological changes as those induced by HE treatment in B16F10-Nex2 cells [Figure 9b].

In vivo antitumor activity of Octacosane and Triacontane

The antitumor activities of octacosane and triacontane were investigated in subcutaneous melanoma model. 5×10^4 B16F10-Nex2 Cells were injected subcutaneously in C57Bl/6 mice and daily doses of 500 μg of Octacosane and Triacontane were injected at peripheral sites in relation to the original cell grafting. Treatment procedure resulted in a significant delay of tumor progression with a significant antitumor effect of octacosane ($P = 0.017$) and triacontane ($P = 0.04$) compared to the vehicle control (5% DMSO in PBS) [Figure 6]. In addition, the survival rate of treated groups was significantly increased in triacontane ($P = 0.018$) and octacosane ($P = 0.032$) treated animals [Figure 10b]. No toxic effects, loss of weight, or alteration in animal behavior were observed during the treatment with octacosane and triacontane.

DISCUSSION

In this study, we observed that fractions and compounds in the heptanic extract of flowers from *Pyrostegia venusta* exhibit promising cytotoxic activity against malignant melanoma *in vitro* and *in vivo*, which enhances the therapeutic opportunities that this plant fits to be used in the treatment of different diseases.[37]

We show that murine melanoma cells react to the heptane extract of *P. venusta* by undergoing apoptosis. Hallmarks of apoptosis such as plasma membrane blebbing without

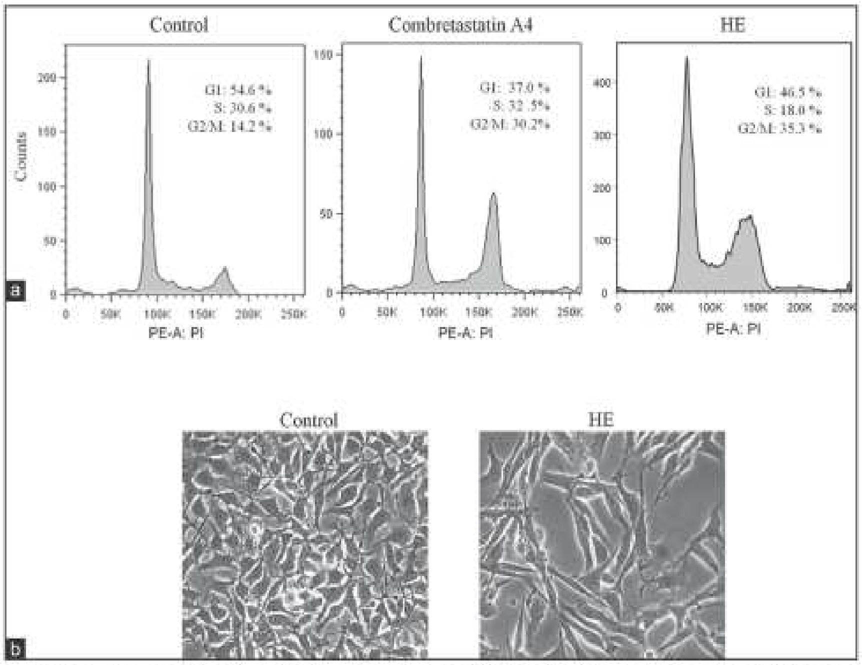

AQ1

Figure 5: Effect of HE on the melanoma cell cycle. (a) Cell cycle analysis of B16F10-Nex2 tumor cells treated with 25 μg/ml HE and 75 μM of CA4 for 24 h. (b) Representative images of tumor cell morphology following HE treatment

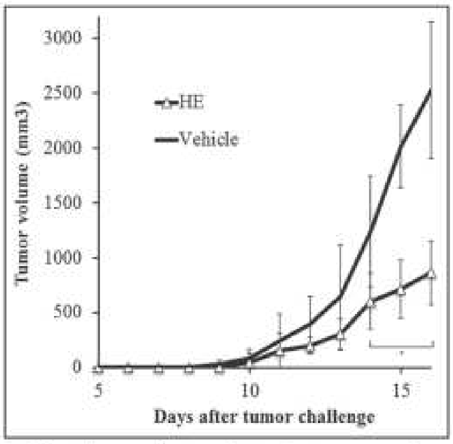

AQ1

Figure 6: HE antitumor effect against subcutaneous melanoma. Six-week-old male C57BL/6 mice were injected subcutaneously with 5x104 B16F10-Nex2 tumor cells. Peritumor treatment started 24 h after tumor inoculation. HE (400 μg) in 100μl PBS was injected in daily doses and the tumor size was measured seven times a week with a caliper until the tumor volume reached a maximum of 3000 mm3, when animals were sacrificed. The control group was treated with PBS/DMSO 5%. $^{*}P<0.05$

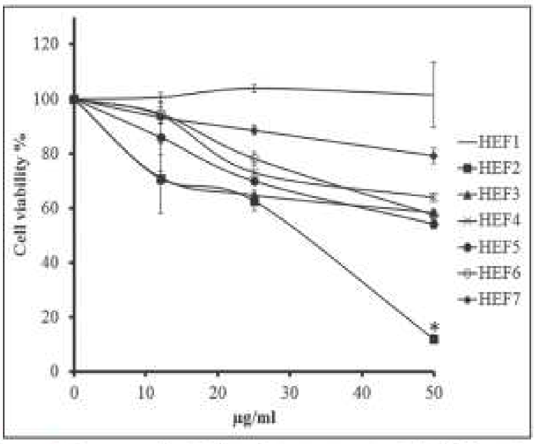

AQ1

Figure 7: Tumor cell viability after treatment with HE fractions. B16F10-Nex2 cells (104) were seeded in 96-well plates and incubated with different concentrations of HE fractions for 24 h. Assays were performed in triplicates. $^{*}P<0.05$

lysis, cell shrinkage, mitochondria permeabilization, chromatin condensation and DNA fragmentation, and phosphatidylserine surface expression were observed during the treatment of murine melanoma cells with HE *in vitro*, confirming the apoptotic nature of cell death.[7,38]

Apoptosis can be variously induced, as by death receptor ligands interacting on the plasma membrane (receptor or extrinsic pathway) or by mitochondrial pathways (intrinsic pathway).[39] We suggest that the mechanism by which HE treated cells undergo apoptosis is related to the intrinsic pathway, as evidenced by the production of superoxide anions in the mitochondria of HE treated cells. Free radicals, particularly ROS, have been proposed as common mediators of apoptosis.[36,40] Mitochondria are involved in the production of reactive oxygen species, mainly superoxides and hydrogen peroxide and mitochondrial membrane damage results in the leakage of superoxide anions into the cytosol.[41]

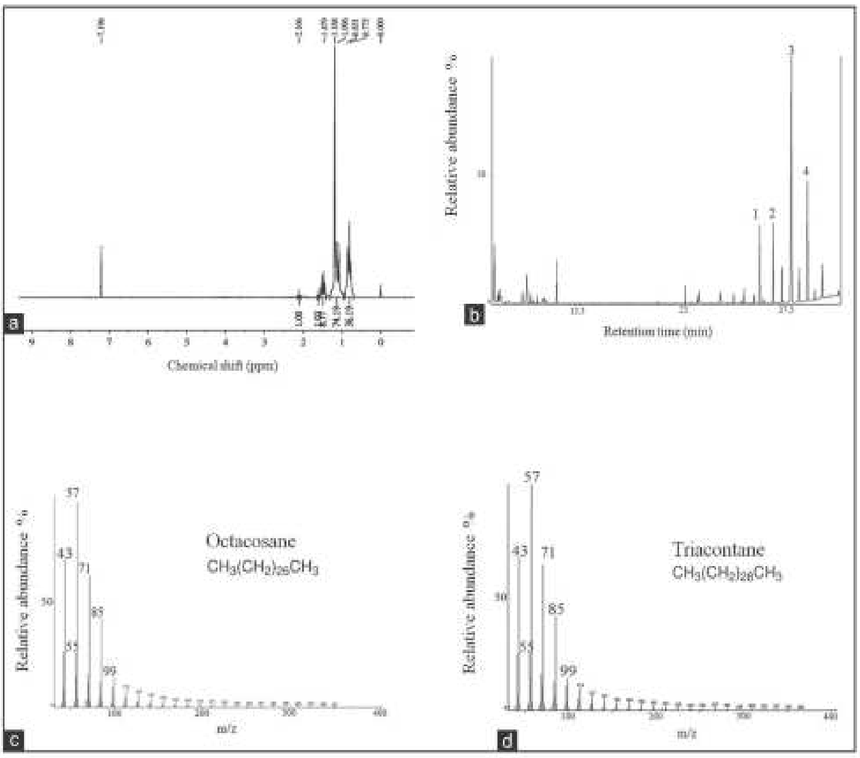

AQ1 **Figure 8:** (a) 1H NMR spectrum of fraction HEF2 (~ CDCl3, 200 MHz)-the signal at ~ 7.24 ppm corresponding to hydrogens of residual CHCl3 in deuterated solvent; (b) GC-MS of HEF2 components with 4 main alkane species with the retention times of (1) tetracosane (C24H50), (2) hexacosane (C26H54), (3) octacosane (C28H58), (4) triacontane (C30H62), and 3 other minor species as listed in Table 3; (c) Mass spectrum of octacosane (GC component 3) and (d) triacontane (GC component 4), further identified by co-injection with standard n-octacosane, Rt 37.7 min, MM 620 Da, and triacontane, Rt 39.57 min, MM 422 Da

In eukaryotic cells, plant derived compounds can promote dissipation of the mitochondrial membrane potential ($\Delta\Psi m$) resulting in leakage of pro-apoptotic factors mainly cytochrome c.[30] Once in the cytoplasm, cytochrome c associates with Apaf-1 and then procaspase-9 (and possibly other proteins) to form the apoptosome. Heat-shock proteins play a role in the pathway to modulate apoptosis. Caspase-9 activates other downstream caspases such as caspase-3 that constitute the major caspase activity in apoptotic cells.[42,43]

In a study with pyrimethamine in metastatic melanoma, this drug, which generates ROS, induced upstream caspase activation (caspase-8), bypassing CD95/Fas engagement.[44] Kim and colleagues also showed that N, N-dimethyl phytosphingosine could induce caspase-8-dependent cytochrome c release and apoptosis through ROS generation in human leukemia cells.[45] We observed that an apoptotic peptide (C7H2) inducing caspase 8 produced abundant superoxide anions in B16F10-Nex2 cells.[29] Other mechanisms by which ROS promote caspase-9 activation[46] have also been described. Oxidative modification of caspase-9 by ROS could mediate its interaction with Apaf-1, independently from the increased release of cytochrome c, and thus promote auto-cleavage and activation. Such mechanism may facilitate apoptosome formation and caspase-9 activation under oxidative stress conditions.[39]

We showed that HE treatment induced caspases 2, 3, 8 and 9, besides disruption of the mitochondrial membrane potential and release of superoxide anions. Caspase-2 activation could induce cell cycle regulation and tumor suppression.[47] It is unique among the caspases because it has features of both initiator and effector caspases.[48] Prasad and colleagues reported that ROS generation induce the activation of caspase-2 in human leukemic cells and the simultaneous activation of caspases 8 and 9. Cross-talk between these initiator caspases is mediated by the proapoptotic protein Bid.[49] It is possible that the HE induced activation of caspase-8 as mediated by ROS, and leading to apoptosis may involve the caspase-8-Bid-Bax pathway.

The antitumor activity of HE also involved the cell cycle arrest in over 40% treated cells. It is still unclear whether checkpoint genes are involved that could mediate mitochondrial apoptotic signaling,[50] or the expression and translocation of Bax.[51] Thus, specific studies of induced cell death signaling should be performed with the isolated active compounds from HE in order to better characterize their mechanism of action involved in the induction of cell cycle arrest and apoptosis.

The cytotoxic potential of the heptane extract (HE) of *P.venusta* flowers on murine melanoma B16F10-Nex2 cells is related to the alkane rich active fraction, which is also active against several human cancer cells lines *in vitro*. HE was studied according to the criterion of the American National Cancer Institute, which states that the IC_{50} limit to consider a crude extract requiring further purification is 30 µg/ml.[52] Previous phytochemical studies on *P. venusta* flower extracts from India identified stigmasterol, β-sitosterol, β-amyrin and oleanolic acid compounds.[52] Recently, a complete characterization of phytochemicals occurring in the methanolic extract of *P.venusta* showed predominantly, myoinositol, hexadecanoic acid, linoleic acid, oleic acid, stigmasteryl tosylate, diazoprogesterone, arabipyranose. Moreover, these methanolic extracts showed antioxidant activity *in vivo* and *in vitro*, verified by DPPH, ABTS and FRAP assays, although the compounds responsible for the antioxidant activity were not investigated.[53,54]

In the present work, the active fraction HEF2 of the heptane extract of *P.venusta* flowers did not contain triterpenoids and/or steroids but rather, a mixture of saturated hydrocarbons in which triacontane and octacosane predominated. Previous works have shown that straight-chain saturated hydrocarbons have antitumor activities in different systems. Takahashi *et al.*, (1995) have found that hentriacontane, the main component in their bioactive fraction, showed the highest antitumor activity.[55] This same compound predominates in the epicuticular wax in leaves from *Kigelia pinnata*, and is responsible for the plant protection against UV radiation and for its antitumour potential.[56] The saturated hydrocarbon gentriacontan ($C_{31}H_{64}$), present in the chloroform extract of *Clinopodium vulgare*, was reported to inhibit the growth of Erlich ascites tumor in mice, and also possesses antitumor activity against CEM and K-562 human leukemia cell lines *in vitro*.[57] Gomez-Flores *et al.*, found that the observed antitumor activity against lymphoma cells was due primarily to the presence of hentriacontane in the leaves of *C. vulgare*.[58] More recently, it has been described that intracellular eicosanoid metabolites regulate mitochondrial function and induce apoptosis.[59] Recently, both octacosane and triacontane were found in the same proportions in a lipid fraction from the ether extract of *Solanum elaeagnifolium* as promising antibacterial agents.[60] Thus, the alkane rich HEF2 fraction from *P. venusta* flowers is in line with these studies, being responsible for the observed tumor apoptosis effects of HE.

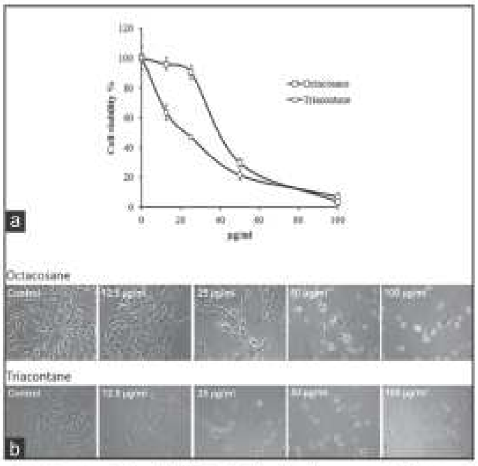

Figure 9: Cytotoxicity of HE individual alkanes. (a) Cytotoxicity of octacosane and triacontane in B16F10-Nex2 cells after 18 h. (b) Tumor cell morphology after incubation with different concentrations of octacosane and triacontane

Most importantly, mice treated with HE showed a marked reduction in the subcutaneous tumor progression indicating an important activity of this plant extract against primary melanoma, and the same antitumor activity *in vivo* was further confirmed when mice were treated with isolated octacosane and triacontane.

In this work, octacosane and triacontane had to be solubilized in low amounts of dimethylsulfoxide (DMSO) to be tested, and probably their anti-tumor effect depends on the alkane-DMSO complex formed. It has been

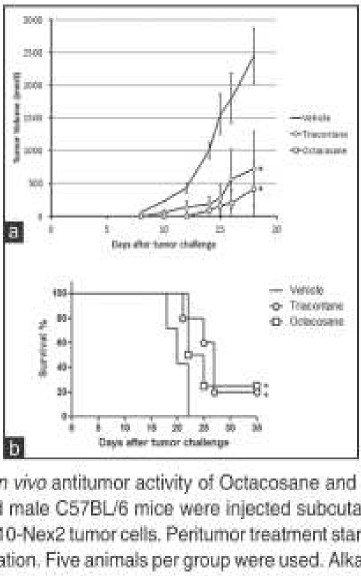

Figure 10: *In vivo* antitumor activity of Octacosane and Triacontane. Six-week-old male C57BL/6 mice were injected subcutaneously with 5×104 B16F10-Nex2 tumor cells. Peritumor treatment started 24 h after tumor inoculation. Five animals per group were used. Alkanes (500 µg) were injected in 100 µl of 5% DMSO in PBS. Daily doses were given during all treatment period. Tumor size was measured seven times a week with a caliper until the tumor volume reached a maximum of $3000 mm^3$ when the animals were sacrificed. The control group was treated with vehicle PBS/DMSO 5%. *$P<0.05$, indicates significant differences between groups

shown that in pure water, long chain n-alkane exhibits an intermittent oscillation between the collapsed and the extended coiled conformations. When the mole fraction of DMSO is 0.05, its concentration in the first hydration layer around the hydrocarbon of chain length 30 ($n = 30$) is of 17%. The formation of such hydrophobic environment around the hydrocarbon chain is the reason for the collapsed conformation gaining additional stability.[61] Such conformation of the alkane-DMSO combination allowed the observed antitumor activity of both octacosane and triacontane *in vitro* and *in vivo*, with no systemic toxicity observed in mice receiving DMSO alone.

Besides, DMSO presents great ability to penetrate tissues, which justifies its use in many therapeutical protocols in dermatology. It increases the effectiveness of the percutaneous penetration of many substances, facilitating their diffusion across the stratum corneum and promotes transport into the local blood vessels, as demonstrated by increasing the penetration of many agents, including 5-fluorouracil in the treatment of superficial tumors and warts.[62-65] Combination therapy of DMSO with different drugs enhances the healing of cutaneous diseases, such as acral lick dermatitis, arthritis, mastitis and scleroderma, and it is considered to have a low toxicity.[66,67] The current use of DMSO regards its application in intravenous, subcutaneous and oral routes. Several recent works have presented DMSO as vehicle of different anticancer compounds administered systemically or topically in 1 ~ 10% solution.[68-71]

CONCLUSION

The Experimental Oncology Unit routinely tests natural products for anti tumor activities mainly focusing on melanoma. As pointed out before (Introduction) several plant-derived products induce apoptosis in neoplastic cells but not in normal cells. The nature of the anti tumor agents varies in terms of distribution, solubility and chemical composition. Surprisingly, heptane extracts but not aqueous extracts of Pyrostegia venusta were cytotoxic to melanoma cells *in vitro* and *in vivo*, and the active compounds are saturated aliphatic hydrocarbons. Since peritumor injections of the active alkanes protected against melanoma in a mouse model, suggestion has been made that these compounds might also be therapeutic in mostly epidermal and slowly invasive human melanomas, such as acral lentiginous melanoma, as an adjuvant treatment to surgical excision. Regional perfusion chemotherapy in addition to excision is significantly more efficient in the treatment of acral melanoma than excision alone.

ACKNOWLEDGMENTS

The present work was supported by Fundação de Amparo à Pesquisa do Estado de São Paulo (FAPESP), and Conselho Nacional de Desenvolvimento Científico e Tecnológico (CNPq).

REFERENCES

1. Guimaraes FS, Abud AP, Oliveira SM, Oliveira CC, Cesar B, Andrade LF, *et al.* Stimulation of lymphocyte anti-melanoma activity by co-cultured macrophages activated by complex homeopathic medication. BMC Cancer 2009;9:293.
2. Sawada N, Kataoka K, Kondo K, Arimochi H, Fujino H, Takahashi Y, *et al.* Betulinic acid augments the inhibitory effects of vincristine on growth and lung metastasis of B16F10 melanoma cells in mice. Br J Cancer 2004;90:1672-8.
3. Ozben T. Mechanisms and strategies to overcome multiple drug resistance in cancer. FEBS Lett 2006;580:2903-9.
4. Krementz ET, Feed RJ, Coleman WP 3rd, Sutherland CM, Carter RD, Campbell M. Acral lentiginous melanoma. A clinicopathologic entity. Ann Surg 1982;195:632-45.
5. Rashid OM, Schaum JC, Wolfe LG, Brinster NK, Neifeld JP. Prognostic variables and surgical management of foot melanoma: Review of a 25-year institutional experience. ISRN Dermatol 2011;2011:384729.
6. Fidler IJ, Nicholson GL. Tumor cell and host properties affecting the implantation and survival of blood-borne metastatic variants of B16 melanoma. Isr J Med Sci 1978;14:38-50.
7. Kroemer G, Galluzzi L, Vandenabeele P, Abrams J, Alnemri ES, Baehrecke EH, *et al.* Classification of cell death: Recommendations of the Nomenclature Committee on Cell Death 2009. Cell Death Differ 2009;16:3-11.
8. Adams JM, Cory S. Bcl-2-regulated apoptosis: Mechanism and therapeutic potential. Curr Opin Immunol 2007;19:488-96.
9. Zeisel SH. Antioxidants suppress apoptosis. J Nutr 2004;134:3179S-80.
10. Kass GE, Eriksson JE, Weis M, Orrenius S, Chow SC. Chromatin condensation during apoptosis requires ATP. Biochem J 1996;318 (Pt 3):749-52.
11. Golstein P, Kroemer G. Cell death by necrosis: Towards a molecular definition. Trends Biochem Sci 2007;32:37-43.
12. Baehrecke EH. Caspase activation finds fertile ground. Dev Cell 2003;4:608-9.
13. Hanahan D, Weinberg RA. Hallmarks of cancer: the next generation. Cell 2011;144:646-74.
14. Hanahan D, Weinberg RA. The hallmarks of cancer. Cell 2000;100:57-70.
15. Raff M. Cell suicide for beginners. Nature 1998;396:119-22.
16. Banjerdpongchai R, Kongtawelert P, Khantamat O, Srisomsap C, Chokchaichamnankit D, Subhasitanont P, *et al.* Mitochondrial and endoplasmic reticulum stress pathways cooperate in zearalenone-induced apoptosis of human leukemic cells. J Hematol Oncol 2010;3:50.
17. Kluza J, Lansiaux A, Wattez N, Hildebrand MP, Léonce S, Pierré A, *et al.* Induction of apoptosis in HL-60 leukemia and B16 melanoma cells by the acronycine derivative S23906-1. Biochem Pharmacol 2002;63:1443-52.
18. Mashele S, Fuku SL. Evaluation of the antimutagenic and mutagenic properties of asparagus laricinus. Med Technol SA 2011;25:33-36

20. Youn MJ, Kim JK, Park SY, Kim Y, Park C, Kim ES, *et al.* Potential anticancer properties of the water extract of Inonotus [corrected] obliquus by induction of apoptosis in melanoma B16-F10 cells. J Ethnopharmacol 2009;121:221-8.
21. Park HJ, Han ES, Park DK. The ethyl acetate extract of PGP (Phellinus linteus grown on Panax ginseng) suppresses B16F10 melanoma cell proliferation through inducing cellular differentiation and apoptosis. J Ethnopharmacol 2010;132:115-21.
22. Hu W, Zhang C, Fang Y, Lou C. Anticancer properties of 10-hydroxycamptothecin in a murine melanoma pulmonary metastasis model *in vitro* and in vivo. Toxicol *In vitro* 2011;25:513-20.
23. Tavakkol-Afshari J, Brook A, Mousavi SH. Study of cytotoxic and apoptogenic properties of saffron extract in human cancer cell lines. Food Chem Toxicol 2008;46:3443-7.
24. Mesquita ML, de Paula JE, Pessoa C, de Moraes MO, Costa-Lotufo LV, Grougnet R, *et al.* Cytotoxic activity of Brazilian Cerrado plants used in traditional medicine against cancer cell lines. J Ethnopharmacol 2009;123:439-45.
25. Napolitano DR, Mineo JR, de Souza MA, de Paula JE, Espindola LS, Espindola FS. Down-modulation of nitric oxide production in murine macrophages treated with crude plant extracts from the Brazilian Cerrado. J Ethnopharmacol 2005;99:37-41.
26. Veloso CC, Bitencourt AD, Cabral LD, Franqui LS, Dias DF, dos Santos MH, *et al.* Pyrostegia venusta attenuate the sickness behavior induced by lipopolysaccharide in mice. J Ethnopharmacol 2010;132:355-8.
27. Ferreira DT, Alvares PS, Houghton PJ, Braz R. Chemical constituents from roots of Pyrostegia venusta and considerations about its medicinal importance. Quimica Nova 2000;23:42-6.
28. Cardozo NP, Parreira MC, Alves PL, Bianco S. Foliar area estimate of two sugarcane-infesting weeds using leaf blade linear dimensions. Planta Daninha 2009;27:683-7.
29. Arruda DC, Santos LC, Melo FM, Pereira FV, Figueiredo CR, Matsuo AL, *et al.* Beta-actin-binding complementarity-determining region 2 of variable heavy chain from monoclonal antibody c7 induces apoptosis in several human tumor cells and is protective against metastatic melanoma. J Biol Chem 2012;287:14912-22.
30. Matsuo AL, Figueiredo CR, Arruda DC, Pereira FV, Scutti JA, Massaoka MH, *et al.* Alpha-Pinene isolated from Schinus terebinthifolius Raddi (Anacardiaceae) induces apoptosis and confers antimetastatic protection in a melanoma model. Biochem Biophys Res Commun 2011;411:449-54.
31. Balonov K, Khodorova A, Strichartz GR. Tactile allodynia initiated by local subcutaneous endothelin-1 is prolonged by activation of TRPV-1 receptors. Exp Biol Med (Maywood) 2006;231:1165-70.
32. Kwon YH, Jung SY, Kim JW, Lee SH, Lee JH, Lee BY, *et al.* Phloroglucinol inhibits the bioactivities of endothelial progenitor cells and suppresses tumor angiogenesis in LLC-tumor-bearing mice. PLoS One 2012;7:e33618.
33. Suzuki T, Shimizu T, Yu HP, Hsieh YC, Choudhry MA, Schwacha MG, *et al.* Tissue compartment-specific role of estrogen receptor subtypes in immune cell cytokine production following trauma-hemorrhage. Appl Physiol 2007;102:163-8.
34. Park D, Bae DK, Jeon JH, Lee J, Oh N, Yang G, *et al.* Immunopotentiation and antitumor effects of a ginsenoside Rg (3)-fortified red ginseng preparation in mice bearing H460 lung cancer cells. Environ Toxicol Pharmacol 2011;31:397-405.
35. Moreira IC, Lago JH, Young MC, Roque NF. Antifungal aromadendrane sesquiterpenoids from the leaves of Xylopia brasiliensis. J Braz Chem Soc 2003;14:828-31.
36. Moreira IC, Roque NF, Contini K, Lago JH. Sesquiterpenos e hidrocarbonetos dos frutos de Xylopia emarginata (Annonaceae). Rev Bras Farmacogn 2007;17:55-8.
37. Moreira CG, Horinouchi CD, Souza-Filho CS, Campos FR, Barison A, Cabrini DA, *et al.* Hyperpigmentant activity of leaves and flowers extracts of Pyrostegia venusta on murine B16F10 melanoma. J Ethnopharmacol 2012;141:1005-11.
38. Mates JM, Sanchez-Jimenez FM. Role of reactive oxygen species in apoptosis: implications for cancer therapy. Int J Biochem Cell Biol 2000;32:157-70.
39. Hengartner MO. The biochemistry of apoptosis. Nature 2000;407:770-6.
40. Zuo Y, Xiang B, Yang J, Sun X, Wang Y, Cang H, *et al.* Oxidative modification of caspase-9 facilitates its activation via disulfide-mediated interaction with Apaf-1. Cell Res 2009;19:449-57.
41. Liu SX, Davidson MM, Tang X, Walker WF, Athar M, Ivanov V, *et al.* Mitochondrial damage mediates genotoxicity of arsenic in mammalian cells. Cancer Res 2005;65:3236-42.
42. Jiang X, Wang X. Cytochrome c promotes caspase-9 activation by inducing nucleotide binding to Apaf-1. J Biol Chem 2000;275:31199-203.
43. Gottlieb E, Armour SM, Harris MH, Thompson CB. Mitochondrial membrane potential regulates matrix configuration and cytochrome c release during apoptosis. Cell Death Differ 2003;10:709-17.
44. Giammarioli AM, Maselli A, Casagrande A, Gambardella L, Gallina A, Spada M, *et al.* Pyrimethamine induces apoptosis of melanoma cells via a caspase and cathepsin double-edged mechanism. Cancer Res 2008;68:5291-300.
45. Kim BM, Choi YJ, Han Y, Yun YS, Hong SH. N, N-dimethyl phytosphingosine induces caspase-8-dependent cytochrome c release and apoptosis through ROS generation in human leukemia cells. Toxicol Appl Pharmacol 2009;239:87-97.
46. Sato T, Machida T, Takahashi S, Iyama S, Sato Y, Kuribayashi K, *et al.* Fas-mediated apoptosome formation is dependent on reactive oxygen species derived from mitochondrial permeability transition in Jurkat cells. J Immunol 2004;173:285-96.
47. Kumar S. Caspase 2 in apoptosis, the DNA damage response and tumour suppression: Enigma no more? Nat Rev Cancer 2009;9:897-903.
48. Zhivotovsky B, Orrenius S. Caspase-2 function in response to DNA damage. Biochem Biophys Res Commun 2005;331:859-67.
49. Prasad V, Chandele A, Jagtap JC, Sudheer KP, Shastry P. ROS-triggered caspase 2 activation and feedback amplification loop in beta-carotene-induced apoptosis. Free Radic Biol Med 2006;41:431-42.
50. Pietenpol JA, Stewart ZA. Cell cycle checkpoint signaling: Cell cycle arrest versus apoptosis. Toxicology 2002;181-182:475-81.
51. Ostrakhovitch EA, Cherian MG. Role of p53 and reactive oxygen species in apoptotic response to copper and zinc in epithelial breast cancer cells. Apoptosis 2005;10:111-21.
52. Suffness M, Pezzuto JM. Assays Related to Cancer Drug Discovery. In: Hostettmann K, editor. Methods in Plant Biochemistry: Assays for Bioactivity. London: Acad. Press; 1990. p. 71-133.
53. Krishna V, Sharma S, Pareek RB, Singh P. Terpenoid constituents from some indigenous plants. J Indian Chem Soc 2002;79:550-2.
54. Roy P, Amdekar S, Kumar A, Singh V. Preliminary study of the antioxidant properties of flowers and roots of Pyrostegia venusta (Ker Gawl) Miers. BMC Complement Altern Med 2011;11:69.
55. Takahashi C, Kikuchi N, Katou N, Miki T, Yanagida F, Umeda M. Possible anti-tumour-promoting activity of components in Japanese soybean fermented food, Natto: Effect on gap junctional intercellular communication. Carcinogenesis 1995;16:471-6.
56. Olubunmi A, Olatunji AG. Epicuticular wax and volatiles of *kigelia pinnata* leaf extract. Ethno leaflets. 2010;14:797-806.

57. Dzhambazov B, Daskalova S, Monteva A, Popov N. *In vitro* screening for antitumour activity of Clinopodium vulgare L. (Lamiaceae) extracts. Biol Pharm Bull 2002;25:499-504.
58. Gomez-Flores R, Quintanilla-Licea R, Verde-Star MJ, Morado-Castillo R, Vazquez-Diaz D, Tamez-Guerra R, *et al.* Long-chain alkanes and ent-Labdane-type diterpenes from Gymnosperma glutinosum with cytotoxic activity against the murine lymphoma L5178Y-R. Phytother Res 2012;26:1632-6.
59. Moon SH, Jenkins CM, Liu X, Guan S, Mancuso DJ, Gross RW. Activation of mitochondrial calcium-independent phospholipase A2gamma (iPLA2gamma) by divalent cations mediating arachidonate release and production of downstream eicosanoids. J Biol Chem 2012;287:14880-95.
60. Amer WM, Abouwarda AM, El Garf IA, Dawoud GT, Abdelmohsen G. Phytochemical composition of *Solanum elaeagnifolium cav*. And its antibacterial activity. Int J Bio Pha Ali Sci (IJBPAS) 2013;2:1282-306.
61. Ghosh R, Banerjee S, Chakrabarty S, Bagchi B. Anomalous behavior of linear hydrocarbon chains in Water -DMSO binary mixture at low DMSO concentration. J Phys Chem 2011;B115:7612-20.
62. Capriotti K, Capriotti JA. Dimethyl sulfoxide: History, chemistry, and clinical utility in dermatology. J Clin Aesthet Dermatol 2012;5:24-6.
63. Stoughton RB, Fritsch W. Influence of dimethylsulfoxide (dmso) on human percutaneous absorption. Arch Dermatol 1964;90:512-7.
64. Goldmann L, Igelman JM, Kitzmiller K. Investigative studies with DMSO in dermatology. Ann N Y Acad Sci 1967;141:428-36.
65. Coldman MF, Kalinovsky T, Poulsen BJ. The *in vitro* penetration of fluocinonide through human skin from different volumes of DMSO. Br J Dermatol 1971;85:457-61.
66. Manjunath P, Shivaprakash BV. KrishiVigyan Kendra, Aland road, Gulbarga, UAS, Raichur, Karnataka. Pharmacology and Clinical Use of Dimethyl Sulfoxide (DMSO): A Review. Int J Mol Vet Res 2013;3:23-33.
67. Scherbel AL, McCormack LJ, Layle JK. Further observations on the effect of dimethyl sulfoxide in patients with generalized scleroderma. (Progressive systemic sclerosis). Ann N Y Acad Sci 1967;141:613-29.
68. Balonov K, Khodorova A, Strichartz GR. Tactile allodynia initiated by local subcutaneous endothelin-1 is prolonged by activation of TRPV-1 receptors. Exp Biol Med 2006;231:1165-70.
69. Suzuki T, Shimizu T, Yu HP, Hsieh YC, Choudhry MA, Schwacha MG, *et al.* Tissue compartment-specific role of estrogen receptor subtypes in immune cell cytokine production following trauma-hemorrhage. Appl Physiol 2007;102:163-8.
70. Kwon YH, Jung SY, Kim JW, Lee SH, Lee JH, Lee BY, *et al.* Phloroglucinol inhibits the bioactivities of endothelial progenitor cells and suppresses tumor angiogenesis in LLC-tumor-bearing mice. PLoS One 2012;7:e33618.
71. Ireland DJ, Greay SJ, Hooper CM, Kissick HT, Filion P, Riley TV, *et al.* Topically applied Melaleucaalternifolia (tea tree) oil causes direct anti-cancer cytotoxicity in subcutaneous tumour bearing mice. J Dermatol Sci 2012;67:120-9.

Cite this article as: Citation will be included before issue gets online***

Source of Support: Nil, **Conflict of Interest:** None declared.

Author Queries???

AQ1: Kindly provide editable image

AQ2: Kindly provide expansion

Anexo 2

TRABALHOS PUBLICADOS

FEBS Open Bio 4 (2014) 153–161

journal homepage: www.elsevier.com/locate/febsopenbio

A novel cell-penetrating peptide derived from WT1 enhances p53 activity, induces cell senescence and displays antimelanoma activity in xeno- and syngeneic systems☆

Mariana H. Massaoka, Alisson L. Matsuo, Carlos R. Figueiredo, Natalia Girola, Camyla F. Faria, Ricardo A. Azevedo, Luiz R. Travassos*

Experimental Oncology Unit (UNONEX), Department of Microbiology, Immunology and Parasitology, Federal University of São Paulo (UNIFESP), São Paulo, SP 04023-062, Brazil

ARTICLE INFO

Article history:
Received 10 December 2013
Received in revised form 7 January 2014
Accepted 14 January 2014

Keywords:
Malignant melanoma
Wilms tumor 1 (WT1)
Senescence
p53

ABSTRACT

The Wilms tumor protein 1 (WT1) transcription factor has been associated in malignant melanoma with cell survival and metastasis, thus emerging as a candidate for targeted therapy. A lysine–arginine rich peptide, WT1-pTj, derived from the ZF domain of WT1 was evaluated as an antitumor agent against A2058 human melanoma cells and B16F10-Nex2 syngeneic murine melanoma. Peptide WT1-pTj quickly penetrated human melanoma cells and induced senescence, recognized by increased SA-β-galactosidase activity, enhanced transcriptional activity of p53, and induction of the cell cycle inhibitors p21 and p27. Moreover, the peptide bound to p53 and competed with WT1 protein for binding to p53. WT1-pTj treatment led to sustained cell growth suppression, abrogation of clonogenicity and G2/M cell cycle arrest. Notably, *in vivo* studies showed that WT1-pTj inhibited both the metastases and subcutaneous growth of murine melanoma in syngeneic mice, and prolonged the survival of nude mice challenged with human melanoma cells. The 27-amino acid cell-penetrating WT1-derived peptide, depends on C^3 and H^{16} for effective antimelanoma activity, inhibits proliferation of WT1-expressing human tumor cell lines, and may have an effective role in the treatment of WT1-expressing malignancies.

1. Introduction

The Wilms tumor protein 1 (WT1) is a transcription factor that plays an important role in cellular development and cell survival. It is abnormally expressed in several human cancers and could be a target of therapeutic agents. Structurally, the WT1 protein contains four C_2H_2 Krüpple-like zinc-fingers (ZF) in the C-terminal domain, which are important for DNA binding, RNA binding and interaction with other proteins [1]. Originally described as a tumor suppressor gene in pediatric nephroblastoma [2,3], the overexpression, conformational changes and cytoplasmic localization of WT1 in different malignancies such as mesothelioma, ovarian cancer, leukemia, osteosarcomas, glioblastomas and malignant melanomas [4,5] demonstrated oncogenic properties of this protein. In malignant melanoma, the most aggressive and lethal form of skin cancer, WT1 expression has been reported in more than 80% tumor cells but not in epidermal keratinocytes, melanocytes and benign melanocytic nevi *in vivo* [6]. Notably, RNAi silencing of WT1 induces apoptosis in B16F10 murine melanoma cells [7] and displays antimetastatic activity [8].

The oncogenic role of WT1 in cancer stimulates attempts at neutralizing this tumor-associated antigen. Recently, the anticancer therapy that employs peptides, which can directly target cancer cells, has emerged as an alternate strategy to restrain the progression of tumor growth and metastases [9]. Antitumor peptides may act binding to and inhibiting oncogenes or proteins with aberrant expression in tumor cells. They cause cell cycle arrest and/or induce apoptosis, block signaling mediators and receptors, inhibit angiogenesis, and mediate tumor environment homing of cytotoxic peptide sequences [10–15]. Certain peptides are cell-penetrating (CPPs) or Trojan peptides, with short amphipathic and cationic sequences that permit their penetration across the cell membrane, and thus exert direct anticancer activity [16]. These peptides may be carriers of a variety of antitumor molecules [17,18].

In the present work, we show that a novel WT1-derived peptide (WT1-pTj) is a cell-penetrating antitumor agent that suppresses both proliferation and clonogenicity of B16F10-Nex2 melanoma cells

---

Abbreviations: C PEP, control peptide; CL-ELISA, chemiluminescence ELISA; CPP, cell-penetrating peptide; pTj, Trojan peptide; SA-βGal, senescence-associated β-galactosidase; TMZ, Temozolomide; WT1, Wilms tumor protein 1; ZF, zinc-finger.

* Corresponding author. Address: Unidade de Oncologia Experimental (UNONEX), Universidade Federal de São Paulo (UNIFESP), Rua Botucatu 862, 8 andar, São Paulo, SP 04023-062, Brazil. Tel.: +55 11 5576 4551; fax: +55 11 5571 5877.

E-mail address: travassos@unifesp.br (L.R. Travassos).

2211-5463/$36.00 © 2014 The Authors. Published by Elsevier B.V. on behalf of Federation of European Biochemical Societies. All rights reserved.
http://dx.doi.org/10.1016/j.fob.2014.01.007

through an irreversible G2/M cell cycle arrest and induction of cellular senescence. In addition to morphological changes and irreversible growth inhibition, senescent cells expressed the senescence-associated β-galactosidase and formed hetero-chromatin foci [19], associated with enhanced transcriptional activation of p53, and accumulation of cyclin-dependent kinase inhibitors $p21^{Cip1}$ and $p27^{Kip1}$, which have been used as markers of senescence [20].

Most importantly, WT1-pTj displayed a remarkable antimetastatic activity in the syngeneic B16F10-Nex2 melanoma model and prolonged survival of nude mice subcutaneously challenged with human A2058 melanoma cells. Both results emphasize the potential of this novel antitumor peptide to be developed as a therapeutic drug.

The potential use of bioactive peptides as anti-cancer drugs has been investigated in our laboratory and considerable progress has been made using peptides derived from immunoglobulins and from transcription factors [21,22].

2. Materials and methods

2.1. Peptides

A 27-residue synthetic peptide (WT1-pTj) corresponding to amino acids 349–375 of the human WT1 protein (GenBank: CAI95758) and the control peptide (C PEP, with C3A and H16A) were synthesized by Peptide 2.0 Inc. (Chantilly, VA) at 90–99% purity, with amidated C-terminal amino acid, and were completely solubilized in PBS or culture medium. The WT1-pTj peptide is 100% identical to the related sequence of mouse WT1 protein, corresponding to amino acids 426–452 (GenBank: NP659032). Structures and molecular masses of the peptides are depicted on Table 1.

2.2. Cell lines and culture conditions

Cell lines were originally obtained from Ludwig Institute for Cancer Research, São Paulo, Brazil, or donated by Prof. Luis F. Lima Reis, Hospital Sirio-Libanez, São Paulo, Brazil. These are long established cell lines, acquired from public culture collections or transferred from Ludwig Institute in New York, and maintained in appropriate conditions to serve as standard tumor cell lines for local studies and collaborative research. Animal experiments were carried out using protocols approved by the Ethics Committee for Animal Experimentation of Federal University of Sao Paulo, Brazil (CEP No. 1280/10).

The murine melanoma B16F10-Nex2 subline was established at the Experimental Oncology Unit (UNONEX), Federal University of São Paulo, UNIFESP, as described [23] and used ever since in subcutaneous and metastatic syngeneic models in mice. The human tumor cell lines A2058 and SK-MEL-28 (melanoma), MCF-7 and MDA-MB231 (breast carcinoma), OVCAR-3 (ovarian carcinoma) and HL-60 (acute leukemia) were maintained in complete medium consisting of RPMI-1640 (Gibco, Grand Island, NY) supplemented with 10 mM N-2-hydroxyethylpiperazine-N_2 ethanesulphonic acid (HEPES; Sigma–Aldrich, St. Louis, MO), 24 mM sodium bicarbonate, 40 mg/l gentamicin (Hipolabor, Minas Gerais, Brazil), pH 7.2, and 10% fetal bovine serum (FBS; Gibco, Grand Island, NY).

The human fibroblast cell line HFF and mouse embryonic fibroblasts (MEFs) were a gift from Luis F. Lima Reis, Hospital Sirio-Libanez, São Paulo. The HFF cell line was maintained in minimum essential medium Eagle (Gibco, Grand Island, NY) with 2 mM L-glutamine and Earle's balanced saline solution adjusted to contain 1.5 g/l sodium bicarbonate, 0.1 mM non-essential amino acids, and 1.0 mM sodium pyruvate, and 10% FBS. MEF cell line was maintained in DMEM (Gibco, Grand Island, NY) medium supplemented as described above. All cell lines were cultured at 37 °C, in humid atmosphere and 5% CO_2.

2.3. Confocal microscopy

A2058 human melanoma cells (4×10^4) were plated in round coverslips and incubated at 37 °C for 24 h. Cells were treated with 0.5 mM fluorescein isothiocyanate (FITC)-labeled-WT1-pTj for 1 h at 37 °C. After incubation, tumor cells were fixed and permeabilized with methanol for 15 min at room temperature, followed by blocking with 0.2% gelatin for 10 min at 37 °C. Nuclear staining was carried out with 10 μg/ml of DAPI (Invitrogen, Eugene, OR). Cells were then washed in PBS and coverslips mounted onto slides with 4 μl Vectashield (Sigma, St. Louis, MO) and imaged using a Carl Zeiss LSM780 confocal microscope (Jena, Germany).

For time dependent WT1-pTj localization, A2058 cells were incubated for 15 min, 1 and 24 h with 0.5 mM biotinylated-WT1-pTj (b-WT1-pTj), washed 3 times in PBS, and fixed with 3.7% paraformaldehyde for 30 min. Cells were then permeabilized in 0.1% Triton X-100 for 30 min followed by blocking for 1 h with 150 mM NaCl, 50 mM Tris and 0.25% BSA, all from Sigma–Aldrich, MO. After washing in PBS, cells were incubated with 10 μg/ml DAPI and streptavidin-FITC (1:200 from stock solution) used as secondary fluorophore for biotinylated peptide, and were both incubated for 15 min at 37 °C. Stained cells on coverslips were examined for peptide intracellular localization using a Confocal Leica SP5 microscope with a 100 × oil immersion objective (Leica, Wetzlar, Germany). The *Z* series was acquired according to sampling criteria built into the software for sequential imaging of DAPI, which stains the nucleus (blue, excitation/emission = 350/470 nm) and FITC, which monitors peptide localization (green, at excitation/emission = 488/525 nm). Images were processed with the ImageJ software (http://rsb.info.nih.gov/ij/).

2.4. Cell viability

The effects of WT1-pTj and C PEP on cell viability were determined by Trypan blue exclusion assay. For EC_{50} determination, cells (5×10^3/well) were seeded and cultivated in 96-well plates for 12 h at 37 °C. Cells were incubated with increasing concentrations of the peptides (0–1 mM) for 24 h, were detached with Trypsin–EDTA 0.25% solution (Sigma–Aldrich, St. Louis, MO) and the number of viable cells counted using a Neubauer chamber (Electron Microscopy Sciences, Hatfield, PA). The growth kinetics of A2058 cells (10^3/well) during 96 h in presence of WT1-pTj or C PEP at different concentrations was determined by cell counting every 24 h.

2.5. Colony formation

Anchorage-independent growth of peptide-treated melanoma cells was determined in soft agar. A2058 cells (10^3) in culture medium with 10% FBS, 0.35% agar and 0.5 mM WT1-pTj or C PEP, were plated on a bottom agar layer containing medium, 10% FBS and 1% agar in a 6-well culture plate. After 6 days of cell plating, more peptide (0.5 mM WT1-pTj or C PEP) and culture medium (300 μl) were added to the corresponding wells. Colonies were stained with 0.5% crystal violet in 70% ethanol and counted 11 days after initial treatment using a vertical microscope.

Alternatively, clonogenicity was tested in peptide-treated A2058 cells (10^3) seeded in 6-well plates. After 5 days, 500 μl of 0.5 mM WT1-pTj or C PEP or culture medium were added in the corresponding wells. 10 days after plating, colonies were stained with 0.5% crystal violet in 70% ethanol for 10 min and counted in a stereomicroscope.

To assess the colony formation ability after drug removal, A2058 cells (10^3) were left untreated or treated with 0.5 mM WT1-pTj, 0.5 mM C PEP or 0.5 mM Temozolomide (TMZ; Sigma–Aldrich, St. Louis, MO). After 4 days, cells were harvested and equal numbers of untreated and treated cells were seeded (10^3) in 6-well plates and cultivated for additional 4 days in fresh media. Colonies were stained and quantified as mentioned above.

Table 1.
Peptide sequences and molecular mass.

Name	Sequence	Mass (Da)
WT1-pTj	KDCERRFSRSDQLKRHQRRHTGVKPFQ-NH_2	3395.84
b-WT1-pTj	biotin-CGGKDCERRFSRSDQLKRHQRRHTGVKPFQ-NH_2	3839.38
FITC-WT1-pTj	KDCERRFSRSDQLKRHQRRHTGVKPFQK-FITC	3914.53
C PEP	KDAERRFSRSDQLKRAQRRHTGVKPFQ-NH_2	3297.71

2.6. Chemiluminescence ELISA (CL-ELISA)

Binding of p53 to WT1-pTj was examined by CL-ELISA. Recombinant p53 (Novus Biotechnology, Littleton, CO), 100 ng in 50 μl of carbonate buffer (15 mM Na_2CO_3, 35 mM $NaHCO_3$, 0.2 g/l NaN_3, pH 9.6) was left to adhere overnight at 4 °C onto wells of maxisorp opaque ELISA plates (Nunc^{TM}, Nalge Nunc International, Dusseldorf, Germany). Plates were blocked for 1 h at 37 °C with 1% BSA in PBS-Tween 0.05%. After 3 washes in PBS-Tween 0.05%, 1 μM biotinylated-WT1-pTj was incubated for 1 h at 37 °C. Streptavidin-peroxidase (1:2000; Sigma–Aldrich, St. Louis, MO) was added and the reaction was evaluated by chemiluminescence using ECL solution (Millipore, Billerica, MA) in a luminometer (SpectraMax, Molecular Devices Software Pro 5.2, Sunnyvale, CA) at 470 nm. Chemiluminescence readings are expressed as Relative Luminescence Units (RLU).

Competitive ELISA was performed to investigate whether WT1-pTj competes with WT1 protein for binding to p53. To that end, 100 ng of recombinant p53 protein in carbonate buffer was dispensed in wells of ELISA microplate (96-well) and left overnight at 4 °C. Blocking and washing preceded the addition of 100 ng of recombinant WT1 (Jena Bioscience, Jena, Germany), followed by 1-h incubation at 37 °C. After washing 3 times in PBS-Tween 0.05%, WT1-pTj or C PEP were incubated at different concentrations for 1 h at 37 °C. Binding of WT1 to p53 was detected using anti-WT1 monoclonal antibody (1:1000, Millipore, Billerica, MA). After incubation for 1 h at 37 °C, the plate was extensively washed in PBS-Tween 0.05% and the secondary anti-mouse IgG coupled to peroxidase (1:2000; Sigma–Aldrich, St. Louis, MO) was added. The plate was washed 3 times in PBS and the reaction was evaluated by chemiluminescence as described above.

2.7. Luciferase reporter assay

Detection of p53 activity was performed using the Cancer 10-pathway Reporter Array (SA Biosciences, Fredrick, MD) following the manufacturer's instructions. After A2058 melanoma cells transfection, they were left untreated or treated with 0.5 mM WT1-pTj or 0.5 mM C PEP, and further incubated for 24 h. Luciferase activity was measured using the Dual Luciferase Assay system (Promega, Madison, WI) on a luminometer (SpectraMax, Molecular Devices Software Pro 5.2, Sunnyvale, CA). Firefly luciferase was the experimental reporter and *Renilla* luciferase was the internal control for normalizing transfection efficiencies.

2.8. SA-β-galactosidase activity

A2058 cells (10^3) were cultivated in 6-well plates and then left untreated or treated with 0.5 mM WT1-pTj, 0.5 mM C PEP or 0.5 mM TMZ (Positive control) [24] for 4 days. Cells were washed to remove the peptides and TMZ, following incubation with complete fresh medium for additional 3 days. SA-β-galactosidase activity was detected with the Senescence β-galactosidase Kit (Cell Signaling, Beverly, MA), following the manufacturer's instructions. To quantify SA-β-galactosidase activity, at least 100 cells were counted in three random fields using an inverted light microscope.

2.9. Lysosomal vacuolation observed with acridine orange

Lysosomes from A2058 cells (10^3/well) plated in 4-well chambers and treated or not with 0.5 mM WT1-pTj or 0.5 mM C PEP for 4 days at 37 °C, were observed following incubation with 1 μg/ml acridine orange (Sigma–Aldrich, St. Louis, MO) for 15 min. A Nikon BioStation IM-Q inverted microscope (red, excitation/emission = 490/650 nm) was used.

2.10. Cell cycle analysis

A2058 cells were seeded in 12-well plates at 2×10^5 cells per well and incubated overnight without serum for cell cycle synchronization. Cells were treated or not with 0.5 mM WT1-pTj or 0.5 mM C PEP for 24 h. After incubation, cells were harvested with trypsin–EDTA 0.25%, washed with PBS and centrifuged. Pellets were stained with propidium iodide (PI) in 0.1% Triton X-100, 0.1% sodium citrate, 50 μg/ml PI (Sigma–Aldrich, St. Louis, MO) and 300 μg/ml RNAse A (Invitrogen, Eugene, OR) for 30 min at 4 °C in the dark. Flow cytometric analysis used a FACSCanto II flow cytometer (Becton Dickinson, San Jose, CA). Post-acquisition analysis used the FlowJo software (Tree Star Inc., Ashland, OR). For evaluation of DNA content, 20,000 events were acquired from at least three independent experiments.

2.11. Western blotting

A2058 cells (10^6) treated with 0.5 mM WT1-pTj or 0.5 mM C PEP for 24 h after cell cycle synchronization or untreated cells (Control) were lysed for protein extraction with RIPA buffer (50 mM Tris–Cl, pH 7.5, 150 mM NaCl, 1% Nonidet P-40, 0.5% sodium deoxycholate, and 0.1% SDS) supplemented with protease and phosphatase inhibitors (Sigma–Aldrich, St. Louis, MO). After 20 min incubation on ice, the cell lysates were collected after centrifugation at 1500 rpm. The protein concentration of lysates was determined by Bradford method (Bio-Rad, Hercules, CA). Proteins (15 μg) were separated by SDS–PAGE and transferred to a nitrocellulose membrane (Millipore, Billerica, MA). Immunoblotting was run with antibodies against p53, phospho-p53 (Ser15, Ser392), p27, p21, cyclin B1, phospho-cdc2 (Tyr15), and β-actin, all purchased from Cell Signaling Technology (Beverly, MA). β-actin was used as the protein loading control. Secondary antibodies conjugated with IgG horseradish peroxidase were purchased from Sigma–Aldrich (St. Louis, MO) and immunoreactivity was detected using the Immobilon solution (Millipore, Billerica, MA). Protein bands were detected using the UVItec Alliance gel documentation system (UVItec, Cambridge, UK).

2.12. Experimental melanoma models in vivo

The Ethics Committee for animal experimentation of Federal University of São Paulo approved all experiments using mice, CEP No. 1280, 2010. All *in vivo* experiments were performed at least twice.

In the lung metastasis model, male, six-to-eight week-old, C57BL/6 mice were challenged e.v. with 5×10^5 syngeneic B16F10-Nex2 melanoma cells in 100 μl of PBS. Animals ($n = 5$ per group) were treated the day after tumor challenge, with 5 daily i.p. doses of 300 μg of C PEP, 300 μg of WT1-pTj or vehicle (PBS). After 14 days, lungs were collected from animals of each group, and inspected for lung colonization.

In the syngeneic subcutaneous (s.c.) tumor model, B16F10-Nex2 cells (10^5/animal) were inoculated into the right flank of C57BL/6 mice. Once nodules reached 200 mm^3, mice ($n = 5$ per group) received 5 i.p. doses of 300 μg of WT1-pTj, 300 μg of C PEP or PBS on alternate days. The human A2058 melanoma cells (4×10^6/animal) were injected subcutaneously in athymic nude mice ($n = 5$ per group), treated with 300 μg of C PEP, 300 μg of WT1-pTj or vehicle (PBS) for 5 consecutive days. Peritumor therapy started the day after inoculation of melanoma cells. The tumor volume (V), measured daily with a caliper, was calculated by the formula $V = 0.52 \times d^2 \times D$, where d and D are the short and long diameters of the tumor, respectively. Mice were sacrificed when the tumor size reached 3000 mm^3.

2.13. Statistical analysis

Data are expressed as mean values ± standard deviations (SD) of multiple replicates. All data are representative of at least two independent experiments. p-Values were calculated by Student's t-test and considered significant if less than 0.05. Statistical differences among treated groups in the s.c. tumor model were assessed by the Gehan–Breslow–Wilcoxon test. The Kaplan–Meier method was used to calculate survival curves, and log-rank test was used to compare the survival rates of different groups. All statistical analyses were done using Prism Graphpad Software (San Diego, CA).

3. Results

3.1. WT1-pTj displays effective antimelanoma activity in vivo

The WT1-pTj peptide but not the C PEP control peptide, with two amino acids replaced by alanine, significantly reduced the number of lung metastatic nodules in the syngeneic B16F10-Nex2 melanoma model (Fig. 1A). Melanoma cells were injected endovenously in C57Bl/6 mice and treatment consisted in 5 daily i.p. injections of 300 μg of either peptide or vehicle (PBS), starting the day after tumor cell challenge.

By using subcutaneous B16F10-Nex2 melanoma graft in syngeneic mice, the tumor was left to grow until it reached 200 mm^3. Peptides were then injected i.p., with 5 doses of 300 μg/animal in alternate days. WT1-pTj rather than the C PEP control clearly delayed melanoma growth, even after tumor establishment (Fig. 1B).

The WT1-pTj protective activity was also evaluated using a human melanoma xenograft in nude mice. Animals were challenged with human melanoma cells s.c., and treated daily, for 5 days, with 300 μg WT1-pTj or C PEP. Peritumor therapy started one day after inoculation of melanoma cells. As observed in Fig. 1C, WT1-pTj was effective in delaying the growth of human melanoma-bearing nude mice using *in situ* injections. Moreover, the survival of mice treated with WT1-pTj was significantly prolonged in comparison to that of the PBS and C PEP control groups (Fig. 1D).

It should be noted that in all *in vivo* experiments mice maintained healthy physical appearance, normal activity levels and normal weight throughout the study period, showing no toxic effects of peptides. Notwithstanding, an effective antimetastatic activity and a remarkable therapeutic efficacy of WT1-pTj peptide against melanoma were shown.

3.2. WT1-pTj peptide rapidly translocates into human melanoma cells

The direct effects of WT1-pTj on human melanoma cells were investigated. Considering the characteristics of the peptide, Trojan-like properties, and effects related to zinc-finger interactions could be predicted. In fact, WT1-pTj is a 27-mer lysine–arginine rich peptide, from the C-terminal region of WT1, which contains part of the second zinc-finger (ZF) domain of WT1. The analogous peptide, with alanine substitutions at cysteine-3 and histidine-16, both involved in the ZF motif, was used as a suitable control peptide (C PEP). Viable non-permeabilized A2058 human melanoma cells were exposed to 0.5 mM FITC-labeled WT1-pTj for 1 h. Using confocal microscopy, we observed that the peptide entered the cells showing a diffuse distribution in the cytoplasm and was also seen in the nucleus within 1 h, confirming the Trojan nature of the peptide (Fig. 2A).

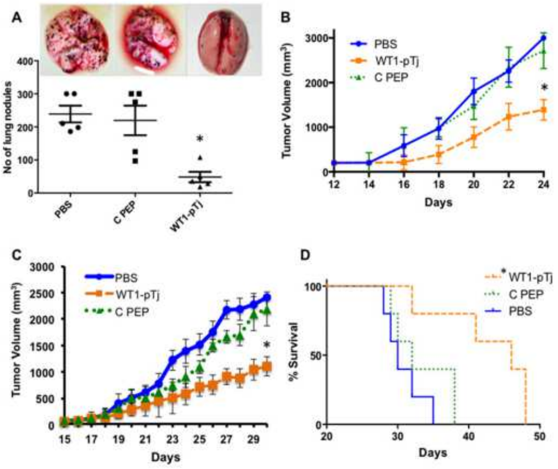

Fig. 1. Protective effect of WT1-pTj *in vivo*. (A) Lung colonization of B16F10-Nex2 endovenously inoculated in C57BL/6 mice. Animals received 5 i.p. doses of 300 μg of C PEP, 300 μg of WT1-pTj or vehicle (PBS) on consecutive days; $^*p = 0.02$ versus C PEP. (B) Effect of WT1-pTj on subcutaneous growth of B16F10-nex2 melanoma tumor. Once nodules reached 200 mm^3, mice were randomized and received 5 alternate i.p. injections of 300 μg of WT1-pTj or C PEP; $^*p < 0.05$ versus C PEP. (C) Effect of WT1-pTj on A2058 tumor growth in nude mice. Animals were treated with peritumor injections of 300 μg of WT1-pTj, 300 μg of C PEP or vehicle (PBS) for 5 consecutive days, starting on day 1 post-tumor cell challenge; $^*p < 0.05$ in comparison with C PEP. (D) Survival of nude mice grafted with human melanoma after treatment with WT1-pTj, C PEP or PBS; $n = 5$ mice per group; $^*p = 0.0185$ in comparison with C PEP.

A2058 cells were also incubated with biotinylated-WT1-pTj (b-WT1-pTj) for 15 min, 1 and 24 h, then were fixed and permeabilized, followed by incubation with streptavidin-FITC and DAPI. Images taken 15 min after exposure to 0.5 mM of b-WT1-pTj showed predominantly membrane and cytoplasmic staining. After 1 and 24 h the peptide was completely distributed in the cells, particularly in the nucleus where it colocalized with nuclear DNA (Fig. 2B).

3.3. WT1-pTj inhibits the proliferation of WT1-expressing tumor cells

The effect of WT1-derived peptide on cell viability was determined by Trypan blue exclusion staining. Assuming the potential oncogenic role of WT1 in tumor cells [25], the peptide could modify this phenotype by structural interference. WT1-pTj did not induce cell death, but inhibited the proliferation of different WT1-expressing cancer cell lines (Table 2). As indicated by EC_{50} values, WT1-pTj induced growth inhibition of B16F10-Nex2 murine melanoma cells, A2058 and SK-MEL-28 human melanoma cells, MCF-7 and MDA-MB231 human breast cancer cells and OVCAR-3 human ovarian cancer cells, and was less effective against HL-60 human leukemia cells. Treatment with the peptide blocked cell proliferation but did not induce a death mechanism *in vitro*. No effect on the proliferation of normal murine or human fibroblasts was detected, showing a selective activity of WT1-pTj on tumor cells.

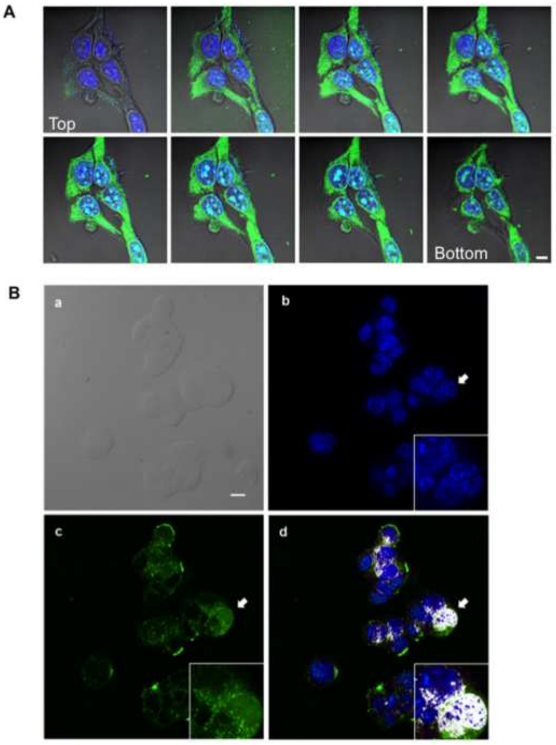

Fig. 2. Intracellular distribution of WT1-pTj in A2058 human melanoma cells. (A) Cells were treated with FITC-labeled WT1-pTj for 1 h at 37 °C and visualized by confocal microscopy. Sequence (Z-stacks) showing the distribution of FITC-labeled peptide (green) and the nuclei stained with DAPI (blue). Bar = 10 μm. (B) Co-localization of WT1-pTj and nuclear DNA in human melanoma cells. A2058 cells were treated with biotinylated WT1-pTj for 24 h, fixed with paraformaldehyde, and permeabilized with Triton X-100. (a) Differential interference contrast (DIC) image; (b) Cells stained with DAPI; (c) Cells treated with streptavidin-FITC; (d) Merge, showing nuclear colocalization of WT1-pTj. Inserts: high magnification of cells indicated by arrows. Scale bar = 10 μm. (For interpretation of the references to colour in this figure legend, the reader is referred to the web version of this article.)

Table 2.
Antiproliferative activity of WT1-pTj on WT1-expressing tumor cell lines and nontumor forming cell lines.

Cell lines	EC_{50}[a] (mol/l x 10^{-3})
A2058 human melanoma	0.455 ± 0.032
SK-MEL-28 human melanoma	0.680 ± 0.020
B16F10-Nex2 murine melanoma	0.466 ± 0.067
MCF-7 human breast cancer	0.247 ± 0.058
MDA-MB231 human breast cancer	0.759 ± 1.40
OVCAR-3 human ovarian cancer	0.208 ± 0.02
HL-60 human acute leukemia	>1
HFF human foreskin fibroblast	>1
MEF murine embryonic fibroblast	>1

[a] EC50 is the concentration that decreases viability by 50% in a dose-dependent survival curve.

3.4. *WT1-pTj but not C PEP displays strong antiproliferative effects on human melanoma cells*

Since *WT1* gene is essential for melanoma cells proliferation and metastasis [26,27,8] we examined whether WT1-pTj and more specifically, the truncated ZF-motif of WT1-pTj, displayed anti-melanoma proliferative effects. Human A2058 melanoma cells were incubated with WT1-pTj or C PEP (A^3C, $A^{16}H$) at 0.125 to 0.5 mM and the cell number of viable cells determined every 24 h for 4 days. We found that treatment with WT1-pTj resulted in a dose-dependent inhibition of proliferation of melanoma cells when compared to untreated cells. The number of cells remained stable from 24 to 96 h when treated with WT1-pTj at 0.5 mM, suggesting that the peptide had a sustained cytostatic effect on these cells. No significant changes on proliferation were observed in C PEP-treated cells, except at the highest dose after 96 h of incubation (Fig. 3A).

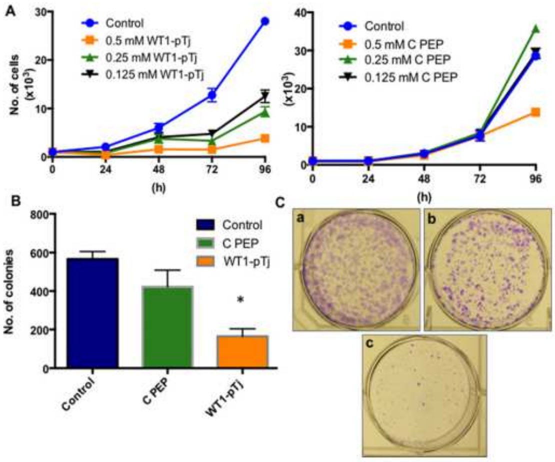

Fig. 3. Effects of WT1-pTj on proliferation and clonogenic ability of human melanoma cells. (A) A2058 cells (10^3/well) were treated with WT1-pTj (left) or C PEP (right) at the indicated concentrations for 96 h, and cell proliferation was daily monitored by Trypan blue exclusion assay; (B) A2058 cells were suspended in 300 μl of 0.5 mM WT1-pTj, 0.5 mM C PEP, or unsupplemented culture medium (Control) and cultivated on soft-agar medium. The number of colonies was determined 11 days after the first treatment; $^*p < 0.02$. (C) Representative photomicrographs of colony formation assay. A2058 cells were plated on (a) untreated culture medium (Control), (b) medium treated with 0.5 mM C PEP, or (c) treated with 0.5 mM WT1-pTj. After 5 days, culture media were aspirated and fresh medium with the respective peptides at 0.5 mM was added. After 10 days incubation, colonies were stained with crystal violet and counted on a stereomicroscope. Data represent means ± SD of three independent experiments. (For interpretation of the references to colour in this figure legend, the reader is referred to the web version of this article.)

Han et al. [28] reported on the transfection of MCF-7 human breast cancer cells with constructs containing only the ZF domains of WT1 and consequent reduction in the expression of proteins important for the survival and tumor cell proliferation, such as c-myc, Bcl-2 and amphregulin, also interfering with the clonogenic ability of breast cancer cells. Based on these findings we tested the influence of WT1-pTj on tumor cell clonogenicity. As observed, treatment with 0.5 mM WT1-pTj drastically decreased the number of A2058 colonies both in semi-solid soft-agar medium (Fig. 3B) and directly in culture plates (Fig. 3C), when compared to untreated or C PEP-treated cells. In the anchorage-independent growth assay in soft-agar, treatment with WT1-pTj reduced colony formation by 70.8%, as compared to 25.4% with C PEP. Quantification of cell growth on plates showed only 20 colonies after WT1-pTj treatment for 9 days, whereas cell incubation in unsupplemented complete culture medium or with 0.5 mM PEP C, resulted in 300 and 248 colonies, respectively.

3.5. *WT1-pTj enhances the transcriptional activity of p53 in melanoma cells and competes with WT1 protein for binding to p53*

WT1 binds to DNA and can interact also with several intracellular proteins [29]. A physical and functional association between WT1 and the product of *p53* tumor suppressor gene [30] has been demonstrated. Such interaction was shown to cross-modulate transactivation properties. WT1 interacts with p53 through zinc fingers 1 and 2, stabilizes p53, enhances p53-mediated transcriptional activation, and antagonizes p53-mediated apoptosis triggered by ultraviolet radiation [31].

Since the sequence of WT1-pTj covers part of a ZF motif involved

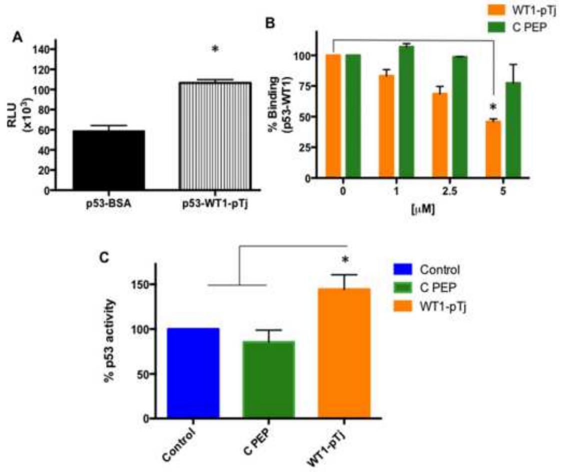

Fig. 4. Binding of WT1-pTj to p53, displacement of p53 bound to WT1, and WT1-pTj modulation of transcriptional activity of p53. (A) The interaction between p53 and WT1-pTj was determined using biotinylated peptide and CL-ELISA; $^*p < 0.01$. (B) Competitive inhibition of WT1 association to p53 was evaluated in wells coated with recombinant p53, incubated with WT1 and then exposed to WT1-pTj or C PEP at indicated concentrations. Binding of p53 to WT1 was quantified with anti-WT1 monoclonal antibody; $^*p < 0.02$ compared to C PEP effect. (C) A2058 cells were transfected with the p53-responsive luciferase reporter construct, and then treated with 0.5 mM WT1-pTj or 0.5 mM C PEP for 24 h. The ratio of firefly to Renilla luciferase was determined and normalized to the value obtained for untreated cells (=100%). Data are representative of two independent experiments. $^* p < 0.02$ compared to Control (untreated) and C PEP systems.

in the p53 interaction [31] we considered the possibility that the peptide might also bind to p53. As shown in Fig. 4A, CL-ELISA using recombinant p53 and biotinylated WT1-pTj confirmed the association between the peptide and the protein. In addition, using competitive ELISA we verified that WT1-pTj dose-dependently inhibited WT1-p53 complex formation (Fig. 4B). Further, in A2058 melanoma cells transfected with a p53-responsive luciferase reporter construct, WT1-pTj (but not C PEP) enhanced p53 transcriptional activation (Fig. 4C). Together, these results suggest that WT1-pTj interacts with p53, and may decrease the association between p53 and WT1. In parallel, it caused p53 access to specific transcriptional response elements on DNA.

3.6. *WT1-pTj induces G2/M cell cycle arrest and senescence features in human melanoma cells*

The cell cycle of melanoma cells was examined by flow cytometry to better characterize the mechanism by which WT1-pTj suppresses tumor cell proliferation. Treatment with WT1-pTj effectively arrested the cell-cycle progression in A2058 cells, depleting the S-phase compartment (from 20.2% to 6% when compared to Control) and increasing the G2/M (from 10.5% to 27% when compared to Control) phase compartment (Fig. 5A). A2058 cells treated with C PEP showed no significant differences regarding the cell cycle profile when compared to the Control system, suggesting that the ZF-coordinating region is essential for the antiproliferative effects.

In addition, we evaluated the predominant signal pathways arbitrating cell cycle arrest in human melanoma cells under peptide treatment. As shown in Fig. 5B, by Western blotting analysis we determined that total p53 levels were not significantly affected in cells treated with WT1-pTj. Nevertheless, a decrease in serine 392 phosphorylation and an increase in serine 15 phosphorylation were observed upon WT1-pTj treatment. Additionally, increased levels of both p27$^{\mathrm{Kip1}}$ and p21$^{\mathrm{Cip1}}$, known to regulate both G1–S and G2–M transitions, were detected in WT1-pTj-treated cells. Furthermore, in order to elucidate the nature of the cell-cycle arrest caused by WT1-pTj, we examined the expression of cell cycle-regulating factors at the G2/M phase. We found that the protein levels of cyclin B1 and phospho-cdc2 (Tyr15) were markedly down regulated in WT1-pTj-treated A2058 cells. These results associate the inhibitory effects of WT1-pTj to blocking of the cell cycle progression at G2/M phase and modulation of p53 and downstream signaling cascades.

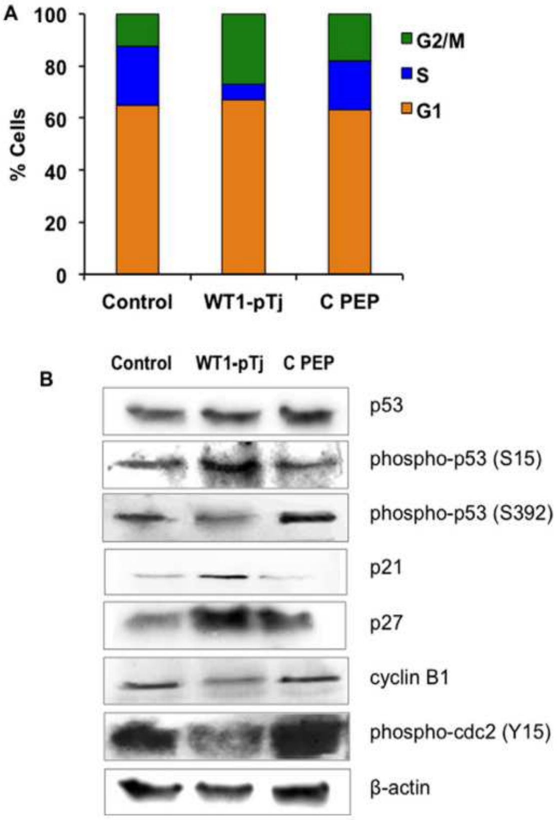

Fig. 5. Effect of WT1-pTj on cell cycle progression and modulation of p53, and downstream mediators, in human melanoma cells. (A) A2058 cells were treated either with 0.5 mM WT1-pTj or 0.5 mM C PEP, for 24 h, and the cell cycle profile was examined by flow cytometry. Control, unsupplemented culture medium. Results are representative of three independent experiments. (B) Cellular extracts from A2058 cells exposed to 0.5 mM WT1-pTj or 0.5 mM C PEP were subjected to immunoblotting with antibodies specific for p53, phospho-p53, p27, p21, phospho-cdc2 and cyclin B1. Protein load was normalized to β-actin.

Several reports have shown the central role of p53 in controlling senescence [32], which is characterized by stable and irreversible loss of cell proliferation [33]. Particularly in melanoma, telomere dysfunction [34] oncogene activation [35] and anticancer agents [36] can activate p53 and its signaling partners (e.g. p16$^{\mathrm{Ink4A}}$, Rb and p21$^{\mathrm{Cip1}}$), which are thus implicated in the suppression of tumor initiation and progression.

Owing to the up-regulation of p53 activity, along with the morphological changes (e.g. large cells and cytoplasmic vacuolization) and the sustained inhibition of cellular proliferation observed in WT1-pTj-treated cells, we hypothesized that the peptide could induce cellular senescence. A2058 cells were incubated with WT1-pTj, C PEP or TMZ (positive control) or in unsupplemented culture medium (Control), for 4 days. Cells were washed to remove the peptides and incubated for additional 4 days in fresh medium. Melanoma cells barely resumed proliferation after removing WT1-pTj (Fig. 6A). Further, as depicted in Fig. 6B, the remaining cells treated with WT1-pTj exhibited altered morphology and stained positively for SA-β-galactosidase (72%), a

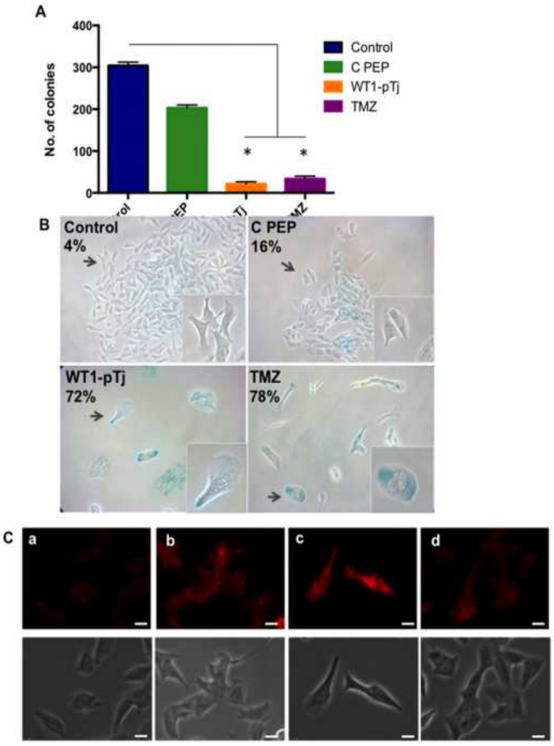

Fig. 6. Induction by WT1-pTj of cellular senescence in human melanoma cells. (A) Quantification of colonies formed after removal of the peptides and TMZ. A2058 cells were treated with WT1-pTj, C PEP and TMZ for 4 days. Cells were detached and equal numbers of untreated and treated cells were seeded and cultivated in fresh media for additional 4 days. The number of colonies was scored in three independent experiments performed in duplicates; $^*p < 0.01$ compared to Control and C PEP. (B) Representative photomicrographs (original magnification 400 ×) of A2058 cells treated with 0.5 mM WT1-pTj, C PEP or TMZ (positive control) for 4 days. Thereafter the peptides and TMZ were washed out and cells were stained for SA-β-Gal after incubation for additional 3 days in fresh media. Positive cells for SA-β-Gal were visualized under a phase contrast microscope and expressed as percentage of total cells counted at random. (C) Acridine orange was used to stain acidic vesicular organelles in untreated control cells (a); serum starved cells for 24 h (positive control) (b); cells treated with 0.5 mM WT1-pTj (c); cells treated with C PEP (d), for 4 days. Images are representative of two independent experiments performed in duplicates. Bars = 10 μM.

widely used senescence biomarker [36]. In contrast, C PEP caused little reduction in the number of colonies as compared to untreated cells, and a minor effect on senescence induction (16%) when compared to WT1-pTj. Thus, the proliferative capacity of WT1-pTj-treated cells was lost even upon removal of the peptide.

The SA-β-galactosidase has been shown to be a manifestation of residual lysosomal activity after alkalinization, only detectable due to the increased lysosomal content in senescent cells [37]. Therefore, we examined the lysosomal content in melanoma cells treated either with WT1-pTj or C PEP, using the lysosomotropic agent acridine orange. Staining of A2058 cells with acridine orange showed a marked increase in the number and size of lysosomes in senescent cells after treatment with 0.5 mM WT1-pTj for 4 days as visualized by fluorescence microscopy (Fig. 6C). Most of the C PEP-treated cells exhibited minimal red fluorescence. These results, along with the molecular mechanism underlying WT1-pTj-induced growth arrest, strongly suggest that WT1-pTj-treated cells undergo cellular senescence.

4. Discussion

Peptide-based antitumor therapy explores the high affinity and specificity of peptides for particular targets, the low toxicity and good tissue penetration [38]. Our laboratory has focused on antitumor peptides derived from internal sequences of immunoglobulins and transcription factors [22]. In the current study, we report on a peptide derived from WT1, endowed with anti-melanoma properties. Both human melanoma and B16F10 murine melanoma were sensitive to the WT1-pTj Trojan peptide.

WT1 called our attention due to its high expression and immunogenicity in B16F10 murine melanoma (unpublished results). In comparison with human cancer, WT1 has emerged as an important target expressed in hematologic and solid tumors. There is, indeed, plenty of evidence supporting the role of WT1 in the oncogenic process of melanoma. The function of WT1 in transcriptional regulation, as well in RNA metabolism and translation, has been extensively reviewed [25,39]. WT1 overexpression has been detected in melanoma patients' samples and melanoma cells, whereas no WT1 staining has been observed in the majority of benign melanocytic nevi, epidermal keratinocytes and melanocytes [4,40]. RNAi silencing of WT1 inhibited melanoma proliferation associated with down-regulation of nestin and zyxin [6], sensitized B16F10 cells to conventional chemotherapeutic agents (e.g. doxorubicin and cisplatin) and reduced lung metastases, emphasizing WT1 function in melanoma progression [8].

The WT1-pTj peptide contains part of a particularly reactive zinc-finger domain, and owing to its abundant basic amino acid composition, exhibits cell-penetrating properties. The peptide was able to arrest tumor cell growth and induce senescence in human melanoma cells. A significant antimelanoma activity *in vivo* was also observed using subcutaneous and metastatic models in mice. Increased levels of active p53 and enhanced transcriptional activation were associated with WT1-pTj-induced senescence in A2058 human melanoma cells. Cyclin-dependent kinase inhibitors $p27^{Kip1}$ and $p21^{Cip1}$ mediated the sustained cell cycle arrest. The typical senescent phenotype in WT1-pTj-treated cells included enlarged cytoplasm, and cellular increase of both SA-β-galactosidase activity and lysosomal content. To exert its activities, peptide WT1-pTj, like WT1, does not bind to p53 promoter but physically interacts with the p53 protein itself. In fact, we have shown that the peptide competes with WT1 for protein binding to p53, supporting the hypothesis that the peptide may prevent important interactions of WT1 with its partners, including p53, and therefore disturb relevant pro-tumor signaling of the original protein via the ZF domain. Protein-protein interaction of WT1 with p53 modulates binding to different promoters determining gene expression or repression. As with WT1, we demonstrated that peptide WT1-pTj activated p53 to act as a transcription factor in a luciferase gene expression system.

Therapy-induced senescence is a novel therapeutic approach to treat cancers [41]. Standard chemotherapy and radiotherapy, besides inducing DNA damage and cytotoxicity, may trigger a robust senescence response *in vitro* and *in vivo* [42,43]. Pro-senescence therapy may also be achieved with greatly reduced toxicity.

The molecular mechanism underlying therapy-induced senescence conferred by WT1-pTj treatment depends on p53 transcriptional activation and is correlated with p53 post-transcriptional phosphorylation at Ser15 and Ser392. Consistent with previous findings that have reported on specific changes in p53, a sustained treatment triggers a p53-dependent senescence program. Prolonged β-interferon stimulation switched on p53 in two steps involving first, dephosphorylation at serine 392, and then, phosphorylation of p53 at serine 15 leading to its transcriptional activity [44]. Similar posttranslational modifications of p53 were observed in replicative senescence in human fibroblasts [45].

Likewise in WT1-pTj induced senescence of melanoma cells, reduced phosphorylation at S392 and increased phosphorylation at S15, were observed. Activation of p53 by phosphorylation, rendering an important effector of senescence [46,47] leads to the transcriptional activation of target genes. In agreement, we observed the induction of the senescence molecular markers $p21^{Cip1}$ and $p27^{Kip1}$ [41] in A2058 cells exposed to WT1-pTj. Our results excluded p16^{Ink4A}-Rb signal activation in WT1-pTj-induced cellular senescence (data not shown), in line with previous data showing that p16 is frequently inactivated in melanoma [48,49].

Cell cycle analysis revealed that WT1-pTj inhibition of melanoma cell proliferation was caused by cell cycle arrest at G2/M phase, accompanied by a decrease in the number of cells in the S phase. The G2–M transition is positively regulated by Cdc2/cyclin B complex [50], which is controlled by phosphorylation at various sites, including the inhibitory phosphorylation at tyrosine-15 and threonine 14 by Wee1 and Myt1 [51,52]. A decrease in the levels of phospho-cdc2 (Tyr15), cdc2, cyclin A and cyclin B1 has been associated with cell cycle arrest at G2/M [53]. Similarly, we found a significant decrease in cyclin B1 and phospho-cdc2 (Tyr15) expression after treatment with WT1-pTj, in contrast with C PEP-treated cells. In conclusion, modulation of p53 activity and activation of downstream signaling is essential for senescence response in WT1-pTj-treated cells. These events depend on the ZF-coordinating region because C PEP elicited no similar response.

Given the limited expression of WT1 in adult animals, restricted to few cell types of the urogenital system [3], this factor might otherwise be an optimal target for treatment of WT1-expressing malignancies. In the field of targeted therapies, CPPs (cationic cell-penetrating peptides) have been used to overcome permeability barriers in the tumor and to mediate cargo delivery into cancer cells, leading to the development of tumor-specific molecular therapeutics. CPP-mediated transduction has been used to inhibit nuclear oncoprotein translocation [54], modulate oncoprotein signaling [10], enable apoptotic cell-death [16,55], and deliver oligonucleotides [56] to cancer cells. Presently, we show that peptide WT1-pTj exhibits trojan properties and exerts protective effects in experimental melanoma therapy. In addition to antiproliferative effects mediated by WT1-pTj treatment *in vitro*, the peptide inhibited human melanoma progression, in nude mice.

Conventional chemotherapeutic drugs act mainly through induction of apoptosis, and their reduced efficacy in melanoma patients is related to the high resistance of melanoma cells [57]. Therapy-induced senescence may represent an alternate functional approach to improve cancer therapy [58,59].

To conclude, our present study reports on the senescence-inducing peptide WT1-pTj as a promising candidate to eradicate tumor cell progression, including those that fail to respond to conventional antitumor therapies. The WT1-pTj is unique in that it derives from an oncoprotein, is cell-penetrating by itself, induces cellular senescence and effectively protects in a cancer preclinical model.

Conflict of interest statement

The authors have no conflicts of interest to declare.

Acknowledgments

The authors thank the Ludwig Institute for Cancer Research, São Paulo branch, Dr. O. Keith Okamoto from the University of São Paulo, and Dr. Luiz F. L. Reis from Sirio-Libanez Hospital for the cell lines used in the present study. The State of São Paulo Research Support Foundation (FAPESP), Brazil, supported this work through Grants 2010/51423-0 and 2012/19476-2. L.R.T. is a research fellow from the Brazilian National Research Council (CNPq).

References

[1] Yang, L. (2007) A tumor suppressor and oncogene: the WT1 story. Leukemia 21, 868–876.
[2] Call, K.M. (1990) Isolation and characterization of a zinc finger polypeptide gene at the human chromosome 11 Wilms' tumor locus. Cell 60, 509–520.
[3] Pelletier, J. (1991) WT1 mutations contribute to abnormal genital system development and hereditary Wilms' tumour. Nature 353, 431–434.
[4] Nakatsuka, S. (2006) Immunohistochemical detection of WT1 protein in a variety of cancer cells. Mod. Pathol. 19, 804–814.
[5] Oji, Y. (1999) Expression of the Wilms' tumor gene WT1 in solid tumors and its involvement in tumor cell growth. Jpn. J. Cancer Res. 90, 194–204.
[6] Wagner, N. (2008) The Wilms' tumor suppressor WT1 is associated with melanoma proliferation. Pflugers Arch. 455, 839–847.
[7] Zamora-Avila, D.E. (2007) RNAi silencing of the WT1 gene inhibits cell proliferation and induces apoptosis in the B16F10 murine melanoma cell line. Melanoma Res. 17, 341–348.
[8] Zamora-Avila, D.E. (2009) WT1 gene silencing by aerosol delivery of PEI-RNAi complexes inhibits B16-F10 lung metastases growth. Cancer Gene Ther. 16, 892–899.
[9] Thundimadathil, J. (2012) Cancer treatment using peptides: current therapies and future prospects. J. Amino Acids 2012, 967347.
[10] Giorello, L. (1998) Inhibition of cancer cell growth and c-Myc transcriptional activity by a c-Myc helix 1-type peptide fused to an internalization sequence. Cancer Res. 58, 3654–3659.
[11] Bonfanti, M. (1997) p21WAF1-derived peptides linked to an internalization peptide inhibit human cancer cell growth. Cancer Res. 57, 1442–1446.
[12] Rosca, E.V. (2011) Anti-angiogenic peptides for cancer therapeutics. Curr. Pharm. Biotechnol. 12, 1101–1116.
[13] Tan, M. (2006) Selective inhibition of ErbB2-overexpressing breast cancer *in vivo* by a novel TAT-based ErbB2-targeting signal transducers and activators of transcription 3-blocking peptide. Cancer Res. 66, 3764–3772.
[14] Cardo-Vila, M. (2010) From combinatorial peptide selection to drug prototype (II): targeting the epidermal growth factor receptor pathway. Proc. Natl. Acad. Sci. U.S.A. 107, 5118–5123.
[15] Matsuo, A.L. (2011) A new phage-display tumor-homing peptide fused to antiangiogenic peptide generates a novel bioactive molecule with antimelanoma activity. Mol. Cancer Res. 9, 1471–1478.
[16] Johansson, H.J. (2008) Characterization of a novel cytotoxic cell-penetrating peptide derived from p14ARF protein. Mol. Ther. 16, 115–123.
[17] Niesner, U. (2002) Quantitation of the tumor-targeting properties of antibody fragments conjugated to cell-permeating HIV-1 TAT peptides. Bioconjug. Chem. 13, 729–736.
[18] Massodi, I. (2009) Inhibition of ovarian cancer cell metastasis by a fusion polypeptide Tat-ELP. Clin. Exp. Metastasis 26, 251–260.
[19] Caino, M.C., Meshki, J. and Kazanietz, M.G. (2009) Hallmarks for senescence in carcinogenesis: novel signaling players. Apoptosis 14, 392–408.
[20] Bringold, F. and Serrano, M. (2000) Tumor suppressors and oncogenes in cellular senescence. Exp. Gerontol. 35, 317–329.
[21] Arruda, D.C. (2012) beta-Actin-binding complementarity-determining region 2 of variable heavy chain from monoclonal antibody C7 induces apoptosis in several human tumor cells and is protective against metastatic melanoma. J. Biol. Chem. 287, 14912–14922.
[22] Massaoka, M.H. (2013) Melanoma: perspectives of a vaccine based on peptides. In: M. Giese (Ed.), Molecular Vaccines: From Prophylaxis to Therapy. Wien: Springer-Verlag, pp. 397–412.
[23] Dobroff, A.S. (2002) Protective, anti-tumor monoclonal antibody recognizes a conformational epitope similar to melibiose at the surface of invasive murine melanoma cells. Hybrid Hybridomics 21, 321–331.
[24] Mhaidat, N.M. (2007) Temozolomide induces senescence but not apoptosis in human melanoma cells. Br. J. Cancer 97, 1225–1233.
[25] Hohenstein, P. and Hastie, N.D. (2006) The many facets of the Wilms' tumour gene, WT1. Hum. Mol. Genet. 15(Spec No 2), R196–R201.
[26] Zapata-Benavides, P. (2012) WT1 silencing by RNAi synergizes with chemotherapeutic agents and induces chemosensitization to doxorubicin and cisplatin in B16F10 murine melanoma cells. Oncol. Lett. 3, 751–755.
[27] Michiels, J.F. (2010) PPARbeta activation inhibits melanoma cell proliferation involving repression of the Wilms' tumour suppressor WT1. Pflugers Arch. 459, 689–703.
[28] Han, Y. (2007) The zinc finger domain of Wilms' tumor 1 suppressor gene (WT1) behaves as a dominant negative, leading to abrogation of WT1 oncogenic potential in breast cancer cells. Breast Cancer Res. 9, R43.
[29] Englert, C. (1998) WT1–more than a transcription factor? Trends Biochem. Sci. 23, 389–393.
[30] Maheswaran, S. (1993) Physical and functional interaction between WT1 and p53 proteins. Proc. Natl. Acad. Sci. U.S.A. 90, 5100–5104.
[31] Maheswaran, S. (1995) The WT1 gene product stabilizes p53 and inhibits p53-mediated apoptosis. Genes Dev. 9, 2143–2156.
[32] Itahana, K., Dimri, G. and Campisi, J. (2001) Regulation of cellular senescence by p53. Eur. J. Biochem. 268, 2784–2791.
[33] Larsson, L.G. (2011) Oncogene- and tumor suppressor gene-mediated suppression of cellular senescence. Semin. Cancer Biol. 21, 367–376.
[34] Sviderskaya, E.V. (2003) p16/cyclin-dependent kinase inhibitor 2A deficiency in human melanocyte senescence, apoptosis, and immortalization: possible implications for melanoma progression. J. Natl. Cancer Inst. 95, 723–732.
[35] Wajapeyee, N. (2008) Oncogenic BRAF induces senescence and apoptosis through pathways mediated by the secreted protein IGFBP7. Cell 132, 363–374.
[36] Cozzi, S.J. (2006) Induction of senescence in diterpene ester-treated melanoma cells via protein kinase C-dependent hyperactivation of the mitogen-activated protein kinase pathway. Cancer Res. 66, 10083–10091.
[37] Kurz, D.J. (2000) Senescence-associated (beta)-galactosidase reflects an increase in lysosomal mass during replicative ageing of human endothelial cells. J. Cell.

Sci. 113, 3613–3622.

[38] Bitler, B.G. and Schroeder, J.A. (2010) Anti-cancer therapies that utilize cell penetrating peptides. Recent Pat. Anticancer Drug Discov. 5, 99–108.

[39] Roberts, S.G. (2005) Transcriptional regulation by WT1 in development. Curr. Opin. Genet. Dev. 15, 542–547.

[40] Henderson, E.J. and Pentland, B. (1991) Home pass assessment in neurorehabilitation practice. J. Adv. Nurs. 16, 1439–1443.

[41] Nardella, C. (2011) Pro-senescence therapy for cancer treatment. Nat. Rev. Cancer 11, 503–511.

[42] te Poele, R.H. (2002) DNA damage is able to induce senescence in tumor cells *in vitro* and *in vivo*. Cancer Res. 62, 1876–1883.

[43] Sidi, R. (2011) Induction of senescence markers after neo-adjuvant chemotherapy of malignant pleural mesothelioma and association with clinical outcome: an exploratory analysis. Eur. J. Cancer 47, 326–332.

[44] Moiseeva, O. (2006) DNA damage signaling and p53-dependent senescence after prolonged beta-interferon stimulation. Mol. Biol. Cell 17, 1583–1592.

[45] Webley, K. (2000) Posttranslational modifications of p53 in replicative senescence overlapping but distinct from those induced by DNA damage. Mol. Cell. Biol. 20, 2803–2808.

[46] Herbig, U. (2004) Telomere shortening triggers senescence of human cells through a pathway involving ATM, p53, and p21(CIP1), but not p16(INK4a). Mol. Cell 14, 501–513.

[47] Di Micco, R. (2006) Oncogene-induced senescence is a DNA damage response triggered by DNA hyper-replication. Nature 444, 638–642.

[48] Castellano, M. (1997) CDKN2A/p16 is inactivated in most melanoma cell lines. Cancer Res. 57, 4868–4875.

[49] FitzGerald, M.G. (1996) Prevalence of germ-line mutations in p16, p19ARF, and CDK4 in familial melanoma: analysis of a clinic-based population. Proc. Natl. Acad. Sci. U.S.A. 93, 8541–8545.

[50] Innocente, S.A. (1999) p53 regulates a G2 checkpoint through cyclin B1. Proc. Natl. Acad. Sci. U.S.A. 96, 2147–2152.

[51] McGowan, C.H. and Russell, P. (1993) Human Wee1 kinase inhibits cell division by phosphorylating p34cdc2 exclusively on Tyr15. EMBO J. 12, 75–85.

[52] Wells, N.J. (1999) The C-terminal domain of the Cdc2 inhibitory kinase Myt1 interacts with Cdc2 complexes and is required for inhibition of G(2)/M progression. J. Cell. Sci. 112, 3361–3371.

[53] Deep, G. (2006) Silymarin and silibinin cause G1 and G2-M cell cycle arrest via distinct circuitries in human prostate cancer PC3 cells: a comparison of flavanone silibinin with flavanolignan mixture silymarin. Oncogene 25, 1053–1069.

[54] Lin, Y.Z. (1995) Inhibition of nuclear translocation of transcription factor NF-kappa B by a synthetic peptide containing a cell membrane-permeable motif and nuclear localization sequence. J. Biol. Chem. 270, 14255–14258.

[55] Selivanova, G. (1997) Restoration of the growth suppression function of mutant p53 by a synthetic peptide derived from the p53 C-terminal domain. Nat. Med. 3, 632–638.

[56] Kanazawa, T. (2012) Suppression of tumor growth by systemic delivery of anti-VEGF siRNA with cell-penetrating peptide-modified MPEG-PCL nanomicelles. Eur. J. Pharm. Biopharm. 81, 470–477.

[57] Grossman, D. and Altieri, D.C. (2001) Drug resistance in melanoma: mechanisms, apoptosis, and new potential therapeutic targets. Cancer Metastasis Rev. 20, 3–11.

[58] Jing, H. (2011) Opposing roles of NF-kappaB in anti-cancer treatment outcome unveiled by cross-species investigations. Genes Dev. 25, 2137–2146.

[59] Schmitt, C.A. (2002) A senescence program controlled by p53 and p16INK4a contributes to the outcome of cancer therapy. Cell 109, 335–346.

Biochimie xxx (2013) 1–13

Contents lists available at ScienceDirect

Biochimie

journal homepage: www.elsevier.com/locate/biochi

Research paper

Cytotoxic effects of dillapiole on MDA-MB-231 cells involve the induction of apoptosis through the mitochondrial pathway by inducing an oxidative stress while altering the cytoskeleton network

Adilson Kleber Ferreira [a,1], Paulo Luiz de-Sá-Júnior [a,**,1],
Kerly Fernanda Mesquita Pasqualoto [b,1], Ricardo Alexandre de Azevedo [b],
Diana Aparecida Dias Câmara [a], André Santos Costa [a], Carlos Rogério Figueiredo [c],
Alisson Leonardo Matsuo [c], Mariana Hiromi Massaoka [c], Aline Vivian Vatti Auada [b],
Ivo Lebrun [b], Mariana Celestina Frojuello Costa Bernstorff Damião [d],
Maurício Temotheo Tavares [d], Fátima Maria Motter Magri [e], Irina Kerkis [a],
Roberto Parise Filho [d,*]

[a] *Laboratory of Genetics, Butantan Institute, Vital Brasil Avenue 1500, 05503-900 Sao Paulo, Brazil*
[b] *Biochemistry and Biophysical Laboratory, Butantan Institute, Vital Brasil Avenue 1500, 05503-900 Sao Paulo, Brazil*
[c] *Experimental Oncology Unit (UNONEX), Microbiology, Immunology and Parasitology Dept, Federal University of São Paulo, Rua Botucatu 862, 04023-062 Sao Paulo, Brazil*
[d] *Department of Pharmacy, School of Pharmaceutical Sciences, University of Sao Paulo, Prof. Lineu Prestes Avenue, 580, 05508-000 Sao Paulo, Brazil*
[e] *Center for Biological Sciences and Health (CCBS), Mackenzie Presbyterian University, Consolação Avenue, 930, 01302-907 Sao Paulo, Brazil*

ARTICLE INFO

Article history:
Received 15 June 2013
Accepted 6 December 2013
Available online xxx

Keywords:
Piper aduncum
Dillapiole
Antitumoral
Apoptosis
Cell cycle
ROS
Molecular modeling

ABSTRACT

Breast cancer is the world's leading cause of death among women. This situation imposes an urgent development of more selective and less toxic agents. The use of natural molecular fingerprints as sources for new bioactive chemical entities has proven to be a quite promising and efficient method. Here, we have demonstrated for the first time that dillapiole has broad cytotoxic effects against a variety tumor cells. For instance, we found that it can act as a pro-oxidant compound through the induction of reactive oxygen species (ROS) release in MDA-MB-231 cells. We also demonstrated that dillapiole exhibits antiproliferative properties, arresting cells at the G0/G1 phase and its antimigration effects can be associated with the disruption of actin filaments, which in turn can prevent tumor cell proliferation. Molecular modeling studies corroborated the biological findings and suggested that dillapiole may present a good pharmacokinetic profile, mainly because its hydrophobic character, which can facilitate its diffusion through tumor cell membranes. All these findings support the fact that dillapiole is a promising anticancer agent.

1. Introduction

Breast cancer is one of the most common human malignancies and the second leading cause of cancer-related deaths among women [1]. Despite substantial improvements in survival, resistance to therapy and subsequent progression of disease are still observed in metastatic patients [2]. Therapeutic regimens against breast cancer include both chemo- and radiotherapy, and in advanced stages of the disease surgery intervention can be required [3]. In spite of the many advances achieved in breast cancer treatment during the last ten years, many patients still succumb to this illness and new therapeutic approaches are needed [4]. Therefore, investigation of the molecular mechanisms involved in the development and progression of breast cancer is crucial for the discovery of effective and non-cytotoxic compounds for chemoprevention and treatment [5].

Natural products, mostly plant-derived products, occupy an important place in cancer chemotherapy [6]. Substances derived from medicinal plants are known to be effective chemo-preventive and/or antitumoral agents in experimental models of carcinogenesis [7]. The

---

* Corresponding author. Tel.: +55 11 3091 3793; fax: +55 11 3091 3815.
** Corresponding author. Tel.: +55 11 2627 9718; fax: +55 11 3091 3815.
E-mail addresses: paulsaj2001@yahoo.com.br (P.L. de-Sá-Júnior), roberto.parise@usp.br (R. Parise Filho).

[1] These authors contributed equally to this work.

0300-9084/$ – see front matter © 2013 Elsevier Masson SAS. All rights reserved.
http://dx.doi.org/10.1016/j.biochi.2013.12.008

Please cite this article in press as: A.K. Ferreira, et al., Cytotoxic effects of dillapiole on MDA-MB-231 cells involve the induction of apoptosis through the mitochondrial pathway by inducing an oxidative stress while altering the cytoskeleton network, Biochimie (2013), http://dx.doi.org/10.1016/j.biochi.2013.12.008

bioactive compounds from the Piperaceae family, for instance, which comprises a large variety of species [8,9], can be used as models for promising molecular modifications envisaging more specific therapeutic responses. Covering approximately three thousand species, the *Piper* genus is prominent for having distinct biological activities. Dillapiole (1) (Fig. 1), a phenylpropanoid, is the main component of *Piper aduncum* [10,11] essential oil and is also present in other *Piper* species such as: *Piper banksii* [12], *Piper guineense* [13,14], *Piper novae hollandiae* [15] and *Piper marginatum* [16]. Previous studies revealed its antileishmanial [17], anti-inflammatory [18], antifungal [10] and acaricidal [19] activity, nevertheless its cytotoxic effect have not been studied yet.

Safrole (2), a phenylpropanoid structural-related to dillapiole, is also found in *Piper* genus [20], which presents some interesting biological properties [21–24]. Previous research indicates that safrole (2) can induce apoptosis in human oral cancer cells [25] as well as cell cycle arrest and apoptosis in human leukemia cells through the endoplasmic reticulum (ER) stress-associated signaling based on the production of ROS [26]. The structural similarity of safrole and dillapiole is obvious, but there is no previous reports addressing a potential antitumor activity of dillapiole.

The current study was designed to evaluate the *in vitro* antitumor activity of dillapiole in MDA-MB-231 breast cancer cells. Our results have revealed that this molecule is cytotoxic to a variety of tumors cells. Also, dillapiole inhibited proliferation and migration of MDA-MB-231 cells by arresting them at the G0/G1 phase and the disruption of the cytoskeleton contributed to the inhibition of cell migration. Furthermore, the dillapiole apoptotic effects coincided with the increase in ROS production by the mitochondria, which is in agreement with the data showing that dillapiole induces mitochondrial depolarization, increasing the transient intracellular Ca^{2+}, cytochrome *c* release, caspase-3 activity in MDA-MB-231 cells. Additionally, the calculated molecular properties support the suitable pharmacokinetic and pharmacodynamic profiles of dillapiole. Overall, dillapiole is a compound with potential antitumor effects on MDA-MB-231 cells, suggesting that this molecule is a potential hit for the design of novel anticancer drugs.

2. Materials and methods

2.1. General procedures

Reagents and solvents were commercial grade, used as supplied. Chromatography separations were performed using 70–230 mesh silica gel. Thin-layer chromatography was carried out on Merck silica plates (0.25 mm layer thickness). NMR spectra were recorded using a Bruker AC-300 Spectrometer at 300 MHz (^1H) and 75 MHz (^{13}C) with tetramethylsilane as an internal reference and $CDCl_3$ as a solvent. Chemical shifts are given in parts per million (ppm), coupling constants in Hertz (Hz), and splitting patterns were designated as follows: s, singlet; br s, broad singlet; d, doublet; t, triplet; q, quartet, and m, multiplet. Gas chromatography-mass spectrometry (GC–MS) was performed using a 17A/QP5050A Shimadzu-brand GC–MS apparatus: Class 5000 software; column: BXP5-30 m, 0.25 mm ID; helium as carrier gas (flow rate 2.5 mL/min). The ionization mode was EL at 70 eV. Temperature program was from 60 °C (rate 8 °C/min) to 320 °C (35 min). The detector and injector temperatures were both 250 °C.

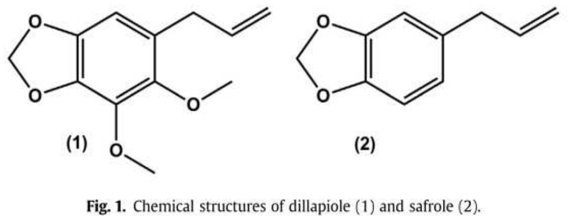
(1) (2)

Fig. 1. Chemical structures of dillapiole (1) and safrole (2).

2.2. Extraction of dillapiole from *P. aduncum*

P. aduncum leaves were collected in March and August, 2011, in Ubatuba, São Paulo, Brazil. Identification was carried out at the Botanical Laboratory of Mackenzie Presbyterian University (MPU). The *P. aduncum* leaves exsiccate was stored in the MPU herbarium (no. 01092). The collected vegetable material underwent extraction of its essential components through hydrodistillation, using a modified Clevenger-type apparatus. The crude essential oil was extracted with dichloromethane, then dried with anhydrous Na_2SO_4, filtered, and kept in a freezer (−15 °C), using an amber glass flask [18].

2.3. Purification of dillapiole (1)

Pure dillapiole was used to carried out the bioassays. Purification and isolation procedures were perform as previously reported in Refs. [17,18]. Briefly, the crude essential oil was obtained by hydrodistillation and diluted with dichloromethane. GS–MS chromatography was carried out to determine the percentage of dillapiole in crude extract. The results showed that dillapiole is the majority compound and represents for almost 89% of the essential oil. Mass spectrometry data analysis together with hydrogen nuclear magnetic resonance spectroscopy (^1H NMR) confirmed that dillapiole was the main component of the crude extract. After that, dillapiole was isolated and purified by column chromatography using hexanes/ethyl acetate (1:1), as solvent system. Additionally, the isolated sample was characterized by GC–MS and was further used to evaluate the cytotoxic activity. Viscous yellow liquid. (1.5 g yield) ^1H NMR ($CDCl_3$, 300 MHz, δ = ppm): 3.31 (d, 2H, H-8); 3.81 (s, 3H, H-11); 4.08 (s, 3H, H-12); 5.05–5.15 (m, 2H, H-10); 5.88–6.05 (m, 1H, H-9); 5.98 (s, 2H, H-1); 6.40 (s, 1H, H-6). ^{13}C NMR (CDCl3, 75 MHz, δ = ppm): 34.5 (C8); 60.3 (C11); 60.8 (C12); 101.5 (C1); 102.4 (C6); 115.9 (C10); 122.1(C5); 132.3 (C2); 136.5 (C9); 142.0 (C7); 143.6 (C4); 145.1 (C3).

2.4. Molecular modeling approach

The three-dimensional (3D) molecular model of dillapiole was built, in its neutral form, using the HyperChem 7.0 MM + force field (Hypercube, Inc., 2002), without any constrains, and employing the crystal data from 6-[1-(4-ethoxyphenyl)ethyl]-5-methoxy-1,3-benzodioxole [27] as starting geometry. Partial atomic charges were computed with AM1 semiempirical method [28], also implemented in HyperChem 7.0 (Hypercube, Inc., 2002). MOLSIM 3.2 software [29] was used to carry out energy-minimization (steepest descent and conjugate gradient methods; convergence criterion of 0.01 kcal/mol) and molecular dynamics (MD) simulations (1 ns; step size of 1 fs). Output trajectory file was recorded every 20 ps resulting in a conformational ensemble profile (CEP) of 50,000 conformers. The lowest-energy conformation was selected from the CEP equilibrium region, and the total potential energy (E_T) of that conformation corresponds to the summation of the following intramolecular energy contributions: stretching ($E_{stretch}$), bending (E_{bend}), torsional (E_{tors}), Lennard-Jones or 1–4 interactions (E_{1-4}), electrostatic (E_{charge}), van der Waals (E_{vdW}), hydrogen bonding (E_{Hb}), and solvation (E_{solv}). Then, the lowest-energy conformation was energy-minimized [29] and, subsequently, used as starting geometry to calculate molecular properties of distinct nature. Electronic properties as partial atomic charges from electrostatic potential using a grid based method [30] and the

Please cite this article in press as: A.K. Ferreira, et al., Cytotoxic effects of dillapiole on MDA-MB-231 cells involve the induction of apoptosis through the mitochondrial pathway by inducing an oxidative stress while altering the cytoskeleton network, Biochimie (2013), http://dx.doi.org/10.1016/j.biochi.2013.12.008

related electrostatic potential (EP) were computed with the B3LYP (Becke, three-parameter, Lee–Yang–Parr) [31] hybrid functional and 6-31(d,p) basis set [32]. EP maps were calculated onto a Connolly molecular surface, using a color scheme ranging from −0.046 (intense red) to 0.046 (intense blue). Negative values of EP (higher electronic density distribution) are depicted in red and positive values in blue (lower electronic density distribution) [33]. Also, the calculated *n*-octanol/water partition coefficient (ClogP), which is a measure of molecular hydrophobicity, was computed based upon the Viswanadhan and co-workers method [34], implemented in Marvin 5.8.0 package, Calculator Plugins [35].

2.5. Cell lines and cell culture

The human breast adenocarcinoma (MCF-7 and MDA-MB-231) and the melanoma (Sbcl-2; Mel-85; SK-MEL-28) cell lines were purchased from the American Type Culture Collection (Manassas, VA, USA). The cells were maintained in RPMI-1640 medium supplemented with 10% fetal calf serum (FCS) (Cultilab, Campinas, SP, Brazil), containing penicillin (100 units/mL) and streptomycin (100 μg/mL, Cultilab, Campinas, SP, Brazil). All cells were cultured at 37 °C in a fully humidified incubator with 5% CO_2. All experiments described were performed at least three times using cells in the exponential growth phase.

2.6. Cell viability assay

Tumor cells in the logarithmic growth phase were plated at a density of 10^4 cells/100 μL into 96-well plates and allowed to adhere overnight. For the evaluation whether caspases are involved with the cytotoxic effects of dillapiole, cells were pre-treated with a specific inhibitor of cyclophilin and with 40 μM Z-VAD-fmk, a pan-caspase inhibitor, for 2 h. Subsequently, the culture medium was replaced with medium containing different concentrations of dillapiole. After 24 h of treatment, cell viability was determined by MTT (3-[4,5 dimethylthiazol-2-yl]-2,5-diphenyltetrazolium bromide). Briefly, 20 μL of MTT reagent (Sigma–Aldrich, St. Louis, USA) were added to each well at a final concentration of 5 mg/mL, incubated for 4 h at 37 °C and centrifuged at 2000 rpm for 10 min. The medium was discarded and 100 μL of dimethylsulfoxide were added to each well. Each experiment was performed using six replicates for each drug concentration and was repeated in tree independent experiments.

2.7. Wound-healing assay

MDA-MB-231 (2.5 × 10^5 cells) were grown to confluence in a 12-well plate, placed in medium containing 1% serum for 24 h at 37 °C in an atmosphere of 5% CO_2. Upon reaching confluence, the cell layer was scratched with a sterile plastic tip and then washed twice with culture medium. Next, serum was increased to 5% to facilitate cell migration and the cells were treated with 25 μM or 50 μM dillapiole for 48 h. Cell migration was recorded using a Nikon TE2000E microscope system (Nikon Instrument). The area of wound healing was calculated using WimScratch software.

2.8. Cell cycle analysis

MDA-MB-231 cells were synchronized by deprivation of serum for 24 h and induced to reenter the cell cycle by the subsequent addition of serum. Cells were treated for 24 h with 25, 50 and 100 μM dillapiole. Next, cells were collected and fixed with cold 70% ethanol and stored at −20 °C. Cells were washed, re-suspended in PBS and incubated at 37 °C for 45 min with 10 mg/mL RNase and 1 mg/mL propidium iodide (PI) (SIGMA, St. Louis, MO). Flow cytometric analysis was performed using a FACScalibur flow cytometer (Becton Dickinson, San Jose, CA). Cell DNA content in the different cell cycle phases was determined using Modfit LT software (Verity Software House, Topsham, ME).

2.9. Evaluation of apoptosis by flow cytometry

For the detection and evaluation of apoptosis, MDA-MB-231 cells were treated with 25, 50 and 100 μM dillapiole for 24 h, then washed with PBS (500 μL/well), harvested (including suspension cells) and incubated with 2 μM YO-PRO-1 (Life Technologies Eugene, Oregon, USA) and 10 μM of PI in PBS for 30 min at room temperature in the dark. The cells were immediately analyzed by flow cytometry using 488 nm excitation in a FACScalibur flow cytometer (Scalibur-Becton Dickinson, San Jose, CA). Data from three independent experiments were analyzed using the FlowJo software.

2.10. Measurement of the mitochondrial transmembrane potential

The mitochondrial membrane potential (ΔΨm) was evaluated using the tetramethyl-rhodamine ethyl ester (TMRE) probe (Invitrogen-Molecular Probes). Briefly, MDA-MB-231 cells (10^6 cells/well) were seeded in 6-well plates and incubated for 24 h. After 24 h of treatment with 25 and 50 μM dillapiole, 20 nM TMRE were added to cell cultures maintained at 37 °C for 45 min. Fluorescence was measured using a FACScan flow cytometry system (Becton Dickinson, San Jose, CA). A total of 10,000 cells/sample were analyzed and the mean fluorescence intensity and percentage of cells in each population were recorded.

2.11. Measurement of changes in free intracellular calcium concentration ($[Ca^{2+}]$i) by microfluorimetry

Changes in $[Ca^{2+}]$i were determined by microfluorimetry using FlexStation III (Molecular Devices Corp., Sunny Valley, CA). MDA-MB-231 cells were seeded at a density of 5 × 10^4 cells per well in black-well plates with clear bottom in serum-free medium. Cells were then incubated for 60 min at 37 °C with the Flexstation Calcium Kit in the presence of 2.5 mM probenecid in a final volume of 200 mL/well. Samples were excited at 485 nm, and fluorescence emission was detected at 525 nm. Samples were read at 1.52 s intervals for 120 s with a total of 79 read-outs per well. After Basal fluorescence intensity for $[Ca^{2+}]$i levels in non-stimulated cells were monitored for 20 s, then 25 μM dillapiole or 50 mM ATP (positive control) or 50 mM H_2O (negative control), were added to the cells. Next, the induction of transient $[Ca^{2+}]$i was monitored for up to 100 s. Responses to agonist addition were determined as peak fluorescence minus the basal fluorescence intensity using the SoftMax1Pro software (Molecular Devices Corp.).

2.12. Caspase-3 activity assay

After 12 h of treatment with 25 or 50 μM dillapiole, the cells were washed twice with cold PBS and then scraped in 5 mL of cold protease assay buffer (25 mM HEPES, pH 7.5, 5 mM EDTA, 2 mM dithiothreitol, and 0.1% detergent) and sonicated to lyse the cells. The lysates were collected and stored at −70 °C until analyzed. Briefly, 50 μL of 1× reaction buffer were added to each well used in the assay and incubated at 37 °C for 5 min. Caspase activity was measured using the substrate Ac-YVAD-AMC using the caspase-3 fluorometric assay kit from Biovision. Flow cytometric analysis was performed using a FACScan flow cytometry system (Becton Dickinson, San Jose, CA). Data from three independent experiments were analyzed using the FlowJo software.

Please cite this article in press as: A.K. Ferreira, et al., Cytotoxic effects of dillapiole on MDA-MB-231 cells involve the induction of apoptosis through the mitochondrial pathway by inducing an oxidative stress while altering the cytoskeleton network, Biochimie (2013), http://dx.doi.org/10.1016/j.biochi.2013.12.008

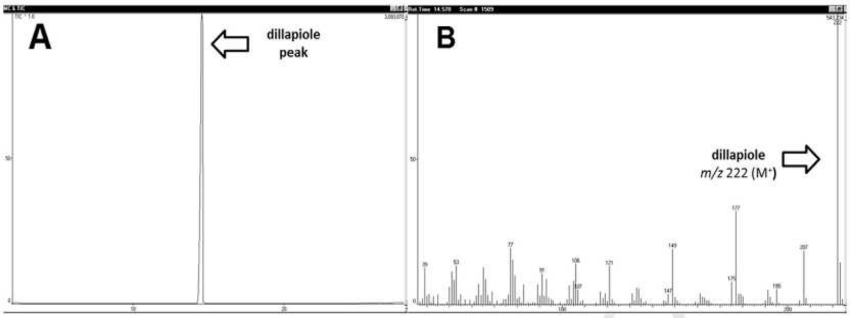

Fig. 2. GC–MS analysis of pure dillapiole. (A) Chromatogram and (B) mass spectrum obtained for the pure compound.

2.13. Determination of cytochrome c by flow cytometry

MDA-MB-231 cells were treated with 25 or 50 μM dillapiole for 12 h and stained with PE-labeled anti-human antibody or isotype control IgG (Santa Cruz, CA, USA). Cells were first fixed with 3.7% paraformaldehyde and permeabilized with Triton X-100 0.02%, then stained with FITC labeled anti-cytochrome *c* or isotype control antibody (Santa Cruz, CA, USA). The percentages of cells expressing Bcl-2, Cyclin D1 and p53 was determined using a FACScalibur flow cytometer (Becton Dickinson, San Jose, CA). Data from three independent experiments were analyzed using the FlowJo software.

2.14. Confocal laser scanning microscopy

MDA-MB-231 cells were seeded onto sterile glass cover slips in 24-well plates. Next, cells were treated with dillapiole at the concentration of 25 μM or 50 μM. After treatment, the cells were fixed with 3.7% paraformaldehyde and permeabilized in 0.02% triton-x diluted in PBS containing 10% bovine fetal serum. To analyze the effect of dillapiole on actin filaments, cells were labeled with FITC-phalloidin (Invitrogen-Molecular Probes, Eugene, OR) in a buffer containing 0.5% Triton X-100, 1 mg/mL RNase in 2× PBS. For mitochondria studies, the cells were stained with MitoTracker® red

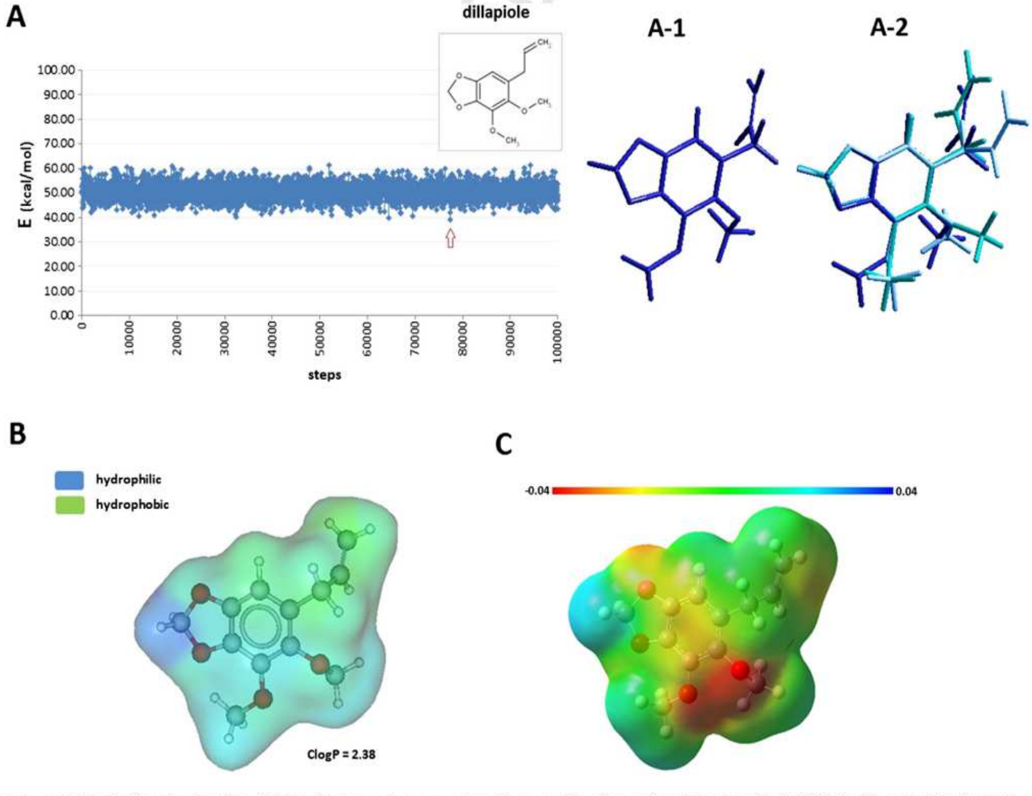

Fig. 3. Molecular modeling findings for dillapiole. (A) Plot of energy value versus steps for an equilibration region of the dillapiole CEP (100 ps) from the MD simulation (1 ns): (A-1) the lowest-energy conformer selected (dark blue stick molecular model); (A-2) superimposition of the three more frequent conformers (light blue, cyan, and dark blue stick molecular models), including the selected conformation (dark blue). (B) Map of lipophilic potential and calculated *n*-octanol/water coefficient partition (ClogP) for the selected conformer from the MD simulation. Hydrophilic regions are in blue and the hydrophobic in green. (C) Map of the electrostatic potential (MEP) for the selected conformer from the MD simulation [color range: −0.04 (red) to 0.04 (blue)]. Dillapiole is presented in ball-tube molecular model (carbon atoms in gray, oxygen in red, and hydrogen in white) in B and C.

Please cite this article in press as: A.K. Ferreira, et al., Cytotoxic effects of dillapiole on MDA-MB-231 cells involve the induction of apoptosis through the mitochondrial pathway by inducing an oxidative stress while altering the cytoskeleton network, Biochimie (2013), http://dx.doi.org/10.1016/j.biochi.2013.12.008

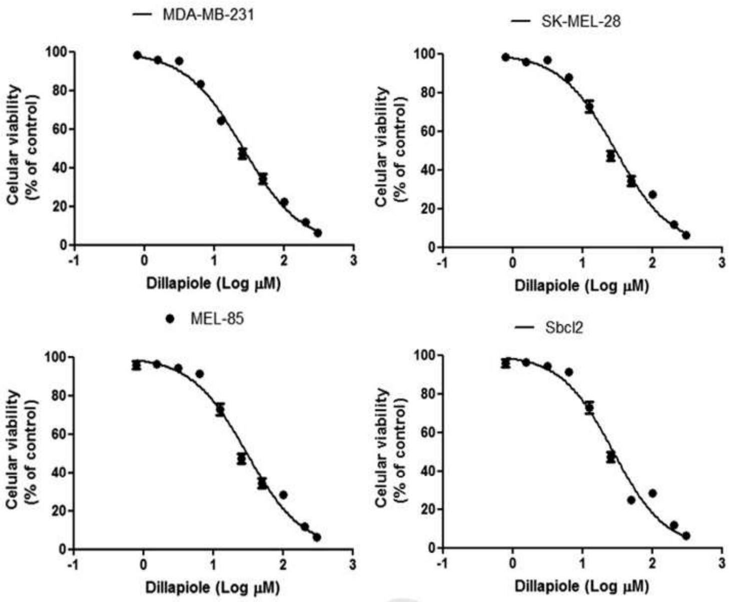

Fig. 4. Cytotoxic effects of dillapiole on tumor cell lines. Cells were plated at a density of 10^4/well and treated with dillapiole for 24 h. Cell viability was evaluate by MTT colorimetric assay. Cell viability is expressed as the percentage of cells comparing the optical density (540 nm) of the treated cells with the optical density of the untreated cells. The data are representative of three independent experiments performed in triplicate.

for 45 min under growth conditions. For ROS detection, cells were incubated with 2′,7′-dichlorofluorescein diacetate (H2DCFH-DA, Sigma, St Louis MO) (5 mM), for 10 min at 37 °C in the dark. Image analysis was performed with a confocal laser scanning microscope (Carl Zeiss LSM 700; Leica, Mannheim, Germany). Post-acquisition image processing, background correction, adjustment of brightness and contrast and export to tiff format were done with Image J software (version 14.1) National Institutes of Health (Bethesda, Maryland, USA).

2.15. Statistical analysis

All values were expressed as mean ± SD. Each value is the mean of at least three independent experiments in each group. For significance analyses Student's *t*-tests and One way analysis of variance (ANOVA) were calculated using GraphPad Prism 4.0. *p* values < 0.05, 0.01 and 0.001 were considered significant.

3. Results

3.1. GC–MS analysis of dillapiole

After purification, GC–MS analysis revealed the presence of only one compound (Fig. 2). The gas chromatogram, presented in Fig. 2A, shows that dillapiole was successfully isolated and purified from its essential oil (purity ~ 100%). Furthermore, according to the mass spectra analysis (Fig. 2B), the content had a molecular mass corresponding to that found for dillapiole (m/z 222 [M^+]).

3.2. Molecular modeling findings

The purpose of a theoretical approach was to find a more energetically favorable conformation for dillapiole, to calculate its molecular properties and, finally, to provide some insights regarding structure-activity relationships. The findings from MD simulations are presented in Fig. 3A. MD simulations of dillapiole reached the thermodynamic equilibrium in approximately 300,000 simulation steps. Part of the CEP (100 ps) from where the lowest-energy conformation (dark blue; A-1) was chosen as well as the superimposition of the more frequent 3D conformers (A-2) can be visualized (stick or tube molecular models). The side chain of dillapiole, which has a double bond between the C_{11} and C_{12} positions, did not remain in the same plane of the benzodioxole ring. The more frequent conformers present the side chain turned to the back side of the benzodioxole ring, and the total potential energy (E_T) found for the selected conformer from CEP was 35.35 kcal/mol.

Lipophilicity, expressed through the calculated *n*-octanol/water partition coefficient (ClogP) and visualized through the maps of lipophilic potential (MLP), was also considered (Fig. 3B). Dillapiole presented a ClogP value of 2.38, indicating a hydrophobic character, meaning the ability to cross hydrophobic barriers such as cell membranes in order to reach their target, for instance. Even when no barriers are to be crossed (such as in *in vitro* studies), the drug

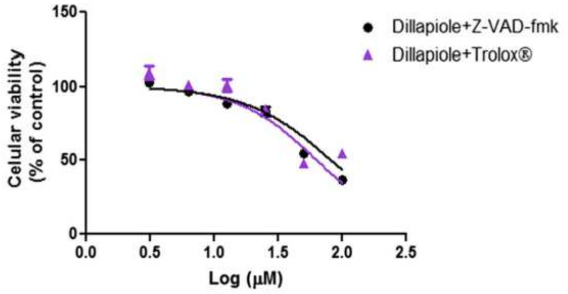

Fig. 5. Cytotoxic effects of Dillapiole on MDA-MB-231. Cells were plated at a density of 10^4/well and pre-treated with 40 μM z-VAD-fmk, a pan-caspase inhibitor and an antioxidant agent, Trolox®, followed by the addition of dillapiole. The MTT shows that z-VAD-fmk and Trolox® reduce the cytotoxic potency of dillapiole on MDA-MB-231 after 24 h of treatment. The data are representative of three independent experiments performed in triplicate.

Please cite this article in press as: A.K. Ferreira, et al., Cytotoxic effects of dillapiole on MDA-MB-231 cells involve the induction of apoptosis through the mitochondrial pathway by inducing an oxidative stress while altering the cytoskeleton network, Biochimie (2013), http://dx.doi.org/10.1016/j.biochi.2013.12.008

has to interact with a target system such as an enzyme or receptor where the binding site is usually hydrophobic. Otherwise, the drug should not be so hydrophobic that it would be poorly soluble in the aqueous phase such that it might get 'trapped' in fat depots and never reach the intended interaction site. In addition, a hydrophilic/hydrophobic molecular balance is needed to provide suitable pharmacodynamics and pharmacokinetic profiles. The MLP property gives the information regarding that balance and can be explained using a color scheme, where blue corresponds to hydrophilic regions and green to hydrophobic regions.

Regarding the partial atomic electrostatic potential charges (ESP, CHELPG), the C_{10} atom (attached to aromatic ring) in dillapiole is positively charged (0.3254). This datum indicates that dillapiole could likely suffer a nucleophilic attack, but only in the opposite face of its side chain direction where there is no steric hindrance. The electronic density distribution can be visualized through the EP map (Fig. 3C), and a more neutral/positive region can be visualized on the side chain, particularly on the C_{10} atom (green). The electronic properties are also fundamental in the molecular recognition process, and are more strictly related to the pharmacodynamics profile (ligand–receptor interactions).

3.3. Dillapiole induces cytotoxic effects on tumor cell lines

The cytotoxic properties of dillapiole were investigated using the MTT assay, a well-documented method to assess cell viability. Tumor

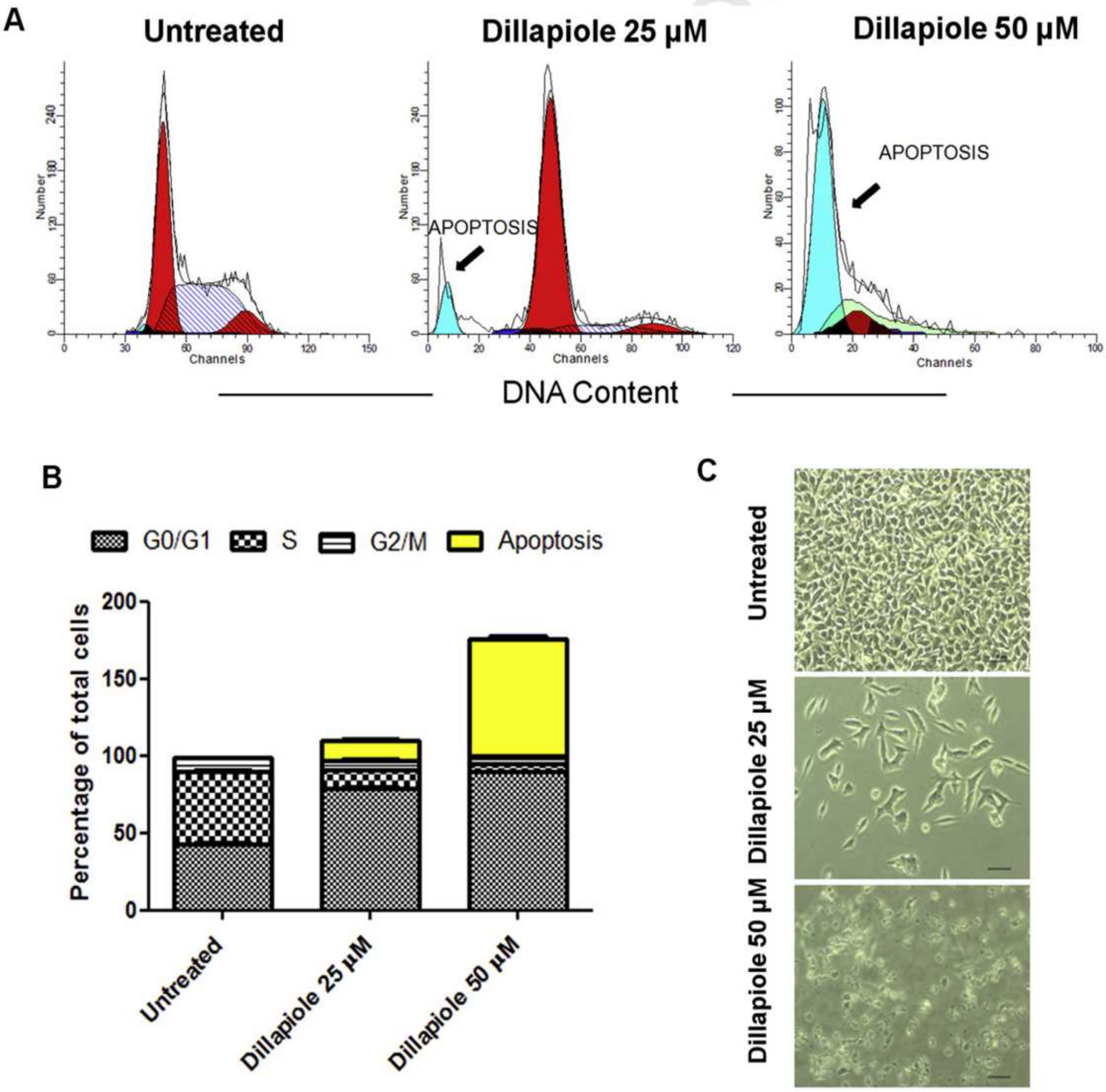

Fig. 6. Dillapiole induces apoptotic and morphological alterations on MDA-MB-231 cells. (A) Apoptosis (sub-G1) and DNA profile induced after treatment with dillapiole for 24 h at different concentrations (25 and 50 µM) analyzed, after propidium iodide staining, by flow cytometry (arrow indicates sub-G1 peak). (B) Cluster bar chart of cell cycle showing the percentage distributions of the cell cycle phases in the three cell groups. (C) MDA-MB-231 cells morphological changes after treatment with dillapiole. After 24 h of incubation, morphological changes such as appearance of inner vacuoles and apoptotic bodies, characteristic signals of apoptosis, were observed under the inverted phase-contrast microscope and were also photographed. The data are representative examples for duplicate tests. Original magnification, ×200.

Please cite this article in press as: A.K. Ferreira, et al., Cytotoxic effects of dillapiole on MDA-MB-231 cells involve the induction of apoptosis through the mitochondrial pathway by inducing an oxidative stress while altering the cytoskeleton network, Biochimie (2013), http://dx.doi.org/10.1016/j.biochi.2013.12.008

cells were incubated for 24 h with different concentrations of the compound. The results show that dillapiole presents cytotoxic effects, reducing cell viability in all tumor cells tested in this work. The IC_{50} values of dillapiole on MDA-MB-231, SK-MEL-28, MEL-85 and Sbcl2 were 25 μM, 27 μM, 28 μM and 26 μM, respectively. These results indicate that there is no difference between tumor cell lines in response to dillapiole (Fig. 4). Next, we evaluated its anticancer effects using MDA-MB-231 cells as a model. Prior to treatment with dillapiole, cells were pre-incubated with a pan-caspase inhibitor, z-VAD-fmk, and an antioxidant agent, Trolox®. Interestingly, the inhibitors dramatically decreased cytotoxic effects of dillapiole on MDA-MB-231 cells. The IC_{50} value of dillapiole on cells pre-treated with z-VAD-fmk is 63 μM, and with Trolox® is 82 μM (Fig. 5). An unanticipated finding is that dillapiole is cytotoxic in a caspase-dependent manner. Additionally, the release of ROS indicates a possible mechanism of action of dillapiole on MDA-MB-231 cells.

3.4. *Cell cycle changes induced by apoptotic effects of dillapiole on MDA-MB-231 cells*

In this study, we investigated the anti-proliferative effects of dillapiole on MDA-MB-231 cells. Our data clearly show that the cytotoxic effects of dillapiole correlate with its ability to induce apoptosis as evidenced by the sub-G1 apoptotic peak. As shown in Fig. 6A, induction of apoptosis in MDA-MB-231 cells was more efficient ($^{**}p < 0.01$) at 50 μM than at 25 μM, reducing the number of tumor cells between the S and G2/M phases of the cell cycle. Additionally, treatment with 25 μM dillapiole does not induce apoptosis, but exhibits a higher potency in blocking cell progression by arresting cells at the G0/G1 phase ($^{**}p < 0.01$) (Fig. 6B). When treated with 50 μM dillapiole, typical apoptosis morphological changes, such as the retraction of membrane and nuclei, were also observed (Fig. 6C). These findings further support the hypothesis that dillapiole, at 50 μM, induces apoptosis in MDA-MB-231 cells.

3.5. *Dillapiole attenuates MDA-MB-231 cell migration in response to wound scratch*

To examine the effect of dillapiole on MDA-MB-231 cell migration, we employed an *in vitro* assay. Here, we show that 50 μM of dillapiole induces apoptosis on MDA-MB-213 cells. However, we used 25 μM dillapiole to investigate whether the anti-proliferative effects correlate with the inhibition of cell migration. Cell migration was significantly ($^{***}p < 0.001$) inhibited by 25 μM dillapiole when compared to untreated cells and an increased rate of wound healing could be observed at all time points examined (Fig. 7A and B).

3.6. *Dillapiole induces apoptosis in MDA-MB-231 cells*

Apoptosis is a strategy of tumor elimination involving a number of signal pathways. To investigate the molecular mechanism of dillapiole-mediated cell apoptosis, we evaluated whether the externalization of phosphatidylserine (PS), a hallmark of early apoptosis, might be involved. In comparison with untreated cells, the treatment with dillapiole at 25 μM induces apoptosis in MDA-MB-231 cells. Of note, the exposure of PS residues on the outer surface of the plasma membrane was more significant ($^{***}p < 0.001$) upon treatment with 50 μM dillapiole. Interestingly, we also demonstrate that dillapiole, at the higher concentration, significantly induces necrosis instead of apoptosis (Fig. 8A and B). These results corroborate the data showing that dillapiole-induced apoptosis is mediated by a mitochondria-dependent pathway. It is interesting to note that inhibition of cancer cell growth occurs most likely by apoptosis instead of via cytostatics mechanisms.

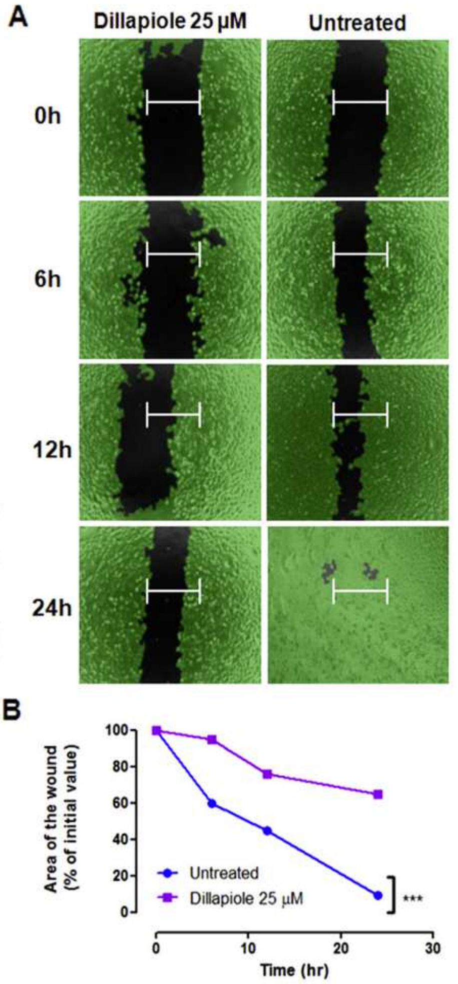

Fig. 7. Effect of dillapiole on MDA-MB-231 cell migration. (A) MDA-MB-231 cells were seeded in a 12-well plate, then scraped to create a clean 1 mm wide wound area. Cells then were treated for 24 h with dillapiole at concentrations 25 μM and photographed and measured at 0 (t0), 6, 12, and 24 h after wounding. The wound areas were then analyzed and calculated using online image analysis software Wimasis. (B) Significant differences are indicated as: $^{***}p < 0.001$ statistically different from the dillapiole versus untreated.

3.7. *Dillapiole induces mitochondrial membrane potential ($\Delta\psi m$) disruption in MDA-MB-231 cells*

To evaluate whether apoptosis induced by dillapiole in MDA-MB-213 cells is associated with the changes in $\Delta\psi$m, cells were stained with mitotracker, a cationic fluorophore that accumulates in mitochondria and treated with 25 μM or 50 μM dillapiole for 6 h. The percentage of stained cells and the total fluorescence intensity were determined by flow cytometry. In untreated cells, red mitochondria could be seen by confocal laser scanning microscopy throughout the cytoplasm without morphological changes indicating a high $\Delta\psi$m. In contrast, cells treated with both concentrations of dillapiole showed a reduction in the intensity of fluorescent staining and the formation of peripheral clusters could be observed (Fig. 9A). Our investigation by flow cytometry confirms that dillapiole 24 h reduces significantly ($^{***}p < 0.001$) $\Delta\psi$m in MDA-MB-213 cells, which can lead to an increase mitochondrial permeability transition (MPT). It demonstrates that dillapiole can induce apoptosis trough the mitochondrial pathway (Fig. 9B and C).

Please cite this article in press as: A.K. Ferreira, et al., Cytotoxic effects of dillapiole on MDA-MB-231 cells involve the induction of apoptosis through the mitochondrial pathway by inducing an oxidative stress while altering the cytoskeleton network, Biochimie (2013), http://dx.doi.org/10.1016/j.biochi.2013.12.008

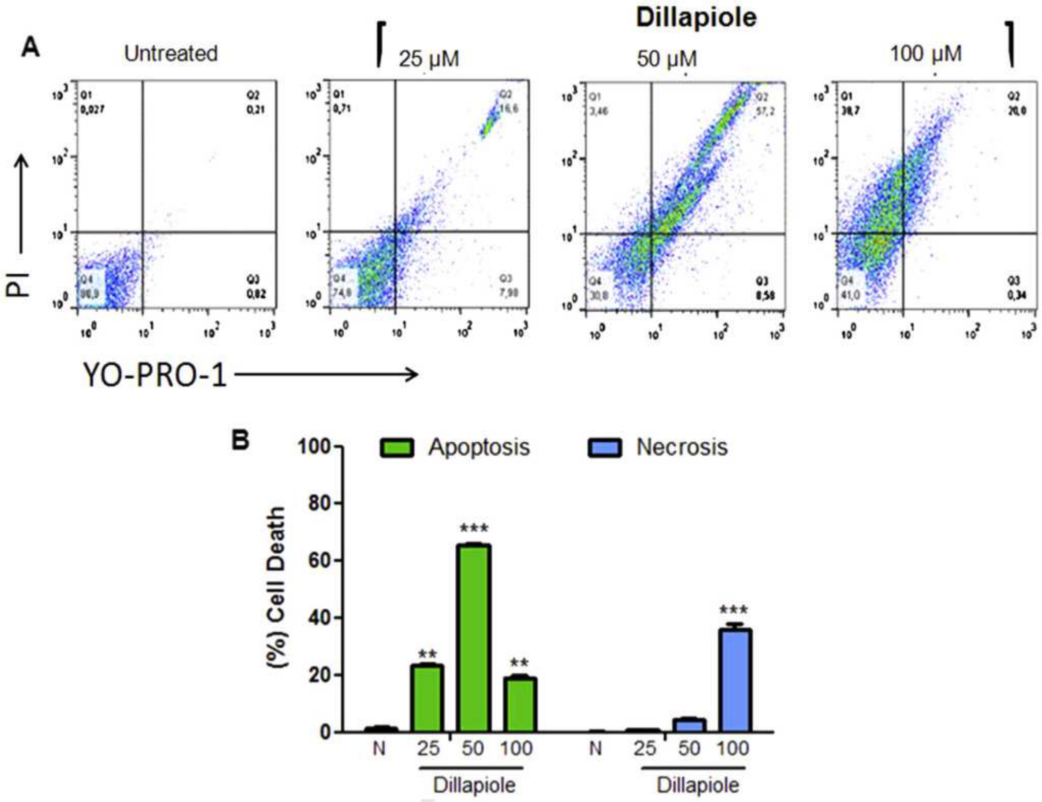

Fig. 8. Dillapiole preferentially triggers apoptosis in MDA-MB-231 cells. (A) Dot plot displays YO-PRO/PI double staining, which is representative of apoptotic and/or necrotic cells. 50 μM of dillapiole induces primarily apoptosis while high dosages, such 100 μM, induces necrosis. (B) Representation of the number of cells in different cell death processes. Significant differences between dillapiole and untreated are indicated as: $^{***}p < 0.001$ and $^{**}p < 0.001$.

3.8. Treatment with dillapiole induces transient [Ca^{2+}]i in MDA-MB-231 cells

Calcium is an important second messenger involved in several intracellular responses that can determined the fate of cells, such as NO production or ER stress, and a number of pro-apoptotic drugs induce mobilization of this ion. Our results show that 25 μM dillapiole induce a transient influx of extracellular calcium from intracellular compartments. Notably, we observed that treatment with dillapiole promotes calcium release increasing fluorescence by around 30 units in MDA-MB-231 cells (Fig. 10).

3.9. Dillapiole triggers a rapid disruption of the cytoskeleton and increases ROS production during apoptosis of MDA-MB-231 cells

To further evaluate the details of the apoptotic effects of dillapiole on MDA-MB-231 cells, the cytoskeleton and nuclei were stained with phalloidin and PI, respectively. In untreated cells, an examination of the cytoskeleton and nuclei after 12 h of dillapiole treatment showed a large number of long actin filaments. In addition, several tumor cells containing multiple nuclei could be seen. In MDA-MB-231 cells treated with 25 μM dillapiole, an important retraction of actin filaments with formation of short filaments and an increase of ROS production were observed in the cytoplasm. This can cause a disruption of focal adhesions, which, in turn, inhibits binding of cells to the matrix, triggering apoptosis. In contrast, treatment with 50 μM dillapiole led to nuclear fragmentation and complete disruption of actin filaments. Notably, stained microfilaments were observed clustered at the sites of apoptotic bodies formation (Figs. 11 and 12).

3.10. Dillapiole induces caspase-3 activity and cytochrome c release in MDA-MB-231 cells

Ac-YVAD-AMC, a specific caspase-3 substrate, was used to determine whether the mitochondrial pathway cascade is involved in the induction of apoptosis by dillapiole on MDA-MB-231 cells. Cells were treated for 12 h with dillapiole at the concentration of 25 μM or 50 μM. After treatment, caspase-3 activity was measured through a fluorometric assay. Here, we demonstrated that dillapiole caused a marked induction of apoptosis in MDA-MB-231 cells by increasing caspase-3 activity. Next, we investigated whether the release of cytochrome *c* was accompanied by an increase of caspase-3 activity. Interestingly, this correlation was observed with the treatment with dillapiole at both concentrations tested (Fig. 13A). Additionally, dillapiole is able to induce apoptosis through the intrinsic mitochondrial pathway in MDA-MB-231 cells. However, 50 μM dillapiole was significantly ($^{***}p < 0.001$) more effective in the induction of cytochrome *c* release than 25 μM ($^{**}p < 0.01$) (Fig. 13A).

4. Discussion

Therapeutic regimens, aiming at cancer eradication, encompass both radiotherapy and chemotherapy and, in advanced cases, when traditional treatment fails, tumor resection figures as the last

Please cite this article in press as: A.K. Ferreira, et al., Cytotoxic effects of dillapiole on MDA-MB-231 cells involve the induction of apoptosis through the mitochondrial pathway by inducing an oxidative stress while altering the cytoskeleton network, Biochimie (2013), http://dx.doi.org/10.1016/j.biochi.2013.12.008

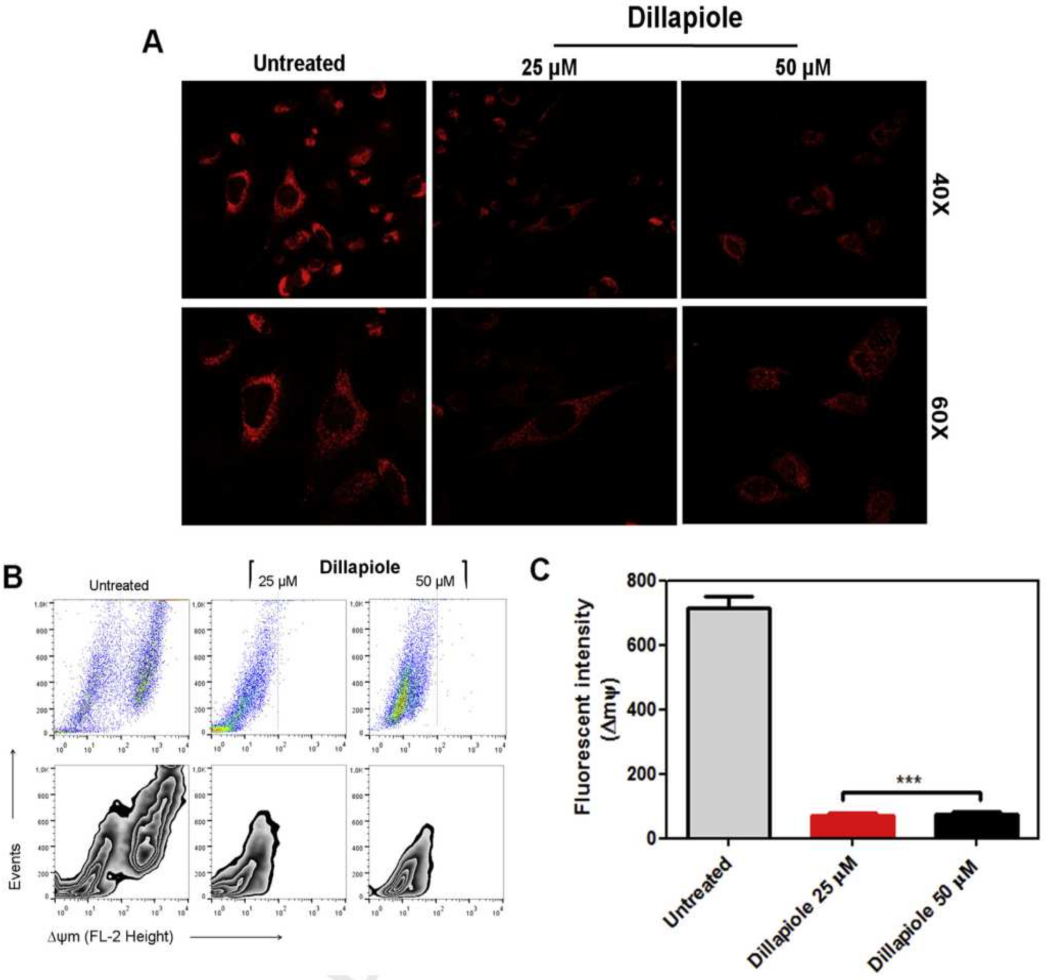

Fig. 9. Dillapiole induces a disruption in the mitochondrial transmembrane potential (Δψm) in MDA-MB-231 cells. (A) The depolarization of mitochondria is demonstrated by a reduction of fluorescence intensity in MDA-MB-231 cells stained with MitoTracker®. (B) Representative dot plots obtained from the FACS analysis of MDA-MB-231 cells stained with TMRE. (C) Depolarization of the mitochondria is demonstrated by a reduction of fluorescence intensity in MDA-MB-231 cells. Data are the means ± SD. $^{***}p < 0.001$ from at least three independent experiments.

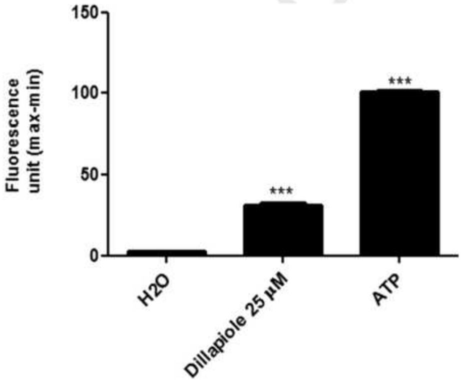

Fig. 10. Characterization of dillapiole-induced $[Ca^{2+}]$i elevations in MDA cells. Changes of maximal peak heights of $[Ca^{2+}]$i responses induced by dillapiole 25 µM were measured in MDA cells by microfluorometry. ATP was used as a positive control and H_2O as a negative control.

option [36]. In those advanced cases, eventually, tumor resection might not bring good prognosis, contributing to a decline in life quality, or even lead to death. Therefore, the search for and the development of new therapeutics targeting cancer cells must continue [37]. Here, we used several methods to describe the antitumor effects of dillapiole on MDA-MB-231 cells. Moreover, molecular modeling findings helped us to elucidate some relevant properties that make dillapiole as an excellent hit for anticancer drug discovery.

Regarding to the calculated molecular properties, they support the hydrophilic/hydrophobic balance of dillapiole (ClogP = 2.38), particularly the MLP property (color scheme, Fig. 3B). The positive ClogP value also indicates a more hydrophobic character for this molecule. Regarding the MEP property, dillapiole molecular surface is more neutral/positively (green to blue) than negatively (yellow to red) charged (Fig. 3C). In conclusion, this property could facilitate the interaction with the tumor cell, which has generally a more negatively charged membrane.

Regarding our antitumoral assays, one of our most important results shows that dillapiole is cytotoxic to all tumor cell lines

Please cite this article in press as: A.K. Ferreira, et al., Cytotoxic effects of dillapiole on MDA-MB-231 cells involve the induction of apoptosis through the mitochondrial pathway by inducing an oxidative stress while altering the cytoskeleton network, Biochimie (2013), http://dx.doi.org/10.1016/j.biochi.2013.12.008

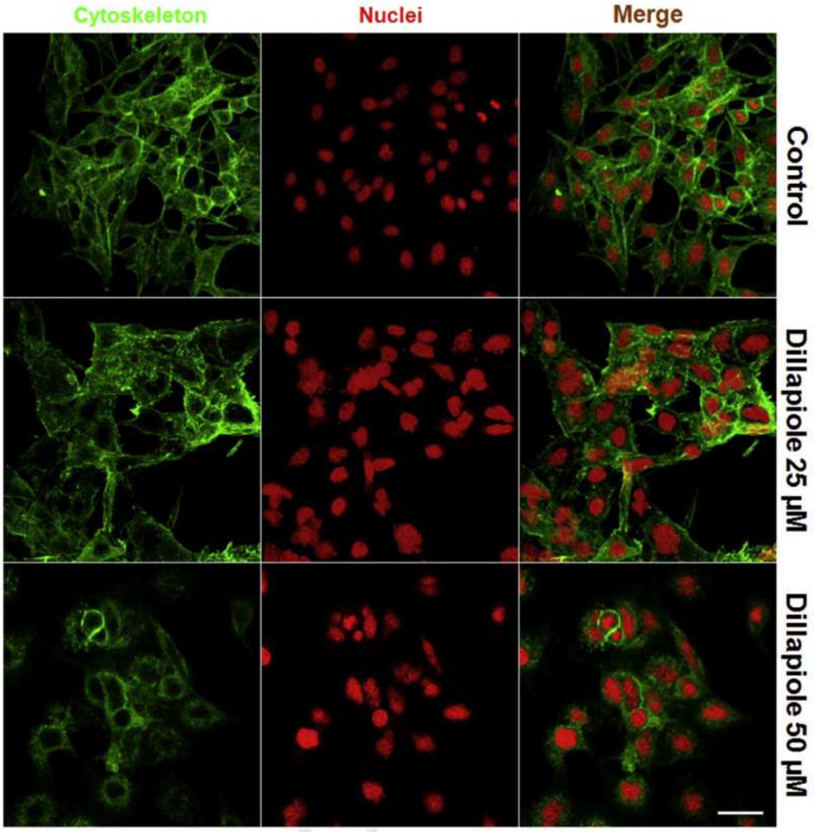

Fig. 11. Confocal microscopy of the cytoskeleton of dillapiole-treated MDA-MB-231 cells. Actin filaments are labeled in green (Phalloidin-FITC) and the nucleus in red (PI). Dose-dependent failure in actin polymerization/depolymerization dynamics induced by dillapiole, compared to control, leading to cell morphology changes (Magnification 60×).

screened. Interestingly, the different levels of dillapiole cytotoxicity did not correlate with the obtained IC_{50} values. This finding, though preliminary, suggests that dillapiole can be cytotoxic to the tumor cells tested independently of their sensitivity level. Furthermore, cytotoxic the potency of dillapiole on MDA-MB-231 cells was reduced when cells were pre-treated with the pan-caspase inhibitor, z-VAD-fmk, and the inhibitor of ROS production, Trolox®. It was the first evidence that dillapiole could be acting as a pro-oxidant agent, mediating an increase of intracellular concentration of ROS, which in turn would induce cell damage and cell death in a caspase-dependent manner. In order to complement our results showing that dillapiole induces ROS release in MDA-MB-231 cells, we also demonstrate that ROS accumulates in the cytoplasm, subsequently inducing cell death [38]. Of note, increase of ROS in cytoplasm and in mitochondrial compartment is considered a key step in the induction of cell death. It can also induce caspase activation, which in turn leads to apoptosis. These data suggest that the decrease in the cytotoxic effects of dillapiole could be associated with caspases inhibition. Indeed, the presence of ROS and caspases may play a crucial role in the antitumor activity of dillapiole on MDA-MB-231 cells. However, ROS can also induce cell death by necrosis through ATP depletion [39,40]. This led us to investigate whether dillapiole induces apoptosis in MDA-MB-231 cells. The first evidence that dillapiole has apoptotic effects on

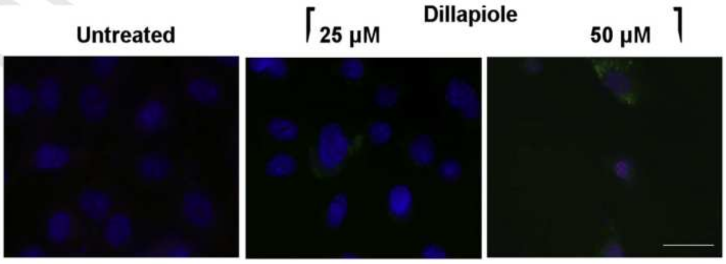

Fig. 12. Confocal microscopy of ROS production in dillapiole-treated MDA-MB-231 cells. ROS are labeled in green (H2DCFH-DA) in the cytoplasm. Dillapiole induced an increase in ROS release after 24 h of treatment, as compared to the untreated cells. (Magnification 60×).

Please cite this article in press as: A.K. Ferreira, et al., Cytotoxic effects of dillapiole on MDA-MB-231 cells involve the induction of apoptosis through the mitochondrial pathway by inducing an oxidative stress while altering the cytoskeleton network, Biochimie (2013), http://dx.doi.org/10.1016/j.biochi.2013.12.008

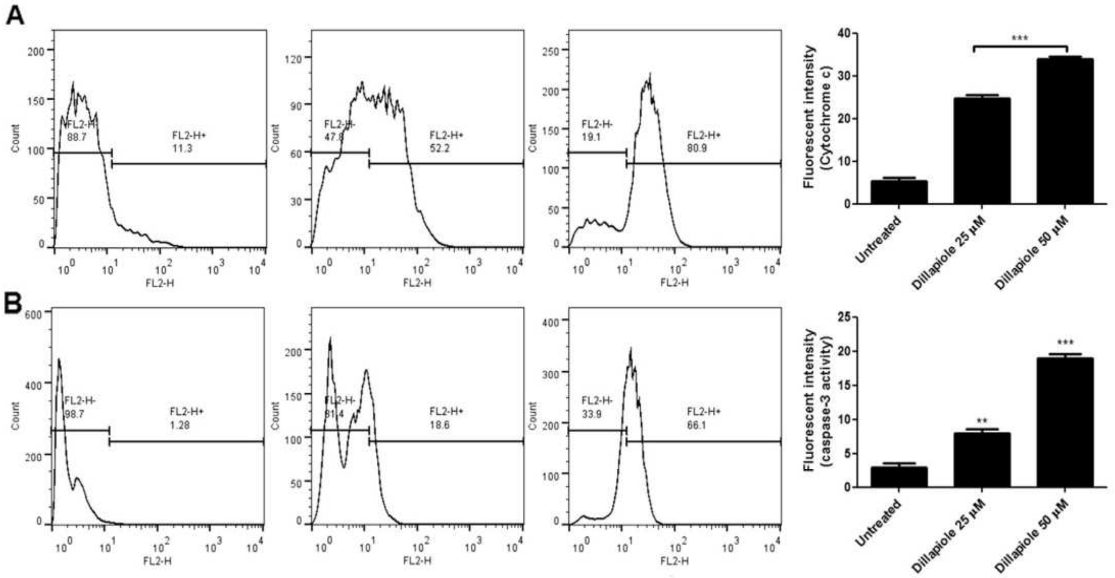

Fig. 13. Dillapiole induces apoptosis through the mitochondrial pathway in MDA-MB-231 cells. Cells were treated with dillapiole for 24 h, then collected as described in Materials and methods. (A) Expression of cytochrome *c* was detected through fluorescence intensity analysis by FACS, while (B) caspase-3 activity was measured through a fluorometric assay, using a specific substrate, Ac-YVAD-AMC. Data are the means ± SD. $^{***}p < 0.001$ and $^{**}p < 0.001$ from at least three independent experiments.

MDA-MB-231 cells is an increase of the sub-G1 peak. Apoptotic cells can display drastic alterations, with loss of cytoplasmic membrane integrity, and then appear in sub-G1 [41]. We also show that dillapiole exerts an anti-proliferative activity on MDA-MB-231 cells by arresting them in the G0/G1 phase, though a thorough investigation of the mechanism involved is still needed.

Next, we sought to determine whether dillapiole blocks MDA-MB-231 cells migration. Interestingly, suppression of MDA-MB-231 cancer cells migration by dillapiole was probably caused by arrest at the G0/G1 phase of the cell cycle. Therefore, our major finding was that dillapiole inhibits the migration of tumor cells, which is an important step required for breast cancer metastasis [42]. Since dillapiole inhibits cell migration, the next step was to investigate whether the disruption of the cytoskeleton might be mechanistically involved in the antimigration activity. We found that dillapiole does affect the cytoskeleton organization, inducing a remarkable cytoplasm retraction, which, in turn, affects cell architecture, growth, motility and survival. Indeed, the two latter events are crucial steps for tumor spreading as well as are related to poor outcomes in cell survival and motility [43]. Whether this process results from the direct effect of dillapiole on actin fibers or it is due to ROS generation remains under investigation. Nevertheless, we suggest that dillapiole is able to inhibit tumor proliferation through the disruption of actin filaments in MDA-MB-231 cells.

To further investigate MDA-MB-232 cells death induced by dillapiole, the cells were stained with YO-PRO-1/PI and subjected to flow cytometry. Dillapiole induces apoptosis at all concentrations tested, and that kind of action can in turn be associated with its pro-oxidant effects. Accordingly, the number of cells dead by apoptosis increased when cells were treated with 50 μM dillapiole. Additionally, morphological changes related to apoptosis, such as cell detachment and cell rounding, shrinkage and blebbing formation were observed. In contrast, dillapiole at 100 μM concentration induced necrosis, indicating that its apoptotic effects depend on concentration. It is therefore likely that such effects could be mediated by a strong ROS production when dillapiole is used at higher concentrations (100 μM). Also, an imbalance between the production and neutralization of ROS may cause catastrophic effects to cells, such as the inactivation of proteins, the degradation of lipids and DNA, culminating in necrosis [44]. Moreover, it is noteworthy that dillapiole, at a lower concentration (25 μM), induces apoptosis of MDA-MB-231 cells, which are known to be resistant to apoptosis [45].

The induction of cell death by apoptosis is a well-known strategy for the development of chemotherapeutic agents in the fight against cancer [46]. As discussed above, our findings show that dillapiole has antitumor effects on MDA-MB-231 cells through the induction of apoptosis. Our investigations regarding ROS release induced by dillapiole, indicate that it is a sufficient condition to trigger apoptosis through the mitochondrial pathway in MDA-MB-231 cells. Accordingly, the collapse of Δψm and the simultaneous increase in $[Ca^{2+}]$i can result in the activation of a wide variety of Ca^{2+}-sensitive enzymes [47,48]. It may generate signaling molecules for the recruitment of the mitochondrial apoptotic pathway in MDA-MB-231 cells and, consequently, trigger the activation of effector caspases. In this study, using Ac-YVAD-AMC, a specific caspase-3 substrate, we confirmed that dillapiole induces apoptosis through the mitochondrial-dependent pathway in MDA-MB-231 cells. Indeed, the release of cytochrome *c* to the cytosol from the mitochondria during apoptosis induced by dillapiole can, in turn, provoke rearrangement and heptaoligomerization of Apaf-1, namely, the apoptosome [49,50]. The apoptosome is responsible for activation of the initiator caspases, such as caspase-9, which sequentially can directly activate caspase-3, an enzyme responsible for the inter-nucleosomal DNA fragmentation, an important feature of apoptotic cell death that can be associated with our *in vitro* outcome. Based on these data, it is reasonable to suggest that the increase in caspase-3 activation induced by dillapiole is mediated by the release of cytochrome *c*.

In conclusion, we have demonstrated here, for the first time, that dillapiole has broad cytotoxic effects against a variety of tumor cells. For instance, we found that dillapiole can act as a pro-oxidant compound through the induction of ROS release in MDA-MB-231 cells. We also demonstrate that dillapiole exhibits anti-

Please cite this article in press as: A.K. Ferreira, et al., Cytotoxic effects of dillapiole on MDA-MB-231 cells involve the induction of apoptosis through the mitochondrial pathway by inducing an oxidative stress while altering the cytoskeleton network, Biochimie (2013), http://dx.doi.org/10.1016/j.biochi.2013.12.008

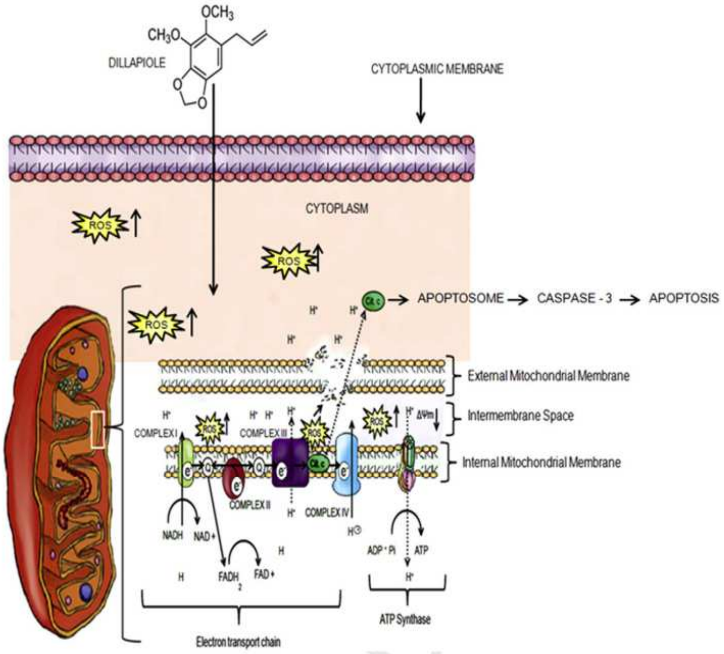

Fig. 14. Hypothesis for the mechanism of apoptosis induction by dillapiole in MDA-MB-231 cells through the mitochondrial pathway. Once in the cytoplasm, dillapiole increases ROS production, which induces depolarization of the mitochondrial membrane (Δψm) and increases mitochondrial permeability transition-pore (PTP). The consequent release of cytochrome *c* into the cytoplasm induces apoptosis through the activation of caspase-3.

proliferative properties, arresting cells at the G0/G1 phase. Additionally, its antimigration effects can be associated with the disruption of actin filaments, which in turn can prevent tumor cell metastasis. A model of the mechanisms of dillapiole-induced cell death by apoptosis is presented in Fig. 14. Dillapiole stimulates ROS production, that subsequently induces mitochondrial dysfunction, cytochrome *c* release, triggering caspase-3 activation, which results in cell apoptosis. Further investigations are needed to more precisely understand the mechanism of dillapiole-induced ROS release in MDA-MB-231 cells. The next step is to perform an evaluation of dillapiole antitumor effects in a preclinical model to establish a therapeutic hypothesis. Overall, dillapiole is a compound that has potential *in vitro* anticancer effects, suggesting that it is a promising hit in the fight against cancer.

Competing interests

The authors have declared that no competing interests exist.

Acknowledgments

The authors are grateful to the Provost's Office for Research of University of Sao Paulo for financial support, to Professor Leoberto Costa Tavares, coordinator of Laboratory for Designing and Development of New Drugs, Department of Biochemical and Pharmaceutical Technology, Faculty of Pharmacy at University of Sao Paulo, whom kindly allowed the use of a workstation to perform the *in silico* analysis, and to the Chem21 Group, Inc., for the MOLSIM 3.2 software academic license.

References

[1] A. Jemal, R. Siegel, E. Ward, T. Murray, J. Xu, M.J. Thun, Cancer statistics, CA Cancer J. Clin. 57 (2007) 43–66.

[2] J.T. Ribeiro, L.T. Macedo, G. Curigliano, L. Fumagalli, M. Locatelli, M. Dalton, A. Quintela, J.B. Carvalheira, S. Manunta, L. Mazzarella, J. Brollo, A. Goldhirsch, Cytotoxic drugs for patients with breast cancer in the era of targeted treatment: back to the future? Ann. Oncol. 23 (2012) 547–555.

[3] J.J. Jobsen, J. Van-der-Palen, M. Brinkhuis, F. Ong, H. Struikmans, Sequence of radiotherapy and chemotherapy in breast cancer after breast-conserving surgery, Int. J. Radiat. Oncol. Biol. Phys. 82 (2012) e811–817, http://dx.doi.org/10.1016/j.ijrobp.2011.11.020.

[4] P.G. Tsoutsou, Y. Belkacemi, J. Gligorov, A. Kuten, H. Boussen, N. Bese, M.I. Koukourakis, Optimal sequence of implied modalities in the adjuvant setting of breast cancer treatment: an update on issues to consider, Oncologist 15 (2010) 1169–1178.

[5] G. Llaverias, C. Danilo, I. Mercier, K. Daumer, F. Capozza, T.M. Williams, F. Sotgia, M.P. Lisanti, P.G. Frank, Role of cholesterol in the development and progression of breast cancer, Am. J. Pathol. 178 (2011) 402–412, http://dx.doi.org/10.1016/j.ajpath.2010.11.005.

[6] J. Gao, W.A. Morgan, A. Sanchez-Medina, O. Corcoran, The ethanol extract of *Scutellaria baicalensis* and the active compounds induce cell cycle arrest and apoptosis including upregulation of p53 and Bax in human lung cancer cells, Toxicol. Appl. Pharmacol. 254 (2011) 221–228.

[7] J.W. Li, J.C. Vederas, Drug discovery and natural products: end of an era or an endless frontier? Science 325 (2009) 161–165.

[8] T.G. Yunker, The Piperaceae of Brazil: I-*Piper*-group I, II, III, IV, Hohenia 2 (1972) 19–366.

[9] V.S. Parmar, S.C. Jain, K.S. Bisht, R. Jain, P. Taneja, A. Jha, O.D. Tyagi, A.K. Prasad, J. Wengel, C.E. Olsen, P.M. Boll, Phytochemistry of the genus Piper, Phytochemistry 46 (1997) 597–673.

[10] R.R.P. Almeida, R.N.P. Souto, C.N. Bastos, M.H.L. da Silva, J.G.S. Maia, Chemical variation in *Piper aduncum* and biological properties of its dillapiole-rich essential oil, Chem. Biodivers. 6 (2009) 1427–1434.

[11] C.B. Bernard, H.G. Krishnamurty, D. Chauret, T. Durst, B.J.R. Philogène, P. Sánchez-Vindas, C. Hasbun, L. Poveda, L. San Román, J.T. Arnason, Insecticidal defenses of Piperaceae from the neotropics, J. Chem. Ecol. 21 (1995) 801–813.

[12] J.W. Lorder, R.H. Neam, Constituents from *Piper banksii*, Phytochemistry 11 (1972) 2645–2646.

[13] A.P. Martins, L. Salgueiro, R. Vila, F. Tomi, S.C. Igueral, J. Casanova, A.P. Cunha, T. Adzet, Essential oils from four *Piper* species, Phytochemistry 49 (1998) 2019–2023.

[14] O. Ekundayo, I. Laakso, R.M. Adegbola, B. Oguntimein, A. Sofowora, R. Hiltunen, Essential oil constituents of Ashanti pepper (*Piper guineense*) fruits (berries), J. Agric. Food Chem. 36 (1988) 880–882.

[15] J.W. Loder, A. Moorhouse, G.B. Russell, Tumour inhibitory plants. Amides of *Piper novae-hollandiae* (Piperaceae), Aust. J. Chem. 22 (1969) 1531–1538.

Please cite this article in press as: A.K. Ferreira, et al., Cytotoxic effects of dillapiole on MDA-MB-231 cells involve the induction of apoptosis through the mitochondrial pathway by inducing an oxidative stress while altering the cytoskeleton network, Biochimie (2013), http://dx.doi.org/10.1016/j.biochi.2013.12.008

[16] L.S. Ramos, M.L. Silva, A.I.R. Luz, M.G.B. Zoghbi, J.G.S. Maia, Essential oil of *Piper marginatum*, J. Nat. Prod. 49 (1986) 712–741.

[17] R. Parise-Filho, K.F.M. Pasqualoto, F.M.M. Magri, A.K. Ferreira, B.A.V.G. Da-Silva, M.C.F.C.B. Damião, M.T. Tavares, R.A. Azevedo, A.V.V. Auada, M.C. Polli, C.A. Brandt, Dillapiole as antileishmanial agent: discovery, cytotoxic activity and preliminary sar studies of dillapiole analogues, Arch. Pharm. 345 (2012) 934–944.

[18] R. Parise-Filho, M. Pastrello, C.E.P. Camerlingo, G.J. Silva, L.A. Agostinho, T. Souza, F.M.M. Magri, R.R. Ribeiro, C.A. Brandt, M.C. Polli, The anti-inflammatory activity of dillapiole and some semisynthetic analogues, Pharm. Biol. 49 (2011) 1173–1179.

[19] M.J.C. Araújo, C.A.G. Câmara, F.S. Born, M.M. Moraes, C.A. Badji, Acaricidal activity and repellency of essential oil from *Piper aduncum* and its components against *Tetranychus urticae*, Exp. Appl. Acarol. 57 (2012) 139–155.

[20] E.H.A. Andrade, L.M.M. Carreira, M.H.L. Silva, J.D. Silva, C.N. Bastos, P.J.C. Sousa, E.F. Guimarães, J.G.S. Maia, Variability in essential-oil composition of *Piper marginatum* sensu lato, Chem. Biodivers. 5 (2008) 197–208.

[21] P.P. Diaz, B.C. Ramos, G.E. Matta, New C_6–C_3 and C_6–C_1 compounds from *Piper lenticellosum*, J. Nat. Prod. 49 (1986) 690–691.

[22] C.B. Bernard, H.G. Krishinamurty, D. Chauret, T. Durst, B.J.R. Philogene, P. Sanchés-Vindas, C. Hasbaun, L. Poveda, L.S. Roman, J.T. Arnason, Inseticidal defenses of Piperaceae from the neotropics, J. Chem. Ecol. 21 (1995) 801–814.

[23] M. Fazolin, J.L.V. Estrela, V. Catani, M.S. Lima, M.R. Alécio, Toxicidade do óleo de *Piper aduncum* L. a adultos de *Cerotoma tingomarianus* Bechyné (Coleóptera: Chrysomelidae), Neotrop. Entomol. 34 (2005) 485–489.

[24] V.A. Facundo, A.S.P. Silveira, S.M. Morais, Constituents of *Piper alatabacum* Trel & Yuncker (Piperaceae), Biochem. Syst. Ecol. 33 (2005) 753–756.

[25] F.S. Yu, J.S. Yang, C.S. Yu, C.C. Lu, J.H. Chiang, C.W. Lin, J.G. Chung, Safrole induces apoptosis in human oral cancer HSC-3 cells, J. Dent. Res. 90 (2011) 168–174.

[26] C.S. Yu, A.C. Huang, J.S. Yang, C.C. Yu, C.C. Lin, H.K. Chung, Y.P. Huang, F.S. Chueh, J.G. Chung, Safrole induces G0/G1 phase arrest via inhibition of cyclin E and provokes apoptosis through endoplasmic reticulum stress and mitochondrion-dependent pathways in human leukemia HL-60, cells, Anticancer Res. 32 (2012) 1671–1679.

[27] P. Ala, D.S.C. Yang, 6-[1-(4-Ethoxyphenyl)ethyl]-5-methoxy-1,3-benzodioxole, Acta Crystallogr. C51 (1995) 1917–1919.

[28] M.J.S. Dewar, E.G. Zoebisch, E.F. Healy, J.J.P. Stewart, AM1: a new general purpose quantum mechanical molecular model, J. Am. Chem. Soc. 107 (1985) 3903–3909.

[29] D. Doherty, MOLSIM: Molecular Mechanics and Dynamics Simulation Software – User's Guide, Version 3.2, The Chem21 Group Inc., Lake Forest, IL, 2002.

[30] C.M. Breneman, K.B. Wiberg, Determining atom-centered monopoles from molecular electrostatic potentials. The need for high sampling density in formamide conformational analysis, J. Comput. Chem. 11 (1990) 361–373.

[31] A.D. Becke, A new mixing of Hartree-Fock and local density-functional theories, J. Chem. Phys. 98 (1993) 1372–1377.

[32] M.A. Robb, J.R. Cheeseman, J.A. Montgomery, T. Vreven, K.N. Kudin, J.C. Burant, J.M. Millam, S.S. Iyengar, J. Tomas, E.V. Baron, B. Mennucci, M. Cossi, G. Scalmani, N. Rega, G.A. Petersson, H. Nakatsuji, M. Hada, M. Ehara, K. Toyota, R. Fukuda, J. Hasegawa, M. Ishida, T. Nakajima, Y. Honda, O. Kitao, H. Nakai, M. Klene, X. Li, J.E. Knox, H.P. Hratchian, J.B. Cross, V. Bakken, C. Adamo, J. Jaramillo, R. Gomperts, R.E. Stratmann, O. Yazyev, A.J. Austin, R. Cammi, C. Pomelli, J.W. Ochterski, P.Y. Ayala, K. Morokuma, G.A. Voth, P. Salvador, J.J. Dannenberg, V.G. Zakrzewski, S. Dapprich, A.D. Daniels, M.C. Strain, O. Farkas, D.K. Malick, A.D. Rabuck, K. Raghavachari., J.B. Foresman, J.V. Ortiz, Q. Cui, A.G. Baboul, S. Clifford, J. Cioslowski, B.B. Stefanov, G. Liu, A. Liashenko, P. Piskorz, I. Komaromi, R.L. Martin, D.J. Fox, T. Keith, M.A. Al-Laham, C.Y. Peng, A. Nanayakkara, M. Challacombe, P.M.W. Gill, B. Johnson, W. Chen, M.W. Wong, C. Gonzalez, J.A. Pople, Gaussian, Inc., Wallingford CT, 2004.

[33] GaussView for Windows, version 5.0, Gaussian, Inc., Pittsburgh, PA, 2000–2008.

[34] V.N. Viswanadhan, A.K. Ghose, G.R. Revankar, R.K. Robins, Atomic physicochemical parameters for three-dimensional-structure-directed quantitative structure-activity relationships. 2. Modeling dispersive and hydrophobic interactions, J. Chem. Inf. Comput. Sci. 29 (1989) 163–172.

[35] Marvin Beans 5.8.0 Software – Calculator Plugins, Chemaxon, Ltd., Budapeste 1037, Hungary, 2012.

[36] R. Emmadi, E.L. Wiley, Evaluation of resection margins in breast conservation therapy: the pathology perspective-past, present, and future, Int. J. Surg. Oncol. 2012 (2012) 1–9.

[37] T. Fukutomi, Clinical practice and outcome of breast-conserving treatment: the effectiveness of preoperative systemic chemotherapy, Breast Cancer 13 (2006) 147–151.

[38] G.V. Park, Y. Choi, Y.S. Kim, H.K. Lee, D. Kim, D.Y. Hur, ROS and ERK1/2-mediated caspase-9 activation increases XAF1 expression in dexamethasone-induced apoptosis of EBV-transformed B cells, Int. J. Oncol. 43 (2013) 29–38.

[39] J. Montero, C. Dutta, D. Van-Bodegom, D. Weinstock, A. Letai, p53 regulates a non-apoptotic death induced by ROS, Cell Death Differ. (2013), http://dx.doi.org/10.1038/cdd.2013.52.

[40] Y.C. Ye, H.J. Wang, L. Yu, S. Tashiro, S. Onodera, T. Ikejima, RIP1-mediated mitochondrial dysfunction and ROS production contributed to tumor necrosis factor alpha-induced L929 cell necroptosis and autophagy, Int. Immunopharmacol. 14 (2012) 674–682.

[41] A. Tinari, A.M. Giammarioli, V. Manganelli, L. Ciarlo, W. Malorni, Analyzing morphological and ultrastructural features in cell death, Meth. Enzymol. 442 (2008) 1–26.

[42] M. Yu, A. Bardia, B.S. Wittner, S.L. Stott, M.E. Smas, D.T. Ting, S.J. Isakoff, J.C. Ciciliano, M.N. Wells, A.M. Shah, K.F. Concannon, M.C. Donaldson, L.V. Sequist, E. Brachtel, D. Sgroi, J. Baselga, S. Ramaswamy, M. Toner, D.A. Haber, S. Maheswaran, Circulating breast tumor cells exhibit dynamic changes in epithelial and mesenchymal composition, Science 339 (2013) 580–584.

[43] D.X. Nguyen, P.D. Bos, J. Massagué, Metastasis: from dissemination to organ-specific colonization, Nat. Rev. Cancer 9 (2009) 274–284.

[44] B. Saberi, M. Shinohara, M.D. Ybanez, N. Hanawa, W.A. Gaarde, N. Kaplowitz, D. Han, Regulation of H_2O_2-induced necrosis by PKC and AMP-activated kinase signaling in primary cultured hepatocytes, Am. J. Physiol. Cell Physiol. 295 (2008) c50–63.

[45] A. Ciucci, P. Gianferretti, R. Piva, T. Guyot, T.J. Snape, S.M. Roberts, M.G. Santoro, Induction of apoptosis in estrogen receptor-negative breast cancer cells by natural and synthetic cyclopentenones: role of the IkappaB kinase/nuclear factor-kappaB pathway, Mol. Pharmacol. 70 (2006) 1812–1821.

[46] A.K. Ferreira, V.W. Freitas, D. Levy, J.L. Ruiz, S.P. Bydlowski, R.E. Rici, O.M. Filho, G.O. Chierice, D.A. Maria, Anti-angiogenic and anti-metastatic activity of synthetic phosphoethanolamine, PLoS One (2013), http://dx.doi.org/10.1371/journal.pone.0057937.

[47] C. Giorgi, F. Baldassari, A. Bononi, M. Bonora, E. De-Marchi, S. Marchi, S. Missiroli, S. Patergnani, A. Rimessi, J.M. Suski, M.R. Wieckowski, P. Pinton, Mitochondrial Ca^{2+} and apoptosis, Cell Calcium 52 (2012) 36–43.

[48] L. Scorrano, S.A. Oake, J.T. Opferman, E.H. Cheng, M.D. Sorcinelli, T. Pozzan, S.J. Korsmeyer, BAX and BAK regulation of endoplasmic reticulum Ca^{2+}: a control point for apoptosis, Science 300 (2003) 135–139.

[49] Q. Hu, D. Wu, W. Chen, Z. Yan, Y. Shi, Proteolytic processing of Caspase-9 zymogen is required for apoptosome-mediated activation of Caspase-9, J. Biol. Chem. 288 (2013) 15142–15147.

[50] S. Yuan, C.W. Akey, Apoptosome structure, assembly, and procaspase activation, Structure 21 (2013) 501–515.

Please cite this article in press as: A.K. Ferreira, et al., Cytotoxic effects of dillapiole on MDA-MB-231 cells involve the induction of apoptosis through the mitochondrial pathway by inducing an oxidative stress while altering the cytoskeleton network, Biochimie (2013), http://dx.doi.org/10.1016/j.biochi.2013.12.008

Toxicology and Applied Pharmacology 266 (2013) 385–398

Contents lists available at SciVerse ScienceDirect

Toxicology and Applied Pharmacology

journal homepage: www.elsevier.com/locate/ytaap

RPF101, a new capsaicin-like analogue, disrupts the microtubule network accompanied by arrest in the G2/M phase, inducing apoptosis and mitotic catastrophe in the MCF-7 breast cancer cells

Paulo Luiz de-Sá-Júnior [a,1], Kerly Fernanda Mesquita Pasqualoto [b,1], Adilson Kleber Ferreira [a,1], Maurício Temotheo Tavares [c], Mariana Celestina Frojuello Costa Bernstorff Damião [c], Ricardo Alexandre de Azevedo [b], Diana Aparecida Dias Câmara [a], Alexandre Pereira [a], Dener Madeiro de Souza [a], Roberto Parise Filho [c,*]

[a] *Laboratory of Genetics, Butantan Institute, Vital Brasil Avenue 1500, Postal Code: 05503-900, Sao Paulo, Brazil*
[b] *Biochemistry and Biophysical Laboratory, Butantan Institute, Vital Brasil Avenue 1500, Postal Code: 05503-900, Sao Paulo, Brazil*
[c] *Department of Pharmacy, School of Pharmaceutical Sciences, University of Sao Paulo, Prof. Lineu Prestes Avenue, 580, Postal Code: 05508-000, Sao Paulo, Brazil*

ARTICLE INFO

Article history:
Received 2 July 2012
Revised 5 November 2012
Accepted 19 November 2012
Available online 10 December 2012

Keywords:
Capsaicin-like analogue
RPF101
Molecular modeling
Cell cycle
Antitumoral
Apoptosis

ABSTRACT

Breast cancer is the world's leading cause of death among women. This situation imposes an urgent development of more selective and less toxic agents. The use of natural molecular fingerprints as sources for new bioactive chemical entities has proven to be a quite promising and efficient method. Capsaicin, which is the primary pungent compound in red peppers, was reported to selectively inhibit the growth of a variety tumor cell lines. Here, we report for the first time a novel synthetic capsaicin-like analogue, RPF101, which presents a high antitumor activity on MCF-7 cell line, inducing arrest of the cell cycle at the G2/M phase through a disruption of the microtubule network. Furthermore, it causes cellular morphologic changes characteristic of apoptosis and a decrease of $\Delta\psi m$. Molecular modeling studies corroborated the biological findings and suggested that RPF101, besides being a more reactive molecule towards its target, may also present a better pharmacokinetic profile than capsaicin. All these findings support the fact that RPF101 is a promising anticancer agent.

Introduction

Breast cancer is the leading cause of death among women worldwide. About 63,300 cases of breast carcinoma in situ are expected to be newly diagnosed in 2012 (Siegel et al., 2012). Despite many efforts made in surgical management, radiotherapy and new combined chemotherapy, there is a need for the development of more selective and less toxic agents (Geyer et al., 2006). One of the key hallmarks of cancer cells is their ability to evade apoptosis, which, among other important roles, is a controlled process of elimination of irreversibly damaged cells (Jin and El-Deiry, 2005). The loss of apoptosis control has been observed in many cancers. As a result, the apoptotic machinery is seen today as a promising target for drug development (Debatin and Krammer, 2004; Fesik, 2005; Kaufmann and Earnshaw, 2000).

Natural products, mainly secondary metabolites produced by living organisms, have a long history as a source of novel therapeutics. It has been recognized that natural product structures having high chemical diversity, biochemical specificity and other molecular properties could turn out to be favorable as lead structures for drug discovery (Koehn and Carter, 2005). Recently, capsaicin (Fig. 1A) or N-vanillyl-8-methyl-1-nonenamide, the primary pungent and irritating ingredient present in a variety of red peppers of the genus *Capsicum* (Walpole et al., 1993a,b,c), was reported to selectively inhibit the growth of tumor cells (Maity et al., 2010). Despite previous discordant results from studies that determined its potential mutagenic and carcinogenic activity (Surh and Lee, 1996), subsequent investigations have shown that capsaicin induces apoptosis in a wide variety of tumor cells (Huang et al., 2009; Ito et al., 2004; Kim et al., 2010; Sánchez et al., 2007; Thoennissen et al., 2010; Wu et al., 2006). Additional studies reported that capsaicinoids displayed in vitro and in vivo antitumor activity (Oh et al., 2008). In cultured cells, capsaicin blocked the cell migration in breast cancer, while in mice, oral consumption of capsaicin decreased the size of MDAMB 231 breast cancer tumors by 50%, and inhibited the development of pre-neoplastic breast lesions by up to 80%. Also, direct injection of capsaicin led to an 80% reduction in tumor size (Thoennissen et al., 2010). Thus, capsaicin can be considered a potential lead against malignant tumors. However, the molecular mechanisms and the signaling pathways leading to capsaicin-induced

---

[*] Corresponding author. Fax: +55 11 3091 3815.
E-mail address: roberto.parise@usp.br (R. Parise Filho).
[1] These authors contributed equally to this work.

0041-008X/$ – see front matter © 2012 Elsevier Inc. All rights reserved.
http://dx.doi.org/10.1016/j.taap.2012.11.029

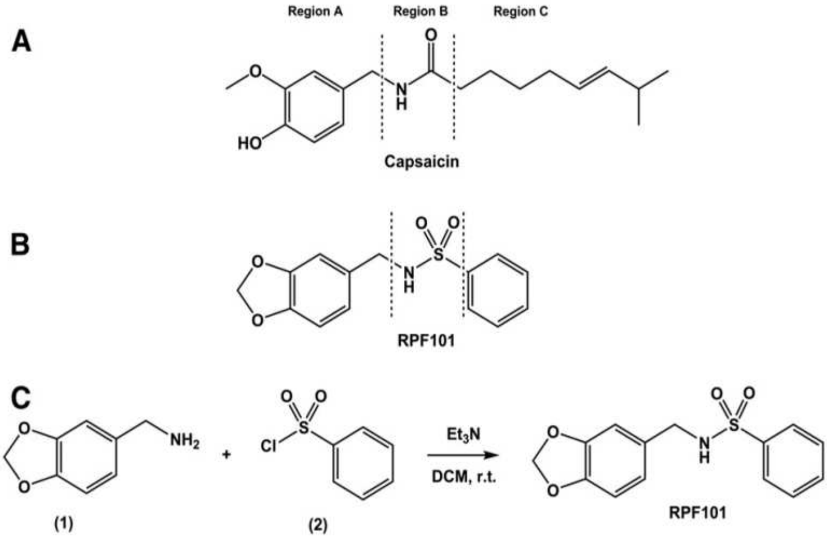

Fig. 1. (A) Structure of capsaicin, highlighting regions A, B and C. Region A: methylcatechol system; Region B: amide bond; Region C: lipophilic side-chain; (B) Structure of RPF101. Regions A, B and C possess the same structural/electronic similarity to capsaicin; (C) Synthesis of RPF101. Piperonylamine (1) was sulfonylated by benzenesulfonyl chloride (2) to give RPF101.

cell death are still unclear and need further investigation (Ghosh and Basu, 2010). In addition, there is a real concern to elucidate if compounds exhibiting chemical/molecular features similar to capsaicin would also present anticancer effects.

Considering that, a structural analogue of capsaicin, named as RPF101 (ID code) (Fig. 1B), was design and synthesized, and its chemical/molecular properties and biological responses are presented in this study. The designing approach was based upon a systematic change in the capsaicin structure, which was divided in three parts as follows: the methylcatechol group (Region A), amide bond in the middle region (Region B), and alkyl side chain (Region C).

Firstly, in region A, a ring closure was performed at the methylcatechol group in order to achieve the 1,3-benzodioxole bicyclic system. This type of molecular modification could provide important advantages for the analogue since the benzodioxole system is a privileged structure presented in a series of substances with antitumor activity, such as podophyllotoxin, etoposide, and teniposide (Brandão et al., 2010). Besides, more suitable lipophilic properties and a hydrogen bond acceptor character, which are relevant features to improve pharmacokinetic and pharmacodynamic profiles (Barreiro and Fraga, 1999), are covered by this particular molecular modification.

Regarding the structural analyses of capsaicin, the strategy on region B was centered in the replacement of amide bond by a bioisosteric sulfonamide group. Bioisosterism strategy can be used to improve the potency, selectivity and pharmacokinetics of key compounds, or generate new intellectual property (Patani and LaVoie, 1996). The replacement of amide bonds, particularly, by suitable bioisoster groups, which maintain similar geometric, electronic, or hydrogen bonding properties, have been well succeed and extensively applied (Black et al., 2005).

Finally, the alkyl side chain in region C was modified by employing homology and rigidification strategies in order to keep the lipophilic character of that part of the molecule. Moreover, as presented in Fig. 1C, the RPF101 analogue was easily synthesized from piperonylamine (1) by coupling with benzenesulfonyl chloride (2), in one step (Cunico et al., 2011).

The antitumor effects of RPF101 in MCF-7 human breast-cancer cells and whether the caspase-independent pathway is involved together with the comparison of molecular properties between prototype and analogue were considered the goals of this study.

Materials and methods

Materials and RPF101 synthesis. Reagents and solvents were commercial grade and were used as supplied. ^1H and ^{13}C NMR spectra were recorded at 300 MHz and 75 MHz respectively, and chemical shifts are expressed as δ units using tetramethylsilane (TMS) as an internal standard. The spectral splitting patterns are described as follows: s, singlet; d, doublet; dd, double doublet; t, triplet; m, multiplet; and bt, broad triplet peak. High resolution mass spectra (HRMS) were measured with a Bruker Daltonics Micro-TOF spectrometer with an ESI source coupled to a Waters HPLC system. Melting points were recorded on an Electrothermal 9100 melting point apparatus and were uncorrected. General synthetic procedure: Piperonylamine (**1**) (5.0 mmol) was dissolved in dichlorometane (10 ml) and then triethylamine (5.2 mmol) and dimethylformamide (catalytic) were added. The reaction mixture was stirred for 30 min under nitrogenous atmosphere, and then benzenesulfonyl chloride (**2**) (5.0 mmol) was added dropwise, and stirred for an additional 24 h at room temperature. The organic layer was washed with 5% HCl aqueous solution, water, brine and dried over $MgSO_4$. The solvent was removed under high vacuum and the product RPF101 was obtained after recrystalization in hot hexane:dichloromethane solution. White solid, yield 80.2% (1.17 g). ^1H NMR (300 MHz, $CDCl_3$, ppm) δ: 7.88 (2H, dd, $J^1 = 1.5$ Hz, $J^2 = 1.8$ Hz, 11, 15-ArH), 7.61–7.50 (3H, m, $J = 1.4$ Hz, 12, 13, 14-ArH), 6.71–6.63 (3H, m, 3, 4, 6-ArH), 5.93 (2H, s, 7-OCH_2O), 4.80 (1H, bt, 9-NH), 4.08 (2H, d, $J = 5.8$ Hz, 8-CH_2); ^{13}C NMR (75 MHz, $CDCl_3$, ppm) δ: 147.9 (C1), 147.3 (C2), 140.0 (C10), 132.7 (C5), 130.0 (C11, C15), 129.1 (C12, C14), 127.1 (C13), 121.4 (C4), 108.4 (C6), 108.2 (C3), 101.1 (C7), 47.2 (C8); HRMS (ESI) m/z Calc. for: $C_{14}H_{13}NO_4S + H$: 291.0565, found: 291.0562; m.p.: 77.1–77.6 °C.

Molecular modeling approach. The three-dimensional (3D) molecular models of capsaicin and its derivative were built up, in their neutral forms, using the HyperChem 7.0 MM+ force field (Hypercube, Inc., 2002) without any constrains. The crystal data from 3-chloro-N-(4-hydroxy-3-metoxy-benzyl)-2,2-diethylpropanamide (cif file; Huang et al., 2010) was employed as the starting geometry. Partial atomic charges were computed with AM1 semi-empirical method (Dewar et al., 1985), also implemented in HyperChem 7.0 (Hypercube, Inc., 2002). The MOLSIM 3.2 software (Doherty, 2002) was used to perform energy-minimization (steepest descent and conjugate gradient methods; convergence criterion of 0.01 kcal/mol) and molecular dynamics (MD) simulations. MD simulations of 1 ns (step size of 1 fs) at 310 K were performed for each molecular model. Output trajectory file was recorded in 20 ps steps resulting in a conformational ensemble profile (CEP) of 50,000 conformers for each investigated molecule. The lowest-energy conformation was selected from CEP, and the hydration shell model proposed by Forsythe and Hopfinger (1973) was employed to estimate the solvation energy contribution. The hydrogen bonding intramolecular energy contribution was also computed for the selected lowest-energy conformation. The total potential energy (ET) of each selected conformation corresponds to the summation of the following intramolecular energy contributions: stretching ($E_{stretch}$), bending (E_{bend}), torsional (E_{tors}), Lennard–Jones or 1–4 interactions (E_{1-4}), electrostatic (E_{charge}), van der Waals (E_{vdW}), hydrogen bonding (E_{Hb}), and solvation (E_{solv}).

The lowest-energy conformation of each molecule from MD simulations was energy-minimized (MOLSIM 3.2; Doherty, 2002) and, subsequently, used as starting geometry to calculate molecular properties of distinct nature (electronic, steric, hydrophobic). Electronic properties, such as partial atomic charges from electrostatic potentials using a grid based method (CHELPG; Breneman and Wiberg, 1990), dipole moment (μ), molecular orbital energies (E_{HOMO}, energy of the highest occupied molecular orbital; E_{LUMO}, energy of the lowest unoccupied molecular orbital), and electrostatic potential (EP), were computed with the B3LYP (Becke, three-parameter, Lee-Yang-Parr) (Becke, 1993) hybrid functional and 6–31(d,p) basis (Gaussian 03 W, 2004; Gaussian, Inc.). EP maps were calculated onto a Connolly molecular surface, using a color scheme ranged from −0.046 (intense red) to 0.046 (intense blue). Negative values of EP (higher electronic density distribution) are depicted in red and positive values in blue (lower electronic density distribution) (GaussView 5.0, Gaussian, Inc., 2000–2008). The molecular volume (V) of RPF101 and capsaicin was calculated using the grid method reported by Bodor and co-workers (Bodor et al., 1989) with the atomic radii of Gavezzotti (1983). The binding surface was specified as van der Waals and the density of grid points was set as 50 points on cube side (HyperChem 7.0, Hypercube, Inc., 2002). Also, the calculated octanol/water partition coefficient (ClogP), which is a measure of molecular hydrophobicity, was computed based upon Viswanadhan et al. (1989), implemented in the Marvin 5.8.0 package, Calculator Plugins (ChemAxon, Ldt., 2012).

Cell culture. The human breast adenocarcinoma MCF-7 and MDA-MB-231 cells were purchased from the American Type Culture Collection (Manassas, VA) and melanoma cells (Sbcl-2; Mel-85; SK-Mel-28) were gently provided by Dr. Roger Chammas from the Department of Radiology and Oncology, Faculty of Medicine, University of Sao Paulo, São Paulo, Brazil. The cells were maintained in RPMI-1640 medium supplemented with 10% fetal calf serum (FCS) (Cultilab, Campinas, SP, Brazil) and an antibiotic solution of penicillin (100 units/ml) and streptomycin (100 μg/ml). All cells were cultured at 37 °C in a fully humidified incubator with 5% CO_2. All experiments described were performed at least three times using cells in the exponential growth phase.

Cell viability assay. The MTT (3-[4,5-dimethylthiazol-2-yl]-2,5-diphenyl-tetrazolium bromide) assay was used to evaluate cell viability and proliferation. Briefly, cells in the logarithmic growth phase were plated at a density of 10^4 cells/ml in 96-well plates. Twenty-four hours later, the cells were treated with capsaicin and RPF101 at the concentrations of 6.25 to 200 μM for further 24 h. 10 μl of MTT (5 mg/ml) was then added to each well and incubated again under the same conditions described above for 3 h. The medium was carefully aspirated and 100 μl of DMSO was added to each well to dissolve the formazan crystal formed. The optic density (OD) was measured at 540 nm in a microplate reader (Thermoplate TP Reader, Tokay Hit, Japan). Percentage of growth inhibition was equal to [1-(OD of treated/OD of control)] × 100.

Cell proliferation assay. MCF-7 cells were seeded at 2×10^3 cells/well on 96-well plates and treated with capsaicin and RPF101 at concentrations from 12.5 to 100 μM for 96 h. Cell proliferation was monitored by the 3-(4,5-dimethylthiazol-2-yl)-2,5-diphenyltetrazolium bromide (MTT) assay and cell survival was shown as relative absorbance.

Three-dimensional (3D) cell culture. To test the response of MCF-7 cells to RPF101 treatment, the cells were cultured in Matrigel 3D (Trevigen, Gaithersburg, USA) for 10 days at 37 °C in a fully humidified incubator with 5% CO_2. The cells were then treated with 32 μM RPF101 for 24 h. After treatment, the morphological aspects of the cells were analyzed using an Olympus CK2 light microscope.

Evaluation of cytotoxicity by Hoechst/PI staining. The appearance of apoptotic and necrotic cells was monitored by double staining with Hoechst 33342 and propidium iodide (PI), (SIGMA, St. Louis, MO) using a fluorescence microscope (Nikon). The cells were grown overnight in six-well plates, and after 24 h of treatment with 53 μM capsaicin and 32 μM RPF101, 1 μl Hoechst 33258 (0.13 mM) and 1 μl PI (1 mg/ml) were added to each well. After 15 min of incubation at room temperature in the dark, the cells were examined under a fluorescence microscope. The cells were classified based on their morphological and staining characteristics as: alive (pale blue fluorescence), early apoptotic cells (intensive bright blue fluorescence), late apoptotic cells (blue-violet fluorescence) and necrotic (red fluorescence) (Gasiorowski et al., 2001). Representative areas of cells stained after 24 h of treatment were chosen for documentation.

Apoptosis assay by acridine orange staining. Acridine orange enters both viable and nonviable cells and emits a green fluorescence if intercalated into double stranded nucleic acid or red fluorescence if bound to single stranded nucleic acid. Cells were plated in 96-well plates, grown overnight and the next day exposed to 53 μM capsaicin and 32 μM RPF101. After the treatment, the medium containing the compound was removed and 1 μl of acridine orange (1 μg/ml) (Chemical Co., St. Louis, MO) was added to each well and incubated for 15 min in order to distinguish apoptotic cells. Staining intensity was determined by fluorescence microscopy (Nikon) at 200× magnification.

DNA fragmentation assay. The cells (10^5/well) were plated in 6-well plates and treated with 53 μM capsaicin and 32 μM RPF101, or equal volume of culture medium (control). After 24 h of incubation, the cells were treated with a lysis buffer (10 mM EDTA, 50 mM Tris–HCl pH 8.0, 0.25% NP-40, 0.5 mg/ml proteinase K) at 50 °C for 2 h. The DNA was precipitated with 2.5 ml of a solution containing ethanol 70% and NaCl 3 M overnight at room temperature. The samples were then centrifuged at 12,000 *g* for 30 min at 4 °C. The precipitate was washed with 70% ethanol and dried at room temperature. The DNA pellet was then dissolved in TE buffer (1 mM EDTA, 10 mM Tris–HCl pH 8.0) containing RNase (10 μg/ml) and incubated at 37 °C for 1 h. The concentration of the extracted DNA was measured in a spectrophotometer (SPECTRAmax, Molecular Devices, USA) at 260 nm. DNA fragmentation was analyzed by electrophoresis in a 2% agarose gel containing ethidium bromide (0.5 μg/ml). After electrophoresis, the gel was visualized under UV illumination (Hoefer, Macrovue UV, 20) and photographed using the Doc-Print Photo Documentation system.

Detection of apoptosis by flow cytometry. The cells were treated with the test compounds for 24 h, then washed with PBS (500 μl/well), harvested (including suspension cells) and incubated with 2 μM

Table 1
Calculated molecular properties for capsaicin and RPF101.

Compounds	$E_{STRETCH}$ kcal/mol	E_{BEND} kcal/mol	E_{TORS} kcal/mol	E_{1-4} kcal/mol	E_{VDW} kcal/mol	E_{CHARGE} kcal/mol	E_{HB} kcal/mol	E_{SOLV} kcal/mol	E_T kcal/mol
RPF101	9.11	13.10	−1.18	12.83	−2.39	−28.75	−6.02	−11.19	−14.49
capsaicin	9.72	14.14	8.81	15.82	−2.63	−5.81	−17.77	−1.41	20.87
	ClogP	μ Debye	V Å^3	E_{HOMO} kcal/mol	E_{LUMO} kcal/mol	GAP kcal/mol	ClogP/μ		
RPF101	2.15	5.09	239.37	−134.16	−14.48	−119.68	0.42		
capsaicin	3.75	3.26	310.60	−137.88	−4.61	−133.28	1.15		

YO-PRO-1 (Life Technologies) and 10 μM of PI in PBS for 30 min at room temperature in the dark. The cells were immediately analyzed by flow cytometry using 488 nm excitation in a FACScalibur flow cytometer (Scalibur-Becton Dickinson, San Jose, CA). The data from three independent experiments were analyzed with the *CellQuest* program.

Measurement of mitochondrial transmembrane potential. The mitochondrial membrane potential (ΔmΨ) was measured using the tetramethyl-rhodamine ethyl ester (TMRE) assay, monitored by flow cytometry. MCF-7 cells (10^6 cells/well) were seeded in 6-well plates and incubated for 24 h. After 12 h of treatment with 53 μM capsaicin or 32 μM RPF101, 20 nM TMRE were added to cell cultures maintained at 37 °C for 45 min. The fluorescence was measured by flow cytometry in a FACScalibur flow cytometer. A total of 10,000 cells/sample were analyzed and the mean fluorescence intensity and percentage of cells in each population (M1 and M2) were recorded.

Cell cycle analysis. Cells were treated with 32 μM RPF101 and capsaicin 53 μM for 24 h. Briefly, cells were washed and resuspended in PBS, incubated at 37 °C for 45 min with 10 mg/ml RNase and 1 mg/ml PI, then again incubated for 30 min at 37 °C. Flow cytometry analysis was performed using a FACScalibur flow cytometer. The DNA content in the different cell cycle phases was determined using Modfit LT software (Verity Software House, Topsham, ME).

Confocal laser scanning microscopy. MCF-7 cells were seeded onto sterile glass cover slips in 24-well plates. Cells were treated with 53 uM capsaicin or 32uM RPF101 and the, they were fixed with 3.7% paraformaldehyde and permeabilized in 0.05% triton-x diluted in PBS containing 10% bovine fetal serum. Next, the cells were incubated in the dark at 37 °C with the monoclonal anti-β-tubulin (Abcam) antibody (primary antibody), were applied to coverslips containing monolayer cultures and then incubated for 45 min at 37 °C, then rinsed 3× briefly in PBS. Coverslips were incubated at 37 °C for 45 min with the secondary antibodies (FITC labeled Goat-anti-mouse IgG (Santa Cruz)), rinsed briefly 3× in PBS then incubated with PI for 3 min at 37 °C and rinsed briefly 3× in PBS. Image analysis was performed with a confocal laser scanning microscope (Carl Zeiss LSM 700; Leica, Mannheim, Germany). Post-acquisition image processing, background correction, adjustment of brightness and contrast and export to tiff format were done with Image J software (version 14.1) National Institutes of Health (Bethesda, Maryland, USA).

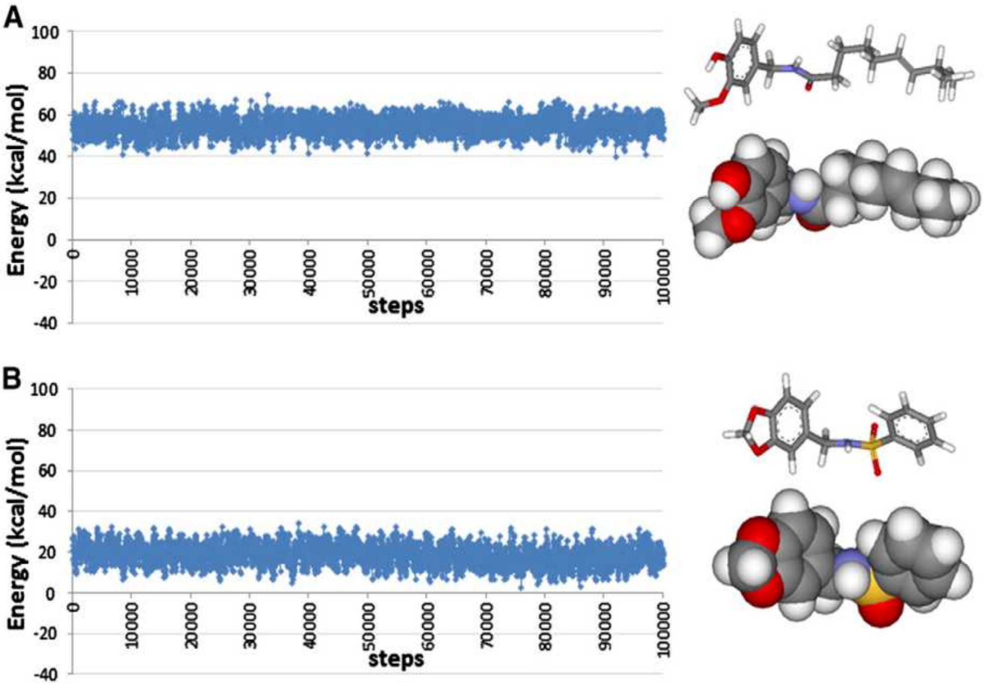

Fig. 2. Plot of energy values versus steps for an equilibration region of the CEP (100 ps) from MD simulation (1 ns at 298 K) where the lowest-energy conformer of each molecule was selected: (A) capsaicin, and (B) RPF101. The energy values (kcal/mol) correspond to the summation of the following intramolecular energy contributions: stretching, bending, torsional, 1–4 or Lennard–Jones, van der Waals, and electrostatic. The lowest-energy conformation selected from each CEP is presented as space-filling CPK (Corey–Pauling–Koltun) and stick models. Carbon atoms are displayed in gray, oxygen in dark gray, and hydrogen in white (ViewerLite 5.0, Accelrys, Inc., 2002).

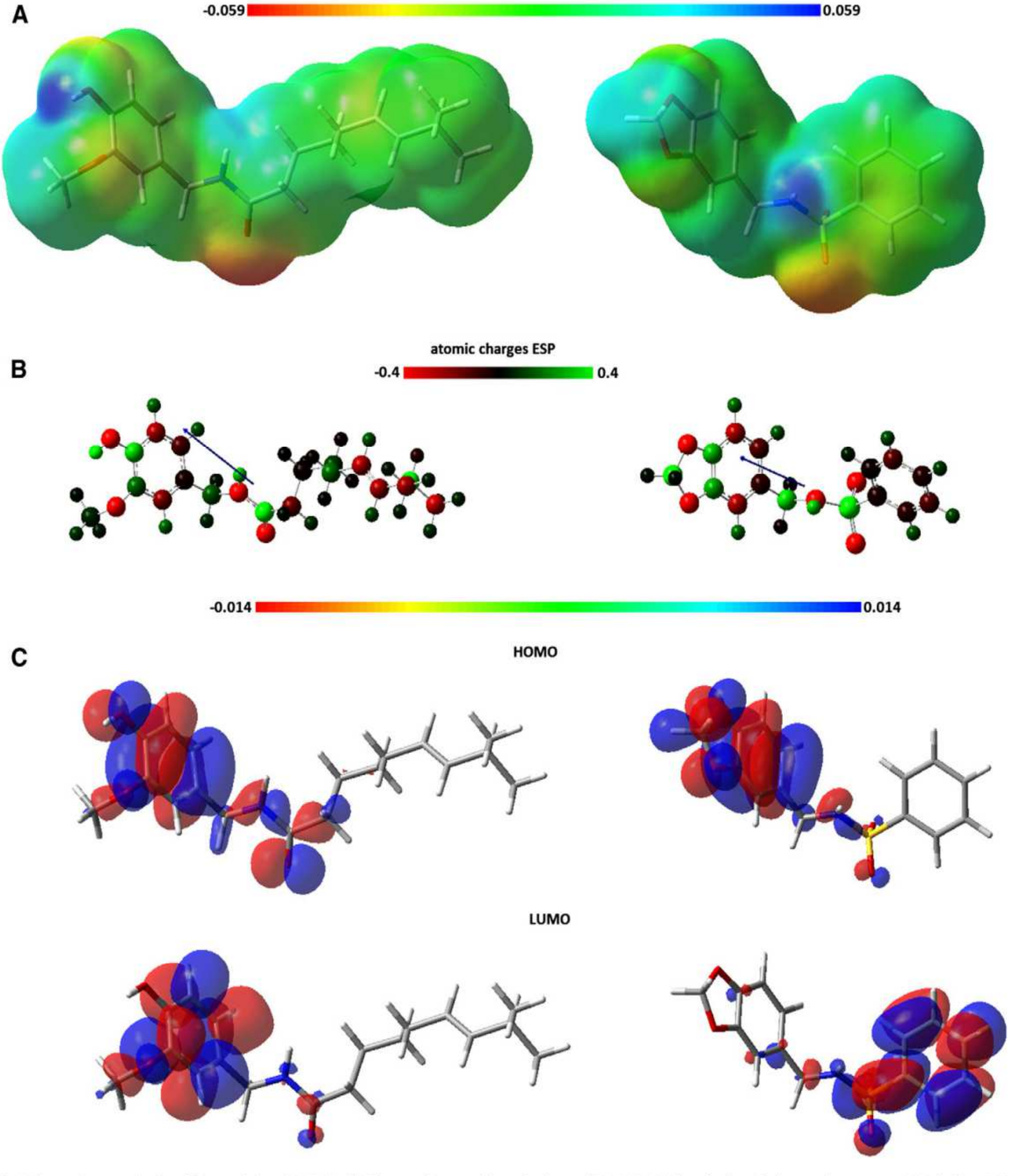

Fig. 3. Electronic properties found for capsaicin and RPF101. (A) Electrostatic potential atomic charges (ESP, CHELPG) by color [atomic charge color ramp: −0.404 (red) to 0.404 (green)]; (B) total dipole moment vector (blue arrows), and maps of electrostatic potential (MEPs) [color range: −0.046 (intense red) to 0.046 (intense blue)]. The molecules are presented as ball-wire models (carbon atoms in gray, oxygen in red, and hydrogen in white). (C) Distribution of molecular orbital maps, HOMO and LUMO [color range: −0.021 (red) to 0.021 (blue)]. The molecules are showed as stick models (carbon atoms in gray, oxygen in red, and hydrogen in white) (GaussView 5.0, Gaussian Inc., 2000–2008).

Statistical analysis. All values were expressed as mean ± SD. Each value is the mean of at least three independent experiments in each group. One way analysis of variance (ANOVA) with Tukey post-hoc test was carried out to determine significant differences from untreated controls. The asterisk (*) indicates the values that are significantly different from the control (**$p<0.05$ and ***$p<0.001$).

Results

RPF101 synthesis and identification

The active molecule (RPF101) was successfully synthesized using the described method with an 80% yield of the pure product, which

Table 2
The cytotoxic effects of RPF101 and capsaicin in several human tumor cell lines.

Cell line (tissue)	Inhibitory concentration 50% (IC_{50}) (μM)	
	RPF101	Capsaicin
MCF-7 (MAMMARY)	32.0	53.0
MDA-MB-231 (mammary)	14.2	21.7
SK-MEL-28 (skin)	19.1	14.1
Sbcl2 (skin)	17.5	20.1
Mel-85 (skin)	15.7	15.2

was identified by ^1H and ^{13}C NMR spectra. From the molecular ion signal at m/z 291 (mass spectrum), the composition of $C_{14}H_{13}NO_4S$ was ascertained. The NMR spectrum of RPF101 was also consistent with the molecular formula obtained by HRMS. Full characterization has been carried out in this work, and NMR data are presented in Materials and methods. The melting point between 77.1 and 77.6 °C confirmed the compounds' purity.

Molecular modeling findings

The purpose of a theoretical approach was to find energetically more favorable conformations for capsaicin and RPF101, calculate the molecular properties and, finally, provide some insights regarding structure–activity relationships. Table 1 presents the thermodynamic parameters found for the lowest-energy conformation selected from MD simulation of each molecule, and the values obtained for the calculated molecular properties [lipophilicity (ClogP), electronic (μ, E_{HOMO}, E_{LUMO}, gap $= E_{HOMO} - E_{LUMO}$), and intrinsic/steric (V)].

The findings from the MD simulations are presented in Fig. 2A and B. MD simulations (1 ns at 310 K) of capsaicin (Fig. 2A) and RPF101 (Fig. 2B) reached the thermodynamic equilibrium in approximately 300,000 simulation steps. Part of the CEP (100 ps) from where the lowest-energy conformation of each molecule was chosen and, also, the 3D representation of selected conformers, such as space filling CPK and stick or tube molecular models, can be visualized in Fig. 2A and B. The space filling CPK model considers the van der Waals radius of each chemical element in the molecular structure. This type of molecular model can provide insights regarding the steric hindrance of some chemical elements or substituent groups in the molecular system. The van der Waals volume values computed for capsaicin and its derivative were 310.60 and 239.37 Å^3, respectively (Table 1).

As already mentioned, the thermodynamic parameters, such as intramolecular energy contributions and total potential energy (ET), found for the selected lowest-energy conformation of each molecule, and are listed in Table 1. The capsaicin structure has more degrees of freedom than its derivative and the ET value (more positive) reflects this structural difference.

EP maps, partial atomic CHELPG charges in color and dipole moment vector are showed in Fig. 3A, B and C. The electronic density distribution can be visualized through the EP maps. The higher electronic density (yellow to red) is distributed on the carbonyl region of capsaicin and corresponding sulfonyl region of RPF101 (Fig. 3A). The partial atomic electrostatic potential charges (ESP, CHELPG) are represented in a color range from red (negative; −0.4) to green (positive; 0.4) (Fig. 3B). The carbon carbonyl in the lead compound is in bright green color and its charge value is positive (0.6109). The corresponding sulfur (sulfonyl) in RPF101 also has a positive CHELPG value (0.9073). Otherwise, the carbon neighbor to the benzodioxole ring is three-fold more positive (0.3231; bright green) than the corresponding carbon of capsaicin (0.1232; dark green), which is attached to the aromatic ring.

The dipole moment (μ) vector can be visualized as blue arrows in Fig. 3B. By definition, the dipole moment is the product of the total amount of positive or negative charge and the distance between their centroids. The μ values are listed in Table 1 and this electronic property is related to the molecule's polarity. Additionally, the dipole moment provides useful information for the deduction of the molecular geometry of a molecule. Capsaicin presents a lower μ value (3.26 Debye) in comparison to RPF101 (5.09 Debye). It has a more linear molecular geometry than the benzodioxole derivative, which is shorter and more bent.

The lipophilic property, expressed through the calculated n-octanol/water partition coefficient (ClogP), is also listed in Table 1. The partition coefficient reveals the hydrophobic character of a drug or compound. Both molecules have a hydrophobic character, but capsaicin presents a higher ClogP value (3.75) than RPF101 (2.15). The hydrophobic/hydrophilic molecular balance is needed to provide suitable pharmacodynamic and pharmacokinetic profiles. But, there is an optimum value for lipophilicity. In this study, the ratio between ClogP and μ values was considered as a measure of the compound's molecular hydrophobic/hydrophilic balance and related to its antitumor activity. Capsaicin presented higher ClogP/μ value than RPF101, indicating that its ClogP/μ value (1.15) would be the maximum limit to show antitumor activity, for instance. Then, our theoretical findings are in agreement with those experimentally observed, RPF101 was more active than capsaicin probably because its ClogP/μ value was lower than 1.15.

The molecular orbital energies (E_{HOMO} and E_{LUMO}; kcal/mol) as well as the difference between them (gap $= E_{HOMO} - E_{LUMO}$; kcal/mol) were computed for the selected lowest-energy conformation of each molecule and are listed in Table 1. Also, the HOMO and LUMO maps for

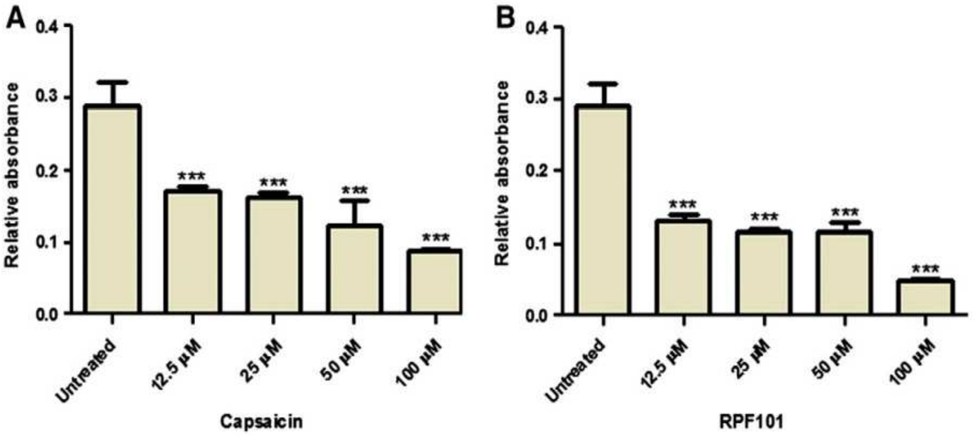

Fig. 4. Antiproliferative effect of RPF101 on MCF-7 cells. (A and B) Effect of different concentrations of RPF101 (100; 50; 25; 12.5; 6.25 μM) on cell proliferation after 24 h of exposure using the MTT assay. The data are the means ± SD from three independent experiments. ***$p<0.001$ as compared to the untreated cells.

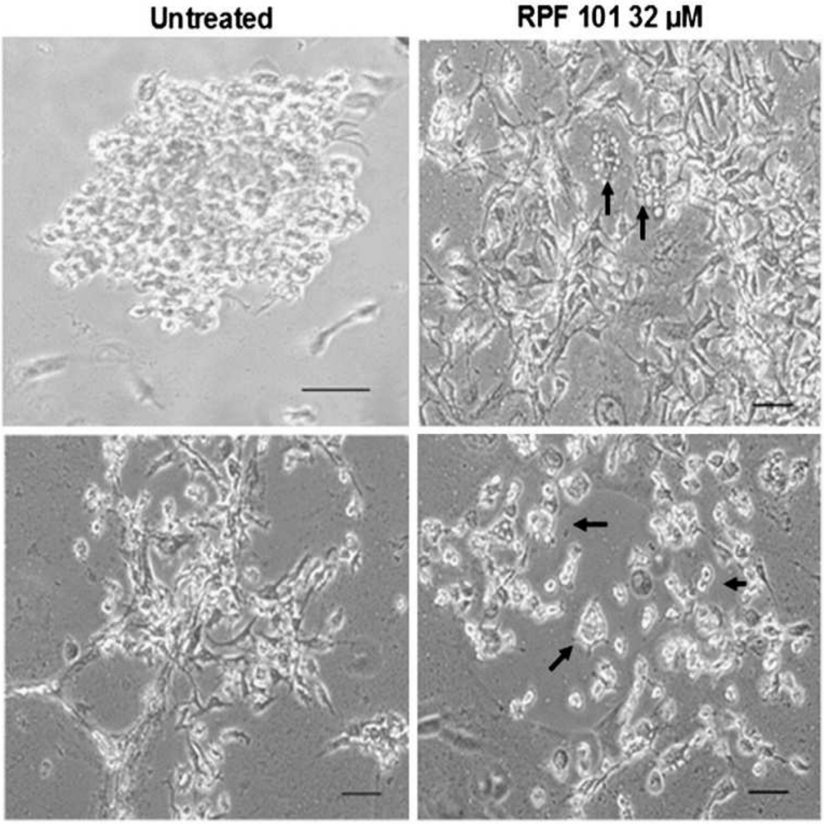

Fig. 5. Morphological analysis of RPF 101 on MCF-7 cells grown in Matrigel 3D. Untreated cell shown a formation of spheroid-like structures by forming aggregates of cells. RPF101 changes the morphology of MCF-7 cells characteristics of apoptosis (arrows), such as, cell shrinkage and pyknosis. Scale bars: 20 mm.

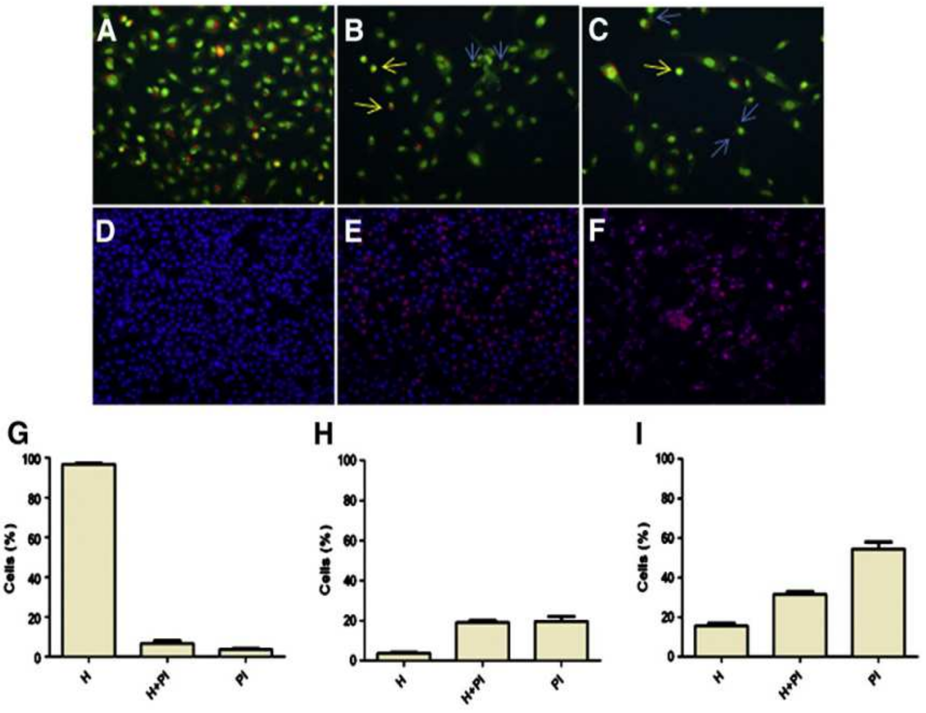

Fig. 6. Assessment of morphological changes of apoptosis by acridine orange and Hoechst/PI staining: Cells were exposed to (A); RPF101 (B) or capsaicin (C). After 24 h of incubation, 200 μl of the AO fluorescent dyes (1 μg/ml) were added and, after 5 min exposure, the wells were photographed with a fluorescence microscope. Yellow arrows show cells with shrunk cytoplasm and blue arrows show apoptotic bodies. Cell viability assessment by Hoechst (H)/propidium iodide staining (PI): (D) The control culture of MCF-7, containing live cells with Hoechst pale blue stained nuclei. (E) MCF-7 cells after incubation with RPF101 for 24 h, showing dead cells with pink and red nuclei. (F) MCF-7 cells after incubation with capsaicin. In (G, H and I) quantification of MCF-7 cell viability after incubation with RPF101 and capsaicin for 24 h is presented. Data are the mean ± S.D. of three different experiments performed in duplicate.

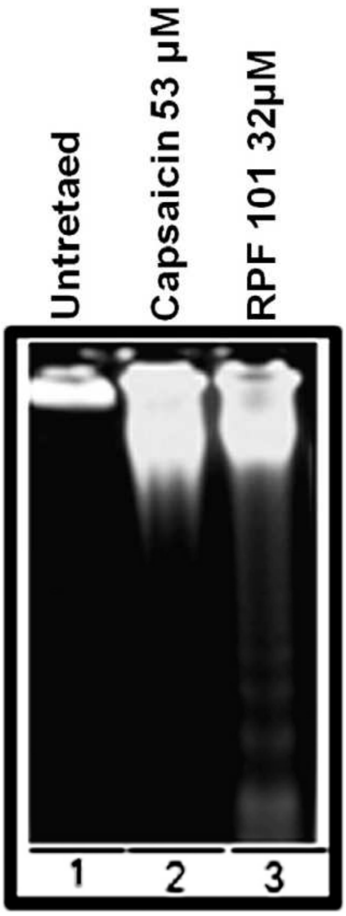

Fig. 7. Induction of DNA fragmentation on MCF-7 cells by RPF101. Ladder-like pattern of DNA fragmentation into oligonucleosome-length fragments was detected in agarose gel electrophoresis on MCF-7 cells, after 24 h of treatment with RPF101.

each compound are showed in Fig. 3C. The E_{HOMO} values as well as the HOMO maps distributions did not show significant differences regarding the two investigated molecules. On the other hand, RPF101 had a 10-fold more negative E_{LUMO} value (-14.48 kcal/mol) than capsaicin (-4.61 kcal/mol). Additionally, the LUMO map distributions were in opposite sides regarding the two molecules. The gap values (see Table 1) point out the benzodioxole derivative as a more reactive molecule than capsaicin.

Effects of RPF101 on cell viability and proliferation

We studied the effects of RPF101 and capsaicin on the viability and proliferation of MCF-7 cells using the MTT assay. As shown in Table 2, RPF101 and capsaicin were considerably cytotoxic to all tumors cells screened here. RPF101 was cytotoxic to MCF-7 cells at 32 µM and the IC_{50} of capsaicin on these same cell lines was 53 µM. These values were used as references for the investigation of the biological activities of RPF101. For the proliferation tests, 2×10^3 cells were plated in a 96-well plate and incubated for 48 h. We observed that RPF101 presented an antiproliferative effect at the concentrations of 12.5, 25 and 50 µM, while capsaicin presented the same effect only at the concentrations of 12.5 and 25 µM (Fig. 4A and B).

Morphological evaluation of RPF101 toxicity in 3D culture

Although screening on in vitro 2D cell culture provides valuable information about cytotoxic effects of the compounds, it does not accurately predict the in vivo toxicity. For this purpose the effect of RPF101 was evaluated in 3D matrices. The light microscopy of the cultures showed that untreated MCF-7 cells cluster within the voids of the matrix forming spheroid-like structures, similar to the structural characteristics of the tumor in vivo. Otherwise, MCF-7 treated with 32 µM RPF101 presented important morphological changes. No sphere-shaped cell clusters could be seen such as that observed in the in vivo tumor. Additionally, morphological changes characteristic of apoptosis, such as, cell shrinkage and pyknosis were visible through light microscopy (Fig. 5).

RPF101 induces morphological changes typical of apoptosis in MCF-7 cells

The AO/PI staining technique was employed in order to better evaluate the morphological changes of the MCF-7 cells in response to the treatment with RPF101 and capsaicin. In the control group, green live cells with normal morphology with uniform distribution were observed (Fig. 6A). On the other hand, RPF101 and capsaicin treated MCF-7 cells appeared green with nuclear margination and apoptotic blebbing formation. Cell shrinkage was another phenomenon induced by both RPF101 and capsaicin (Fig. 6B and C). These results suggest that RPF101 induces apoptosis. In order to confirm the MTT assay results, we evaluated the viability of MCF-7 cell lines through the Hoechst 33342/PI cell viability assay, which allows visualization and quantification of living, apoptotic and dead cells. Hoechst 33342 is a dye that enters living cells with intact membranes, staining the nucleus a pale blue. Fig. 6D shows the nuclei of living cells that were not treated. Fig. 6E shows MCF-7 cells treated with RPF101 and Fig. 6F shows cells treated with capsaicin. The highly condensed chromatin of the apoptotic cell nuclei are stained in bright blue, whereas the nuclei of the necrotic cells are stained in red by PI. This differential staining allows a quantitative analysis of the MCF-7 cells' viability. The untreated MCF-7 cells died at very low rates (7%), which we attribute to high confluence of the cells (Fig. 6G). When the MCF-7 cells were treated with RPF101 for 24 h, approximately equal percentages (approximately 20%) of pink and red cells were observed (Fig. 6H). Capsaicin induced approximately 15% of pink cells (apoptosis) and 55% of red cell (necrosis) (Fig. 6I).

Detection of apoptosis in the MCF-7 cells by agarose gel electrophoresis

The fragmentation of DNA into 200 bp fragments is commonly associated with apoptosis in many cell types. In order to investigate whether the morphological changes observed in MCF-7 treated with RPF101 were consistent with apoptosis, the DNA was extracted from treated cells and electrophoresed in a 2% agarose gel. As depicted in Fig. 7, the fragmented DNA was not detected in MCF-7 treated with capsaicin. However, fragmented DNA was present in MCF-7 treated with RPF101, which is another evidence that this compound induces apoptosis (Fig. 7).

RPF 101 is more potent than capsaicin in the induction of apoptosis on MCF-7 cells

In order to verify if capsaicin and RPF101 at the concentrations of 53 µM 32 µM, respectively, induce the externalization of phosphatidylserine, a hallmark of apoptosis, a YO-PRO-1/PI analysis using flow cytometry was performed. In fact, double staining MCF-7 cells with YO-PRO-1/PI (Fig. 8A) showed that RPF101 induces cell death by apoptosis (76.3%) as well as capsaiscin (62.3%) (Fig. 8B). This is in agreement with our previous results showing that capsaicin does induce apoptosis effects, but in contrast with the morphological observations of cells treated with capsaicin stained by Hoechst 33342/PI. However, RPF101 is more effective in the induction of apoptosis when compared to capsaicin. Taken together, these results demonstrated

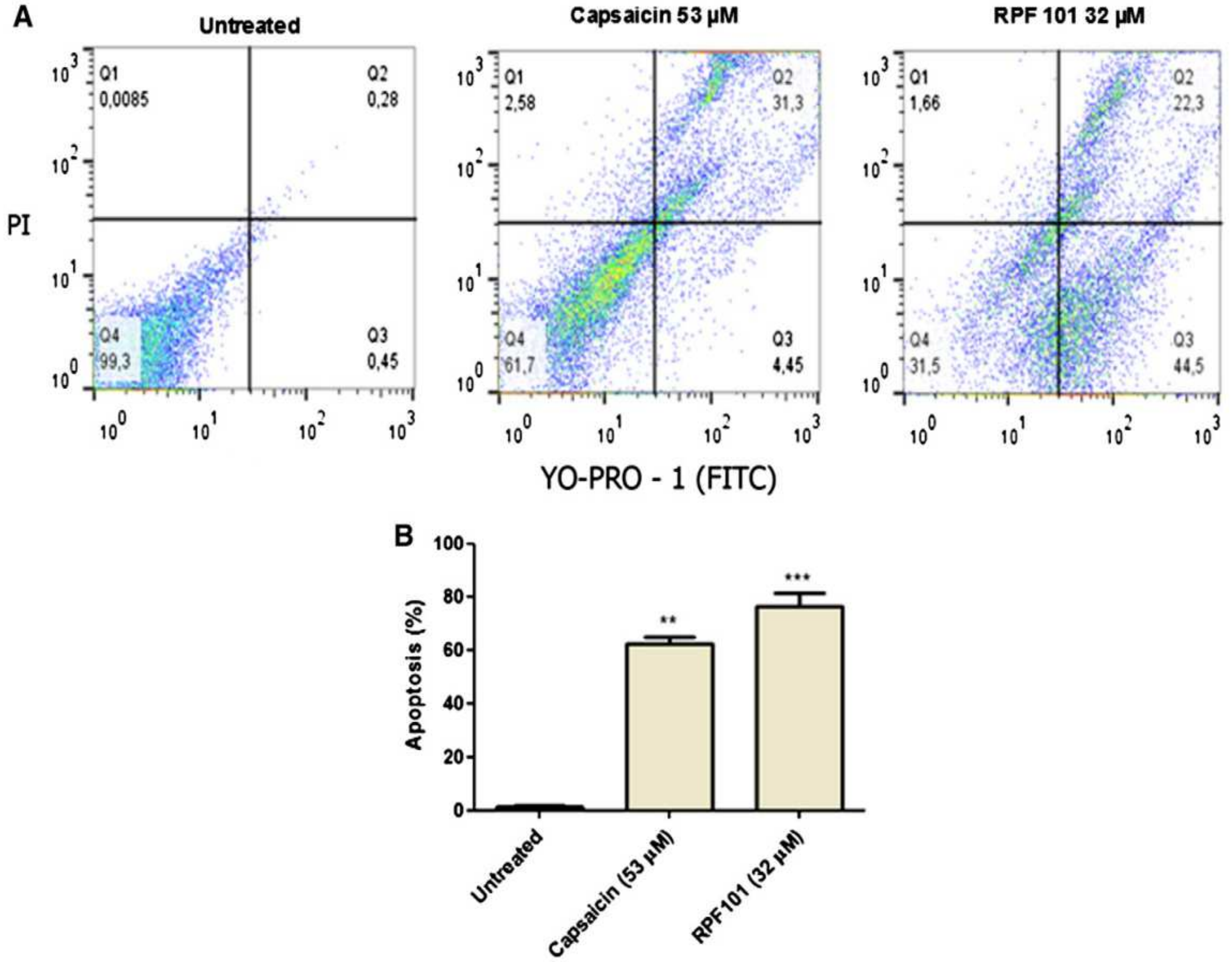

Fig. 8. Apoptotic effect of capsaicin and RPF101 assessed using YO-PRO-1/PI double staining. Dot plot representative shows the cell population in apoptosis after 12 h of treatment (A). As shown in bar plots (B), RPF101 treatment increased the number of cells in apoptosis when compared with capsaicin. Bar plots are the averages ± S.D. of three independent experiments.

that the new capsaicin analogue induces antitumor effects by apoptosis in MCF-7 cells.

RPF101 and capsaicin induce depolarization of mitochondria

Apoptosis is known to be activated in response to a cell death stimulus through the mitochondrial pathway in a variety of tumor cells. The disruption of the mitochondrial membrane potential during apoptosis induced by capsaicin and RPF101 after 24 h of treatment was evaluated. The cell death by apoptosis is associated with mitochondrial depolarization in MCF-7 cells, as shown in Fig. 9A. The treatment with capsaicin and RPF101 significantly reduced ($^{**}p<0.05$) the TMRE fluorescence signal, analyzed through a 3D dot plot, indicating that $\Delta m\Psi$ decreases in response to the treatment (Fig. 9B and C).

Cell cycle arrest at the G2/M phase induced by RPF101

Also, it was evaluated whether RPF101 induced changes in the cell cycle on MCF-7 breast cancer cells. Then, cells were treated for 24 h with 53 µM capsaicin, and 32 µM RPF101. The treatment with RPF101 was more effective than with capsaicin (38.7%), a fact corroborated by an increase in the percentage of cells in the G2/M phase (5%). This arrest prevents the progression of cells through mitosis, causing a reduction of the number of cells at the G1 phase. In addition, the arrest in the G2/M phase was probably associated with a concomitant decrease in the percentage of cells in S phase (Fig. 10A and B).

RPF101 causes disruption of microtubule fuse in the MCF-7 cells

Compounds that induce an arrest of the cell cycle at G2/M are known to target the cellular microtubules causing an aberrant formation of the mitotic fuse. Due to the blockage in G2/M and the induction of apoptosis, by RPF101, it was evaluated whether this occurs through a disruption of the microtubule organization in MCF-7 cells. Cells were treated with 53 µM capsaicin and 32 µM RPF101 for 12 h and visualized by confocal microscopy. The microtubule polymerization in untreated cells exhibited normal morphology, showing bipolar mitosis and a polyploid nucleus in the majority of the tumor cells. In addition, it was found that the nuclei in spindles had different geometries. Otherwise, cells treated with RPF101 exhibited a reduced number of mitosis and disrupted microtubule polarization fuses. These are hallmarks of arrest of the cell cycle at the G2/M phase. Moreover, the number of polyploid cells decreased and they exhibited an arrangement typical of catastrophic mitosis with a lack of apoptotic microtubules. It is important to notice that capsaicin induced the vacuolization of the cytoplasm. These data suggest that the apoptotic effects of RPF101 occurred through a disruption of microtubule arrangements (Fig. 11).

Discussion

The present study evaluated the antitumor effects of RPF101, a novel structural capsaicin-like analogue. Herein, it was demonstrated that RPF101 induces cytotoxic effects in all tumor cells screened in

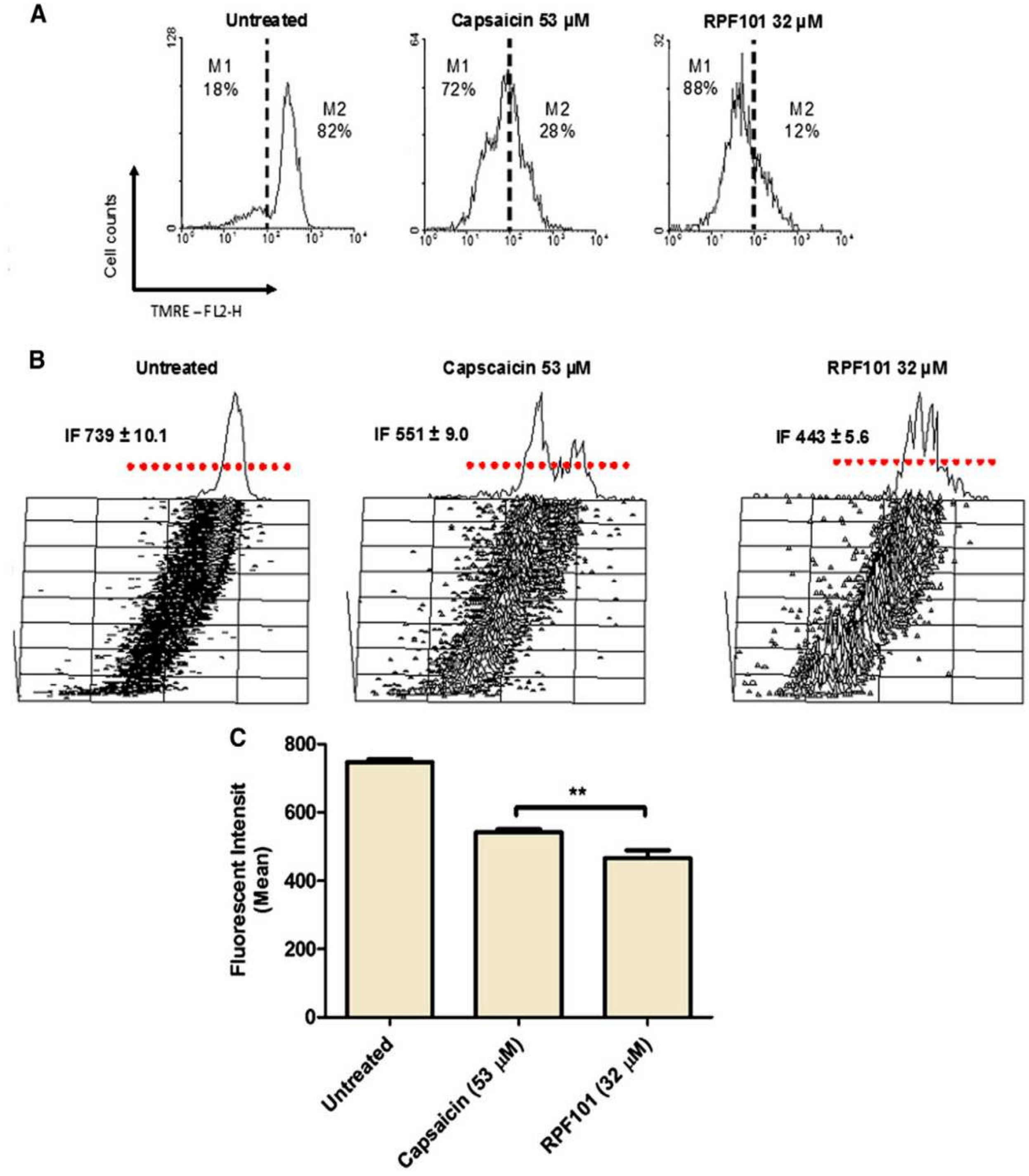

Fig. 9. Capsaicin and RPF101 cause disruption of the mitochondrial membrane potential (ΔmΨ). MCF-7 cells were treated for 6 h and ΔmΨ was measured by TMRE fluorescence, analyzed by flow cytometry. There is a substantial shift in percentage of cells treated with capsaicin and RPF101 from M1 (high ΔmΨ) to M2 (low ΔmΨ) (A). The decreased of ΔmΨ was also noticed by 3D fluorescence intensity analysis, indicating that a decrease of the ΔmΨ is a hallmark of the apoptosis induced by capsaicin and its analogue, the RPF101 (B and C). Data are the mean ± S.D. of three different experiments performed in triplicate.

this work. The findings have important implications for the development of novel antitumor agents since the chosen cell lines were considered very close to the clinical situation. On the other hand, the cells represent different tumors, including also those resistant to chemotherapy agents as melanoma and breast cancer cells. Indeed, RPF101 presented the additional advantage of blocking tumor cell proliferation at lower concentrations than capsaicin and, consequently, has higher antitumor activity. The use of 3D cell culture systems provided accuracy to the evaluation effect of a novel antitumoral compound, as RPF101. This technique has been used in studies that involve the screening of new compounds, which can provide similar extracellular matrix (Galluzzi et al., 2009; Lee et al., 2009). Our investigation confirms that RPF101 affects the overall morphology of MCF-7 cells, disrupting the formation of structures that resemble the

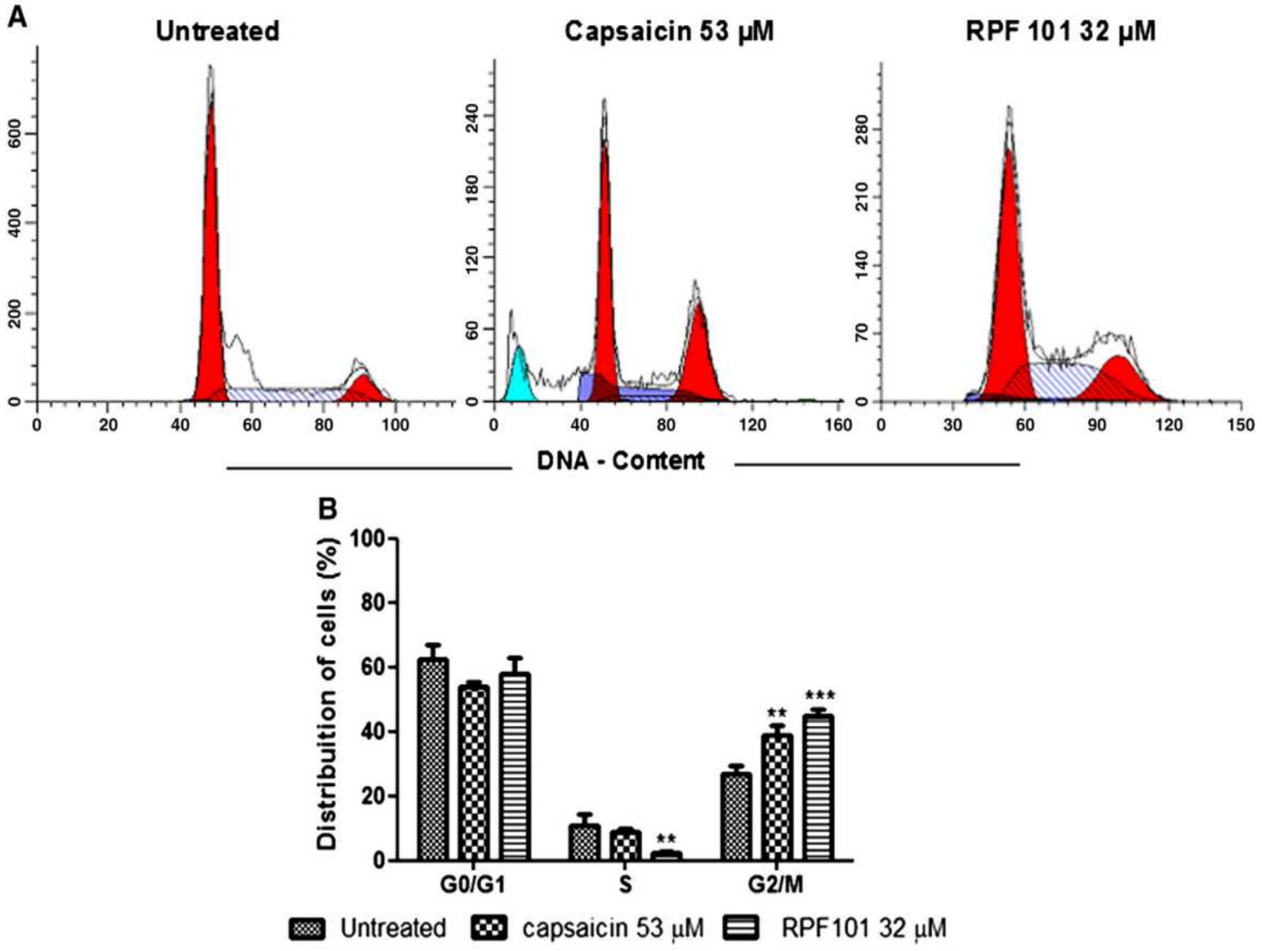

Fig. 10. Effects of capsaicin and RPF101 on the cell cycle progression. (A) Cell cycle analyses of MCF-7 cells are shown in representative histograms performed by flow cytometry. (B) RPF101, induces cell cycle arrest at the G2/M phase, while capsaicin induces apoptosis, recognized as a sub-G1 (blue peak). The % of cells is shown in the histogram as mean ± SD from three independent experiments. Data are the mean ± S.D. of three different experiments performed in duplicate.

in vivo architecture of those cells. Since this behavior provides a representative way of how the tumor cells respond in vivo to the treatment, it can be suggested that RPF101 is a promising antitumoral compound. However, further studies are required to establish this therapeutical hypothesis.

The apoptotic effects of capsaicin and its analogue were explored using several methods to evaluate cell death, and to further elaborate studies to provide deeper insight into the mechanisms underlying induction of cell death, following the treatment with RPF101. The MCF-7 cell line was chosen since it does not express caspase-3, the central executioner member of the cysteine-aspartic proteases family, and also the more important hub in caspases pathways, and for this reason, MCF-7 is generally more resistant to apoptosis (Danial and Korsmeyer, 2004; Liang et al., 2011). The Hoechst 33342/PI cell viability assay, after treatment with RPF101 demonstrated that the effect of this compound was not merely the impairment of the plasma membrane (characterizing necrosis), but the result of a coordinated process, typical of cells which are undergoing apoptosis. Although Hoechst/PI staining is a widely used method to quantify cell death process, this technique does not distinguish cells in early apoptosis from those in late apoptosis or even in necrosis. In order to better characterize what kind of cell death each compound induces, the cells were subjected to flow cytometry after staining with YO-PRO-1/PI. The results show that RPF101 has better apoptotic potential than capsaicin. These findings taken together with the microscopy results, allowed an accurate quantification of the percentage of apoptotic cells.

It is well known that the induction of apoptosis represents a goal for therapy against cancer and, indeed, many new anticancer molecules have been developed that trigger apoptosis. Mitochondria play a key role in the activation of apoptosis, and its depolarization triggers cell death through the release of apoptotic proteins from the mitochondria to the cytoplasm (Ferreira et al., 2012). Here, capsaicin and RPF101 induced dysfunctions in mitochondria, leading to depolarization, and reducing $\Delta\psi m$.

In agreement with these results, by using acridine orange staining, it was showed that caspsaicin and RPF101 induce morphological changes characteristic of apoptosis, such as cell detachment and cell rounding, shrinkage, blebbing formation, and chromatin condensation (Elmore, 2007).

To corroborate the interpretation on the morphological changes induced by RPF101, its potential to induce internucleosomal DNA fragmentation, another hallmark of the apoptotic process, was also investigated (Galluzzi et al., 2009). In fact, many groups have demonstrated that capsaicin triggers apoptosis, however neither apoptotic nor necrotic fragmented DNA was observed after treatment with this compound.

The pattern of DNA degradation is a highly specific, but this is not a very sensitive method, requiring a larger amount of cells which, at

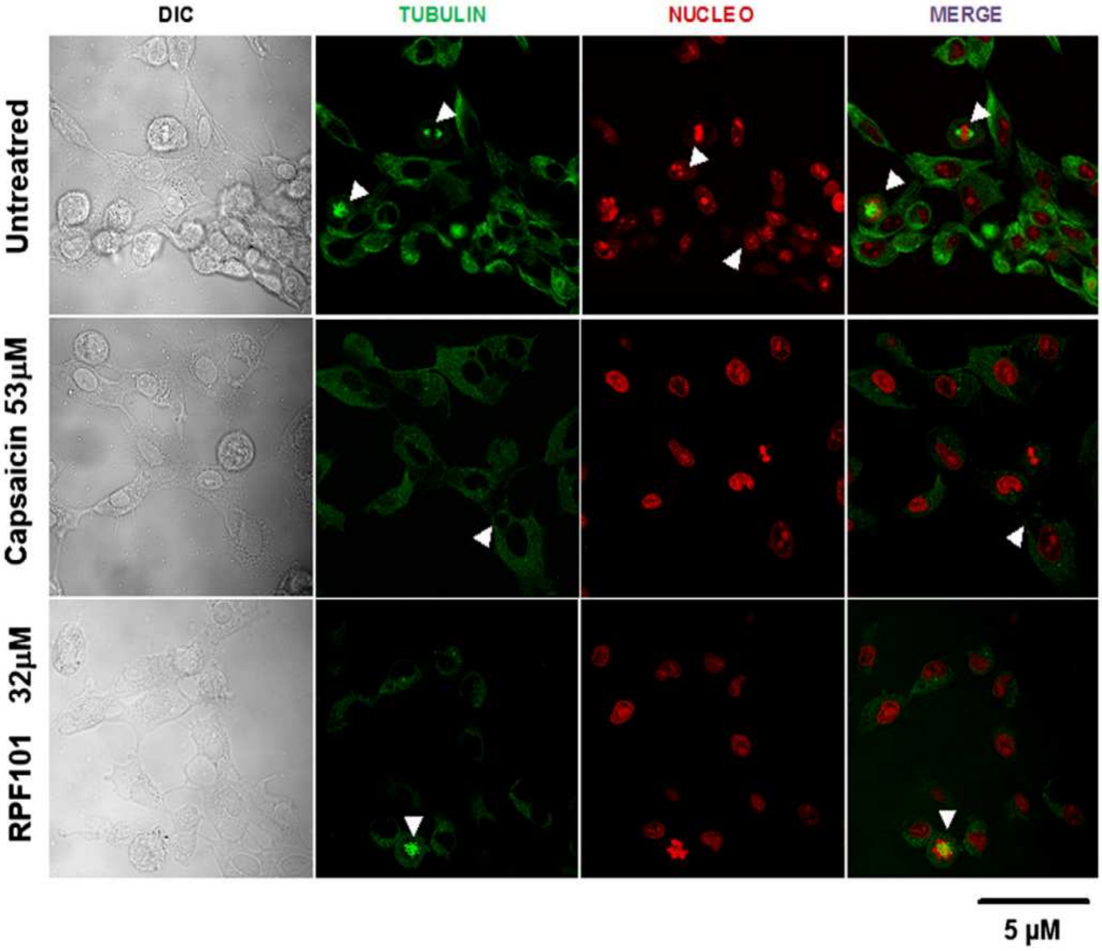

Fig. 11. RPF101 induces disruption of microtubules, blocking mitosis in MCF-7 cells. Immunofluorescence staining of alpha-tubulin (FITC: green) PI staining of nuclei, imaged by confocal microscopy. Notice that untreated cells present polyploid nuclei and present bipolar mitosis, while next to the nuclei linear filaments of alpha-tubulin (microtubules) can be seen. Arrow shows that the treatment with capsaicin induces an irregular nuclear contour and vacuolization of the cytoplasm, which are characteristics of apoptosis. RPF101 disrupts the mitotic fuse and apoptotic microtubule network assembly. Arrowheads indicate cells with irregular mitotic microtubules, a situation that leads them to mitotic catastrophe.

least partially, can explain the absence of DNA fragments after treatment with capsaicin. Otherwise, the typical DNA laddering, corresponding to DNA fragmentation, was observed after treatment of MCF-7 cells with RPF101. This reinforces the potential of RPF101 to induce apoptosis. Taken together, these in vitro results concerning cell death suggest that RPF101 has better apoptotic potential when compared to its prototype, capsaicin. The findings pointed out to a controlled cell death – apoptosis – and not to necrosis, even in caspase-3 deficient cells as MCF-7. RPF101 showed to be a potential *hit*, however further in vivo activity and toxicity studies are needed to assess the real potential of this novel compound as an anticancer agent. Moreover, the results obtained in this study can be used as a guideline for further improvement of benzodioxole sulfonamide-like compounds as potential therapeutic antitumor agents.

Deregulation of the cell cycle may result in uncontrolled cell proliferation, which characterizes the malignant phenotype and quickens the tumor cell cycle kinetics. Thus, compounds that can interfere with the cell cycle are attractive for the treatment of cancer. The data showed that RPF101, at the concentration of 32 μM, as well as capsaicin at 50 μM, have a strong antiproliferative activity on MCF-7 cells by arresting them into the G2/M phase. This coincides with the decrease in percentage of cells in the S phase. Although preliminary, this finding suggests that capsaicin and RPF101 would have an antitumor activity by blocking tumor cell progression through the cell cycle. Additionally, apoptosis induced by capsaicin, recognized as the sub-G1 peak, can involve the disruption of the checkpoints in the cell cycle, which is an event preceding the detection of apoptosis (Xiang et al., 2012). Since RPF101 induces an arrest at the G2/M phase, it was checked if capsaicin and its analogue would induce a disruption of the microtubule network. RPF101 interfered with the spindle apparatus' function via the disassembly of microtubules. It is possible to hypothesize that the mitotic arrest induced by RPF101 would be a resulting from the mitotic fuse inhibition, inducing catastrophic mitosis. This is a sufficient condition to trigger cell death by apoptosis (Zhou et al., 2011). In contrast, capsaicin did not disrupt the spindle apparatus, but induced the formation of vacuolization in the cytoplasm, suggesting that it induces apoptosis through a different mechanism in comparison to RPF101.

Regarding the molecular modifications (ring closure, bioisosteric replacement and molecular rigidification), RPF101 was 1.5 fold more potent than the prototype. These structural changes directly reflected in the molecular properties, which were evaluated by applying theoretical methods. For instance, capsaicin presented a higher lipophilic character than RPF101. This finding indicates that the analogue could have a better pharmacokinetic profile since its ClogP value was closer to an ideal range (between 1.5 and 2.0), which could provide better permeability through cellular membranes and, consequently, enhance the antitumor effect. Interestingly, RPF101 has a more negative E_{LUMO} value and a less negative gap value. The gap value suggests that RPF101 would be more reactive than capsaicin and could interact more easily with the target, for instance. The E_{LUMO} value also indicates that a charge transfer complex could be taking place.

In conclusion, it was showed that RPF101, a novel capsaicin analogue, has a higher antitumor activity than capsaicin by inducing an arrest of the cell cycle at the G2/M phase by disrupting the microtubule network in the tumor cells. Also, cellular morphological changes, typical of apoptosis, the decrease of $\Delta\psi m$ and the exposure of phosphatidylserine show that RPF101 is a promising anticancer agent. Based upon the theoretical data obtained in this study, such as the optimum ClogP value (hydrophobic/hydrophilic partition), further molecular modifications will be performed in order to optimize the designing of more potent compounds for the fighting against cancer.

Conflict of interest statement

The authors declare that they have no financial, personal or professional conflict of interest.

Acknowledgments

The authors are grateful to the Provost's Office for Research of the University of Sao Paulo for financial support, to Professor Leoberto Costa Tavares, coordinator of Laboratory for Designing and Development of New Drugs, Department of Biochemical and Pharmaceutical Technology, Faculty of Pharmacy at University of Sao Paulo, whom kindly allowed the use of a workstation to perform the in silico analysis, and to the Chem21 Group, Inc., for the MOLSIM 3.2 software academic license. We also to thank Henrique Krambeck Rofatto, from Laboratório de Parasitologia-Instituto Butantan, for laser scanning confocal microscopy imaging support with Zeiss LSM-510 Meta (FAPESP 00/11624-5).

References

Barreiro, E.J., Fraga, C.A.M., 1999. A utilização do safrol, principal componente químico do óleo de sassafráz, na síntese de substâncias bioativas na cascata do ácido araquidônico: antiinflamatórios, analgésicos e antitrombóticos. Quím. Nova 22, 744–759.

Becke, A.D., 1993. A new mixing of Hartree-Fock and local density-functional theories. J. Chem. Phys. 98, 1372–1377.

Black, W.C., Bayly, C.I., Davis, D.E., Desmarais, S., Falgueyret, J.-P., Léger, S., Chun, S.L., Massé, F., McKay, D.J., Palmer, J.T., Percival, M.D., Robichaud, J., Tsou, N., Zamboni, R., 2005. Trifluoroethylamines as amide isosteres in inhibitors of cathepsin K. Bioorg. Med. Chem. 15, 4741–4744.

Bodor, N., Gabanyi, Z., Wong, C.K., 1989. A new method for the estimation of partition coefficient. J. Am. Chem. Soc. 111, 3783–3786.

Brandão, H.N., David, J.P., Couto, R.D., Nascimento, J.A.P., David, J.M., 2010. Química e farmacologia de quimioterápicos antineoplásicos derivados de plantas. Quím. Nova 33, 1359–1369.

Breneman, C.M., Wiberg, K.B., 1990. Determining atom-centered monopoles from molecular eletrostatic potentials. The need for high sampling density in formamide conformational analysis. J. Comput. Chem. 11, 361–373.

Cunico, W., Gomes, C.R., Ferreira, M.L., Ferreira, T.G., Cardinot, D., de Souza, M.V., Lourenço, M.C., 2011. Synthesis and anti-mycobacterial activity of novel amino alcohol derivatives. Eur. J. Med. Chem. 46, 974–978.

Danial, N.N., Korsmeyer, S.J., 2004. Cell death: critical control points. Cell 116, 205–219.

Debatin, K.M., Krammer, P.H., 2004. Death receptors in chemotherapyand cancer. Oncogene 23, 2950–2966.

Dewar, M.J.S., Zoebisch, E.G., Healy, E.F., Stewart, J.J.P., 1985. AM1: a new general purpose quantum mechanical molecular model. J. Am. Chem. Soc. 107, 3903–3909.

Doherty, D., 2002. MOLSIM: Molecular Mechanics and Dynamics Simulation Software — User's Guide, version 3.2. The Chem21 Group Inc., Lake Forest, IL.

Elmore, S., 2007. Apoptosis: a review of programmed cell death. Toxicol. Pathol. 35, 495–516.

Ferreira, A.K., Meneguelo, R., Pereira, A., Mendonça-Filho, O.R., Chierice, G.O., Maria, D.A., 2012. Anticancer effects of synthetic phosphoethanolamine on Ehrlich ascites tumor: an experimental study. Anticancer. Res. 32, 95–104.

Fesik, S.W., 2005. Promoting apoptosis as a strategy for cancer drug discovery. Cancer Res. 5, 876–883.

Forsythe, K.H., Hopfinger, A.J., 1973. The influence of solvent on the secondary structure of poly (L-alanine) and poly (L-proline). Macromolecular 6, 423–437.

Galluzzi, L., Aaronson, S.A., Abrams, J., Alnemri, E.S., Andrews, D.W., Bazan, N.G., Blagosklonny, M.V., Blomgren, K., Baehrecke, E.H., Borner, C., Bredesen, D.E., Brenner, C.M., Cidlowski, J., Ciechanover, A., Cohen, G.M., De Laurenzi, V., De Maria, R., Deshmukh, M., Dynlacht, B.D., El-Deiry, W.S., Flavell, R.A., Fulda, S., Garrido, C., Golstein, P., Gougeon, M.L., Green, D.R., Gronemeyer, H., Hajnóczky, G., Hardwick, J.M., Hengartner, M.O., Ichijo, H., Jäättelä, M., Kepp, O., Kimchi, A., Klionsky, D.J., Knight, R.A., Kornbluth, S., Kumar, S., Levine, B., Lipton, S.A., Lugli, E., Madeo, F., Malorni, W., Marine, J.C.W., Martin, S.J., Medema, J.P., Mehlen, P., Melino, G., Moll, U.M., Morselli, E., Nagata, S., Nicholson, D.W., Nicotera, P., Nuñez, G., Oren, M., Penninger, J., Pervaiz, S., Peter, M.E., Piacentini, M., Prehn, J.H.M., Puthalakath, H., Rabinovich, G.A., Rizzuto, R., Rodrigues, C.M.P., Rubinsztein, D.C., Rudel, T., Scorrano, L., Simon, H.U., Steller, H., Tschopp, J., Tsujimoto, Y., Vandenabeele, P., Vitale, I., Vousden, K.H., Youle, R.J., Yuan, J., Zhivotovsky, B., Kroemer, G., 2009. Guidelines for the use and interpretation of assays for monitoring cell death in higher eukaryotes. Cell Death Differ. 16, 1093–1107.

Gasiorowski, K., Brokos, B., Kulma, A., Ogorzałek, A., Sko'rkowska, K., 2001. A comparison of the methods applied to detect apoptosis in genotoxically-damaged lymphocytes cultured in the presence of four antimutagens. Cell. Mol. Biol. Lett. 6, 141–159.

GaussView for Windows, version 5.0. Gaussian, Inc., Pittsburgh, PA.

Gaussian 03, Revision C.02, Frisch, M.J., Trucks, G.W., Schlegel, H.B., Scuseria, G.E., Robb, M.A., Cheeseman, J.R., Montgomery JR., J.A., Vreven, T., Kudin, K.N., Burant, J.C., Millam, J.M., Iyengar, S.S., TomasI, J., BaronE, V., MennuccI, B., Cossi, M., Scalmani, G., Rega, N., Petersson, G.A., Nakatsuji, H., Hada, M., Ehara, M., Toyota, K., Fukuda, R., HasegawA, J., Ishida, M., Nakajima, T., Honda, Y., Kitao, O., Nakai, H., Klene, M., Li, X., Knox, J.E., Hratchian, H.P., Cross, J.B., Bakken, V., Adamo, C., Jaramillo, J., Gomperts, R., Stratmann, R.E., Yazyev, O., Austin, A.J., Cammi, R., Pomelli, C., Ochterski, J.W., Ayala, P.Y., Morokuma, K., Voth, G.A., Salvador, P., Dannenberg, J.J., Zakrzewski, V.G., Dapprich, S., Daniels, A.D., Strain, M.C., Farkas, O., Malick, D.K., Rabuck, A.D., Raghavachari, K., Foresman, J.B., Ortiz, J.V., Cui, Q., Baboul, A.G., Clifford, S., Cioslowski, J., Stefanov, B.B., Liu, G., Liashenko, A., Piskorz, P., Komaromi, I., Martin, R.L., Fox, D.J., Keith, T., Al-Laham, M.A., Peng, C.Y., Nanayakkara, A., Challacombe, M., Gill, P.M.W., Johnson, B., Chen, W., Wong, M.W., Gonzalez, C., Pople, J.A., 2004. Gaussian, Inc., Wallingford CT.

Gavezzotti, A., 1983. The calculation of molecular volumes and the use of volume analysis in the investigation of structured media and of solid-state organic reactivity. J. Am. Chem. Soc. 105, 5220–5225.

Geyer, C.E., Forster, F., Lindquist, D., Chan, S., Romieu, G., Pienkowski, T., Jagiello-Gruszfeld, A., Crown, J., Chan, A., Kaufman, B., Skarlos, D., Campone, M., Davidson, N., Berger, M., Oliva, C., Rubin, S.D., Stein, S., Cameron, D., 2006. Lapatinib plus Capecitabine for HER2-Positive advanced breast cancer. N. Engl. J. Med. 355, 2733–2743.

Ghosh, A.K., Basu, S., 2010. Fas-associated factor 1 is a negative regulator in capsaicin induced cancer cell apoptosis. Cancer Lett. 287, 142–149.

Huang, S.P., Chen, J.C., Wu, C.C., Chen, C.T., Tang, N.Y., Ho, Y.T., Lo, C., Lin, J.P., Chung, J.G., Lin, J.G., 2009. Capsaicin-induced apoptosis in human hepatoma HepG2 cells. Anticancer. Res. 29, 165–173.

Huang, Y.L., Wang, W.L., Shan, S., 2010. 3-Chloro-*N*-(4-hydroxy-3-metoxy-benzyl)-2,2-dimethlypropanamide. Acta Crystallogr. E66, o877.

HyperChem Program Release 7.0 for Windows. Hybercube, Inc., Gainesville, FL.

Ito, K., Nakazato, T., Yamato, K., Miyakawa, Y., Yamada, T., Hozumi, N., Segawa, K., Ikeda, Y., Kizaki, M., 2004. Induction of apoptosis in leukemic cells by homovanillic acid derivative, capsaicin, through oxidative stress: Implication of phosphorylation of p53 at Ser-15 residue by reactive oxygen species. Cancer Res. 64, 1071–1077.

Jin, Z., El-Deiry, W.S., 2005. Overview of cell death signaling pathways. Cancer Biol. Ther. 4, 139–163.

Kaufmann, S.H., Earnshaw, W.C., 2000. Induction of apoptosis by cancer chemotherapy. Exp. Cell Res. 256, 42–49.

Kim, J.Y., Kim, E.H., Kim, S.U., Kwon, T.K., Choi, K.S., 2010. Capsaicin sensitizes malignant glioma cells to TRAIL-mediated apoptosis via DR5 up regulation and survivin downregulation. Carcinogenesis 31, 367–374.

Koehn, F.E., Carter, G.T., 2005. The evolving role of natural products in drug discovery. Nat. Rev. Drug Discov. 4, 206–218.

Lee, J., Lilly, G.D., Doty, R.C., Podsiadlo, P., Kotov, N.A., 2009. In vitro toxicity testing of nanoparticles in 3D cell culture. Small 5, 1213–1221.

Liang, X., Xu, K., Xu, Y., Liu, J., Qian, X., 2011. B1-induced caspase-independent apoptosis in MCF-7 cells is mediated by down-regulation of Bcl-2 via p53 binding to P2 promoter TATA box. Toxicol. Appl. Pharmacol. 256, 52–61.

Maity, R., Sharma, J., Jana, N.R., 2010. Capsaicin induces apoptosis through ubiquitin-proteasome system dysfunction. J. Cell. Biochem. 109, 933–942.

Marvin Beans 5.8.0 software — Calculator Plugins. Chemaxon, Ltd., Budapeste 1037, Hungary.

Oh, S.H., Kim, Y.S., Lim, S.C., Hou, Y.F., Chang, I.Y., You, H.J., 2008. Dihydrocapsaicin (DHC), a saturated structural analog of capsaicin, induces autophagy in human cancer cells in a catalase-regulated manner. Autophagy 4, 1009–1019.

Patani, G.A., LaVoie, E.J., 1996. Bioisosterism: A rational approach in dug design. Chem. Rev. 96, 3147–3176.

Sánchez, A.M., Malagarie-Cazenave, S., Olea, N., Vara, D., Chiloeches, A., Díaz-Laviada, I., 2007. Apoptosis induced by capsaicin in prostate PC-3 cells involves ceramide accumulation, neutral sphingomyelinase, and JNK activation. Apoptosis 12, 2013–2022.

Siegel, R., Naishadham, D., Jemal, A., 2012. Cancer statistics, 2012. CA Cancer J. Clin. 62, 10–29.

Surh, Y.J., Lee, S.S., 1996. Capsaicin in hot chilli pepper: carcinogen, co-carcinogen or anticarcinogen? Food Chem. Toxicol. 34, 313–316.

Thoennissen, N.H., Kelly, J., Lu, D., Iwanski, G.B., La, D.T., Abbassi, S., Leiter, A., Karlan, B., Mehta, R., Koeffler, H.P., 2010. Capsaicin causes cell-cycle arrest and apoptosis in ER-positive and -negative breast cancer cells by modulating the EGFR/HER-2 pathway. Oncogene 29, 285–296.

ViewerLite 5.0, Accelrys, Inc., San Diego, CA, 2002.

Viswanadhan, V.N., Ghose, A.K., Revankar, G.R., Robins, R.K., 1989. Atomic physicochemical parameters for three-dimensional-structure-directed quantitative structure–activity relationships. 2. Modeling dispersive and hydrophobic interactions. J. Chem. Inf. Comput. Sci. 29, 163–172.

Walpole, C.S.J., Wrigglesworth, R., Bevan, S., Campbell, E.A., Dray, A., James, I.F., Perkins, M.N., Reid, D.J., Winter, J., 1993a. Analogues of capsaicin with agonist activity as novel analgesic agents: structure–activity studies. 1. The aromatic "A-region". J. Med. Chem. 36, 2362–2372.

Walpole, C.S.J., Wrigglesworth, R., Bevan, S., Campbell, E.A., Dray, A., James, I.F., Perkins, M.N., Reid, D.J., Winter, J., 1993b. Analogues of capsaicin with agonist activity as novel analgesic agents: structure–activity studies. 2. The amide bond "B-region". J. Med. Chem. 36, 2373–2380.

Walpole, C.S.J., Wrigglesworth, R., Bevan, S., Campbell, E.A., Dray, A., James, I.F., Perkins, M.N., Reid, D.J., Winter, J., 1993c. Analogues of capsaicin with agonist activity as novel analgesic agents: structure–activity studies. 3. The hydrophobic side chain "C-region". J. Med. Chem. 36, 2381–2389.

Wu, C.C., Lin, J.P., Yang, J.S., Chou, S.T., Chen, S.C., Lin, Y.T., Lin, H.L., Chung, J.G., 2006. Capsaicin induced cell cycle arrest and apoptosis in human esophagus epidermoid carcinoma CE 81T/VGH cells through the elevation of intracellular reactive oxygen species and Ca^{2+} productions and caspase-3 activation. Mutat. Res. 601, 71–81.

Xiang, T., Li, L., Yin, X., Yuan, C., Tan, C., Su, X., Xiong, L., Putti, T.C., Oberst, M., Kelly, K., Ren, G., Tao, Q., 2012. The ubiquitin peptidase UCHL1 induces G0/G1 cell cycle arrest and apoptosis through stabilizing p53 and is frequently silenced in breast cancer. PLoS One 7, e29783.

Zhou, R.M., Jing, Y.Y., Guo, Y., Gao, C., Zhang, B.Y., Chen, C., Shi, Q., Tian, C., Wang, Z.Y., Gong, H.S., Han, J., Xu, B.L., Dong, X.P., 2011. Molecular interaction of TPPP with PrP antagonized the CytoPrP-induced disruption of microtubule structures and cytotoxicity. PLoS One 6, e23079.

Full Paper

Dillapiole as Antileishmanial Agent: Discovery, Cytotoxic Activity and Preliminary SAR Studies of Dillapiole Analogues

Roberto Parise-Filho[1], Kerly Fernanda Mesquita Pasqualoto[2], Fátima Maria Motter Magri[3], Adilson Kleber Ferreira[2], Bárbara Athayde Vaz Galvão da Silva[1], Mariana Celestina Frojuello Costa Bernstorff Damião[1], Maurício Temotheo Tavares[1], Ricardo Alexandre Azevedo[2], Aline Vivian Vatti Auada[2], Michelle Carneiro Polli[4], and Carlos Alberto Brandt[2]

[1] Faculty of Pharmaceutical Sciences, Department of Pharmacy, University of São Paulo, São Paulo, Brazil
[2] Laboratory of Biochemical and Biophysics, Butantan Institute, São Paulo, Brazil
[3] Center for Biological Sciences and Health (CCBS), Mackenzie Presbyterian University, São Paulo, Brazil
[4] Center for Life Sciences (CCV), Pontificial Catholic University of Campinas, São Paulo, Brazil

In this paper, the isolation of dillapiole (**1**) from *Piper aduncum* was reported as well as the semi-synthesis of two phenylpropanoid derivatives [di-hydrodillapiole (**2**), isodillapiole (**3**)], *via* reduction and isomerization reactions. Also, the compounds' molecular properties (structural, electronic, hydrophobic, and steric) were calculated and investigated to establish some preliminary structure–activity relationships (SAR). Compounds were evaluated for *in vitro* antileishmanial activity and cytotoxic effects on fibroblast cells. Compound **1** presented inhibitory activity against *Leishmania amazonensis* ($IC_{50} = 69.3$ μM) and *Leishmania brasiliensis* ($IC_{50} = 59.4$ μM) and induced cytotoxic effects on fibroblast cells mainly in high concentrations. Compounds **2** ($IC_{50} = 99.9$ μM for *L. amazonensis* and $IC_{50} = 90.5$ μM for *L. braziliensis*) and **3** ($IC_{50} = 122.9$ μM for *L. amazonensis* and $IC_{50} = 109.8$ μM for *L. brasiliensis*) were less active than dillapiole (**1**). Regarding the molecular properties, the conformational arrangement of the side chain, electronic features, and the hydrophilic/hydrophobic balance seem to be relevant for explaining the antileishmanial activity of dillapiole and its analogues.

Keywords: Antileishmanial activity / Cytotoxic activity / Dillapiole / Molecular modeling / SAR studies

Received: May 23, 2012; Revised: July 20, 2012; Accepted: July 24, 2012

DOI 10.1002/ardp.201200212

Introduction

Leishmaniasis is caused by parasites of the *Leishmania* genus and affects more than 12 million people in 88 countries. There are about two to three million new cases each year, and 350 million people are under risk of infection [1]. In the absence of a reliable vaccine, there is an urgent need for effective and safe drugs to replace those currently used, such as pentavalent antimonials, amphotericin B, and pentamidine. In this regard, the development of novel antileishmanial compounds is an imperative need. Many people who live in endemic areas use plants as an alternative to treat the disease [2]. The study of plant-derived drugs, for instance, would be highly recommended for driving the discovery of new potential leishmanicide agents [3–6].

The Piperaceae family comprises a large variety of species and it is known for producing several bioactive compounds [7, 8], which can provide quite attractive molecular modification approaches. Covering approximately 3000 species, the *Piper* genus is prominent for having distinct activities, such as insecticidal, antitumor, antibacterial, antifungal, and anti-inflammatory activities [9–11]. This genus is widely used in popular medicine, and it is found in all tropical regions of the world, with approximately 170 of 700 species occurring in Brazil [11]. The antileishmanial activity of *Piper* species has already been reported [12–14]. In the last few years, the essential oils from *Piper* species have become an important source for searching novel therapeutic alternatives primarily regarding the neglected diseases [15]. Recently, Monzote et al. [16] have shown the antileishmanial activity of the essential

---

Correspondence: Roberto Parise-Filho, Faculty of Pharmaceutical Sciences, University of São Paulo, Av. Prof. Lineu Prestes 580, 05508-900 São Paulo, Brazil
E-mail: roberto.parise@usp.br
Fax: +55 11 3815-4418.

oil from *Piper auritum*. This action is probably due to its essential oil's main component, the phenylpropanoid named safrole (Fig. 1).

Moreover, Bernard et al. [17] have demonstrated that one particularly specie from the Piperaceae, *Piper aduncum* L., certainly contains substances with potential biological properties, among them is a quite potent insecticide named dillapiole [18]. Gottlieb et al. [19] showed that dillapiole (Fig. 1) is the major essential oil component (58–88.4% yield). The structural similarity between safrole and dillapiole, is obvious; however there are no previous reports regarding the antileishmanial activity, so far. Thus, in this study, a preliminary *in vitro* evaluation focusing on the antileishmanial activity of dillapiole and its structurally related semi-synthetic analogues, isodillapiole and di-hydrodillapiole, was performed. The compounds were also submitted to cytotoxic assays. Additionally, the molecular properties of the compounds (structural, electronic, hydrophobic, and steric) were calculated to have some insights on structure–activity relationships (SAR).

Results and discussion

Characterization of dillapiole

The *P. aduncum* leaves were submitted to the extraction of essential oil by steam stripping. At the end of three extractions, about 1.5 g of essential oil was obtained. The Gas chromatography–mass spectrometry (GC–MS) analysis revealed 13 peaks. The chromatogram, presented in Fig. 2A, shows that dillapiole was the most abundant com-

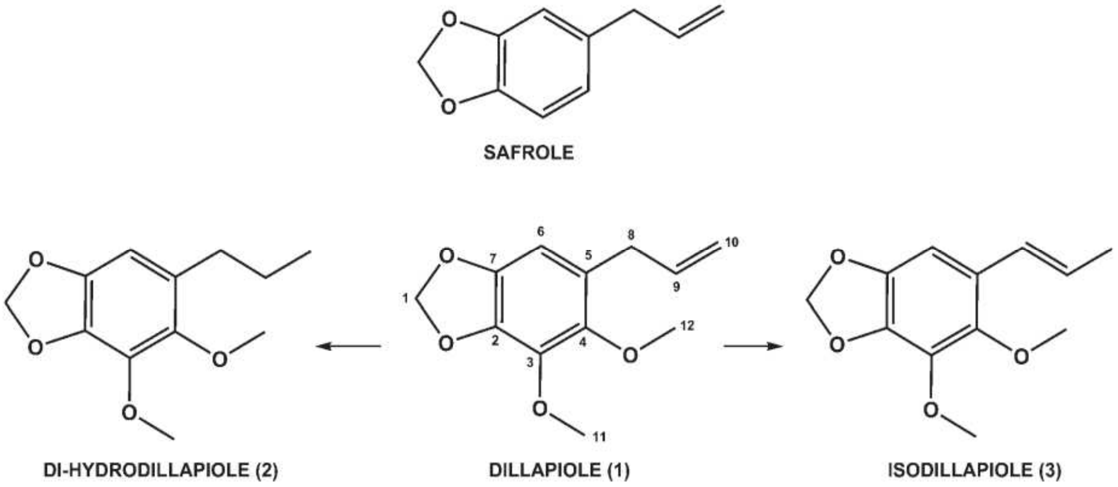

Figure 1. Chemical structures of safrole, dillapiole (**1**), and structural analogues (**2**, **3**).

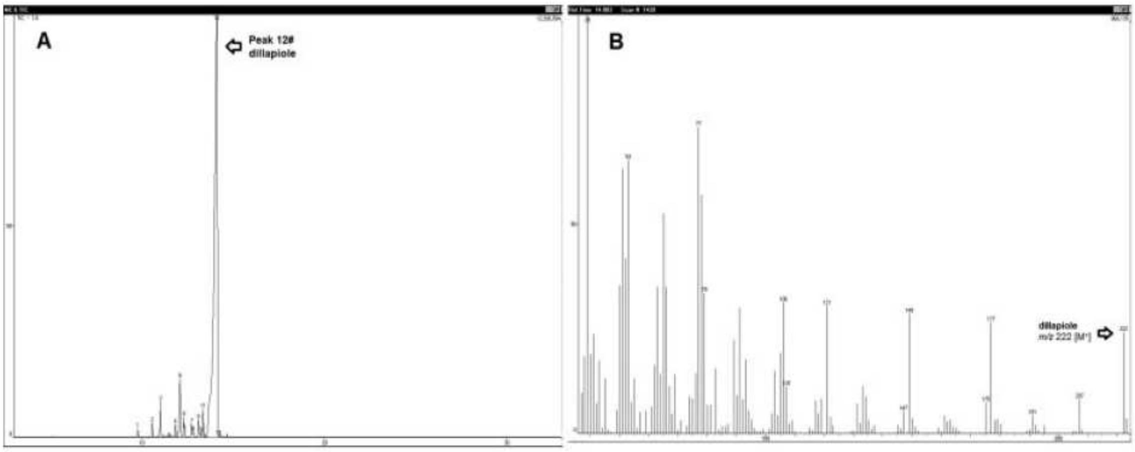

Figure 2. (A) Chromatogram and (B) mass spectrum obtained for the *P. aduncum* extract.

pound in the essential oil (88%). Furthermore, according to the mass spectra analysis (Fig. 2B), the majority of the essential oil content had a molecular mass corresponding to that found for dillapiole (*m*/*z* 222 [M^+]).

Synthesis of dillapiole analogues

Chromatographic partitioning led the isolation of dillapiole, which is the main constituent of the essential oil and it was identified by ^1H and ^{13}C NMR spectra analysis. The pure compound was used for the di-hydrodillapiole and isodillapiole synthesis. Dillapiole (**1**) was reduced by using $NaBH_4$ and $NiCl_2 \cdot 9H_2O$ to obtain di-hydrodillapiole (**2**) (86% yield). The reduction was confirmed by the ^1H NMR spectrum, which revealed the 0.91 and 2.49 ppm triplet signals that are characteristic for the propyl group. Although $NaBH_4$, has been known not to reduce olefins, previous studies reported that the isolated C=C double bond of allyl groups could be reduced with $NaBH_4$, using metal salts (Cu_2Cl_2 or $NiCl_2$) and methanol as a catalytic system [20]. This report suggested that metal salt catalyzes the formation of transient species, followed by its simultaneous decomposition, giving BH_3, which reacts with MeOH, generating hydrogen gas. Our results corroborate the data previously mentioned that the $NaBH_4$–$NiCl_2$ system completely reduced the allyl group of dillapiole. Compound (**1**) was also submitted to isomerization under standard alkaline conditions [21] in order to obtain isodillapiole (**3**) (85% yield). Proton NMR data for compound (**3**) showed that the chemical shift pattern of the H-10 protons was changed after isomerization. In this case, the H-10 protons changed their chemical shift from 3.31 to 2.48 ppm doublet.

In vitro antileishmanial properties

Piper species and their essential oils have been reported to have leishmanicidal activity. It is noteworthy that no previous reports regarding antileishmanial activity of dillapiole were found in the literature. In this study, the compounds dillapiole (**1**) and its semi-synthetic analogues, di-hydrodillapiole (**2**) and isodillapiole (**3**), were tested against *Leishmania brasiliensis* and *Leishmania amazonensis* promastigote forms. Amphotericin B was the reference antileishmanial drug. The findings are presented in Table 1. Compound **1** was the most active in both culture models, and the IC_{50} values were 69.3 and 59.4 μM. The analogues **2** and **3** also showed quite promising effects against promastigote forms. However, in comparison to the natural product (**1**), the antileishmanial activity was decreased about 1.5- to 1.8-fold.

The antileishmanial activity of dillapiole (**1**) was slightly better for *L. brasiliensis* than for *L. amazonensis*. These results suggested that the antileishmanial effect would be probably specie-dependent [22], and *L. brasiliensis* promastigote forms would be more susceptible than *L. amazonensis*. Croft et al. [23] corroborated this situation considering that both parasites have their own metabolic characteristics and a difference would be expected in the activity of different compounds, which probably would be metabolized in different ways. That would also explain why amphotericin B (the most active antileishmanial drug but second-option treatment), was also more efficient in *L. brasiliensis* than in *L. amazonensis*. According to Croft et al. [23], although such change in sensitivity has been reported in several laboratory studies, different assay conditions can lead to a quite distinctive activity values.

Table 1. Effects of dillapiole and its analogues on the growth of *L. amazonensis* and *L. brasiliensis* promastigote forms.

Compounds	Inhibitory concentration IC_{50} (μM)[a]	
	Leishmania amazonensis	***Leishmania brasiliensis***
Dillapiole	69.3 ± 4.9	59.4 ± 4.0
Di-hydrodillapiole	99.9 ± 10.4	90.50 ± 8.6
Isodillapiole	122.9 ± 13.9	109.8 ± 9.5
Amphotericin B	0.054 ± 0.0	0.033 ± 0.0

[a] Values are the mean ± SD of triplicates from three independent experiments ($p < 0.05$).

Regarding molecular structure and function, the *in vitro* studies showed that the antileishmanial activities of the tested compounds seem to be influenced by the nature and conformational arrangement of the side chain. Also, the inhibitory parasite growth ability apparently is related to the presence and position of the double bond in the side chain. The IC_{50} values found for the tested compounds clearly showed that either the reduction of double bond at C_{11}/C_{12} (**2**), or isomerization to C_{10}/C_{11} (**3**), were structural features unfavorable to the leishmanicidal activities. Then, the molecular modification of the allyl group is tolerated, but does not enhance the biological activity.

Cytotoxic assay

Evaluation of morphological changes induced by dillapiole

Morphological changes on 3T3 fibroblasts cells were analyzed in order to evaluate the cytotoxic effects of dillapiole (**1**) and the obtained results are presented in Fig. 3. The untreated cells showed a high confluency of monolayer cells without morphological changes. The morphological changes observed with 100–25 μM of dillapiole (**1**) were the following: reduction in cell volume, cell shrinkage, chromatin condensation, and decreased cell density [24]. At the 12.5 μM concentration, similar morphology and confluency were observed in comparison to the untreated cells.

Cytotoxic activity of dillapiole on 3T3 fibroblast cells

Cytotoxic activity of dillapiole (**1**) was determined to verify the influence of this compound on fibroblast cells viability.

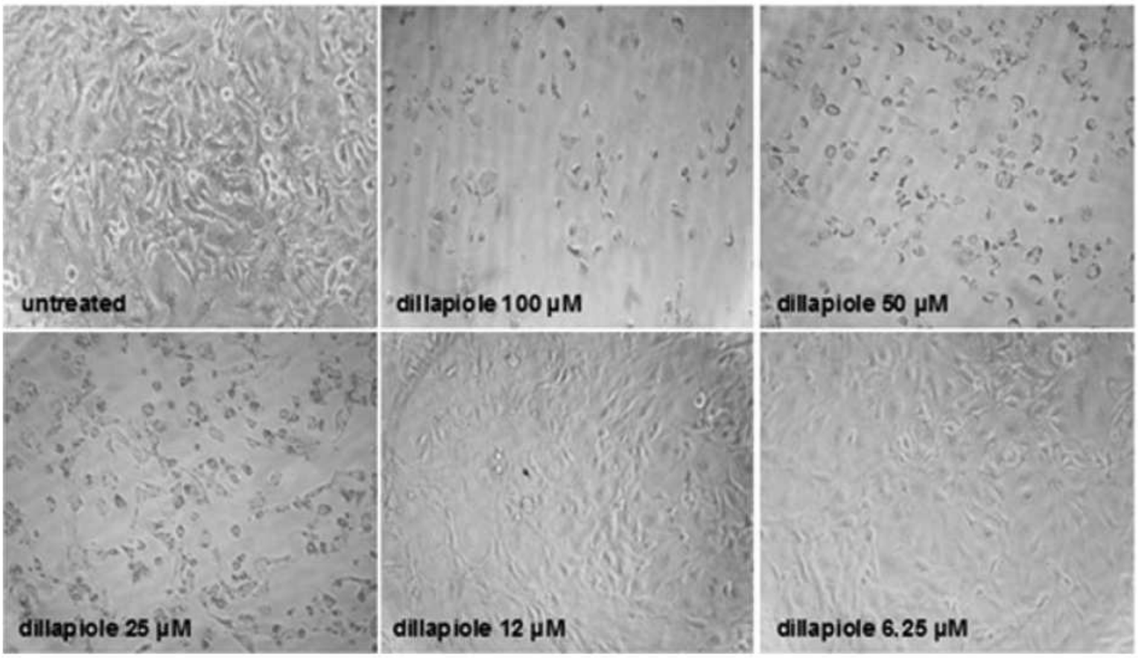

Figure 3. Morphological analysis of 3T3 fibroblast cells treated with dillapiole. After 24 h of treatment, dillapiole at 100–25 μM concentration induced changes in cell morphology and reduced the viability of the 3T3 fibroblast cells. Dillapiole at 12.5 and 6.25 μM did not reduce the cell viability, and the cells' morphology was similar to that of the untreated cells (magnification, 40×). Similar profile was observed in three independent experiments.

Although the toxicity profile of compounds **2** and **3** could be more appropriate than that of the lead compound (dillapiole), their cytotoxic activity was not determined since they had an IC_{50} against leishmania higher than the prototype. However, the results indicated that dillapiole (**1**) induces a dose-dependent cytotoxic effect after 24 h of treatment, presenting an inhibitory concentration of 22 μM (Fig. 4).

Then, compound **1** had low toxic effects on 3T3 fibroblast cells at lower concentrations, but at higher concentrations it can induce significant cytotoxic effects. Although the findings pointed out dillapiole (**1**) as relatively toxic to normal fibroblast cells in comparison to *Leishmania* promastigote forms, they also could suggest that compound **1** might have a dual cytotoxic effect, destroying the parasite and fibroblast cells simultaneously. Interestingly, this type of action is particularly relevant during the latent phase of the disease. Previous reports identified fibroblasts as important host cells for *Leishmania* during the chronic phase of infection, suggesting they might serve as safe targets for the parasites in clinically latent disease [25–27]. In this regard, compound **1** might have leishmanicidal effects even so the parasites are infecting non-phagocytic cells, such as fibroblasts. However, future studies must be performed in order to elucidate if dillapiole can present cytotoxic effects in fibroblast cells

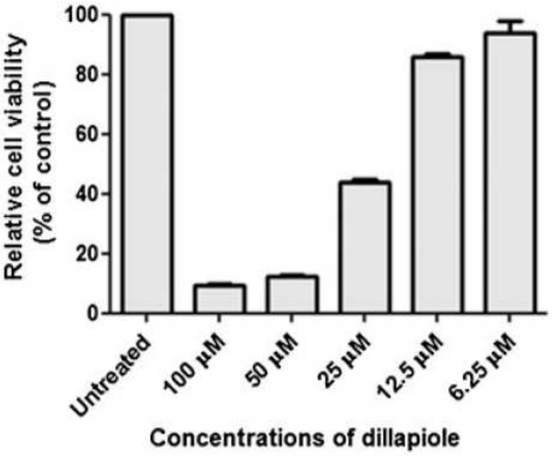

Figure 4. Cytotoxic effects of dillapiole on 3T3 fibroblast cells, after 24 h of treatment. MTT assay shows mouse fibroblast viability after treatment with different concentrations of dillapiole after 24 h. Cell viability is expressed as the viability of optical density values obtained from MTT assay and compared to the untreated cells. The data are the means ± SD from two independent experiments.

co-infected with *Leishmania* parasites. Moreover, the cytotoxic activities for compounds **2** and **3** must be evaluated in the future.

Molecular modeling findings

The purposes of the theoretical approach were to find a conformation energetically more favorable for dillapiole (**1**), di-hydrodillapiole (**2**), and isodillapiole (**3**), calculate its molecular properties, and finally provide some insights regarding structure–activity (leishmanicidal) relationships. In Table 2 are presented the thermodynamic descriptors found for the lowest-energy conformation selected from molecular dynamics (MD) simulation of each molecule, and the values obtained for the calculated molecular properties [lipophilicity (ClogP), electronic (μ, E_{HOMO}, E_{LUMO}, gap = $E_{HOMO} - E_{LUMO}$), and intrinsic/steric (V)].

The findings for MD simulations are presented in Fig. 5A–C. MD simulations (1 ns at 299 K) of dillapiole (Fig. 5A), di-hydrodillapiole (Fig. 5B), and isodillapiole (Fig. 5C) reached the thermodynamic equilibrium in approximately 300 000 simulation steps. Part of the conformational ensemble profile (CEP) (100 ps) from where the lowest-energy conformation of each molecule was chosen and, also, the 3D representation of selected conformers, such as space filling CPK and stick or tube molecular models, can be visualized in Fig. 5A–C.

The space filling CPK model considers the van der Waals radii of each chemical element in the molecular structure. This type of molecular model can provide insights regarding the steric hindrance of some chemical elements or substituent groups in the molecular system. The van der Waals volume values computed for compounds **1**, **2**, and **3** were 202.25, 207.29, and 201.04 Å^3, respectively (Table 2). Compound **2** has two more hydrogen atoms in comparison to the others. Although compounds **1** and **3** share the same number of atoms, their conformational arrangement was distinct and reflected in the molecular volume value.

As already mentioned, the thermodynamic descriptors as intramolecular energy contributions and total potential energy (E_T) found for the selected lowest-energy conformation of each molecule are listed in Table 2. Dillapiole (**1**) and isodillapiole (**3**), which have an unsaturated side chain attached to the aromatic ring of benzodioxole, showed closer E_T values (35.35 and 37.22 kcal/mol, respectively), whereas di-hydrollapiole (**2**), which has a saturated side chain, presented a little higher E_T value (39.83 kcal/mol). This finding is probably because the di-hydrodillapiole (**2**) structure has more degrees of freedom. Furthermore, it is noteworthy that the value of intramolecular hydrogen bonding energy contribution (E_{Hb}) was zero for all three molecules (see Table 2), which means the oxygen atoms in those molecular structures are not available to establish that kind of intramolecular interaction.

Regarding the selected conformations, the main structural difference seems to be the conformational arrangement of the side chain attached to the benzodioxole fragment. To better visualize the side chain arrangement, the selected conformation of each molecule was superimposed on one another using three ordered atomic positions (O_9, C_6, C_4) for fitting and overlay [29], as shown in Fig. 6.

It is well-known that the easiest way to reveal 3D structural features, common or distinct, to a set of compounds is the use of superimposition procedures [30]. Here, the superimposition is obvious because topological analogues are considered. The side chain of dillapiole (**1**), which has a double bond in the C_{11} and C_{12} position, did not remain in the same plane of the benzodioxole rings. Similar behavior was observed for the saturated side chain of di-hydrodillapiole (**3**), but its projection was into the opposite direction in comparison to the lead compound. For isodillapiole (**2**), the side chain remained in the benzodioxole rings' plane. This is probably due to the extension of the resonance effect (from aromatic ring to side chain) particularly provided by the double bond position (C_{10} and C_{11}). In Fig. 7A, atomic CHELPG charges by color, dipole moment vector, and EP maps are shown. The electronic density distribution can be visualized through the EP maps. For compound **3**, the higher electronic density is also

Table 2. Calculated molecular properties for dillapiole and its analogues.

Compound	$E_{stretch}$ (kcal/mol)	E_{bend} (kcal/mol)	E_{tors} (kcal/mol)	E_{1-4} (kcal/mol)	E_{vdW} (kcal/mol)	E_{charge} (kcal/mol)	E_{Hb} (kcal/mol)	E_{solv} (kcal/mol)	E_T (kcal/mol)
Dillapiole	8.16	17.59	4.99	12.39	−1.80	−2.29	0.00	−3.69	35.35
Di-hydrodillapiole	11.02	18.50	2.39	13.20	−0.95	−2.41	0.00	−1.92	39.83
Isodillapiole	6.24	18.95	5.15	13.70	−1.24	−2.47	0.00	−3.11	37.22

	ClogP	V (Å^3)	μ (Debye)	E_{HOMO} (kcal/mol)	E_{LUMO} (kcal/mol)	Gap[a] (kcal/mol)
Dillapiole	2.38	202.25	2.44	−121.96	6.02	−127.99
Di-hydrodillapiole	2.68	207.29	2.08	−121.42	10.42	−131.85
Isodillapiole	2.40	201.04	1.05	−116.55	−15.90	−100.65

[a] Gap = $E_{HOMO} - E_{LUMO}$.

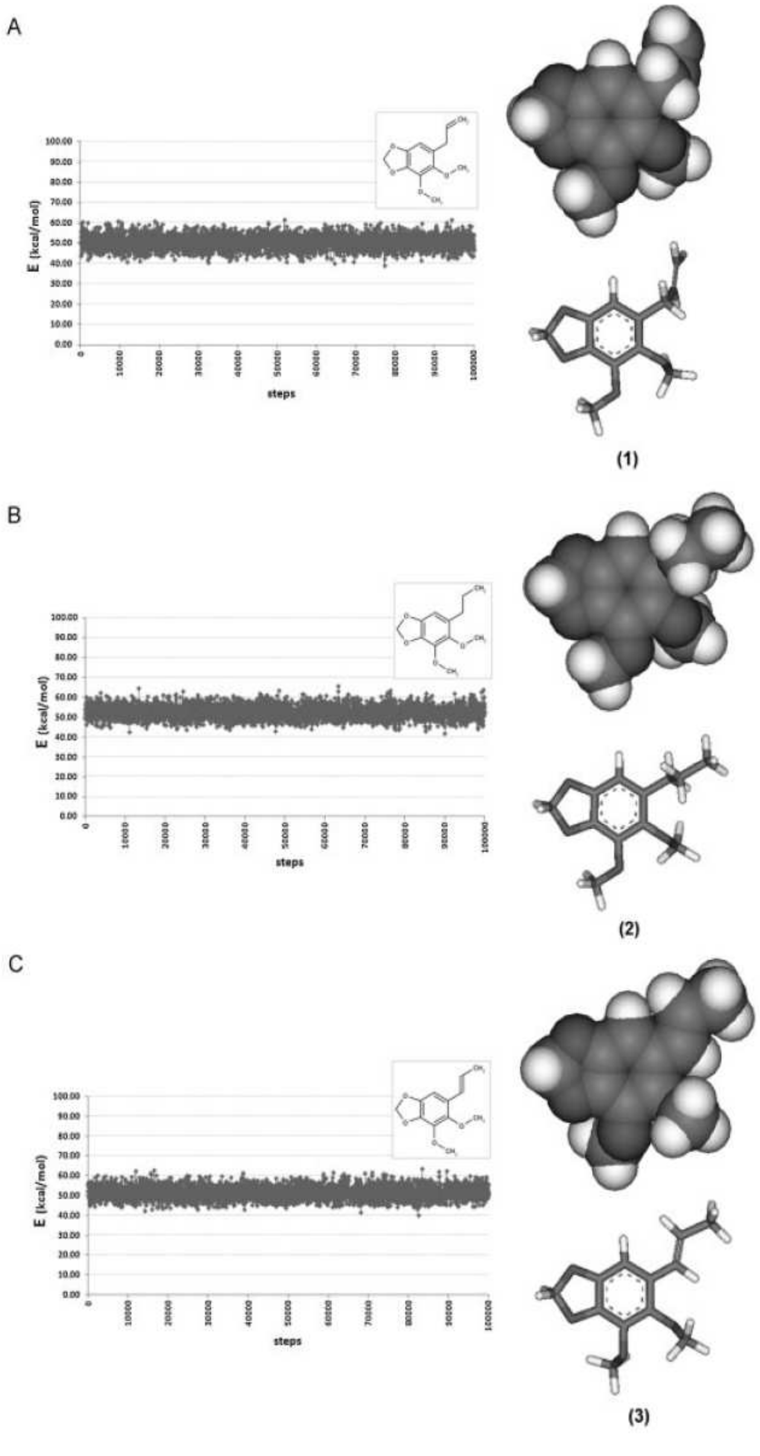

(1)

(2)

(3)

Figure 5. Plot of energy values *versus* steps for an equilibration region of the CEP (100 ps) from MD simulation (1 ns at 298 K) where the lowest-energy conformer of each molecule was selected: (A) dillapiole, (B) di-hydrodillapiole, and (C) isodillapiole. The energy values (kcal/mol) correspond to the summation of the following intramolecular energy contributions: stretching, bending, torsional, 1–4 or Lennard-Jones, van der Waals, and electrostatic. The lowest-energy conformation selected from each CEP is presented as space-filling CPK (Corey–Pauling–Koltun) and stick models. Carbon atoms are displayed in gray, oxygen in dark gray, and hydrogen in white [28].

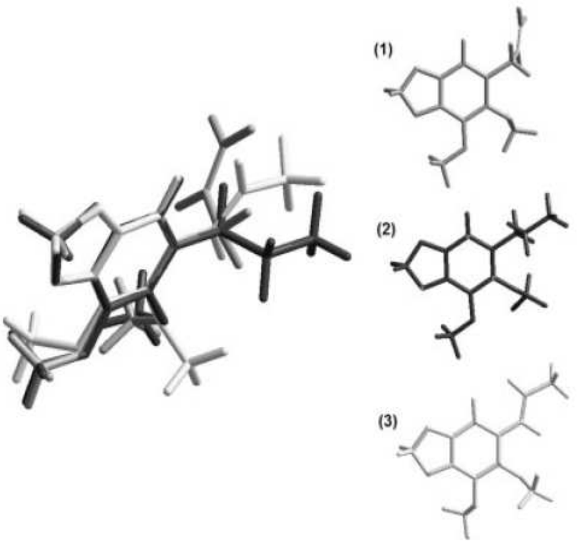

Figure 6. Superposition of dillapiole (**1**, light gray) and its analogues (**2**, dark gray; **3**, white) using the HyperChem 7.0 program [29]. The root-mean square deviation (RMSD) of atomic positions was 0.04 Å.

distributed on the side chain region (yellow color on the aromatic ring and side chain moiety) [Fig. 7A (**3**)], supporting the side chain structural arrangement.

The partial atomic electrostatic potential charges (ESP, CHELPG) are represented by a color range from red (negative; −0.404) to green (positive; 0.404; Fig. 7A). The C_{10} atom (attached to aromatic ring) in the lead compound (**1**) is in bright green color and its charge value is about threefold more positive (0.3254) than that found for compound **2** (0.1445). This data indicates that compound **1** could likely suffer a nucleophilic attack, but only in the opposite face of its side chain direction where there is no steric hindrance. Otherwise, the C_{10} atom has a negative charge value (−0.1030) in compound **3** and establishes a double bond with C_{11} (−0.1038).

The dipole moment (μ) vector can be visualized as blue arrows in Fig. 7A. By definition, the dipole moment is the product of the total amount of positive or negative charge and the distance between their centroids. The μ values are listed in Table 2 and this electronic property is related to the molecule's polarity. Additionally, from the dipole moment information deductions can be made about the molecular geometry of a compound. Compound **3** presented the lowest μ value (1.05) in comparison to compounds **1** (2.44 Debye) and **2** (2.08 Debye), and it is the only compound with a linear molecular geometry (benzodioxole and side chain in the same plane).

The lipophilicity property, expressed through the calculated *n*-octanol/water partition coefficient (ClogP), is also listed in Table 2. The partition coefficient reveals the hydrophobic character of a drug or compound. Compound **2** presented the highest ClogP value (2.68) in comparison to compounds **1** (2.38) and **3** (2.40). Generally, increasing the hydrophobicity of a lead compound can result in an improvement of biological activity. This reflects the fact that drugs have to cross hydrophobic barriers such as cell membranes in order to reach their target. Even if there are no barriers to be crossed, the drug has to interact with a target system such as an enzyme or receptor where the binding site is usually hydrophobic. Otherwise, the drug should not become so hydrophobic that it would be poorly soluble in the aqueous phase, for instance or, alternatively, it might be 'trapped' in fat depots and never reach the intended interaction site. Then, hydrophilic/hydrophobic molecular balance is needed to provide suitable pharmacodynamic and pharmacokinetic profiles.

If the ratio between μ and ClogP properties was considered as a measure of molecular hydrophilic/hydrophobic balance and related to the leishmanicidal activity (compound **1** > **2** > **3**), the theoretical findings would be in agreement with those experimentally observed in this study. That means, the higher the μ/ClogP value, the more active would be the compound. In this regard, the μ/ClogP values found for compounds **1**, **2**, and **3** were 1.02, 0.78, and 0.44, respectively.

The molecular orbital energies (E_{HOMO} and E_{LUMO}; kcal/mol) as well as the difference among them (gap = $E_{\mathrm{HOMO}} - E_{\mathrm{LUMO}}$; kcal/mol) were computed for the selected lowest-energy conformation of each molecule and are listed in Table 2. The gap values give information about molecular reactivity. Additionally, the HOMO and LUMO distribution maps for each compound are displayed in Fig. 7B. Compounds **1** and **2** presented quite similar E_{HOMO} values (−121.96 and −121.42 kcal/mol) whereas compound **3** had a less negative energy value (−116.55 kcal/mol). The main difference in the HOMO distribution maps was on the side chain moiety (Fig. 7B). The molecular orbital lobes are bigger on the side chain of compound **3** (double bond). Also, compound **3**, which has lower leishmanicidal activity, had a less negative (more reactive) gap value (−100.65 kcal/mol) than compounds **1** and **2**.

The positive E_{LUMO} values found for compounds **1** (6.02 kcal/mol) and **2** (10.42 kcal/mol) associated to the positive charge (CHELPG) in the C_{10} atom of the side chain would support the possibility of a nucleophilic approach in a charge–transfer interaction. However, the LUMO distribution map of compound **2** is distinct from that of compound **1**, probably because of the absence of a double bond in the side chain. Regarding the gap values, compound **2** had a more negative (less reactive) gap value (−131.85 kcal/mol) than

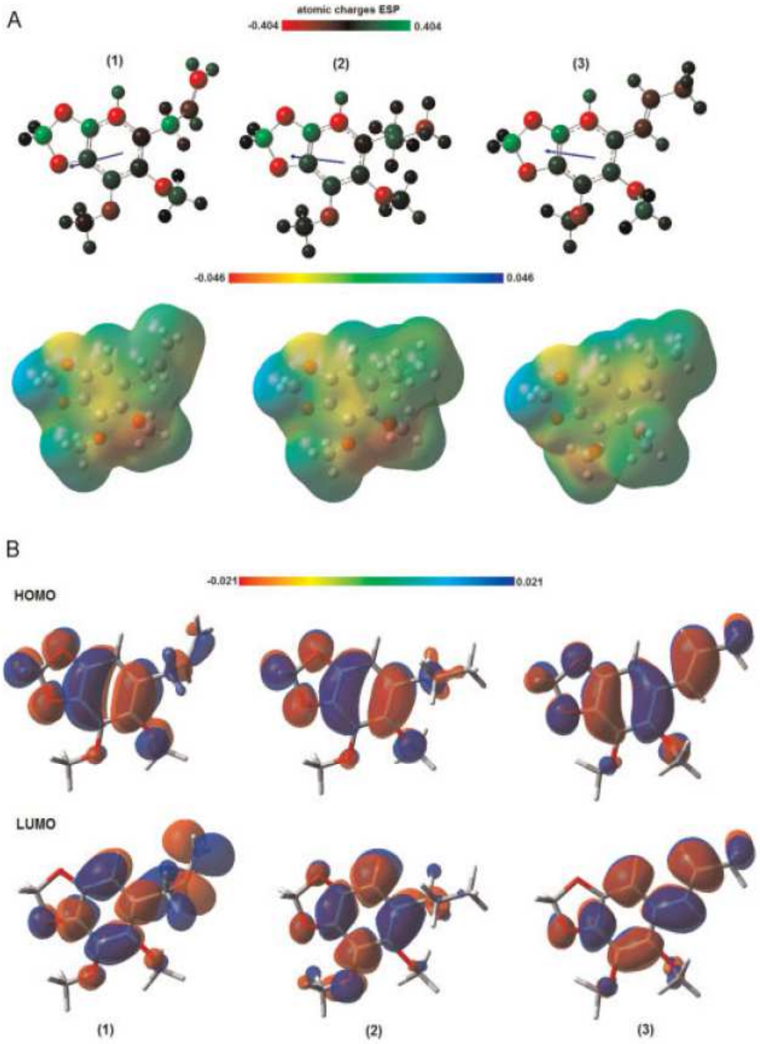

Figure 7. Electronic properties found for dillapiole (**1**) and its analogues (**2**, **3**). (A) Electrostatic potential atomic charges (ESP, CHELPG) by color [atomic charge color ramp: −0.404 (red) to 0.404 (green)]; (B) total dipole moment vector (blue arrows); and maps of electrostatic potential (MEPs) [color range: −0.046 (intense red) to 0.046 (intense blue)]. The molecules are presented as ball–wire models (carbon atoms in gray, oxygen in red, and hydrogen in white). (C) Distribution of molecular orbital maps, HOMO and LUMO [color range: −0.021 (red) to 0.021 (blue)]. The molecules are shown as stick models (carbon atoms in gray, oxygen in red, and hydrogen in white) [31].

compound **1** (−127.99 kcal/mol). Conversely, compound **3** had a negative E_{LUMO} value (−15.90 kcal/mol).

Conclusions

This preliminary study regarding structure–activity relationships has allowed the refinement of structural requirements for the dillapiole action against leishmaniasis. Dillapiole presented relevant effects against both *Leishmania* species, but *L. brasiliensis* proved to be more sensitive. Additionally, dillapiole reduced fibroblast cell viability, indicating that this compound might have antileishmanial effects on non-phagocytic cells in the disease's latent phase. Also, dillapiole did not reduce fibroblast cell viability and no morphological changes were observed, indicating that it is a safe compound. Although dillapiole analogues have exhibited moderate antileishmanial activity, they can also be considered as potential hits.

Molecular modeling approach aided the elucidation of which molecular properties would be important to improve the antileishmanial activity of the lead compound. Structural/conformational arrangement and electronic properties as well as the hydrophilic/hydrophobic balance seem to be crucial, particularly considering the allyl side chain.

The findings indicated that certain phenylpropanoids, such as dillapiole, exhibit interesting antileishmanial properties, and could also have some effects against other intracellular pathogens or phylogenetically related parasites as *Trypanosoma* spp., for instance. The potent leishmanicidal activity of dillapiole reported here represents an exciting advance for developing novel antiprotozoal agents. Indeed, further studies regarding *in vivo* antileishmanial activity are needed and are already in process. Even though, dillapiole and its analogues can be taken as potential candidates for lead optimization and the design of new antileishmanial drugs.

Experimental

General procedures

Reagents and solvents are of commercial grade and were used as supplied. Chromatography separations were performed using 70–230 mesh silica gel. Thin-layer chromatography was carried out on Merck silica plates (0.25 mm layer thickness). GC–MS was performed using a 14B/QP5050A Shimadzu-brand GC-MS apparatus; Class 5000 software; column: SPB-1.30 m, 0.53 mm ID, 1.5 μm film; helium as carrier gas (flow rate 1.5 mL/min). The ionization mode was EL at 70 eV. Temperature program was from 40°C (rate 5°C/min) to 250°C (30 min). The detector and injector temperatures were both 250°C. NMR spectra were recorded using a Bruker AC-300 spectrometer at 300 MHz (^{1}H) and 75 MHz (^{13}C) with tetramethylsilane as internal reference and $CDCl_3$ as solvent. Chemical shifts are given in ppm (parts per million), coupling constants in Hertz, and splitting patterns were designated as follows: s, singlet; br s, broad singlet; d, doublet; t, triplet; q, quartet, and m, multiplet.

Chemistry

Extraction of dillapiole from P. aduncum

Piper aduncum leaves were collected in March and August, 2011, in Ubatuba, Sao Paulo, Brazil. Identification was carried out at the Botanical Laboratory of Mackenzie Presbyterian University (MPU). The exsiccate of *P. aduncum* leaves was stored in the MPU herbarium (no. 01092). The collected vegetable material underwent the extraction of its essential components through hydrodistillation, using a modified Clevenger-type apparatus. The crude essential oil was extracted with dichloromethane, then dried with anhydrous Na_2SO_4, filtered, and kept in a freezer (−15°C), using an amber glass flask. The essential oil composition was further analyzed by GC–MS.

Purification of dillapiole (**1**)

Dillapiole was isolated and purified from the essential oil by using a chromatography column (CC). The CC was packed with silica gel 60 and the eluent system was hexanes/dichloromethane (7:3). The sample was eluted with the same solvent system, and 20 flasks were retrieved. Those that presented only dillapiole were grouped together, mixed, and kept in a freezer at −15°C. The pure sample was used to evaluate the *in vitro* leishmanicidal activity and also to synthesize the analogues. Viscous yellow liquid. ^{1}H NMR ($CDCl_3$, 300 MHz, δ = ppm, J = Hz): 3.31 (d, 2H, H-8); 3.75 (s, 3H, H-11); 4.00 (s, 3H, H-12); 5.01 (d, 2H, H-10); 5.88 (m, 1H, H-9); 6.15 (s, 2H, H-1); 6.35 (s, 1H, H-6). ^{13}C NMR ($CDCl_3$, 75MHz, δ = ppm): 34.5 (C8); 60.3 (C11); 60.8 (C12); 101.5 (C1); 102.4 (C6); 115.9 (C10); 122.1 (C5); 132.3 (C2); 136.5 (C9); 142.0 (C7); 143.6 (C4); 145.1 (C3) (1.5 g yield).

Di-hydrodillapiole (**2**) synthesis

In a 100 mL round-bottomed flask, fitted with a reflux condenser and drying tube, dillapiole (2 mmol; 0.45 g), $NaBH_4$ (20 mmol; 0.75 g), $NiCl_2 \cdot 6H_2O$ (1.5 mmol; 0.36 g) were dissolved in 40 mL of methanol. The mixture was kept under reflux and constant stirring for 24 h. After cooling, the product was filtered and the solution was concentrated to dryness under vacuum and the residue was subjected to flash column chromatography (hexanes/dichloromethane 7:3 v/v). Viscous yellow liquid. ^{1}H NMR ($CDCl_3$, 300 MHz, δ = ppm, J = Hz): 0.91 (t, 3H, H-10, J = 8.0); 1.54 (m, 2H, H-9, J = 8.0 and J = 7.1); 2.49 (t, 2H, H-8, J = 7.1); 3.73 (s, 3H, H-11); 3.95 (s, 3H, H-12); 5.87 (s, 2H, H-1); 6.34 (s, 1H, H-6). ^{13}C NMR ($CDCl_3$, 75 MHz, δ = ppm): 13.86 (C10); 25.60 (C9), 33.57 (C8); 59.85 (C11); 59.91 (C12); 101.00 (C1); 105.38 (C6); 127.39 (C5); 135.54 (C2); 137.59 (C7); 144.39 (C3); 144.45 (C4) (86% yield).

Isodillapiole (**3**) synthesis

In a 25 mL round-bottomed flask, fitted with a reflux condenser and drying tube, dillapiole (24.7 mmol; 4 g) in a 17% solution of potassium hydroxide (3.4 g) was dissolved in 20 mL of butyl alcohol. The reaction was kept under reflux and constant stirring for 24 h. After cooling, the mixture was neutralized with 1.2 mL of concentrated HCl and 8 mL of distilled cold water. The organic phase was washed with three portions of water (20 mL). The organic phase was dried with anhydrous Na_2SO_4. The excess of butyl alcohol was evaporated and the residue was submitted to distillation under reduced pressure. Viscous yellow liquid. ^{1}H NMR ($CDCl_3$, 300 MHz, δ = ppm, J = Hz): 1.86–1.89 (dd, 3H, H-10, J = 6.4 and J = 1.0); 3.75 (s, 3H, H-11); 3.88 (s, 3H, H-12); 5.91 (m, 1H, H-9, J = 15.1 and J = 6.4); 6.05–6.07 (s, 2H, H-1); 6.51–6.59 (d, 1H, H-8, J = 15.1); 6.96 (s, 1H, H-6). ^{13}C NMR ($CDCl_3$, 75 MHz, δ = ppm): 18.81 (C10); 59.81 (C11); 60.10 (C12); 101.51 (C1); 102.76 (C6); 125.51 (C8); 126.62 (C5); 128.34 (C9); 134.56 (C2); 136.01 (C7); 141.43 (C3); 147.50 (C4) (85% yield).

In vitro leishmanicidal activity

The leishmanicidal activity of dillapiole and its analogues were evaluated through the growth inhibition of promastigote forms of *L. amazonensis* (strain MHOM/BR/90/BA125) and *L. brasiliensis* (strain MHOM/BR/94/H−3227). The cells were grown at 26°C in Schneider's medium supplemented with 10% v/v fetal bovine serum (FBS) at 26°C during 24 h. The cells were harvested, resuspended, then counted in a Neubauer chamber, and adjusted to a concentration of 1×10^6 cells/mL. Concentrations of 150–1 μM for dillapiole and analogues were used to evaluate biological activity. All compounds were solubilized in dimethylsulfoxide (DMSO). Amphotericin B was used as reference drug. As negative control, promastigote forms were used in complete Schneider's medium. The substances were analyzed in triplicate and promastigote forms were counted in comparison to negative control. Results were expressed as inhibitory concentration causing 50% (IC_{50}) reduction in parasite growth [32].

Cytotoxic assay

Cell culture

The 3T3 mouse fibroblast cells were kindly provided by Dr. Alisson Leonardo Matsuo of the Universidade Federal de Sao Paulo (UNIFESP). Cells were cultured in Dulbecco's Modified Eagle Medium (DMEM) (Gibco) supplemented with 10 nM HPES, 24 nM sodium bicarbonate, 10% heat-inactivated FCS, and 40 μg/mL gentamicin sulfate. Cells were maintained in humidified air with 5% CO_2 at 37°C.

Morphological observation of cytotoxic effects

The 3T3 fibroblast cell line was grown in 12-well plates and treated with dillapiole 100–12.5 μM for 24 h. The cells were then washed with 1× PBS and added to the culture medium. Morphological changes in the cells induced by dillapiole were observed using a phase inverted microscope (Nikon TMS).

Cytotoxic test

The MTT colorimetric assay was used to evaluate the cytotoxic activity of dillapiole in normal cells. Briefly, the 3T3 fibroblast cells were seeded in 96-well plates at 10^4 cells/well density in 100 μL culture medium. Following 24 h incubation and attachment, the cells were treated with 100–12.5 μM of dillapiole for 24 h. After the end of treatment, cells were exposed to 5 mg/mL MTT for 3 h. Medium was removed, the formazan dye trapped in the living cells was dissolved in DMSO, and absorbance was measured at 570 nm using a microplate reader (Rayto Life and Analytical Sciences C. Ltd, Germany). Then, the IC_{50} value was determined.

Molecular modeling approach

The three-dimensional (3D) molecular models of dillapiole and analogues were built up, in their neutral forms, using the HyperChem 7.0 MM+ force field [29] without any constraints. The crystal data from 6-[1-(4-ethoxyphenyl)ethyl]-5-methoxy-1,3-benzodioxole [33] was employed as starting geometry. Partial atomic charges were computed with AM1 semiempirical method [34], also implemented in HyperChem 7.0 [29]. The MOLSIM 3.2 software [35] was used to carry out energy-minimization (steepest descent and conjugate gradient methods; convergence criterion of 0.01 kcal/mol) and MD simulations. MD simulations of 1 ns (step size of 1 fs) at 299 K, which is the same temperature as in the biological assay, were performed for each molecular model. Output trajectory file was recorded every 20 ps steps resulting in a CEP of 50 000 conformers for each investigated molecule. The lowest-energy conformation was selected from CEP, and the hydration shell model [36] was employed to estimate the solvation energy contribution. The hydrogen bonding intramolecular energy contribution was also computed for the selected lowest-energy conformation. The total potential energy (E_T) of each selected conformation corresponds to the summation of the following intramolecular energy contributions: stretching ($E_{stretch}$), bending (E_{bend}), torsional (E_{tors}), Lennard-Jones or 1–4 interactions (E_{1-4}), electrostatic (E_{charge}), van der Waals (E_{vdW}), hydrogen bonding (E_{Hb}), and solvation (E_{solv}).

The lowest-energy conformation of each molecule from MD simulations was energy-minimized [35] and, subsequently, used as starting geometry to calculate molecular properties of distinct nature (electronic, steric, and hydrophobic). Electronic properties as partial atomic charges from electrostatic potentials using a grid based method [37], dipole moment (μ), molecular orbital energies (E_{HOMO}, energy of the highest occupied molecular orbital; E_{LUMO}, energy of the lowest unoccupied molecular orbital), and electrostatic potential (EP), were computed with the B3LYP (Becke, three-parameter, Lee-Yang-Parr) [38] hybrid functional and 6–31(d,p) basis set [39]. EP maps were calculated onto a Connolly molecular surface, using a color scheme ranging from −0.046 (intense red) to 0.046 (intense blue). Negative values of EP (higher electronic density distribution) are depicted in red and positive values in blue (lower electronic density distribution) [39]. The molecular volume (V) of dillapiole and analogues was calculated using the grid method reported by Bodor et al. [40] with the atomic radii of Gavezzotti [41]. The bounding surface was specified as van der Waals and the density of grid points was set as 50 points on cube side [29]. Also, the calculated octanol/water partition coefficient (ClogP), which is a measure of molecular hydrophopicity, was computed based upon the method of Viswanadhan et al. [42], implemented in the Marvin 5.8.0 package, Calculator Plugins [43].

Statistical analysis

The results were expressed as average + standard average error. The one-way analysis of variance (ANOVA) was employed followed by Student's *t*-test to evaluate the findings. Probability values (p) <0.05 were considered statistically significant [44].

The authors are grateful to Mackpesquisa for financial support, to Professor Leoberto Costa Tavares, coordinator of the Laboratory for Designing and Development of New Drugs, Department of Biochemical and Pharmaceutical Technology, Faculty of Pharmacy at the University of Sao Paulo, who kindly allowed the use of a workstation to perform the in silico analysis, and to the Chem21 Group, Inc., for the MOLSIM 3.2 software academic license.

The authors have declared no conflict of interest.

References

[1] WHO – World Health Organization, **2011**, available <http://www.who.int/leishmaniasis/disease_epidemiology/en/index.html>. Acessed on April 12, 2012.

[2] C. Viegas-Junior, V. S. Bolzani, E. J. Barreiro, *Quím. Nova* **2006**, *29*, 326–337.

[3] V. Cechinel Filho, R. A. Yunes, *Quím. Nova* **1998**, *21*, 99–105.

[4] C. A. Montanari, V. S. Bolzani, *Quím. Nova* **2001**, *24*, 105–111.

[5] M. A. Brenzan, C. V. Nakamura, B. P. Dias Filho, T. Ueda-Nakamura, M. C. M. Young, D. A. G. Cortez, *Parasitol. Res.* **2007**, *101*, 715–722.

[6] P. R. R. Costa, *Rev. Virtual Quim.* **2009**, *1*, 58–66.

[7] T. G. Yunker, *Hohenia* **1972**, *1*, 19–366.

[8] V. Parmar, S. C. Jain, K. S. Bisht, R. Jain, P. Taneja, A. Jha, O. D. Tyagi, A. K. Prasad, J. Wengel, C. E. Olsen, P. M. Boll, *Phytochemistry* **1997**, *46*, 597–673.

[9] J. H. G. Lago, C. S. Ramos, D. C. C. Casanova, A. Morandim, D. C. B. Bergamo, A. J. Cavalheiro, V. S. Bolzani, M. Furlan, E. F. Guimarães, M. C. M. Young, M. J. Kato, *J. Nat. Prod.* **2004**, *67*, 1783.

[10] R. Parise-Filho, M. Pastrello, C. E. P. Camerlingo, G. J. Silva, L. A. Agostinho, T. Souza, F. M. M. Magri, R. R. Ribeiro, C. A. Brandt, M. C. Polli, *Pharm. Biol.* **2011**, *49*, 1173–1179.

[11] D. M. M. H. Silva, C. N. Bastos, *Fitopatol. Bras.* **2007**, *32*, 143–145.

[12] T. S. E. Caio, M. D. Lima, M. A. C. Kaplan, M. M. Nazareth, B. Rossi-Bergmann, *Antimicrob. Agents Chemother.* **1999**, *43*, 1234–1241.

[13] N. Flores, G. Cabrera, I. A. Jiménez, J. Pinero, A. Jiménez, G. Bourdy, F. Cortes-Selva, I. L. Bazzocchi, *Planta Med.* **2007**, *73*, 206–211.

[14] A. Sarkar, R. Sen, P. Saha, S. Ganguly, G. Mandal, M. Chatterjee, *Parasitol. Res.* **2008**, *102*, 1249–1255.

[15] J. P. Antony, L. Fyfe, H. Smith, *Trends Parasitol.* **2005**, *21*, 462–468.

[16] L. Monzote, G. Marley, A. M. Montalvo, S. Ramón, M. Migdalia, *Inst. Oswaldo Cruz.* **2010**, *105*, 168–173.

[17] C. B. Bernard, H. G. Krishinamurty, D. Chauret, T. Durst, B. J. R. Philogene, P. Sanchés-Vindas, C. Hasbaun, L. Poveda, L. S. Roman, J. T. Arnason, *J. Chem. Ecol.* **1995**, *21*, 801–814.

[18] A. K. S. Lobato, D. G. C. Santos, F. C. Oliveira, D. D. S. Gouvêa, G. I. O. S. Torres, J. A. Lima-Junior, C. F. Oliveira-Neto, M. H. L. Silva, *Rev. Bras. Biocien.* **2007**, *5*, 915–919.

[19] O. R. M. Gottlieb, M. Koketsu, M. T. Magalhães, J. G. S. Maia, P. H. Mendes, A. I. Rocha, M. L. Silva, V. C. Wilberg, *Acta Amazonica* **1981**, *11*, 143–148.

[20] M. Narisada, I. Horibe, F. Watanabe, F. Takeda, *J. Org. Chem.* **1989**, *54*, 5308–5311.

[21] M. E. F. Lima, A. J. A. Gabriel, R. N. Castro, *J. Braz. Chem. Soc.* **2000**, *11*, 371–375.

[22] P. J. Guerin, P. Olliaro, S. Sundar, M. Boelvaert, S. L. Croft, P. Desjeux, *Lancet Infect. Dis.* **2002**, *2*, 494–501.

[23] S. L. Croft, S. Sundar, A. H. Fairlamb, *Clin. Microbiol. Rev.* **2006**, *19*, 111–126.

[24] A. K. Ferreira, R. Meneguelo, A. Pereira, O. R. Mendonça Filho, G. O. Chierice, D. A. Maria, *Anticancer Res.* **2012**, *32*, 95–104.

[25] C. Bogdan, N. Donhauser, R. Döring, M. Röllinghoff, A. Diefenbach, M. G. Rittig, *J. Exp. Med.* **2000**, *191*, 2121–2130.

[26] I. Ramírez-Macías, C. Marín, H. Es-Samti, A. Fernández, J. J. Guardia, H. Zentar, A. Agil, R. Chahboun, E. Alvarez-Manzaneda, M. Sánchez-Moreno, *Parasitol. Int.* **2012** [in press].

[27] D. A. Vargas-Inchaustegui, A. E. Hogg, G. Tulliano, A. Llanos-Cuentas, J. Arevalo, J. J. Endsley, L. Soong, *Infect. Immun.* **2010**, *78*, 301–308.

[28] ViewerLite 5.0, Accelrys, Inc. 2002.

[29] HyperChem Program Release 7.0 for Windows, Hybercube, Inc., Gainesville, FL **2002**.

[30] N. C. Cohen, *Guidebook on Molecular Modeling in Drug Design*, Academic Press, San Diego **1996**, 361p.

[31] GaussView for Windows, version 5.0, Gaussian, Inc., 2000–2008.

[32] M. R. Camacho, S. L. Phillipson, P. N. Croft, S. J. Marshall, S. A. Ghazanfar, *J. Ethnopharmacol.* **2003**, *89*, 185–191.

[33] P. Ala, D. S. C. Yang, *Acta Cryst.* **1995**, *51*, 1917–1919.

[34] M. J. S. Dewar, E. G. Zoebisch, E. F. Healy, J. J. P. J. Stewart, *Am. Chem. Soc.* **1985**, *107*, 3903–3909.

[35] D. Doherty, *MOLSIM: Molecular Mechanics Dynamics Simulation Software–User's Guide version 3.2*, The Chem21 Group, Inc., Lake Forest, IL **2002**.

[36] K. H. Forsythe, A. J. Hopfinger, *J. Macromol.* **1973**, *6*, 423–437.

[37] C. M. Breneman, K. B. J. Wiberg, *Comput. Chem.* **1990**, *11*, 361–373.

[38] A. D. Becke, *J. Chem. Phys.* **1993**, *98*, 1372–1377.

[39] Gaussian 03, Revision C.02, M. J. Frisch, G. W. Trucks, H. B. Schlegel, G. E. Scuseria, M. A. Robb, J. R. Cheeseman, J. A. Montgomery, T. Vreven, K. N. Kudin, J. C. Burant, J. M. Millam, S. S. Iyengar, I. J. Tomas, E. V. Baron, B. Mennucci, M. Cossi, G. Scalmani, N. Rega, G. A. Petersson, H. Nakatsuji, M. Hada, M. Ehara, K. Toyota, R. Fukuda, J. HasegawA M. Ishida, T. Nakajima, Y. Honda, O. Kitao, H. Nakai, M. Klene, X. Li, J. E. Knox, H. P. Hratchian, J. B. Cross, V. Bakken, C. Adamo, J. Jaramillo, R. Gomperts, R. E. Stratmann, O. Yazyev, A. J. Austin, R. Cammi, C. Pomelli, J. W. Ochterski, P. Y. Ayala, K. Morokuma, G. A. Voth, P. Salvador, J. J. Dannenberg, V. G. Zakrzewski, S. Dapprich, A. D. Daniels, M. C. Strain, O. Farkas, D. K. Malick, A. D. Rabuck, K. Raghavachari, J. B. Foresman, J. V. Ortiz, Q. Cui, A. G. Baboul, S. Clifford, J. Cioslowski, B. B. Stefanov, G. Liu, A. Liashenko, P. Piskorz, I. Komaromi, R. L. Martin, D. J. Fox, T. Keith, M. A. Al-Laham, C. Y. Peng, A. Nanayakkara, M. Challacombe, P. M. W. Gill, B. Johnson, W. Chen, M. W. Wong, C. Gonzalez, J. A. Pople, Gaussian, Inc. **2004**.

[40] N. Bodor, Z. Gabanyi, C. K. Wong, *J. Am. Chem. Soc.* **1989**, *111*, 3783–3786.

[41] A. Gavezzotti, *J. Am. Chem. Soc.* **1983**, *105*, 5220–5225.

[42] V. N. Viswanadhan, A. K. Ghose, G. R. Revankar, R. K. Robins, *J. Chem. Inf. Comput. Sci.* **1989**, *29*, 163–172.

[43] Marvin Beans 5.8.0 Software – Calculator Plugins 2012, Chemaxon Ltd.: Budapeste 1037, Hungary.

[44] R. R. Sokal, F. J. Rohlf, *Biometry – The Principles and Practice of Statistics*, second edition, W.H. Freemann, New York **1981**, 859 p.